ALTERATION TO THE SHALLOW-WATER TIDES AND TIDAL ASYMMETRY BY TIDAL-STREAM TURBINES

Daniel Potter

A thesis submitted in partial fulfilment

for the degree of Doctor of Philosophy

Lancaster Environment Centre

UK

June 2018

Abstract

Tidal flow velocity asymmetry (FVA) plays a crucial role in residual sediment transport and has been shown to impact significantly on the amount of tidal energy that is technically extractible by tidal-stream turbines (TSTs). TSTs are known to alter tidal hydrodynamics locally, and large arrays of turbines do this on regional scales. However, less is known about the effect of TSTs on the FVA. This thesis explores changes to the FVA and therefore the shallow-water tidal constituents resulting from the deployment of TSTs. Numerical experiments in a uniform rectangular channel were undertaken, using the MIKE21 software package. The effects of single TSTs and multiple TSTs on tidal hydrodynamics were simulated, as well as those of a single TST on sediment transport. Flood-ebb asymmetry in the spatial distribution of current attenuation by the turbines altered the FVA. The overall attenuation of the current led to predictable changes in the total available tidal energy per tidal cycle, and the gross volume of sediment transported. The attenuation of the current by the TSTs was of greater importance to these aspects of the environment than any changes to the FVA that they caused. Changes in the FVA led to changes in the flood-ebb asymmetry of the available power, and the net volume of sediment transported, and were of far greater importance than the overall attenuation of the current in these respects. Multiple turbines deployed in a line along the channel, such that their areas of effect overlapped, had an additive effect on the FVA. When deployed as a row across the channel width, the total area affected by the turbines remained similar to that of a single turbine, so long as an inter-turbine spacing of at least three turbine diameters was maintained.

Declaration

I declare that this Thesis is my own work, and has not been submitted in substantially the same form for the award of a higher degree elsewhere.

–Daniel Potter

Date:......................

Signature:................

Acknowledgements

First and foremost, I would like to thank my supervisors, Dr Andrew Folkard and Dr Suzana Ilić for providing me with the opportunity to undertake a PhD. As I look back over the last three and half years I feel that I have learned so much from working under their supervision, and their guidance and friendship over the course of the project has been invaluable.

This project was funded by NERC through the ENVISON doctoral training program. My thanks go to both for making this project possible.

I must also thank my family for their support throughout the project and my Dad and Jo in particular, especially towards the end of the project. I don't think it would be an overstatement to say that I don't know how I would have gotten over the final hurdles of writing-up without the offer of a place to live and financial support.

Last and by no means least, I would like to thank Niamh, and my friends, both in Lancaster and beyond, for being there to talk to about work, and more importantly, about anything but work.

Dedication

This thesis is dedicated to the memory of my mother, Jane Potter, and my grandparents, Tom and Ann McDonald.

Contents

List of Figures

List of Tables

Symbols

ΔQ_s Net volume of sediment transported per unit width over a tidal cycle

$\Delta Q_{s,bl}$ Net volume of sediment transported as bedload over a tidal cycle per unit width

$\Delta Q_{s,sl}$ Net volume of sediment transported as suspended load over a tidal cycle per unit width

$\Delta Q_{s,tl}$ Net volume of sediment transport as both suspended load and bed load over a tidal cycle per unit width

Δy Width of model element perpendicular to flow

Λ_M Lunar right ascension

Λ_S Solar right ascension

$\boldsymbol{\Omega}$ Angular velocity field of the Earth

$\Omega_{G,1,2}$ Gravitational potential between bodies 1 & 2

$\Omega_{G,P,M}$ Lunar gravitational potential at a point P on the Earth's surface

$\Omega_{T,P,M}$ Lunar tide generating potential at a point P on the Earth's surface

Ψ Relative phase between the M_2 and M_4 tides (in velocity)

Θ Shield's parameter

Θ_c Critical Shield's parameter value, beyond which sediment transport is initiated

α Velocity correction factor

β Relative contribution of a (tidal) constituent interaction to the overall tidal asymmetry

χ Hour angle of the Moon or Sun

δ Declination of the Moon or Sun north or south of the Earth's equator

η Water surface elevation (η_0 is the amplitude of η)

κ Von Karman constant

λ Tidal wavelength

λ_M Lunar *true* ecliptic longitude

λ_S Solar *true* ecliptic longitude

ν Kinematic viscosity

ω Angular speed

ϕ Phase of the tidal wave

ψ Phase of the velocity associated with the tidal wave

ρ Fluid mass density

ρ_s Density of sediment

σ Tidal frequency

τ Bed shear stress

τ' Skin friction

τ'' Form drag

τ_b Bed shear stress

τ_{bi} Bed shear stress in the i direction

τ_{si} Wind shear stress in the i direction

ε Obliquity of orbit (angle between ecliptic and the equatorial planes, Figure 2.3)

ε_0 Ratio of channel cross-section blocked by turbines at $\eta = 0$

ε_M Lunar *true* ecliptic longitude

ε_S Solar ecliptic latitude

φ Lunar angle (Figure 2.1); Lattitude

φ_P Latitude of point P on the Earth's surface

A Tidal-stream turbine rotor swept area; Tidal amplitude; Characteristic order of magnitude of incoming tidal wave; Effective eddy viscosity

a Sediment transport reference level

A_H Horizontal eddy viscosity

As Actual turbine spacing

$A_{S,1}$ Asymmetry between flood and ebb peaks of the tide, calculated from the harmonic analysis ($A_{S,1} = \frac{A_{M4}}{A_{M2}} \cos(\Psi)$)

$A_{S,2}$ Asymmetry between flood and ebb peaks of the tide measured directly from a tidal time-series ($A_{S,2} = 100 \times \frac{u_f - |u_e|}{\langle |u| \rangle}$)

A_v Asymmetry of velocity time-series, calculated by taking the skewness of the imaginary portion of the Hilbert transform of the time-series (following Bruder & Haas [2014])

b Channel width

B_0 Characteristic basin width length-scale

c Phase speed of tidal wave

C_0 Characteristic wave propagation speed

c_a Volumetric bed concentration

C_D Drag coefficient

C_E Electricity consumption

c_e Equilibrium concentration of sediment in suspsension

C_F Bed friction coefficent

C_L Turbine lift coefficent

C_N Total energy consumption

C' Chézy number

c_s Smagorinsky constant

C_T Tidal-stream turbine thrust coefficent

D Turbine diameter

d Grain diameter

D_0 Characteristic basin depth length-scale

d_{50} Median (50th percentile) grain diameter

d_{90} Grain size for which 90% of grains are finer

D_{ast} Non-dimensional sediment diameter

ΔE Difference in energy converted over the flood and ebb phases of the tide

E Channel cross-sectional area; Energy conversion by turbine

e Eccentricity of orbit

E_e Energy converted over the ebb phase of the tide

E_f Energy converted over the flood phase of the tide

$E_{t.c.}$ Energy converted per tidal cycle

f Frequency (units: cycles per mean solar day); Function of sediment and fluid characteristics (from the Bagnold [1966] equation); Coriolis frequency; Suspended load transport correction factor

$\vec{F}_D$ Turbine drag Force

$F_{G,1,2}$ Gravitational force between bodies 1 & 2

$\vec{F}_L$ Turbine lift force

Fp Array footprint

F_T 1D turbine thrust force

G Universal gravitational constant

g Acceleration due to gravity

$\widetilde{\boldsymbol{g}}$ Combined effect of gravity and centrifugal force due to the Earth's rotation

H Tangential component of the tide generating potential; Complex surface elevation

H Total water depth, water depth at $\eta = 0$, h, plus the water surface elevation, η

h Geocentric mean ecliptic longitude; Channel depth at $\eta = 0$

$H(\boldsymbol{v})$ Hilbert transform of the velocity time-series

Is Intended inter-turbine spacing

j_T Tidal energy flux

L Channel Length

l Characteristic length-scale of eddies

L_0 Characteristic basin length length-scale

M Manning number

m Non-negative, real test values used in the Babylonian method to approximate a square root

m_1 Mass of body 1

m_2 Mass of body 2

m_E Mass of the Earth

m_M Mass of the Moon

m_S Mass of the Sun

N Mean longitude of ascending lunar node; Number of tidal turbines deployed in basin; Total number of tidal constituents

N_0 Characteristic tidal elevation length-scale

P Point on the Earth's surface; Flow power

p' Longitude of solar perigee (perihelion)

p Longitude of lunar perigee

p Pressure

p_a Atmospheric pressure

P_T Turbine power

Q Volumetric fluid flow rate

Q_s Volume of sediment transported per unit width

q_s Volumetric sediment transport rate per unit width

$q_{s,bl}$ Volumetric rate of bedload sediment transport per unit width

$Q_{s,bl}^{t.c.}$ Total volume of sediment transported as bedload over a tidal cycle per unit width

Q_s^e Volume of sediment transported per unit width over the ebb phase of the tide

Q_s^f Volume of sediment transported per unit width over the flood phase of the tide

$q_{s,sl}$ Volumetric rate of suspended load sediment transport per unit width

$Q_{s,sl}^{t.c.}$ Total volume of sediment transported as suspend load over a tidal cycle per unit width

$Q_s^{t.c.}$ Total volume of sediment transported per unit width over a tidal cycle

$Q_{s,tl}^{t.c.}$ Total volume of sediment transported as both suspended load and bedload over a tidal cycle per unit width

R Turbine rotor radius

$\boldsymbol{r}$ Point within the fluid

$r_{1,2}$ Distance between bodies 1 & 2

R_E Radius of the Earth

r_M Distance between the Earth & Moon

RPR Relative Percentage Range

r_S Distance between the Earth & Sun

S Radiation stress-tensor

s Geocentric mean longitude; Relative density of sediment (to fluid)

Si Similarity index

S_{ij} Deformation ratem $i, j = x, y$

s_{ij} Components of the radiation stress tensor, $i, j = x, y$

S_v Skewness of the tidal velocity time-series

T Total number of time-steps in time series; Non-dimensional transport stage parameter

t Time

$\hat{u}$ Depth-averaged velocity in the x-direction ($\hat{u}_0$ is the amplitude of $\hat{u}$)

u x-component of the fluid flow velocity

u_0 x-component of upstream velocity

u_e Magnitude of current at maximum ebb

u_f Friction velocity

u_f Magnitude of current at maximum flood

$u_{f,c}$ Critical friction velocity

u_f' Effective friction velocity

Us Uniformity of inter-turbine spacing

u_s x-component of the point-source discharge velocity

$\boldsymbol{v}$ Fluid velocity field; Tidal velocity

v y-component of the fluid flow velocity

$\vec{V_0}$ Upstream velocity

v_0 y-component of upstream velocity

$\vec{V}_{\mathbf{local}}$ Velocity vector local to turbine

v_s y-component of the point-source discharge velocity

w_s Settling velocity

$\hat{x}$ One of the three unit vectors, along with $\underline{\hat{y}}$ & $\underline{\hat{z}}$, that describe the Cartesian coordinate system

x x-coordinate in Cartesian space

$\hat{y}$ One of the three unit vectors, along with $\underline{\hat{x}}$ & $\underline{\hat{z}}$, that describe the Cartesian coordinate system

y y-coordinate in Cartesian space

Z Rouse suspension parameter

$\hat{z}$ One of the three unit vectors, along with $\underline{\hat{x}}$ & $\underline{\hat{y}}$, that describe the Cartesian coordinate system

z z-coordinate in Cartesian space

Acronyms

AT Advection Term

CT Continuity Term

ECA Energy Conversion (flood-ebb) Asymmetry

EEZ Exclusive Economic Zone

EFT Elevation Friction Term

ETT Elevation Turbine Term

FDA Flow Duration Asymmetry

FM Flexible Mesh

FT Friction Term

FVA Flow Velocity Asymmetry

FVCOM Finite Volume Coastal Ocean Modelling System

LST Lateral Stress Term

MCT Marine Current Turbines Ltd.

OREDs Offshore Renewable Energy Developments

PDF Probability Density Function

PV Photovoltaic

QFT Quadratic Friction Term

QTT Quadratic Turbine Term

ROMS Regional Ocean Modelling System

TDA Tidal Duration Asymmetry

TST Tidal Stream Turbine

TT Turbine Term

UK United Kingdom

UKRED United Kingdom Renewable Energy Database

USA United States of America

Chapter 1

Introduction

This thesis is concerned with the extraction of energy from the natural tidal motions of the sea, specifically their kinetic, or "tidal-stream" energy. It reports research carried out using numerical models, and focuses on potential environmental impacts of this extraction. In this chapter, the wider concept of marine renewable energy is first introduced, in the context of its potential to meet the future energy demand in the UK relative to other renewable sources (§1.1). This is followed by a review of the current state of the tidal-stream industry (§1.2) and a review of the environmental impacts related to its development (§1.3). Having given this broad context, the structure of the rest of the thesis is outlined (§1.4).

1.1 Case for Tidal-Stream Energy

The UK Climate Change Act [2008] established the world's first legally binding climate change target, with the aim of reducing the UK's carbon emissions to 20% of the 1990 baseline value by 2050. One of the "common messages", identified through exploration of different strategies to meet this target in the 2050 Pathway Analysis was that decarbonisation of the electricity supply is required [H.M. Government, 2010]. At about the same time, the European Union set a target of 20% of energy consumption from renewable sources by 2020, within which the UK target is 15% by 2020 [European Union, 2009], which at the time of writing still applies to the UK. In response to this directive, the UK published a national energy plan in which "purely illustrative" targets of 30% renewable electricity, 12% renewable heat and

10% renewable transport were outlined. This has since been confirmed as "the UK's plan" by then Secretary of State for Energy and Climate Change Amber Rudd [Energy and Climate Change Committee, 2015].

In the latest Digest of UK Energy Statistics, for 2016, it was reported that 8.9% of UK energy consumption came from renewable sources [BEIS, 2017]. Renewable sources made up 24.6% of total electricity generation, renewable heat made up 6.2% of overall heat, and energy from renewable sources in transport made up 4.5% of total energy consumption. According to this report, the UK is on track to "comfortably exceed" it's target of 30% of electricity generation by 2020 [BEIS, 2017], a view echoed by the National Grid [2016]. However, the National Grid are less optimistic about heat and transport, stating:

> *"While we believe the electricity sector can achieve its contribution to the 2020 renewable targets, we believe the progress required in the heat and transport sector is beyond what can be achieved on time. As a result, none of our* [future energy] *scenarios achieve the 15 percent* [of energy consumption met by renewable sources] *level by the 2020 date."*
> – National Grid [2016], p. 135

The best- and worst-case scenarios from the National Grid [2016] estimate the 15% target being met in 2022 and 2029 respectively, with the best-case scenario being the only scenario to meet the 2050 deadline on time. In order to meet the 2050 target in this best-case scenario the electricity sector requires 100% decarbonisation (i.e. 100% of electricity from renewable sources). In all of the National Grid scenarios from 2016 [National Grid, 2016], and again from 2017 [National Grid, 2017] marine energy (tidal-stream, tidal-range, and wave combined) made up only a very small part of the energy mix. This is despite the significant amount of energy contained within the seas surrounding the UK.

For the M_2 (principal lunar) tide, Cartwright et al. [1980] estimated that tidal energy flux from the open ocean into the seas around Great Britain is 250 GW. Robinson [1979] calculated the M_2 accounts for >80% of the energy flux in the Celtic sea. Assuming this applies to the other seas surrounding Great Britain, then the total tidal energy flux into the seas around Great Britain is $j_T \sim 313$ GW . This

is approximately an order of magnitude larger than the electricity consumption of the UK, $C_E \sim 35$ GW, and of the same order as the total energy consumption of the UK, $C_N \sim 236$ GW [ENERDATA, 2017]. Although j_T is not a good indication of the practical extractable resource, the ratio $j_T/C_N = 1.33$ hints at the potential importance of the tide as an energy source in the UK. This is an energy source as yet largely untapped, both in the UK and worldwide.

The energy in the tide may be converted into electricity using turbines rotated by the movement of water caused by the tide. There are two methods of doing this, one of which is suited to areas of high tidal kinetic energy, and one suited to areas of high tidal potential energy, splitting the tidal resource in to two parts, namely the tidal-stream resource and the tidal range resource respectively. In some regions the passage of the tide is constricted as it passes through channels between two islands, or an island and a headland, or as it passes around a headland. In these regions large tidal currents occur and a turbine may be placed directly in the flow in order to generate electricity. In other regions such as bays and estuaries resonance effects amplify the tidal range. In such regions barrages or lagoons can be used to trap the tide, causing a pressure head difference to occur. The trapped water can then be released through turbines to generate electricity.

Technological restrictions, i.e. limits on maximum/minimum depth and minimum velocity for tidal-stream energy extraction, mean that only a small fraction of the tidal resource may be extracted. Current tidal-stream technology, so-called first-generation devices, operate in waters 25–50 m deep with peak currents ≥ 2.5 m/s [Iyer et al., 2013]. The area of British seas meeting these criteria is 1450 km^2 [Lewis et al., 2015], approximately 0.19% of the UK Exclusive Economic Zone (EEZ), excluding overseas territories. As such the total estimated tidal-stream resource is 1.9 GW, only 0.6% of the estimated total tidal energy flux into British waters. Next generation devices will aim to operate in both deeper and shallower waters and for lower currents. Lewis et al. [2015] in their study for the Irish sea found that moving to a "second generation" device where the peak current requirement was reduced to ≥ 2 m/s increased the tidal-stream resource by a factor of 6. Multiplying the UK wide resource by this factor[1], the second generation tidal-stream resource increases

---

[1]This factor is not necessarily applicable UK wide but has been used here for purely illustrative

to 3.6% of the estimated tidal energy flux into UK waters, 32.6% of UK electricity consumption or 4.8% of total UK energy consumption.

In addition to the tidal-stream resource the estimated UK tidal range resource is 4.6 GW[2] [Crown Estate, 2013] and the estimated UK wave resource is 26 GW, with a practical resource of 8 GW [Crown Estate, 2013]. Taking the practical UK wave resource, the approximate combined UK tidal and wave resource is 14.5 GW, or ∼41% of the 2016 UK electricity demand. Given the local (UK) and global trend of increasing electricity demand [BEIS, 2016, 2017, ENERDATA, 2017], and that future UK electricity supply will need to be 100% renewable in order to meet the government's 2050 target [National Grid, 2016] this considerable, and as yet largely untapped resource could play an important role in the UK's energy future.

As a comparison, in the UK, insolation (amount of solar energy reaching a given area) varies over the year and with latitude, as it does globally. Burnett et al. [2014] calculated the average UK annual solar resource to be 101.2 W/m^2. Multiplying this by the area of the UK gives a total theoretical resource of 24.5 TW, approximately two orders of magnitude larger than the tidal energy flux into UK waters. Taking the Photovoltaic (PV) cell efficiency to be 20%, the total marine energy resource is the equivalent to ∼0.29% of the UK land area covered by PV cells (∼703 km^2, or about the area of Anglesey completely covered by PV cells).

It was seen above that the marine renewable energy resource is small in comparison to the solar resource. However, one of the chief advantages that tidal energy generation holds over other renewable sources, such as solar, or even wave, is its predictability. The tide is forced by the Sun and the Moon and varies with a set of fixed periodicities originating from the orbital periodicities of the Earth-Moon-Sun system (this is discussed further in Chapter 2, §2.1). As such, once the relative strength of the periodicities at a site are known, one can predict reasonably accurately the variation of that resource over any given day in the future[3]. This

purposes.

[2]This figure has been arrived at by summation of the Annual energy output of tidal barrage schemes taken from the literature in Crown Estate [2013], Appendix C, Table 1.

[3]Wave-tide interaction, tide-surge interaction and rising sea-level may all impact on the tidal resource, and all three topics are areas of on-going research (e.g. Hashemi et al. [2015], Lewis et al. [2017], Chen et al. [2017] etc.).

characteristic of tidal energy makes it extremely useful in terms of supply of energy to the grid. Although it is not completely free of the issue of intermittency faced by renewable sources, as at times no energy will be generated (around slack water for tidal-stream) and at other times more energy than required may be generated. But this intermittency is at least known well in advance, and in the case of tidal range developments there is the potential for energy storage [MacKay, 2007, 2009].

Above tidal energy has been introduced in the UK context, and in the context of electricity demand and the potential of tidal energy, and specifically tidal-stream energy, to meet this demand relative to other renewable sources. In summary, first generation tidal-stream energy has the potential to meet 5% of 2015 UK electricity demand, a significant fraction. Moreover, the total UK marine energy resource (tidal-stream, tidal range and wave) could meet $\sim 41\%$ of the 2015 UK electricity demand. The realisation of this resource faces many challenges, in for example deployment and maintenance, and potential environmental impacts. The last of these points will be expanded upon in §1.3.

1.2   The Tidal-Stream Industry in the UK

The history of tidal power in the UK considerably pre-dates the existence of the UK itself, tidal mills having possibly been operational in the 11th century [Minchinton, 1979] and maybe even in Roman Britain [Spain, 2002], thus pre-dating even the constituent states of the UK by several centuries. These historical tidal mills would have been used primarily for milling grain, operating in a fashion similar to mills exploiting riverine flows, but also using sluices to trap the tide [Minchinton, 1979]. The use of the tide to generate electricity anywhere in the world did not occur until some nine centuries later[4], with the completion of the La Rance tidal power station in 1966, the world's first tidal range power station.

In the UK, the effective birth of tidal energy extraction occurred in 1994, when the world's first tidal-stream turbine, a 10 kW system, was tested on Loch Linnhe. This provided the proof of concept for tidal-stream energy generation [Fraenkel,

---

[4]The principle of electromagnetic induction was discovered in 1831 by Michael Faraday, and steam-powered dynamos employing this principal have only been used to generate electricity at industrial scales since the Gramme machine in 1871 [Urbaninsky, 1896].

2010]. Following this, Marine Current Turbines Ltd. (MCT) deployed a pilot-scale 300 kW device, called "Seaflow", near Lynmouth, Devon, in 2003 [Marsh, 2004]. This was followed by MCT's 1.2 MW "SeaGen" turbine deployed in Strangford Lough, Co. Down, which came online in 2008 [Fraenkel, 2010]. This turbine was the world's first operational commercial-scale tidal-stream turbine, and was operational until 2017, when it was decommissioned. The most recent development in the UK tidal-stream industry is the completion of phase 1A of the "MayGen" project in February 2017, which saw 4 1.5 MW rated turbines deployed in the inner sound of Stroma in the Pentland Firth [Atlantis Resources Ltd., 2017a].

The MeyGen project is currently the largest planned tidal-stream project in the world and is being developed by Atlantis Resources Ltd., who in 2015 purchased MCT from Siemens, acquiring all technology, staff seabed rights and the SeaGen project in Strangford Lough [reNEWS, 2015]. The MeyGen project consists of multiple phases: phase 1A, which is currently operational, consists of four 1.5 MW rated turbines, phase 1B consists of a further four 1.5 MW turbines, in phase 1C an additional forty-nine 1.5 MW turbines will be deployed [Atlantis Resources Ltd., 2017b]. The project consists of a further two phases, phase 2 which will take the project to the current grid capacity at the site of 252 MW (equivalent of an additional 111 1.5 MW turbines), and phase 3 which would upgrade the sites grid capacity and take the project up to the lease capacity of 398 MW (equivalent to an additional 97 1.5 MW turbines).

Many other sites around the UK have been leased from the Crown Estate by tidal-stream developers. Tables 1.1 & 1.2 list tidal-stream projects planned for Scotland and the rest of the UK respectively. These developments amount to 507 turbines UK-wide, supplying ~570 MW (~1.6% of UK electricity demand). These numbers do not include the second and third, as-yet un-planned phases of the MeyGen project, and similarly, some other large developments, such as, for example, the Ness of Duncansby, are also not included.

1.3 Potential Environmental Impacts Related to the Development of the Tidal-Stream Industry

Tidal-stream energy projects may impact on the marine environment. The distinction between effects and impacts is made by Boehlert and Gill [2010], who define impacts as the consequences of the "severity, intensity or duration" (Boehlert and Gill [2010], p. 71) of the effects that the deployment, operation and decommissioning (henceforth collectively referred to as development) of Tidal Stream Turbine (TST)s have on the marine environment. It is helpful when discussing the effects of TST developments to do so in terms of environmental stressors and receptors, a method employed by both Boehlert and Gill [2010] and Polagye et al. [2010].

Environmental stressors are defined as any aspects of TST developments that affect the environment. Their identification needs to include their spatial and temporal extents [Boehlert and Gill, 2010]. Receptors are the aspects of the marine environment that may be affected by stressors [Polagye et al., 2010]. The effects of Offshore Renewable Energy Developments (OREDs) are discussed by Gill [2005]. These effects can be summarized loosely as:

- the disruption to the marine environment at all stages of development due to the resuspension of sediment

- increased turbidity

- the mobilization of contaminants contained within sediment and the resuspension of organic matter contained within sediment

- the alteration of local water movements due to the presence of the devices

- loss of habitat during decommissioning if devices are colonized during their deployment

- increased marine noise associated with all stages of development

- the presence of electromagnetic fields associated with power cables

- the potential for direct collision of marine fauna with devices

Table 1.1: List of tidal-stream energy developments around Scotland. Information take from UKRED Marine Map.

Site	Owner(s)	Developer	No. Turbines	Total Power [MW]
Mull of Galloway	Atlantis Resources Ltd. (100%)	-	30	30
Sanda Sound	Oceanflow Energy Ltd. (100%)	-	1	0.04
Mull of Kintyre	Nautricity Ltd. (100%)	-	7	3.5
Sound of Islay	Atlantis Resources Ltd. (92%); ScottishPower Renewables (6%); Dredging, Environmental & Marine Engineering (2%)	ScottishPower Renewables	8	12
West Islay Tidal Energy Farm	DP Energy (100%)	-	30	30
Wave Net Array	Albatern Ltd. (100%)	Albatern Ltd.	6	0.45
SeaGen Kyle Rhea	Atlantis Resources Ltd. (100%)	Atlantis Resources Ltd.	4	8
MeyGen Pentland Firth	Atlantis Resources Ltd. (86.5%); Scottish Enterprise (13.5%)	MeyGen Ltd.	57*	85.5*
Ness of Duncansby	Atlantis Resources Ltd. (92%); ScottishPower Renewables (6%); Dredging, Environmental & Marine Engineering (2%)	-	In Planning	
SeaGen Brough Ness	Atlantis Resources Ltd. (100%)	-	66	99
Brims Tidal Array	OpenHydro (50%); SSE Renewables (50%)	Brims Tidal Array Ltd.	200	200
Westray South	DP Energy (100%)	DP Energy	In Planning	
Lashy Sound	Scotrenewables Tidal Power Ltd. (100%)	Scotrenewables Tidal Power Ltd.	15	30
Shetland Tidal Array	Nova Innovation Ltd. (100%)	Nova Innovation Ltd.	6	0.6
Bluemull Sound	North Yell Development Council (100%)	Nova Innovation Ltd.	1	0.03

Table 1.2: List of tidal-stream developments around the rest of the UK. Information taken from UKRED marine map.

Site	Owner(s)	Developer	No. Turbines	Total Power [MW]
England				
Portland Bill Tidal Site	Atlantis Resources Ltd. (100%)	-	30	30
Northern Ireland				
Fair Head	DP Energy (50%); Dredging, Environmental & Marine Engineering (50%)	Fair Head Tidal Energy Park Ltd.	In Planning	
Minesto Strangford Lough	Minesto AB (100%)	-	1	0.03
Seagen Strangford Lough Array	Atlantis Resources Ltd. (100%)	-	20	20
SeaGen Strangford Lough	Atlantis Resources Ltd. (100%)	Sea Generation Ltd.	Decommissioning	
Wales				
Bardsey Sound Tidal Array	Nova Innovation Ltd. (50%); Ynni Llŷn (50%)	-	In Planning	
Holyhead Deep	Minesto AB (100%)	-	20	10
Ramsey Sound	Tidal Energy Ltd. (100%)	-	Inactive	
SeaGen Anglesey Skerries	Atlantis Resources Ltd. (100%)	-	5	10
St. David's Head	Tidal Energy Developments South Wales Ltd. (100%)	Tidal Energy Developments South Wales Ltd.	Inactive	

These effects, and additional considerations are laid out in terms of environmental stressors by Boehlert and Gill [2010] and Polagye et al. [2010] as;

- the physical presence of the devices

- the dynamic effects of the devices

- chemical effects (resulting from biofouling and increased marine traffic)

- acoustic effects

- electromagnetic effects

- energy removal

The associated environmental receptors are;

- the near-field physical environment

- the far-field physical environment

- the benthic environment

- the pelagic environment

- migratory fish

- resident fish

- marine mammals

- seabirds

- ecosystem interactions

As a measure of the relative importance of the stressor-receptor interactions one can use risk, which "*can be defined as the likelihood of an adverse outcome from an action and can be evaluated by the probability of the occurrence of an event, as well as the resulting consequence*" (Copping et al. [2016], p. 10). Copping et al. [2016] drew from the current state of knowledge in the scientific literature the level of risk – real or perceived – of each potential stressor at the single-device and small-, $\mathcal{O}(10)$ turbines, and large-scale, $\mathcal{O}(100)$ turbines, commercial scales. The potential risk was classified as either low, medium, or high, and is presented for each stressor, at each scale, in Table 1.3.

At the single-turbine-scale the potential risk to the environment is considered low for all stressors bar dynamic device effects. The main concern here is the collision of marine mammals, fish and diving birds with the turbine rotor [Wilson et al., 2007]. The environmental monitoring programme associated with the SeaGen turbine at Strangford Lough recorded the impact of the project on marine mammals and diving birds at the site and detected no major impacts on either [Keenan et al., 2011]. As the scale of the development increases so too does the potential

risk associated with the dynamic device structures, with a high potential risk for large-scale commercial developments assigned by Copping et al. [2016].

For large-scale commercial developments the potential risk is considered greater for all stressors bar chemical effects, which are better understood given the similarity of this stressor to the effects of other marine industries [Copping et al., 2016]. With more turbines there will be more environmental stress, which in part explains the greater potential risk at larger scales. However, uncertainty also contributes to the level of risk assigned [Copping et al., 2015], and large-scale commercial developments do not yet exist, so their impact is not yet well understood. The same can also be said of small-scale commercial developments. The environmental monitoring programme associated with the MayGen project will improve the understanding at this scale. At the time of writing, four 1.5 MW turbines have been deployed. Following phase 1b this will rise to eight turbines, which may be classified as a small-scale commercial development. Eventually this project will reach the size of $\mathcal{O}(100)$ turbines, moving it to the large-scale development classification, and as such, environmental monitoring of this project will reduce the uncertainty of environmental risk at this scale.

Table 1.3: Potential risk posed by the various stressors associated with TST developments, reproduced from Copping et al. [2016]. Green: low risk, orange: medium risk, red: high risk.

Stressor	Single Device Deployment	Small-Scale Commercial	Large-Scale Commercial
Static Device	🟩	🟩	🟧
Dynamic Device	🟧	🟧	🟥
Acoustic	🟩	🟩	🟧
Energy Removal	🟩	🟧	🟧
Electromagnetic	🟩	🟩	🟧
Chemical	🟩	🟩	🟩

The only other stressor whose level of risk increased at the $\mathcal{O}(10)$ turbine scale was energy removal. The removal of kinetic energy from tidal flows will alter the nature of the flow local to the turbine (e.g. Myers and Bahaj [2010], Stallard

et al. [2015], etc.), and for larger arrays, possibly at a regional scale [Karsten et al., 2008, Hasegawa et al., 2011, De Dominicis et al., 2017]. The physical and dynamic presence of the devices will also lead to changes in the local hydrodynamics as an object in a (high Reynolds number) fluid flow will disturb the flow as it is forced to move around the object. Behind the object there will be a disturbed region of the flow, known as the wake, characterised by reduced velocity and rotational flow, which will recover to approximately ambient flow conditions some distance downstream of the object [Tritton, 1988]. Therefore, in the near-field, the presence of a turbine will result in a turbulent wake downstream of the turbine. The rotation of the turbine blades adds additional rotation to the wake (e.g. Chen and Lam [2014a]). Also, the turbine will also offer a blockage to the flow, resulting in acceleration of the flow around the turbine (e.g. Masters et al. [2013]).

In the far-field, turbines cause the tidal flow speed to be reduced (e.g. Garrett and Cummins [2004, 2005], Karsten et al. [2008], Defne et al. [2011], Hasegawa et al. [2011], Ahmadian et al. [2012], Ramos et al. [2013], Fallon et al. [2014], O'Hara-Murray and Gallego [2017], De Dominicis et al. [2017] etc.). The blockage effect also alters the tidal regime and for certain cases can interfere with bay or estuary flushing [Nash et al., 2014]. The effects of TSTs on the far-field physical environment will vary on a site-by-site basis. The alteration to the flow environment in both the near and far field will have a knock-on effect on sediment transport with implications for coastal morphodynamics (e.g. Neill et al. [2009, 2012], Robins et al. [2014] etc.), turbidity, water quality and oxygen demand, due to the resuspension of sediments and contaminants and organic matter contained within those sediments [Gill, 2005]. The alteration to water column hydrodynamics and sediment transport could alter the vertical movement of marine organisms and nutrients and impact benthic species through habitat loss [Boehlert and Gill, 2010]. The flow of water is also important to sessile species for the transport of food, waste, propagules etc. [Shields et al., 2011]. Changes to the hydrodynamics at a site may also have implications for the ability of benthic suspension feeders to feed and on the propagation of odour with an impact on species dependent on olfaction for hunting prey [Shields et al., 2011], larvae identifying suitable adult habitats [Munday et al., 2009], recognising appropriate food, mate recognition, alarm responses, homing and social behaviour

[Carr and Derby, 1986]. At the regional-scale the large-scale extraction of tidal kinetic energy has also been seen to impact on seasonal stratification, which may have knock-on effects for marine ecosystem dynamics and species behaviour [De Dominicis et al., 2017].

In conclusion, changes to the hydrodynamics at both the near- and far-field scales are likely to have important consequences for the marine environment. Despite considerable attention in the literature, there is still much that remains to be understood in this respect, particularly with regards to the ecological consequences. This study addresses this issue, building on current understanding of the hydrodynamically-mediated environmental consequences of tidal-stream energy extraction.

1.4 Synopsis

In Chapter 2 of this thesis a background to the physics of the tides is presented and a review of the state-of-the-art in tidal asymmetry leading to the first statement of the hypotheses and associated research questions that will be explored in this work. Chapter 3 will look at the numerical modelling approach to addressing the research questions presented in Chapter 2. Along with verification of the model, and model sensitivity tests. Chapters 4, 5 & 6 present the results of the experiments undertaken to address the research questions presented in Chapter 2, along with brief discussions of the results. Chapter 7, brings the discussion of results from Chapters 4, 5 & 6 together, relates the findings back to the original hypothesis and considers the limitations of the work. Finally, Chapter 8 draws conclusions from this discussion in Chapter 7 and discusses potential future work.

Chapter 2

Theoretical Background and Development of Hypothesis and Research Questions

In this chapter the tidal forcing on Earth will be discussed to introduce the origins of the astronomic frequencies found in a tidal record (§2.1). The mechanisms through which the higher frequency shallow-water tides are introduced through the non-linear interaction of these astronomic tidal frequencies in shallow waters (§2.2). This will then be followed by a discussion of flood-ebb asymmetries in the tides and how they can be understood through the interaction of certain tidal constituents (§2.3) and the implications of the asymmetries in tidal flows for transport processes and the technically exploitable resource (§2.4). Finally, the discussion throughout the chapter will be brought together to form hypotheses of how the processes that have been discussed will be impacted by tidal-stream turbines (§2.5.1). These hypotheses will then be used to form a set of research questions (§2.5.2) and a brief outline of the experimental methodology that will be employed to address these questions will close out the chapter (§2.5.3).

2.1   The Astronomic Tide

For an understanding of the tides one must begin with Newton, his laws of motion and his theory of gravity. The latter of these states that two bodies, with masses

m_1 and m_2, attract each other with a force defined as:

$$F_{G,1,2} = G\frac{m_1 m_2}{r_{1,2}^2} \tag{2.1.1}$$

where G is the universal gravitational constant and $r_{1,2}$ is the distance between the two bodies. To give the gravitational force between the Earth and Sun or the Earth and Moon, m_1 becomes the mass of the Earth, m_E, m_2 becomes the mass of the Sun, m_S, or the mass of the Moon, m_M, and $r_{1,2}$ becomes the distance between the centre of the Earth and the centre of the Sun, r_S, or the distance between the centre of the Earth and the centre of the Moon, r_M. If we define the gravitational potential of the two bodies as:

$$\Omega_{G,1,2} = -G\frac{m_1 m_2}{r_{1,2}} \tag{2.1.2}$$

then the gravitational force is also given by:

$$F_{G,1,2} = -\nabla\Omega_{G,1,2} \tag{2.1.3}$$

The gravitational potential at a point P on the Earth's surface is given by:

$$\Omega_{G,P,M} = -G\frac{m_M}{\sqrt{R_E^2 + r_M^2 - 2R_E r_M \cos(\varphi)}}$$
$$= -G\frac{m_M}{r_M}\left\{1 + \frac{R_E^2}{r_M^2} - \frac{R_E}{r_M}\cos(\varphi)\right\}^{-\frac{1}{2}} \tag{2.1.4}$$

where R_E is the radius of the Earth and φ is the lunar angle, illustrated in Figure 2.1. The denominator in (2.1.4) comes from applying the cosine rule to the triangle EPM to give the length of the side PM.

The ratio R_E/r_M, can be approximated to be constant, and thus (2.1.4) can be expanded in powers of R_E/r_M, using Legendre polynomials (Whittaker and Watson [1963], §15.1):

$$\Omega_{G,P,M} = -\frac{Gm_M}{r_M}\left\{1 + \left(\frac{R_E}{r_M}\right)\cos(\varphi)\right.$$
$$\left. + \left(\frac{R_E}{r_M}\right)^2\left(\frac{1}{2}\right)(3\cos^2(\varphi) - 1) + \dots\right\} \tag{2.1.5}$$

It is the third term in (2.1.5) that is primarily responsible for lunar tides, as it is the gradient of the potential which gives the gravitational force, (2.1.3). As such, the first term results in no force, and the second results in the force that keeps the Earth in orbit about the Earth-Moon system's centre of mass [Stewart, 2008]. Therefore, the tide-generating potential is given by:

$$\Omega_{T,P,M} = -\frac{Gm_E R_E{}^2}{2r_M{}^3}(3\cos^2(\varphi) - 1) \qquad (2.1.6)$$

The tide generating force resulting from the potential $\Omega_{T,P,M}$ can be decomposed into components tangential and perpendicular to the sea's surface, given by:

$$-\frac{1}{R_E}\frac{\partial \Omega_{T,P,M}}{\partial \varphi} = 2\alpha g \sin(2\varphi) \qquad (2.1.7)$$

and

$$-\frac{\partial \Omega_{T,P,M}}{\partial R_E} = -2\alpha g \left(\cos^2 \varphi - \frac{1}{3}\right) \qquad (2.1.8)$$

respectively, where $g = Gm_E/R_E{}^2$ is acceleration due to gravity and:

$$\alpha = \frac{3}{2}\frac{m_M}{M_E}\left(\frac{R_E}{r_M}\right)^3 \qquad (2.1.9)$$

The size of α is $\sim 8.4 \times 10^{-8}$, thus the component normal to the sea's surface is not large enough to overcome the Earth's own gravitational force (mg for a body of mass m). The tangential component, whilst still small does not have an opposing force, thus it is this component which produces the tides. Figure 2.2 presents a schematic of the tangential component of the tide generating force.
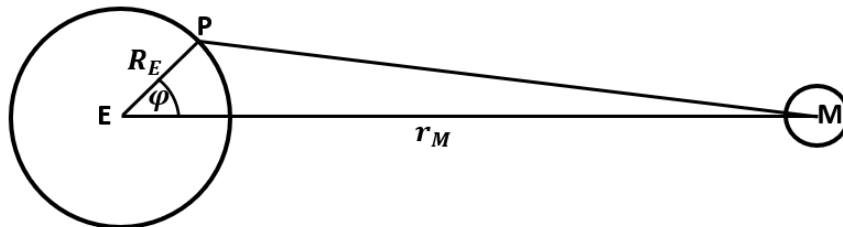
Figure 2.1: Schematic of Earth-Moon system showing a general point P. Reproduced from Pugh [1987], Figure 3:4.
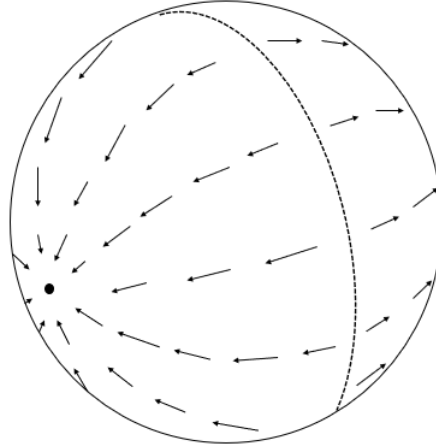
Figure 2.2: Schematic of the tangential component of the tide generating force. The marked point is the point on the Earth's surface directly below the Moon.

The above derivation assumes that the Earth is covered entirely by water and ignores the rotation of the Earth (considering only the rotation of the Moon around the Earth) and the influence of inertia and currents in the ocean. Under these circumstances, the gradient in the gravity field acting on the Earth would result in two 'bulges' of water, one facing the Moon and one on the opposite side of the Earth. As the Moon rotates around the Earth, the bulges move with it.

The tide generating force due to the Sun can be derived in a similar manner, and the result is the same as (2.1.6) but with m_M replaced with m_S and r_M replaced with r_S.

When the rotation of the Earth about its tilted axis is taken into account, the position of the Moon in the sky, as observed from a fixed point, e.g. P, will vary with time. One can re-express the lunar angle φ in terms of the latitude of P, φ_P, i.e. the angular distance P lies north or south of the equator, the declination of the Moon north or south of the Earth's equator, δ, and the *hour angle* of the Moon, χ, which is the difference in longitude between the meridian[1] of P and the meridian of the sub-lunar point[2]:

$$\cos(\varphi) = \sin(\varphi_P)\sin(\delta) + \cos(\varphi_P)\cos(\delta)\cos(\chi) \qquad (2.1.10)$$

---

[1]Imaginary arc from the North Pole to the South Pole connecting points of equal longitude.
[2]The point at which the moon is directly overhead.

Substituting (2.1.10) into (2.1.6) gives:

$$
\Omega_{T,P,i} = \frac{1}{4} G m_i \frac{R_E{}^2}{r_i^3} \left[\underbrace{(3\sin^2(\varphi_P) - 1)(3\sin^2(\delta) - 1)}_{(a)} \right.
$$

$$
+ \underbrace{\sin(2\varphi_P)\sin(2\delta)\cos(\chi)}_{(b)}
$$

$$
\left. + \underbrace{\cos^2(\varphi_P)\cos^2(\delta)\cos 2(\chi)}_{(c)} \right] \quad (2.1.11)
$$

where the i may be replaced by M or S so that (2.1.11) gives the tidal potential of the Moon or Sun at the point P respectively. For the case where $i = S$ then δ and χ in must be the declination and hour angle of the Sun, not the Moon. The period of the solar hour angle is 24 hours and the period of the lunar angle is 24.8412 hours. The three terms enclosed in square brackets therefore separate the lunar and solar periods into three, meaning there are three groups of tidal frequencies; twice daily, (c), daily, (b), and long period, (a), [Pugh, 1987, Stewart, 2008]. These frequency groups will vary both spatially and temporally. Considering only the temporal variation by remaining at the fixed point P, the long period species will vary with the declination of the Moon/Sun and the daily (diurnal) and twice daily (semi-diurnal) species will both vary with twice the frequency of lunar/solar declination.

From (2.1.11) one can arrive at the equilibrium tide by integrating over finite space a differential equation formed by equating spatial gradients of $\Omega_{T,P,i}$ to spatial gradients of the free-surface on the water covered Earth (see Pugh [1987]). This equilibrium tide has amplitudes much smaller than those observed in the real world. However, the energies of the observed tide occur at the same frequencies as those of the equilibrium tide, meaning the development of the equilibrium tide can be used to inform the harmonic development[3] of the observed tide. The equilibrium tide is given by Pugh [1987] as:

---

[3]The decomposition of the tide into the infinite series of sine / cosine waves, which, when superimposed, reproduce the tidal record.

$$\eta = R_E \left(\frac{m_M}{m_S}\right) \left[C_0(t) \left(\frac{3}{2}\sin^2(\varphi_P) - \frac{1}{2}\right) + C_1(t)\sin^2(2\varphi_P) \right.$$
$$\left. + C_2(t)\cos^2(\varphi_P) \right] \quad (2.1.12)$$

where:

$$C_0(t) = \left(\frac{R_E}{r_M}\right)^3 \left(\frac{3}{2}\sin^2(\delta) - \frac{1}{2}\right) \quad (2.1.13)$$

$$C_1(t) = \left(\frac{R_E}{r_M}\right)^3 \left(\frac{3}{4}\sin^2(2\delta)\cos(\chi)\right) \quad (2.1.14)$$

$$C_2(t) = \left(\frac{R_E}{r_M}\right)^3 \left(\frac{3}{4}\cos^2(\delta)\cos(2\chi)\right) \quad (2.1.15)$$

Up to this point the orbit of the Moon around the Earth and the Earth-Moon system around the Sun has been considered circular. In practice both the orbits of planets around the Sun or moons around planets are elliptical. Figure 2.3 presents a schematic of an elliptical orbit, where a body C is orbiting around the larger body A. The point O denotes the centre of the ellipse and the points A and B are the foci of the ellipse, with body A located at point A. The eccentricity of the ellipse, e, is defined as the ratio OA/OCA. When body C is at the point C_A the distance AC is at its minimum, and when body C is at point C_P the distance AC is at its maximum. These points are called the *apogee* and *perigee* of the orbit. The ratio of the distances AC at *apogee* and *perigee*, AC_A/AC_P, is given by $(1+e)/(1-e)$.

The position of the Sun and Moon in the sky can be stated with reference to declination from a plane intersecting the equator and the *right ascension*. The right ascension is the eastward angular distance along the celestial equator from the *vernal equinox*, which is the point at which the ecliptic plane[4] and the equatorial plane intersect. Right ascension and the vernal equinox are illustrated by the schematic in Figure 2.4. The angle between the ecliptic and the equatorial planes, the obliquity, ε, is 23.45^o.

---

[4]The circular path on the celestial sphere which the Sun appears to follow, see Figure 2.4.
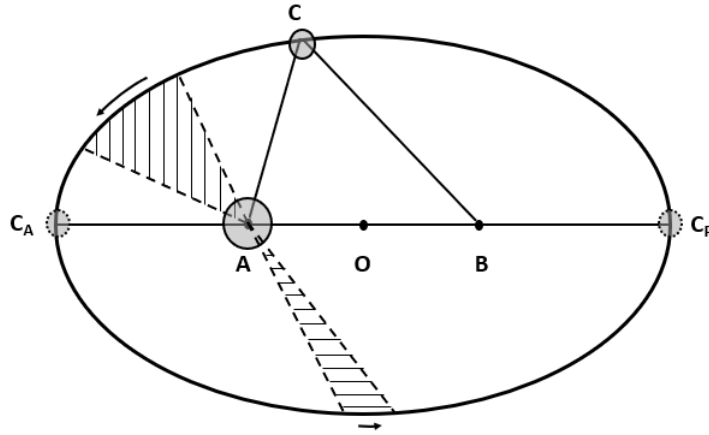
Figure 2.3: Schematic illustrating the properties of an elliptical orbit. Reproduced from Pugh [1987], Figure 3:9.

For the Earth-Sun system, the equilibrium tide, (2.1.12)–(2.1.15), is given in terms of r_S, δ_S (the solar declination) and χ_S (the solar hour angle). The solar distance, r_S is given by [Pugh, 1987]:

$$\frac{\overline{r}_S}{r_S} = (1 + e\cos(h - p')) \tag{2.1.16}$$

where $\overline{r}_S$ is the mean solar distance, h is the geocentric mean ecliptic longitude[5], and p' is the longitude of solar perigee, or perihelion[6].

According to Kepler's second law, the two segments swept out in equal time shown in Figure 2.3 have equal area. This means that the angular speed of C observed from A is not constant, and that C will have maximum angular speed at C_A and minimum angular speed at C_P. This leads to a variation in the elliptical longitude of the Sun, with the *true* ecliptic longitude, λ_S, given by [Pugh, 1987]:

$$\lambda_S = h + 2e\sin(h - p') \tag{2.1.17}$$

Due to the tilt of the Earth's axis there is a regularly varying difference between

---

[5]Angular distance along the ecliptic eastwards from the vernal equinox.

[6]The perihelion is the point in a planets orbit about the Sun at which it is closest to the sun. Due to the perturbing effect of the other planets orbiting the sun the eccentricity of the Earths orbit will vary over long time-scales and so too will the date of perihelion. The perihelion of the Earth's orbit varies with a period of 21,000 (Julian) years.

the ecliptic longitude and right ascension. This results in a modulation of the (solar) right ascension, Λ_S, given by [Pugh, 1987]:

$$\Lambda_S = \lambda_S - \tan^2\left(\frac{\varepsilon_S}{2}\right)\sin(2\lambda_S) \tag{2.1.18}$$

where ε_S is the solar ecliptic latitude[7]. Finally, the solar declination is given in terms of λ_S and ε_S, by:

$$\sin(\delta_S) = \sin(\lambda_S)\sin(\varepsilon_S) \tag{2.1.19}$$

For the Earth-Moon system there is a twofold complication due to the effect of the Sun on the system and the regression of the ascending lunar node. The ascending lunar node is the point at which the Moon, in its orbit, crosses the ecliptic from south to north (illustrated in Figure 2.5). Over a period of 18.61 years this node rotates westward along the ecliptic, resulting in a modulation with a period of 18.61 years in the lunar terms of the equilibrium tide. The lunar distance, r_M, is given by [Pugh, 1987]:

$$\frac{\overline{r}_M}{r_M} = (1 + e\cos(s - p) + \text{solar pertubations}) \tag{2.1.20}$$

where $\overline{r}_M$ is the mean lunar distance, s is the geocentric mean longitude and p is the longitude of lunar perigee, which rotates with a period of 8.85 years. The mean eccentricity of the lunar orbit is $e = 0.0549$, with variations from this mean caused by the effect of the Sun's gravity. The true ecliptic longitude and right ascension of the moon are given by:

$$\lambda_M = s + 2e\sin(s - p) + \text{solar perturbations} \tag{2.1.21}$$

and

$$\Lambda_M = \lambda_M - \tan^2\left(\frac{\varepsilon_M}{2}\right)\sin(2\lambda_M) \tag{2.1.22}$$

where ε_M is the lunar ecliptic latitude, given by:

$$\sin(\varepsilon_M) = \sin(\lambda_M - N)\sin(5.15^o) \tag{2.1.23}$$

---

[7]Angular distance north or south of the ecliptic.

where N is the mean longitude of the ascending lunar node and the 5.15^o is the mean angle between the lunar orbital plane and the ecliptic.
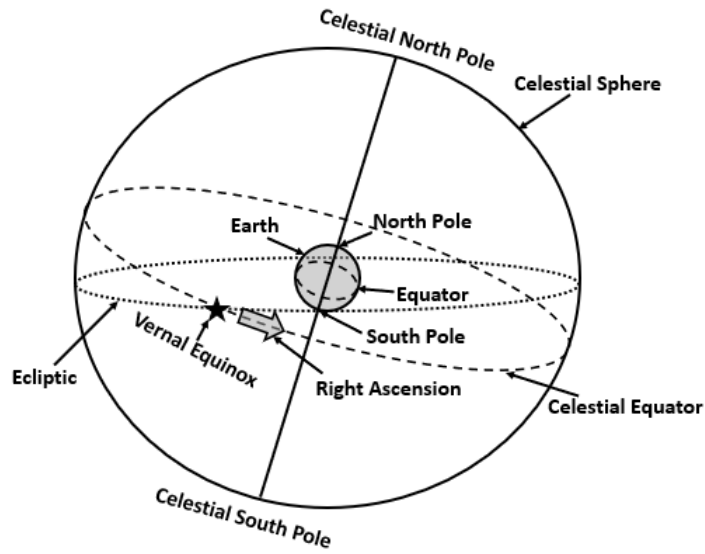
Figure 2.4: Schematic illustrating vernal equinox and right ascension.
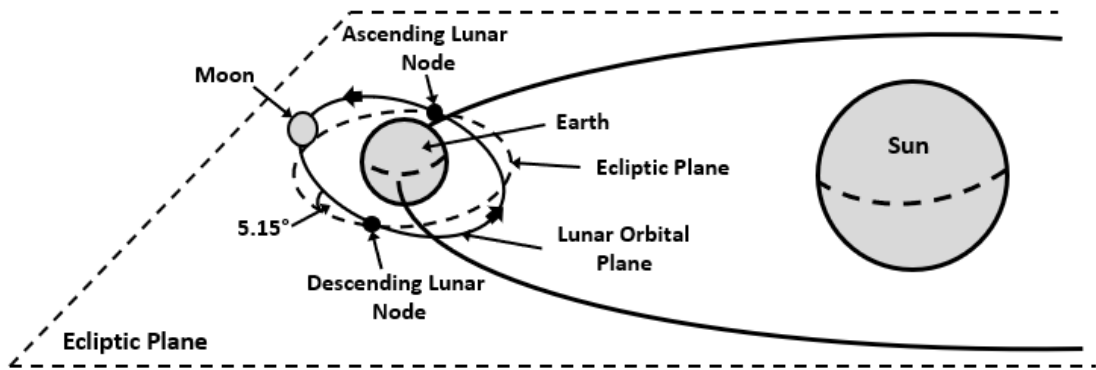
Figure 2.5: Schematic illustrating the ascending & descending lunar nodes.

From these modulations to the lunar and solar equilibrium tides described above one can identify 6 fundamental frequencies summarised in Table 2.1. The equilibrium tide can be expanded as a Fourier series into groups of similar harmonic terms, the angular speeds of these terms have the general form:

$$\omega_n = \sum_{i=1}^{6} n_i \omega_i \qquad (2.1.24)$$

where ω_i are given in Table 2.1, $n_1 = 0, 1, 2$ for the long period, diurnal and semi-diurnal frequency groups respectively, and n_2–n_6 are integer values which

define the tidal constituent.

Table 2.2 lists some of the largest harmonic constituents of the equilibrium tide for each of the three frequency groups. This is not an exhaustive list of constituents. The table in Pugh [1987] (Table 4:1), upon which this table is based, contains more constituents and the table presented by Doodson [1921] contains yet more constituents. From inspection of the relative coefficients presented in this table, one can see that a reasonable approximation of the equilibrium tide may be obtained for only a small number of constituents. The size of these constituents in oceans and seas in the real world and their sizes relative to the M_2 (principal lunar tide, the largest harmonic component of the tide) will be different to the equilibrium tide due to propagation of the tide in ocean basins, and the hydrodynamic responses of the tidal wave to the topology of these basins, the Coriolis force and other reasons discussed in more detail in Pugh [1987] (Chapter 5). The importance of the equilibrium tide is that the actual tide observed at any point in the real world will have its energy at the frequencies of these harmonic constituents.

Table 2.1: Fundamental frequencies of the astronomical motions, from Pugh [1987].

Name	Period Units	Period	Frequency		Angular Speed	
			f [cycles per m.s.d.]	σ [^{o} per m.s. hours]	Symbol	Rate of Change
Mean Solar Day (m.s.d)		1.0000	1.00	15.0	ω_0	χ_M
Mean Lunar Day	[m.s.d]	1.0351	0.9661369	14.4921	ω_1	χ_S
Sidereal Month		27.3217	0.0366009	0.5490	ω_2	s
Tropical Year		365.2422	0.0027379	0.0411	ω_3	h
Moon's Perigee		8.85	0.00030937	0.0046	ω_4	p
Regression of Moon's nodes	[Julian Year]	18.61	0.0001471	0.0022	ω_5	N
Perihelion		20,942	-	-	ω_6	p'

Table 2.2: Largest (in terms of relative amplitude) harmonic tidal constituents from Pugh [1987], Table 4:1 (m.s.d.: mean solar day). From left to right is the name given to the harmonic constituent, then comes n_2–n_6, which along with n_1 are known as the Doodson numbers, after Arthur Doodson who performed the expansion of the equilibrium tide [Doodson, 1921], then the period of the constituent, followed by the relative coefficient of the constituent, which indicates its size relative to the M_2, and finally comes a description of the origin of the constituent.

$n_1 = 0$, Astronomical long-period tides

	s n_2	h n_3	p n_4	N n_5	p' n_6	Period [m.s.d.]	Relative Coefficient $M_2 = 1.00$	Origin
S_a	0	1	0	0	-1	364.96	0.0127	Solar Annual
S_{sa}	0	2	0	0	0	182.70	0.0802	Solar Semi-Annual
M_m	1	0	-1	0	0	27.55	0.0909	Lunar Monthly
M_f	2	0	0	0	0	13.66	0.1723	Lunar Semi-Monthly

$n_1 = 1$, Astronomical diurnal tides

	s n_2	h n_3	p n_4	N n_5	p' n_6	Period [m.s.d.]	Relative Coefficient $M_2 = 1.00$	Origin
O_1	-1	0	0	0	0	1.076	0.4151	Principal Lunar
K_1	1	0	0	0	0	0.997	0.3990	Principal Lunar
	1	0	0	0	0	0.997	0.1852	Principal Solar
P_1	1	-2	0	0	0	1.003	0.1932	Principal Solar
Q_1	-2	0	0	0	0	1.120	0.0794	Larger Elliptical Lunar
M_1	0	0	-1	0	0	1.035	0.0326	Smaller Elliptical Lunar
	0	0	-1	0	0	1.035	0.0117	Smaller Elliptical Lunar
	0	0	-1	0	0	1.035	0.0075	Lunar Parallax
J_1	2	0	-1	0	0	0.962	0.0326	Elliptical Lunar

$n_1 = 2$, Astronomical semi-diurnal tides

	s n_2	h n_3	p n_4	N n_5	p' n_6	Period [m.s.d.]	Relative Coefficient $M_2 = 1.00$	Origin
M_2	0	0	0	0	0	0.518	1.0000	Principal Lunar
S_2	2	-2	0	0	0	0.500	0.4652	Principal Solar
N_2	-1	0	1	0	0	0.527	0.1915	Larger Elliptical Lunar
K_2	2	0	0	0	0	0.499	0.0865	Declination Lunar
	2	0	0	0	0	0.499	0.0402	Declination Solar
ν_2	-1	2	-1	0	0	0.526	0.0346	Larger Evectional
μ_2	-2	2	0	0	0	0.536	0.0306	Variational
L_2	1	0	-1	0	0	0.508	0.0283	Smaller Elliptical Lunar
	1	0	1	0	0	0.508	0.0071	Smaller Elliptical Lunar

2.2 The Shallow-Water Tides

The previous section discussed the tide-generating potential and equilibrium tide. As mentioned in that section the tide observed in the ocean or near the coast may vary considerably from the equilibrium tide in terms of the amplitudes of the harmonic constituents. For example, the large seaward extent of the Patagonian shelf, and the lengths of basins such as the Bay of Fundy, Canada, and the Bristol Channel, UK, leads to amplification of the astronomic tide through resonant effects [Howarth, 1982]. Further discussion of alteration to the astronomic tide is given by Pugh [1987]. Hereinafter, only the distortion to the ocean tide through shallow water processes will be discussed further.

The impact of shallow water processes on the ocean tide will be explored through the hydrodynamic equations, i.e. the mass (or volume) continuity and momentum equations, following Parker [1984]. The momentum and continuity equations for a Newtonian fluid, contained within a basin on the Earth, in a reference frame stationary with respect to the Earth are derived in Appendix A. These equations are, respectively:

$$\frac{D\underline{\boldsymbol{v}}}{dt} + 2\underline{\boldsymbol{\Omega}} \times \underline{\boldsymbol{v}} = -\frac{1}{\rho}\nabla p + \widetilde{\underline{\boldsymbol{g}}} + \nu\nabla^2\boldsymbol{v} \tag{2.2.1}$$

$$\frac{\partial\rho}{\partial t} + \nabla\cdot(\rho\underline{\boldsymbol{v}}) = 0 \tag{2.2.2}$$

where $\underline{\boldsymbol{v}} = \underline{\boldsymbol{v}}(\underline{\boldsymbol{r}}, t)$ is the velocity field, $\underline{\boldsymbol{r}} = x\underline{\hat{x}} + y\underline{\hat{y}} + z\underline{\hat{z}}$ is a point in the fluid, $\underline{\hat{x}}$, $\underline{\hat{y}}$ and $\underline{\hat{z}}$ describe the Cartesian coordinate system, $\underline{\boldsymbol{\Omega}}$ is the angular velocity field of the Earth, $\rho(\underline{\boldsymbol{r}}, t)$ is the fluid mass density, $p(\underline{\boldsymbol{r}}, t)$ is pressure, $\widetilde{\underline{\boldsymbol{g}}}$ is the combined effect of gravity and the centrifugal force due to the Earth's rotation, and ν is the kinematic viscosity.

2.2.1 Tidal-Stream Turbines

The deployment of tidal-stream turbines (TSTs) in this basin can be accounted for by modifying (2.2.1) to include a momentum sink. This momentum sink is based on actuator disk theory, and is derived in Appendix B. The resulting, modified momentum equation is:

$$\frac{D\underline{v}}{dt} + 2\underline{\Omega} \times \underline{v} = -\frac{1}{\rho_0}\nabla p + \widetilde{\underline{g}} + \nu\nabla^2\underline{v} - \frac{1}{2}\delta_T C_T \underline{v}|\underline{v}| \qquad (2.2.3)$$

where C_T is the turbine thrust coefficient, and:

$$\sum_{i=1}^{N} \int_V \delta_T^i \, dV = NA \qquad (2.2.4)$$

where N is the number of turbines deployed in the basin, and A is the swept area of the turbine rotor. In deriving this momentum sink term it has been assumed that the fluid is an incompressible, ideal fluid.

Equations (2.2.2) & (2.2.3) will now be considered in one-dimensional form. The process of converting these equations into a one-dimensional form is presented in Appendix C. A number of assumptions about the basin containing the fluid (and turbines) must be made first. Namely, that:

- the depth of the basin is small compared to the width and length,

- the width is small compared to the length,

- the condition $L_0 \gg C_0 D_0 B_0 \sin\varphi$ is satisfied (L_0 – basin length scale, C_0 – characteristic wave propagation speed, D_0 – basin depth scale, B_0 – basin width scale, and φ is latitude),

- the flow has a high Reynolds number,

- the basin is uniform and rectangular, i.e. mean water depth and basin width are constant, and the width constant for all tidal elevations,

- the deviation of the flow speed from the cross-sectionally averaged value varies little in the along channel direction,

- if turbines are deployed, they are deployed away from the bed, such that the flow speed at the blades is approximately the cross-sectionally averaged value, and varies little over the swept area of the blades,

- there is no wind shear,

- and friction may be represented by a quadratic friction law.

Perhaps the most questionable of these assumptions is that the channel is rectangular and uniform along its the length. In reality, tidal straits and channels are often topographically complex. Souza and Hill [2006] derived an analytical solution for the tidal hydrodynamics in an open channel using this assumption. They found that when applied to the topographically complex Menai Strait, this solution described the tidal hydrodynamics surprisingly well. For a uniform rectangular channel much shorter than the tidal wavelength the assumption that the tidal current velocity does not deviate much from the cross-sectionally averaged value along the length of the channel will be valid away from the channel entrances where flow expansion and constriction may occur.

The length scales of some tidal channels of interest for tidal-stream development are such that they would satisfy the length-scale conditions imposed above. For example Ramsey Sound and the Sound of Islay. Thus, these assumptions are considered appropriate. The assumption of high Reynolds number is also considered appropriate. Flows through tidal channels are typically highly turbulent due to the high flow speeds, shallow water and complex topography, e.g. Zangibadi et al. [2015] and Milne et al. [2017]. Finally, given that higher in the water column flow speeds will be higher, and the flow less turbulent (e.g. Milne et al. [2017]) it is considered an appropriate assumption that developers will target these regions. Indeed, some developer are targeting floating tidal devices, which exploit these flows and potentially offer reduced installation and maintenance costs, e.g. Orbital Marine Power [2019]

The one-dimensional continuity and momentum equations are:

$$\underbrace{\frac{\partial \eta}{\partial t}}_{(a)} + \underbrace{h\frac{\partial \hat{u}}{\partial x}}_{(b)} + \underbrace{\frac{\partial(\eta\hat{u})}{\partial x}}_{(c)} = 0 \qquad (2.2.5)$$

$$\underbrace{\frac{\partial \hat{u}}{\partial t}}_{(d)} + \underbrace{\hat{u}\frac{\partial \hat{u}}{\partial x}}_{(e)} = \underbrace{-g\frac{\partial \eta}{\partial x}}_{(f)} - \underbrace{\frac{C_F \hat{u}|\hat{u}|}{h(1+\eta/h)}}_{(g)} - \underbrace{\frac{\varepsilon_0 C_T \hat{u}|\hat{u}|}{2(1+\eta/h)}}_{(h)} \qquad (2.2.6)$$

Equation (2.2.5) contains a single non-linear term, (c), which will be termed the Continuity Term (CT). Equation (2.2.6) contains three non-linear terms, the Advection Term (AT), (e), the Friction Term (FT), (g), and the Turbine Term (TT), (h). However, on closer inspection, the FT and TT both contain two non-linear

aspects identifiable through the binomial expansion of the $(1 + \eta/h)^{-1}$ part of both terms:

$$\frac{1}{1 + \eta/h} = \left(1 + \frac{\eta}{h}\right)^{-1} = \sum_{n=0}^{\infty} (-1)^n \left(\frac{\eta}{h}\right)^n \sim 1 - \frac{\eta}{h} \qquad (2.2.7)$$

It will be assumed that terms of order $n = 2$ and higher are negligible (as $\eta/h < 1$, so $(\eta/h)^2 \ll 1$). Therefore, (2.2.6) becomes:

$$\underbrace{\frac{\partial \hat{u}}{\partial t}}_{(d)} + \underbrace{\hat{u} \frac{\partial \hat{u}}{\partial x}}_{(e)} = \underbrace{-g \frac{\partial \eta}{\partial x}}_{(f)} - \underbrace{\frac{C_F}{h} \hat{u}|\hat{u}|}_{(g)} + \underbrace{\frac{C_F}{h^2} \eta \hat{u}|\hat{u}|}_{(h)} - \underbrace{\frac{1}{2} \varepsilon_0 C_T \hat{u}|\hat{u}|}_{(i)} + \underbrace{\frac{1}{2h} \varepsilon_0 C_T \eta \hat{u}|\hat{u}|}_{(j)} \qquad (2.2.8)$$

Both the FT and TT have a quadratic aspect, henceforth referred to as the Quadratic Friction Term (QFT) and Quadratic Turbine Term (QTT), (i) and (k) respectively, and an aspect influenced by the free-surface elevation, henceforth referred to as the Elevation Friction Term (EFT) and Elevation Turbine Term (ETT), (j) and (l) respectively.

The steps taken to arrive at (2.2.5) and (2.2.8) (Appendix C) follow closely those taken by Parker [1984] with the exception of the discussion surrounding the turbine terms. Additionally, the harmonic expansions of the non-linear terms in the following sub-sections, and Appendices D and E, will also bare resemblance to those carried out by Parker [1984].

2.2.2   Overtides

If a single-constituent tide forces the free-surface then η and $\hat{u}$ will be given by:

$$\eta(x, t) = \eta_0 \cos(\theta(x, t) + \gamma(x)) \qquad (2.2.9)$$

and

$$\hat{u}(x, t) = \hat{u}_0 \cos(\theta(x, t)) \qquad (2.2.10)$$

respectively, where η_0 and $\hat{u}_0$ are the amplitudes of η and $\hat{u}$, $\theta = \sigma t - \psi(x)$, σ is the tidal frequency, ψ is the phase of $\hat{u}$, $\gamma = \psi(x) - \phi(x)$, and ϕ is the phase of η. Substituting (2.2.9) and (2.2.10) into the CT and AT gives:

$$\frac{\partial(\eta\hat{u})}{\partial x} = \frac{\eta_0\hat{u}_0}{2}\left[\frac{\partial(\phi+\psi)}{\partial x}\sin(2\theta+\gamma) + \frac{\partial\gamma}{\partial x}\sin(\gamma)\right] \qquad (2.2.11)$$

and

$$\hat{u}\frac{\partial\hat{u}}{\partial x} = \frac{\hat{u}_0^2}{2}\frac{\partial\psi}{\partial x}\sin(2\theta) \qquad (2.2.12)$$

(see Appendix D). Substituting (2.2.9) and (2.2.10) into the QFT and EFT and expanding as a Fourier series (expansions carried out in Appendix D) gives:

$$\frac{C_F}{h}\hat{u}|\hat{u}| = \frac{8\hat{u}_0^2 C_F}{3\pi h}\left[\cos(\theta) + \frac{1}{5}\cos(3\theta) - \frac{1}{35}\cos(5\theta)\right] + \dots \qquad (2.2.13)$$

and

$$\frac{C_F}{h^2}\eta\hat{u}|\hat{u}| = \frac{4\eta_0\hat{u}_0^2 C_F}{\pi h^2}\left[\left(\frac{2}{6} + \frac{2}{5}\cos(2\theta) + \frac{1}{35}\cos(4\theta) + \frac{2}{315}\cos(6\theta)\right)\cos(\gamma)\right.$$
$$\left. + \left(\frac{4}{15}\sin(2\theta) - \frac{2}{7}\sin(4\theta) + \frac{1}{21}\sin(6\theta)\right)\sin(\gamma)\right] + \dots \quad (2.2.14)$$

Physically, γ is the phase difference between maximum flood and high water. When $\gamma = \pm\pi/2$, maximum flow occurs when $\eta = 0$. At the other extreme, if $\gamma = 0$, maximum flood would occur at $\eta = \eta_0$ (and maximum ebb at $\eta = -\eta_0$). These two cases describe a standing tide and a progressive tide respectively and either of these cases simplify the expressions (2.2.9), (2.2.11) and (2.2.14). For a progressive tide, $\gamma = 0$, in this case (2.2.9) simplifies to:

$$\eta = \eta_0\cos(\theta) \qquad (2.2.15)$$

(2.2.11) simplifies to:

$$\frac{\partial(\eta\hat{u})}{\partial x} = -\frac{\eta_0\hat{u}_0}{2}\frac{\partial(\phi+\psi)}{\partial x}\sin(2\theta) \qquad (2.2.16)$$

and (2.2.14) simplifies to:

$$\frac{C_F}{h^2}\eta\hat{u}|\hat{u}| = \frac{4\eta_0\hat{u}_0^2 C_F}{\pi h^2}\left(\frac{2}{6} + \frac{2}{5}\cos(2\theta) + \frac{1}{35}\cos(4\theta) + \frac{2}{315}\cos(6\theta)\right) + \dots \quad (2.2.17)$$

In reality the general case, $\gamma \neq 0$, is most likely to apply at a tidal site, i.e. it is unlikely that the tide will be *purely* progressive in general. However, we will persist

with the assumption that $\gamma = 0$ in order to greatly simplify the expansions for the two-frequency tide (§2.2.3).

From the expansions (2.2.12), (2.2.13), (2.2.16) and (2.2.17) one can see how a single-constituent tide interacts with itself, through the non-linear terms to introduce harmonics, known as shallow water tides. If, for example, the astronomic tide is comprised of only the M_2, then (2.2.12) and (2.2.16) will introduce the M_4, (2.2.13) will introduce the M_6, M_{10}, etc., and (2.2.17) will introduce the M_4, M_8, M_{12}, etc.. This type of shallow water tide, is known as an overtide, and henceforth overtides with frequencies $2n_o\theta$, where n_o are odd intergers, will be termed odd overtides, and overtides with frequencies $2n_e\theta$, where n_e are even integers, will be termed even overtides.

2.2.3 Compound Tides

If one now considers the case where the free-surface is forced by a two-constituent tide, equations (2.2.9) and (2.2.10) are rewritten:

$$\eta = \eta_0 \cos(\theta) + \eta_0' \cos(\theta' + \gamma') \tag{2.2.18}$$

$$\hat{u} = \hat{u}_0 \cos(\theta) + \hat{u}_0' \cos(\theta') \tag{2.2.19}$$

where primed terms relate to the second constituent, but are otherwise denoted the same way as for the first constituent. Substitution of (2.2.18) and (2.2.19) into the CT and AT gives:

$$\hat{u}\frac{\partial \hat{u}}{\partial x} = -\frac{1}{2}\left(\hat{u}_0^2 \frac{\partial \psi}{\partial x}\sin(2\theta) + \hat{u}_0'^2 \frac{\partial \psi'}{\partial x}\sin(2\theta') \right.$$
$$\left. + \hat{u}_0\hat{u}_0'\left(\frac{\partial(\psi + \psi')}{\partial x}\sin(\theta + \theta') + \frac{\partial(\psi - \psi')}{\partial x}\sin(\theta - \theta') \right) \right) \tag{2.2.20}$$

$$\frac{\partial(\eta\hat{u})}{\partial x} = -\frac{1}{2}\left(\eta_0\hat{u}_0\frac{\partial(\phi+\psi)}{\partial x}\sin(2\theta) + \eta_0'\hat{u}_0'\frac{\partial(\phi'+\psi')}{\partial x}\sin(2\theta'+\gamma')\right.$$
$$-\eta_0\hat{u}_0'\frac{\partial(\phi'+\psi)}{\partial x}\sin(\theta+\theta') - \eta_0'\hat{u}_0\frac{\partial(\phi+\psi')}{\partial x}\sin(\theta+\theta'+\gamma')$$
$$+\eta_0\hat{u}_0'\frac{\partial(\phi'-\psi)}{\partial x}\sin(\theta-\theta') - \eta_0'\hat{u}_0\frac{\partial(\phi-\psi')}{\partial x}\sin(\theta-\theta'-\gamma')$$
$$\left.+\eta_0'\hat{u}_0'\frac{\partial\gamma'}{\partial x}\sin(\gamma')\right) \quad (2.2.21)$$

(see Appendix E). For the two-constituent case, one runs into a problem when attempting to substitute (2.2.18) and (2.2.19) into the QFT and EFT and expand as a Fourier series. The terms are a function of both θ and θ', so one can no longer expand as a series of θ. To circumnavigate this problem Godin and Gutiérrez [1986] used the Babylonian method (or Hero's method) to approximate a square-root, and the substitution of $|\hat{u}| = \sqrt{\hat{u}^2}$ to avoid the Fourier-series expansion (see Appendix E). The result of this is the approximate expansions of the QFT and EFT for a two-constituent tide:

$$\frac{C_F}{h}\hat{u}|\hat{u}| \sim \frac{C_F}{2h}\left(\hat{u}_0\left(\left(m + \frac{3}{2m}\left(\frac{1}{2}\hat{u}_0^2 + \hat{u}_0'^2\right)\right)\cos(\theta) + \frac{1}{2}\hat{u}_0^2\cos(3\theta)\right.\right.$$
$$\left.+\frac{3}{2}\hat{u}_0\hat{u}_0'(\cos(2\theta-\theta') + \cos(2\theta+\theta'))\right)$$
$$+\hat{u}_0'\left(\left(m + \frac{3}{2m}\left(\hat{u}_0^2 + \frac{1}{2}\hat{u}_0'^2\right)\right)\cos(\theta') + \frac{1}{2}\hat{u}_0'^2\cos(3\theta')\right.$$
$$\left.\left.+\frac{3}{2}\hat{u}_0\hat{u}_0'(\cos(2\theta'-\theta) + \cos(2\theta'+\theta))\right)\right) \quad (2.2.22)$$

$$\frac{C_F}{h^2}\eta\hat{u}|\hat{u}| \sim \frac{C_F}{4h^2}\left(\eta_0\hat{u}_0\left(m + \frac{1}{m}\left(\hat{u}_0^2 + \frac{3}{2}\hat{u}_0'^2\right)\right)\cos(2\theta)\right.$$

$$+ \frac{3}{4m}\eta_0'\hat{u}_0^2\hat{u}_0'\cos(2\theta - \gamma') + \frac{3}{2m}\eta_0\hat{u}_0\hat{u}_0'^2\cos(2\theta')$$

$$+ \eta_0'\hat{u}_0'\left(m + \frac{3}{2m}\left(\hat{u}_0^2 + \frac{1}{2}\hat{u}_0'^2\right)\right)\cos(2\theta' + \gamma')$$

$$+ \frac{1}{4m}\eta_0'\hat{u}_0'^3\cos(2\theta' - \gamma') + \frac{1}{4m}\eta_0\hat{u}_0^3\cos(4\theta) + \frac{1}{4m}\eta_0'\hat{u}_0'^3\cos(4\theta' + \gamma')$$

$$+ \eta_0\hat{u}_0'\left(m + \frac{3}{4m}\left(3\hat{u}_0^2 + \hat{u}_0'^2\right)\right)\cos(\theta - \theta')$$

$$+ \eta_0'\hat{u}_0\left(m + \frac{3}{4m}\left(\hat{u}_0^2 + 3\hat{u}_0'^2\right)\right)\cos(\theta - \theta' - \gamma')$$

$$+ \eta_0\hat{u}_0'\left(m + \frac{3}{4m}\left(3\hat{u}_0^2 + \hat{u}_0'^2\right)\right)\cos(\theta + \theta')$$

$$+ \frac{3}{4m}\eta_0'\hat{u}_0\hat{u}_0'^2\cos(\theta + \theta' - \gamma')$$

$$+ \eta_0'\hat{u}_0\left(m + \frac{3}{2m}\left(\frac{1}{2}\hat{u}_0^2 + \hat{u}_0'^2\right)\right)\cos(\theta + \theta' + \gamma')$$

$$+ \frac{3}{4m}\eta_0\hat{u}_0^2\hat{u}_0'\cos(3\theta - \theta') + \frac{1}{4m}\eta_0'\hat{u}_0^3\cos(3\theta - \theta' - \gamma')$$

$$+ \frac{1}{4m}\eta_0\hat{u}_0'^3\cos(3\theta' - \theta) + \frac{3}{4m}\eta_0'\hat{u}_0\hat{u}_0'^2\cos(3\theta' - \theta + \gamma')$$

$$+ \frac{3}{4m}\eta_0\hat{u}_0^2\hat{u}_0'\cos(3\theta + \theta') + \frac{1}{4m}\eta_0'\hat{u}_0^3\cos(3\theta + \theta' + \gamma')$$

$$+ \frac{1}{4m}\eta_0\hat{u}_0'^3\cos(3\theta' + \theta) + \frac{3}{4m}\eta_0'\hat{u}_0\hat{u}_0'^2\cos(3\theta' + \theta + \gamma')$$

$$+ \frac{3}{4m}\eta_0\hat{u}_0\hat{u}_0'^2\cos(2(\theta - \theta')) + \frac{3}{4m}\eta_0'\hat{u}_0^2\hat{u}_0'\cos(2(\theta - \theta') - \gamma')$$

$$+ \frac{3}{4m}\eta_0\hat{u}_0\hat{u}_0'^2\cos(2(\theta + \theta')) + \frac{3}{4m}\eta_0'\hat{u}_0^2\hat{u}_0'\cos(2(\theta + \theta') + \gamma')$$

$$+ \eta_0\hat{u}_0\left(m + \frac{3}{2m}\left(\frac{1}{2}\hat{u}_0^2 + \hat{u}_0'^2\right)\right)$$

$$\left. + \eta_0'\hat{u}_0'\left(m + \frac{3}{2m}\left(\hat{u}_0^2 + \frac{1}{2}\hat{u}_0'^2\right)\right)\cos(\gamma')\right) \quad (2.2.23)$$

where m is a non-negative, real test value (see Appendix E). If it is assumed that the two constituents making up the tide are the M_2 and S_2, then the assumption that $\eta_0' \sim \eta_0/2$ and $\hat{u}_0' \sim \hat{u}_0/2$ will be made. This assumption is based on the coefficients of these constituents in the tide-generating potential [Doodson, 1921] (see also Table 2.2). With this assumption, and assuming that $\gamma = \gamma' = 0$, (2.2.20)–(2.2.23) simplify to:

$$\hat{u}\frac{\partial \hat{u}}{\partial x} = -\frac{\hat{u}_0^2}{2}\left(\frac{\partial \psi}{\partial x}\sin(2\theta) + \frac{1}{4}\frac{\partial \psi'}{\partial x}\sin(2\theta') + \frac{1}{2}\left(\frac{\partial(\psi+\psi')}{\partial x}\sin(\theta+\theta')\right.\right.$$
$$\left.\left.+\frac{\partial(\psi-\psi')}{\partial x}\sin(\theta-\theta')\right)\right) \quad (2.2.24)$$

$$\frac{\partial(\eta\hat{u})}{\partial x} = -\frac{\eta_0\hat{u}_0}{2}\left(\frac{\partial(\phi+\psi)}{\partial x}\sin(2\theta) + \frac{1}{4}\frac{\partial(\phi'+\psi')}{\partial x}\sin(2\theta')\right.$$
$$-\frac{1}{2}\left(\left(\frac{\partial(\phi'+\psi)}{\partial x} + \frac{\partial(\phi+\psi')}{\partial x}\right)\sin(\theta+\theta')\right.$$
$$\left.\left.-\left(\frac{\partial(\phi'-\psi)}{\partial x} - \frac{\partial(\phi-\psi')}{\partial x}\right)\sin(\theta-\theta')\right)\right) \quad (2.2.25)$$

$$\frac{C_F}{h}\hat{u}|\hat{u}| \sim \frac{C_F\hat{u}_0}{2h}\left(\left(m+\frac{9\hat{u}_0^2}{8m}\right)\cos(\theta) + \frac{1}{2}\left(m+\frac{27\hat{u}_0^2}{16m}\right)\cos(\theta')\right.$$
$$+\frac{1}{2}\hat{u}_0^2\cos(3\theta) + \frac{1}{16}\hat{u}_0^2\cos(3\theta') + \frac{3}{4}\hat{u}_0^2(\cos(2\theta-\theta') + \cos(2\theta+\theta'))$$
$$\left.+\frac{3}{8}\hat{u}_0^2(\cos(2\theta'-\theta) + \cos(2\theta'+\theta))\right) \quad (2.2.26)$$

$$\frac{C_F}{h^2}\eta\hat{u}|\hat{u}| \sim \frac{C_F\eta_0\hat{u}_0}{4h^2}\left(\left(m+\frac{7\hat{u}_0^2}{4m}\right)\cos(2\theta) + \frac{1}{4}\left(m+\frac{133\hat{u}_0^2}{16m}\right)\cos(2\theta')\right.$$
$$+\frac{\hat{u}_0^2}{4m}\cos(4\theta) + \frac{\hat{u}_0^2}{64m}\cos(4\theta') + \left(m+\frac{60\hat{u}_0^2}{32m}\right)(\cos(\theta-\theta') + \cos(\theta+\theta'))$$
$$+\frac{\hat{u}_0^2}{2m}(\cos(3\theta-\theta') + \cos(3\theta+\theta')) + \frac{\hat{u}_0^2}{8m}(\cos(3\theta'-\theta) + \cos(3\theta'+\theta))$$
$$\left.+\frac{6\hat{u}_0^2}{16m}(\cos(2(\theta-\theta')) + \cos(2(\theta+\theta'))) + \left(\frac{5}{4m}+\frac{99\hat{u}_0^2}{64m}\right)\right) \quad (2.2.27)$$

As the two constituents have been taken to be the M_2 and S_2, for the two-constituent case, the expansions (2.2.24) and (2.2.25) introduce the M_4, S_4, MS_4 and MS, (2.2.26) introduces the M_6, S_6, $2MS_2$, $2MS_6$, $2SM_2$ and $2SM_6$, and (2.2.27) introduces the M_4, S_4, M_8, S_8, MS_4, MS, $3MS_8$, $3MS_4$, $3SM_8$, $3SM_4$ and the first overtide of MS_4. Here we see the overtides of both the M_2 and S_2 introduced, and also tidal constituents with frequencies that are a combination of the M_2 and S_2 – compound tides. These compound tides are the result of the two constituents interacting, with each other, through non-linear processes. The expansions (2.2.26)

and (2.2.27) are written as approximations, whereas in reality they would be infinite series, like the expansions (2.2.13) and (2.2.14). From comparison of these two sets of expansions, one can discern the higher order terms omitted from (2.2.26) and (2.2.27) in the approximation. In the above expansions, the compound tide terms have the form $n\theta \pm n'\theta'$. When $n \pm n' = 2n_e$ the compound tide will be referred to as even, and when $n \pm n' = 2n_o$ the compound tide will be referred to as odd, i.e. $(3\theta + \theta') \rightarrow 3\mathrm{MS}_8$, is an even compound tide, and $(2\theta + \theta') \rightarrow 2\mathrm{MS}_6$, is an odd compound tide.

2.2.4 The Impact of Tidal-Stream Turbines on the Overtides and Compound Tides

The expansions of the turbine terms have not been carried out above. However, if one was to do so one would find that the expansions would be the same as those for the friction term, with C_F/h replaced by $\varepsilon_0 C_T/2$. The importance of this is that the turbines will impact both odd and even overtides and compound tides. Adcock and Draper [2014] discuss the effect of turbines on the higher harmonics of the astronomic tidal constituents. Their equations (1) and (2) are the same as (2.2.5) and (2.2.6) in this work, except that the cross-sectional area of the channel is considered uniform in x here. They assume $\eta \ll h$ and $L \ll \lambda$, which leads to the loss of the CT, AT, EFT and ETT. This in turn leads to considerable simplification of the momentum equation necessary in order to arrive at an analytical solution to the equation. However, these assumptions will not be made here (as detailed in the following sub-section).

Adcock and Draper [2014] concluded that turbines will always reduce the even overtides, unless the channel is inertia dominated or the turbine term varies asymmetrically. They reached this conclusion by relaxing the $L \ll \lambda$ assumption and reasoning that the turbines will reduce the volume flux of water through the channel, thus reducing the AT (written $(Q/A)[\partial(Q/A)/\partial x]$ by Adcock and Draper [2014], where A is the channel cross-section, E in this text), and therefore generation of the even overtides. However, local to the turbine the change to u resulting from turbine operation will be more complex, with flow slowed as it passes through the turbines, and accelerated as it is forced around the turbine.

Such changes to the flow suggest increased spatial gradients of velocity local to the turbine, implying a larger AT ($u\partial u/\partial x$) and therefore augmented even overtide generation. Thus, it is reasoned here that even overtides may be both augmented and reduced by turbines, regardless of the dynamic balance of the channel[8], or asymmetric variation of the turbine term (however this may also alter the even overtide generation e.g. ETT, expansion (2.2.17)).

In the discussion above a distinction was made between the odd and even overtides and compound tides. The reasoning for this is illustrated in Figures 2.6 & 2.7, and described below. From examination of Figures 2.6 & 2.7, one can see that with the introduction of the harmonics of the fundamental frequency, a distortion to the total tide is introduced. More correctly, it is the distortions to the tide, by processes such as friction, or indeed the introduction of tidal-stream turbines, that introduce these harmonics of the tide. From Figure 2.6 one can see that the first even overtide represents asymmetric distortion to the tide, whilst from Figure 2.7 it can be seen that the odd overtide represents symmetric distortions to the tide. It was for this reason that the distinction was made between the odd and even harmonics above.

Parker [1991, 2007] gives physical descriptions of some natural mechanisms for the distortion to the astronomic tidal constituents (see Parker [1991] and Parker [2007], §7.6.5). Armed with an understanding of the physical origins of these shallow-water tidal constituents, one can, through a detailed examination of these constituents, gain a strong understanding of the shallow-water distortions to the tide and its cause. In this work this approach will be applied to investigate the changes to the hydrodynamics resulting from the operation of tidal-stream turbines. Beyond reductions to the astronomic tide, as reported by various authors in the literature, e.g. Karsten et al. [2008], which will manifest themselves as reductions to the fundamental constituents (e.g. M_2, S_2, O_1, K_1, etc.), this analysis will look for changes to the shallow-water constituents, with augmentation of the first even harmonic, indicating increased asymmetric distortion to the total tide, being of specific interest.

---

[8]The balance of forces in the channel, indicating the relative importance of, e.g. frictional and inertial forces to the hydrodynamics. See e.g. Vennell [1998].
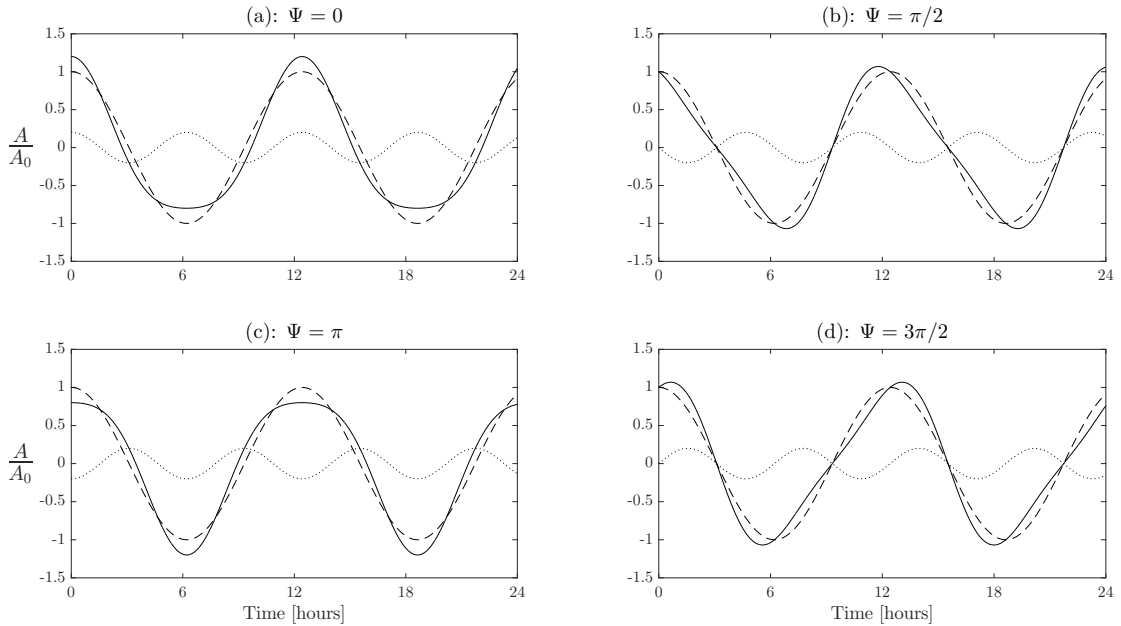
Figure 2.6: Superposition (solid line) of a normalised M_2 wave (dashed line) and a normalised M_4 wave (dotted line) with an amplitude 10 times smaller for various values of the relative phase between the two waves, Ψ.

2.3   Tidal Asymmetry

The term "tidal asymmetry" may be used to refer to a number of types of asymmetry that can occur in the tide. One might first distinguish between horizontal and vertical asymmetries, as in Wang et al. [1999], with vertical asymmetries pertaining to the rise and fall of the tide, i.e. changing water surface elevation, and horizontal asymmetries pertaining to the associated flows, i.e. tidal currents. A further distinction between duration-asymmetry and magnitude-asymmetry (e.g. Dronkers [1986], de Swart and Zimmerman [2009], Gong et al. [2016]) can be made. In the horizontal tide the former refers to an asymmetry in the length of time from peak flood to peak ebb and from peak ebb to peak flood, and the latter refers to an asymmetry in the magnitudes of the peak ebb and peak flood currents. In the vertical tide the former refers to an asymmetry in the duration of the rising and falling tides, whilst the latter refers to an asymmetry in the amplitude of the rise and fall of the tide. In this work the focus will be on changes to tidal currents.

Following Gong et al. [2016] the abbreviations FVA (Flow Velocity Asymmetry) and FDA (Flow Duration Asymmetry) will be used to refer to magnitude and

duration asymmetry in the horizontal tide respectively. A tide may be referred to as flood-dominant if the magnitude of the peak flood current exceeds the magnitude of the peak ebb current, and ebb-dominant if the opposite is true. In semi-diurnal tidal regimes, i.e. regions where the semi-diurnal tidal constituents dominate, and the total tide has two high and low tides of approximately equal size, the asymmetry is commonly, largely dictated by the interaction of the M_2 and M_4 tidal constituents (e.g. Pingree and Griffiths [1979] for UK waters). In diurnal (regions where diurnal tides dominate and there is a single high and low tide per day), or mixed tidal regimes (regions where neither diurnal or semi-diurnal constituents dominate and there are two high and low tides of different heights per day) tidal asymmetry may also be introduced through the interaction of diurnal (e.g. K_1, O_1, etc.) and semi-diurnal (e.g. M_2, S_2, etc.) constituents [Nidzieko, 2010].
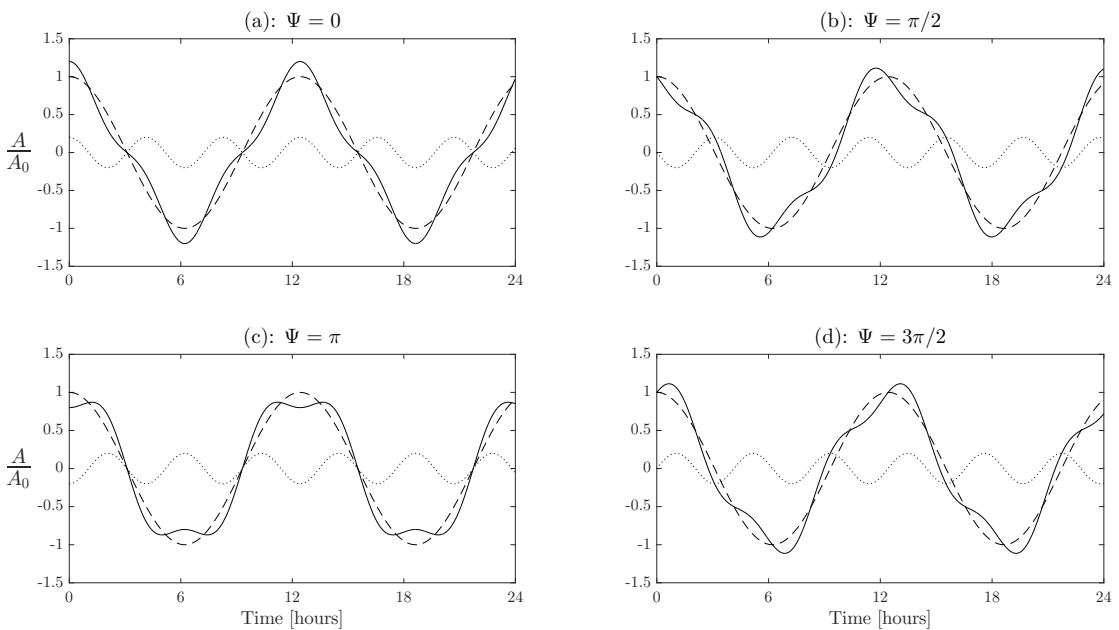
Figure 2.7: Superposition (solid line) of a normalised M_2 wave (dashed line) and a normalised M_6 wave (dotted line) with an amplitude 10 times smaller for various values of the relative phase between the two waves, Ψ.

The introduction of asymmetry through the interaction of the M_2 & M_4 constituents is illustrated in Figure 2.6. This figure bears resemblance to figures in, for example, Pingree and Griffiths [1979], van de Kreeke and Robaczemska [1993] and Neill et al. [2009], as will, therefore, the proceeding discussion. If one takes

the waves in Figure 2.6 to be time-series of the M_2 (dashed line) and M_4 (dotted line) tidal current along with the superposition of the two (solid line), with positive values indicating flow in the flood-direction and negative values indicating flow in the ebb-direction, then one can see that the type of current asymmetry of the current depends on the relative phase between the two constituents, Ψ. In Figures 2.6b & 2.6d, $\Psi = \pi/2$ and $\Psi = 3\pi/2$, and for these two cases there is a FDA with, respectively, the time between peak ebb and peak flood shorter than the time between peak flood and peak ebb and vice-versa. In Figures 2.6a & 2.6c, $\Psi = 0$ and $\Psi = \pi$, and for these two cases there is flood-dominant and ebb-dominant FVA respectively. For intermediate values of Ψ some combination of the two types of asymmetry will occur. Compare what is seen in Figure 2.6 with what is seen in Figure 2.7. The sixth-diurnal overtide, despite distorting the tide does not introduce either type of asymmetry[9]. This is the reason for the distinction between the odd and even overtides and compound tides in the previous sections, as it is primarily the first even overtide that represents asymmetry in UK waters [Pingree and Griffiths, 1979].

The variation of the types of asymmetry with relative phase is periodic. If one defines the maximum flood-dominant FVA case +1 and the maximum ebb-dominant FVA case -1 then the variation in FVA with Ψ behaves like $\cos(\Psi)$. If the ratio of the amplitudes, A, of the two waves, A_{M_4}/A_{M_2}, grows larger then the distortion to the resultant tide, and therefore the degree of asymmetry, will also grow larger. From this one may define a metric for the degree of FVA:

$$A_{S,1} = \frac{A_{M4}}{A_{M2}} \cos(\Psi) \tag{2.3.1}$$

Bruder and Haas [2014] employ a different method for quantifying FDA and FVA, taken from gravity wave analysis [Elgar and Guza, 1985]. This method uses the skewness, S_v, of the velocity time-series:

---

[9]However, the triplet interaction of the M_2, M_4 and M_6 will introduce asymmetry [van de Kreeke and Robaczemska, 1993, Blanton et al., 2002].

$$S_v = \frac{\frac{1}{t}\sum_{t=1}^{T}(\boldsymbol{v}(t) - \overline{\boldsymbol{v}})^3}{\left(\frac{1}{T}\sum_{t=1}^{T}(\boldsymbol{v}(t) - \overline{\boldsymbol{v}})^2\right)^{\frac{3}{2}}} \qquad (2.3.2)$$

where T is the total number of time-indices, $\boldsymbol{v}(t)$ is the velocity at time t, $\overline{\boldsymbol{v}}$ is the temporal mean of $\boldsymbol{v}(t)$, to quantify the FVA. The asymmetry of the time-series, A_v, was then used to quantify the FDA. This is obtained via the skewness of the imaginary portion of the Hilbert transform of the velocity time-series, $H(\boldsymbol{v})$:

$$A_v = S_{\mathrm{imag}(H(\boldsymbol{v}))} \qquad (2.3.3)$$

Bruder and Haas [2014] applied this methodology to synthetic time-series for the M_2 and M_4. Nidzieko [2010] used a similar method to investigate the asymmetry introduced through the interaction of the K_1, O_1 and M_2 tides along the western coast of the USA. The skewness of the time-derivative of the surface elevation, η', was calculated rather than the velocity. The skewness of the full time-series gives the mean asymmetry over the duration of observation [Nidzieko, 2010], but in an approach akin to the calculation of the moving average, Nidzieko [2010] calculated the skewness of η' for 1 lunar day (24.84 hour) sub-sets of the total record using (2.3.2) and showed this method to give a very good approximation of traditional methods using the harmonic analysis, e.g. (2.3.1). The method of Nidzieko [2010] was extended by Song et al. [2011] allowing for the sets of constituents leading to asymmetry to be identified, and for the relative contributions of each of these sets to be determined. The method of Song et al. [2011] is extremely powerful, not only for mixed tidal regimes but also for semi-diurnal regimes as further constituent interactions which contribute to the asymmetry can be considered, and their relative importance determined.

Song et al. [2011] derived the following relationship between the skewness in the time-series of the time derivative of the water surface elevation, $\zeta = \partial\eta/\partial t$, for N constituents, and the interactions between pairs and triplets of constituents:

$$S_{\zeta,N} = \sum_{i}^{N}\beta \qquad (2.3.4)$$

where β is the relative contribution of each interaction where for a pair interaction:

$$\beta = S_{\zeta,2} \cdot \left(\frac{\eta_{0,1}^2 \sigma_1^2 + \eta_{0,2}^2 \sigma_2^2}{\sum_i^N \eta_{0,i}^2 \sigma_i^2} \right)^{\frac{3}{2}} \qquad (2.3.5)$$

and for a triplet interaction:

$$\beta = S_{\zeta,3} \cdot \left(\frac{\eta_{0,1}^2 \sigma_1^2 + \eta_{0,2}^2 \sigma_2^2 + \eta_{0,3}^2 \sigma_3^2}{\sum_i^N \eta_{0,i}^2 \sigma_i^2} \right)^{\frac{3}{2}} \qquad (2.3.6)$$

where $\eta_{0,i}$ is the surface elevation amplitude for constituent i, σ_i is the frequency of constituent i,

$$S_{\zeta,2} = \frac{\frac{3}{2} \eta_{0,1}^2 \sigma_{0,2} \sin(2\psi_1 - \psi_2)}{\frac{1}{2}(\eta_{0,1}^2 + 4\eta_{0,2}^2)} \qquad (2.3.7)$$

and

$$S_{\zeta,3} = \frac{\frac{3}{2} \eta_{0,1} \sigma_1 \eta_{0,2} \sigma_2 \eta_{0,3} \sigma_3 \sin(\psi_1 + \psi_2 + \psi_3)}{\left[\frac{1}{2}(\eta_{0,1}^2 \sigma_1^2 + \eta_{0,2}^2 \sigma_2^2 + \eta_{0,3}^2 \sigma_3^2) \right]^{\frac{3}{2}}} \qquad (2.3.8)$$

The pair and triplet interactions are between sets of constituents that satisfy the frequency relationships $2\sigma_1 = \sigma_2$ and $\sigma_1 + \sigma_2 = \sigma_3$ respectively.

So, with this methodology, following the harmonic analysis of a sufficiently long time-series the relative contribution of the many pairs or triplets of constituents that may introduce Tidal Duration Asymmetry (TDA), an asymmetry in the durations of high and low water, may be determined. To do likewise for the FDA and FVA, following Gong et al. [2016] the above methodology can be applied to the time-series of $\partial u/\partial t$ and u respectively. When combined with the knowledge of the physical origins of the shallow-water constituents, the knowledge of the relative contribution of the interaction of these shallow-water constituents and astronomic constituents (e.g. the M_2-M_4 or M_2-S_2-MS_4 interactions) gives a good insight into the relative importance of the various physical processes leading to distortions to the tide and therefore to the resulting tidal TDA, FDA or FVA. The expansions presented in §2.2 lead to an understanding of the physical origins of the various distortions, and texts such as Parker [1991, 2007], discuss these physical origins in more detail.

The downside to this method in relation to real-world applications is the sparsity of observations. Time-series are usually only available at tide-gauge stations. However, HF radar campaigns (e.g. Thiébaut and Sentchev [2017]), satellite altimetry data (e.g. Egbert and Erofeeva [2002]) or numerical modelling could be used to generate time-series over an area to allow such an analysis.

2.4 Implications of Tidal Asymmetry for Transport and Power

The asymmetry of a tidal flow has little practical importance in itself. The significance of asymmetry in a tidal flow lies in its importance for other processes, such as sediment transport. In the literature, discussion of tidal asymmetry can often be found within a larger discussion regarding sediment transport or morphodynamics, often with regards to estuarine environments. For example, consider bed-load sediment transport. The driver of this transport is the bed-shear stress, τ, resulting from tidal currents (or waves, or both, but only tidal currents will be discussed here), with $\tau \propto \underline{v}^2$, where $\underline{v}$ is the current velocity vector. Given this relationship, any FVA will be exaggerated in τ, leading to net transport in the direction of the dominant current. This is of particular importance for coarser sediments as the threshold for particle motion, the shear-stress required to move sediment of a given size, is higher. The closer the associated threshold velocities to the peak flood/ebb velocities, the greater the degree of asymmetry as the threshold will be exceeded for less and less of the inferior tidal phase in comparison to the dominant tidal phase. Alternatively, the threshold may be exceeded only on the dominant tide. For suspended-load sediment transport the effect of asymmetry is more complicated and it is FDA that is of greater importance to net transport [Groen, 1967, Dronkers, 1986].

For bed-load sediment transport van de Kreeke and Robaczemska [1993] derived an analytical expression for the long-term averaged bed-load sediment transport:

$$\frac{q_{s,bl}}{f u_{\mathrm{M}_2}^3} = \frac{3}{2} \frac{u_{\mathrm{M}_0}}{u_{\mathrm{M}_2}} + \frac{3}{4} \frac{u_{\mathrm{M}_4}}{u_{\mathrm{M}_2}} \cos(\gamma_{\mathrm{M}_4}) + \frac{3}{2} \frac{u_{\mathrm{M}_4}}{u_{\mathrm{M}_2}} \frac{u_{\mathrm{M}_6}}{u_{\mathrm{M}_2}} \cos(\gamma_{\mathrm{M}_4} - \gamma_{\mathrm{M}_6}) \qquad (2.4.1)$$

where u_i is the amplitude of the velocity constituent i, γ_i is the relative phase between the constituent i and the M_2 ($\gamma_{M_n} = n\psi_{M_2}/2 - \psi_{M_n}$), and f is some function of the sediment and fluid characteristics. This latter term arises from the sediment-transport formula used by van de Kreeke and Robaczemska [1993]:

$$q_{s,bl} = f|u|^2 \cdot \text{sign}(u) \qquad (2.4.2)$$

based on Bagnold [1966]. The long-term average refers to a period of "several months", long enough that the variation over the spring-neap cycle, and other beat frequencies is negated. The derivation also makes the assumption that the M_2 current is at least an order of magnitude larger than all other constituents.

From (2.4.1), one can take away that in addition to the interaction between the M_2 and M_4, the interaction of the M_2 with a mean-flow (M_0) and the triple interaction of the M_2, M_4 and M_6 will also lead to net transport, with the magnitude of the latter being an order of magnitude smaller than that resulting from the two former interactions [van de Kreeke and Robaczemska, 1993]. This is despite the interaction between the M_2 and M_6 not introducing net transport, a point also illustrated in Blanton et al. [2002]. On a larger scale Pingree and Griffiths [1979] noted a similarity between bottom stress vectors resulting from the interaction between the M_2 & M_4 and net sediment transport pathways in the waters around the British Isles. This suggests that asymmetry resulting from the M_2-M_4 interaction plays an important role in dictating net bed-load transport pathways not just at the scale of an estuary, but also at the scale of shallow shelf seas such as the North Sea, Irish Sea, English Channel, etc.. This differentiates the study of Pingree and Griffiths [1979] from other key asymmetry texts, e.g. Speer and Aubrey [1985], Dronkers [1986], Friedrichs and Aubrey [1988], Speer et al. [1991], van de Kreeke and Robaczemska [1993] etc., which concern the role of current asymmetry in net transport at the estuary/tidal inlet system scale.

The discussion above regards bed-load transport, which will be of importance for coarser sediment clasts, ≥ 200 μm, rolling or jumping over the bed [Dronkers, 1986]. Sediment may also be transported as suspended load when the upwards fluid forces exceed gravitational particle settling [Bagnold, 1966]. In estuarine environments suspended load is mainly composed of finer sediments between 1–100 μm [Dronkers,

1986]. However, in regions of large tidal currents, such as sites of interest for tidal-stream exploitation, larger clasts may be suspended. The description of suspended-load transport is complicated by cohesive properties, for finer sediments, and time lag effects, applicable to all grain sizes. A time lag between slack water and minimum suspended-load concentration has been observed, e.g. Postma [1954], which can be explained by the fact that during times of increasing current a certain amount of time is needed for the material to be brought into suspension, and during times of decreasing current a certain amount of time is needed for the material to settle out of suspension [Postma, 1954]. Postma [1961] later noted a FDA with the time between maximum ebb and maximum flood being shorter than the time between maximum flood and maximum ebb led to a net transport of suspended material in the flood direction in the Dutch Wadden Sea. Groen [1967] developed a simple quantitative model of the mechanism responsible for the net transport of suspended material resulting from FDA.

Groen [1967] identified, for the case where all current constituents are negligible compared to the M_2, bar the M_4 which has an amplitude half the size of the M_2, and where the M_2 and M_4 currents are in phase, a 38% asymmetry in the volume of sediment transported as suspended-load over the flood and ebb of the tide, favouring the flood. Figure 2.8 presents a reproduction of Figure 1 from Groen [1967], which is essentially an exaggerated version of the plot in the top left panel of Figure 2.6. This plot clearly shows the distortion to the wave leading to a FDA. The time between peak flood and peak ebb is longer than the time between peak ebb and peak flood. Over the former time period there is a longer slack water allowing for more material to settle out of suspension following the flood, leading to a net flood-wards transport of sediment.

Neill et al. [2009], discussed FVA in relation to sediment transport and the impact of Tidal Stream Turbines (TSTs). Based on the theory of Pingree and Griffiths [1979], Neill et al. [2009] hypothesised that TSTs would have a greater impact on large-scale sediment dynamics when deployed in a region of FVA compared to a region where the flow velocities of the flood and ebb tide are symmetric. Through one-dimensional modelling of the Bristol Channel, UK, Neill et al. [2009] offered support for this hypothesis, with as much as 20% difference in bed-level change
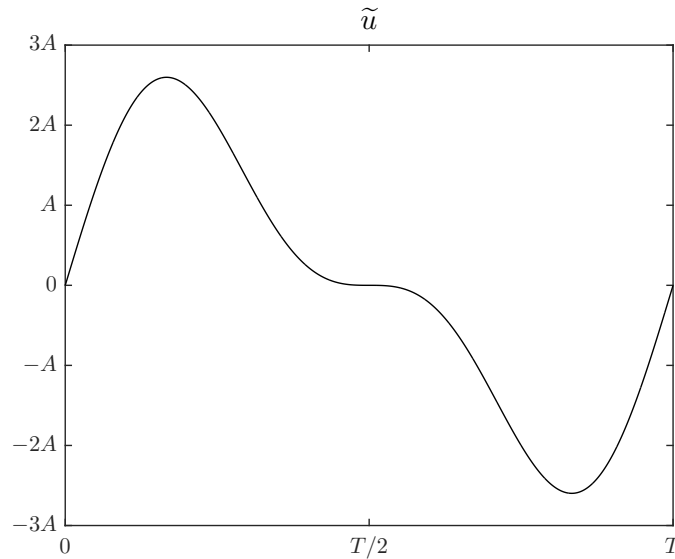
Figure 2.8: Reproduction of Groen [1967] Figure 1, showing an FDA asymmetric wave.

seen between the symmetric and asymmetric cases, averaged over the length of the system.

For reasons similar to those discussed above for sediment transport, asymmetries in tidal currents may also impact the power production of TSTs. This has been discussed in a number of texts in the literature, e.g. Neill et al. [2014], Bruder and Haas [2014], and Robins et al. [2015]. Neill et al. [2014] modelled the deployment of a tidal-stream turbine across 21 different sites in a region suitable for tidal-stream energy exploitation, representing diverse natural FVA conditions. The authors noted the exaggeration of the asymmetry in the current in the turbine power due to the cubic relation between the two, and their modelling indicated a 100% asymmetry turbine power density resulting from a 30% asymmetry in the tidal current (FVA).

Gooch et al. [2009] claim that asymmetry in the power productions leads to less overall power production than if the asymmetry were not present. This is in addition to the skewing of the power supply from four roughly even peaks to two large peaks and two smaller peaks (per day).

In Figure 8 of Robins et al. [2015], hypothetical combined M_2 and M_4 time series for $\Psi = \pi/2$ and $\Psi = \pi$, are plotted along with the practical power that

would be produced over the spring-neap cycle by the prototype 1.2 MW SeaGen-S turbine. Robins et al. [2015] found reduced energy conversion by the turbine for the "asymmetric" (FVA) case compared to the "symmetric" (FDA) case. In their calculations Robins et al. [2015] employed cut-in and cut-out speeds based on the SeaGen-S turbine. Extending their calculation across all sites of interest for tidal-stream energy development across the northwest European shelf seas Robins et al. [2015] noted that where "relatively strong asymmetries" occur there tended to be less practical power production when one considers the M_4 compared to when one does not consider the M_4.

Bruder and Haas [2014], as mentioned above, used the statistical skewness, S_v, (2.3.3), and asymmetry, A_v, (2.3.4), to represent FVA and FDA respectively, in combinations of hypothetical M_2 and M_4 time-series. In their study Bruder and Haas [2014] employ Probability Density Functions (PDFs) of the velocity and power. The beauty of using PDFs is that the relative contributions of velocities to the overall power can be assessed. The peak velocities contributed the most to the overall power, and in the case of a FVA tide, the PDF was bi-modal due to the two differing peaks. In such a tide a turbine designed with a large cut-in speed and rated speed – designed to capture the energy at the peak velocity values – would only capture 65% of the available energy. Compared to 90% for the undistorted and FDA cases, as much of the energy of the lower peak would be excluded.

The above does not account for turbine efficiency however. When Bruder and Haas [2014] considered the turbine efficiency, based on the Betz-limit, 0.59, for two turbines, one with a high cut-in speed and rated speed (first turbine), and another with a moderate cut-in speed and rated speed and reduced efficiency at higher speeds (second turbine), it was the latter that converted energy more efficiently whether the tide was FVA, FDA or undistorted. This is despite the peak velocities contributing most to the available power. For the FVA case a difference of 10% between the two turbines was seen. This was due to the larger cut-in speed leading to much of the power of the smaller peak not being captured by the turbine. For the FDA case the difference was only 6%. The percentage difference in the available energy between the FVA and FDA case was only 2%. However, the percentage difference in the technically exploitable energy between the FVA and FDA cases

was 8% for the second turbine and 12% for the first turbine.

To paraphrase the findings of Bruder and Haas [2014]; as FVA increases more energy is concentrated at the lower end of the velocity distribution, as FDA grows more energy is concentrated near the higher end of the velocity distribution. The implication of this is that when cut-in speeds are considered FVA leads to reduced technically exploitable energy compared to an undistorted tide, whilst for the FDA case, compared to an undistorted tide; for higher rated turbines the technically exploitable energy is increased, and for lower/moderate rated turbines it is reduced.

Bruder and Haas [2014] made no mention of cut-out speed in their study, but it is easy to extrapolate the findings of their work to include this. As the larger velocities contribute more to the available power, if peak velocities exceed the turbine cut-out speed then the most important contribution to the available power is excluded, greatly reducing the technically exploitable power. When the cut-out speed is close to the peak current velocity value for the undistorted case, FVA will have the greatest impact on the technically exploitable energy.

2.5 Hypothesis, Research Questions and Experimental Outline

2.5.1 Hypothesis Development

Thus far in this chapter, the periodic motions of the Earth-Moon-Sun systems have been introduced, and it has been shown how the frequencies of these motions lead to the harmonic development of the equilibrium tide (§2.1). The generation of the harmonics (overtides and compound tides) of these astronomic frequencies has then been introduced (§2.2). It has been shown that, when modelled using a quadratic drag description, the distortions to the tide resulting from a TST introduce the same species of overtides and compound tides as bed friction. That is, all odd and even harmonics. The validity of this statement depends on the characteristic length-scale of the water surface elevation, N_0, being non-negligible in comparison to the characteristic channel depth, D_0. Or, stated more physically, all species of the shallow-water tides will be impacted by the TST so long as the effect of the

TST is flood-ebb asymmetric. This may result from a flood-ebb asymmetry in the blockage ratio of the channel, or due to a FVA in the tidal current in which the turbine is deployed. The former requires N_0 non-negligible compared to D_0. However, the latter may arise in deeper water due to topographic effects on the flow, such as flow separation around a headland, island, or at a channel outlet, or flow constriction at a channel inlet, all of which lead to the generation of the M_4 through the momentum-advection and continuity terms (spatial gradients in the current).

Whilst the harmonic expansions of the non-linear terms can suggest which shallow-water constituents may be impacted by TSTs, they do not offer any insight into how they might be impacted. The analytical work of Adcock and Draper [2014] suggests that the even harmonic tides will be reduced, unless the channel is inertia dominated, or the turbine term is flood-ebb asymmetric. However, this conclusion is based on the reasoning that the volume flux of water in the channel is reduced. In this chapter it was further reasoned that local to the turbine, the pattern of change to the current will be more complex, and thus augmentation of the even overtides may be possible more generally. Further, there are multiple non-linear processes at play, so without solutions to the governing equations it is not possible to say how the even harmonics will be altered. From the above, the first hypothesis that this study will test is therefore that:

> *both odd and even harmonic tides will be altered by the introduction of a TST, locally, as the turbine terms are local, with reductions expected to the odd harmonics and an unknown, and not necessarily similar, change to the even harmonics.*

In the section that followed (§2.3), the way in which the interaction of astronomic tides with their harmonics can introduce asymmetry was discussed. It was seen that in diurnal or mixed regimes the interaction between diurnal and semi-diurnal astronomic tides may also lead to asymmetry. However, this will be set aside as such a regime would lead to a less even temporal distribution of power supply, and will therefore be assumed to be of less interest to a tidal energy developer. Thus, the focus of this study will be on a semi-diurnal regime. Assuming that

in a semi-diurnal regime the M_2 tide dominates (i.e. all other constituents are negligible in comparison), then it will be the M_2-M_4 interaction that dictates the flood-ebb asymmetry (henceforth asymmetry will be taken to refer to FVA and FDA collectively) of the tide. With the form of asymmetry (FVA or FDA) dependant on the phase relationship between the M_2 and M_4 constituents, Ψ, and the strength of the asymmetry dictated by the amplitude ratio of the constituents. Thus, changes to the amplitude and phase of the M_2 or M_4 will alter ambient asymmetry. Reductions to the M_2 amplitude and increases to the M_4 amplitude will increase the size of the asymmetry and vice-versa. Changes to the phase may change both the form of the asymmetry, which, when looking at either FVA or FDA in isolation will also affect their size.

For the flow passing through the turbine the energy at the astronomic frequencies will be reduced, whilst for the flow passing around the turbine the energy at these frequencies will be increased. With no consideration of the change to the even overtides one would expect reduced asymmetry in bypass flow and increased asymmetry in the wakes (inverse relationship between asymmetry and M_2 amplitude, see equations (2.3.1) and (2.3.2)). Taking into account the changes to the M_4 could significantly alter this prediction. All this says nothing about the change to the phases of the constituents. For the M_2 one might expect a phase lag to be added due to the blockage to the tide offered by the turbine(s). Although for a single turbine this effect would be small. Physical intuition cannot be employed to predict the changes to the M_4 phase caused by the turbines in the same way. For the dominant M_2 case, the phase of the M_2 constituent will represent the phase of the tide itself. In contrast, the phases of the harmonics of the M_2 are a mathematical description of the topographic distortion to that tide. Thus, a general prediction of the change to the phase of the harmonics, based on physical intuition is difficult, perhaps impossible, at least prior to a study of the (numerical) solutions to the governing equations. From the above the second hypothesis is therefore that:

> *changes to the current due to a TST will lead to changes to the asymmetry of the flow, both augmentation and reduction, and the changes can be understood through the changes to the constituents that interact to introduce asymmetry.*

Finally, the importance of asymmetry for sediment transport was discussed along with its importance in determining the technically exploitable resource (§2.4). Summarising the two previous hypotheses, TSTs will alter the harmonics of the tide which will alter the ambient flow asymmetry. Combining these hypothesis with the discussion in §2.4 leads to the final hypothesis that:

> *changes to the flow asymmetry will lead to changes in net sediment transport and the technically exploitable resource.*

2.5.2 Research Questions

To focus the experiments that will be carried out to test these hypotheses, they will first be reformulated into a set of research questions. Respectively the three hypotheses may be reformulated into the three following research questions:

1. *How are the harmonic tides altered locally by TSTs?*

2. *How is the flow asymmetry altered locally by TSTs?*

3. *How is net sediment transport and the technically exploitable resource altered locally by TSTs?*

Accounting for the discussion in the preceding sections these three research questions each lead to a set of further sub-questions:

1. *How are the harmonic tides altered locally by TSTs?*

   (a) *How is the alteration to the odd and even harmonics similar/different?*

   (b) *What effect does the variable efficiency of a TST have on its impact on the harmonic tides, in particular cut-in and cut-out speeds?*

   (c) *How sensitive is the effect of a TST to ambient conditions, in particular ambient asymmetry?*

   (d) *How does the impact of a single TST scale across an array of TSTs?*

2. *How is the flow asymmetry altered locally by TSTs?*

(a) *Can the change to the flow asymmetry be predicted from the changes to the tidal constituents (fundamentals and harmonics)?*

(b) *What effect does the variable efficiency of a TST have on its impact on the flow asymmetry, in particular cut-in and cut-out speeds?*

(c) *See 1c).*

(d) *See 1d).*

3. *How is net sediment transport and the technically exploitable resource altered locally by TSTs?*

(a) *Can the change to the technically exploitable resource be predicted from the changes to the flow asymmetry?*

(b) *Can the change to net sediment transport be predicted from the changes to the flow asymmetry?*

Prior to giving an outline of how these research questions will be addressed, the sub-questions will first be qualified briefly. First, for question *1a)*, the discussion around the first hypothesis in §2.5.1 outlines the origin of this question, and likewise, the origin of question *2a)* can be found in the discussion around the second hypothesis.

On the origin of questions *1b)* and *2b)*, consider the turbine term in the momentum equation:

$$\frac{1}{2} \frac{\varepsilon_0 C_T \hat{u} |\hat{u}|}{(1 + \eta/h)} \tag{2.5.1}$$

along with the generic C_T-curve from Bastón et al. [2014], Figure 2.9. The C_T-curve may be broken down into three parts, a part where the turbine is not operational, below the cut-in speed (1 m/s) or above the cut-out speed (4 m/s), a part where the turbine operates with a constant efficiency, between 1 m/s and 2.5 m/s, and a part where the turbine operates at reduced efficiency, between 2.5 m/s and 4 m/s. This may be approximated by the mathematical function:

$$C_T(\hat{u}) = \begin{cases} 0.85, & \text{where } 1 \leq \hat{u} \leq 2.5 \text{ m/s} \\ a\hat{u}^2 + b\hat{u} + c, & \text{where } 2.5 < \hat{u} \leq 4 \text{ m/s} \\ 0, & \text{otherwise} \end{cases} \tag{2.5.2}$$

as the reduced efficiency region fits a quadratic relationship with $\hat{u}$ (taking the current speed to be the 1D velocity $\hat{u}$), where a, b and c are unknown coefficients. Whilst the turbine is operating in the lower efficiency (quadratic) region the turbine term (2.5.1) will be more complex:

$$\frac{1}{2}\frac{\varepsilon_0 a\hat{u}^3|\hat{u}|}{(1+\eta/h)} + \frac{1}{2}\frac{\varepsilon_0 b\hat{u}^2|\hat{u}|}{(1+\eta/h)} + \frac{1}{2}\frac{\varepsilon_0 c\hat{u}|\hat{u}|}{(1+\eta/h)} \tag{2.5.3}$$

than when the turbine is operating in the standard efficiency region:

$$0.425 \times \frac{\varepsilon_0 \hat{u}|\hat{u}|}{(1+\eta/h)} \tag{2.5.4}$$

As such one might expect a different impact on the flow, given the difference in the harmonic expansions of (2.5.3) and (2.5.4) one expects to see.

The even harmonic tides were introduced by the asymmetric effect of the turbine on the flow due to the variation in the blockage ratio caused by the variation of the water surface elevation, as seen in §2.2. Given the dependence of the turbine term on the current speed then one may also expect an asymmetric impact of the turbine on the tide if the flow is initially asymmetric. It is this that leads to questions *1c)* and *2c)*, as one might therefore expect the effect of the turbine on the even overtides, and therefore asymmetry to vary for varying ambient asymmetry conditions.
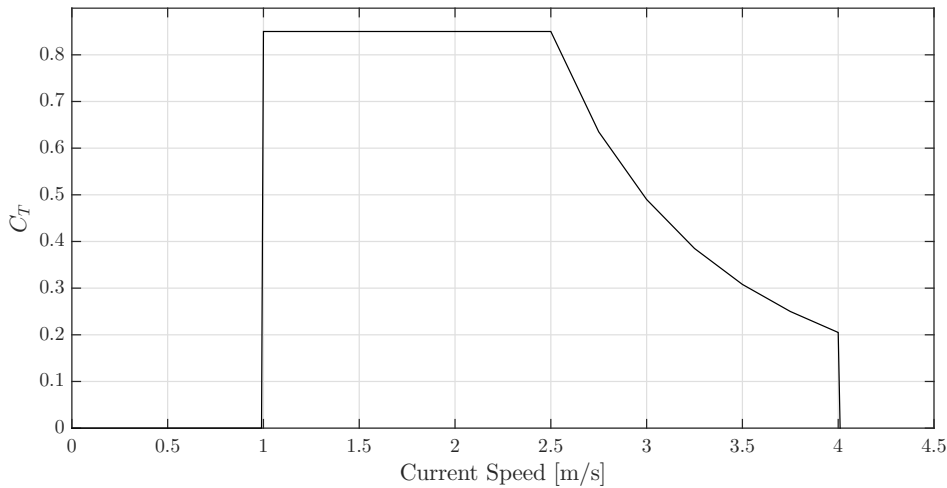
Figure 2.9: Reproduction of the generic tidal-stream turbine thrust coefficient (C_T) curve from Bastón et al. [2014].

Questions *1d)* and *2d)* arise naturally from main questions *1)* and *2)*. The changes to the hydrodynamic conditions by a turbine will alter the hydrodynamic conditions experienced by neighbouring turbines from ambient conditions. Further to this there may be interactions between multiple turbines which alter the nature of the hydrodynamic changes resulting from arrays of turbines.

Finally, in §2.4, the importance of flow asymmetry for both sediment transport and the technically exploitable resource was discussed at length. This discussion implies that changes to the ambient flow asymmetry conditions will lead to changes to the ambient net sediment transport and technically exploitable resource. With this being the case, it leads to questions *3a)* and *3b)* which ask if these changes to the flow asymmetry might be used as a predictor of the knock-on effect for transport and the resource.

2.5.3   Experimental Approach

The lack of publicly available data from TST deployments, and at the time of writing, a lack of commercial-scale TST arrays, leaves only the possibility of a modelling, either physical or numerical, or analytical study to address the above research questions. The analytical approach can be discounted as analytical solutions to the fully non-linear forms of the Navier-Stokes equations are not known, and maintaining the non-linear form of the equations is required as it is the non-linear terms which are responsible for the generation of the harmonic tides. Therefore, a numerical modelling approach will be employed to address the above research questions, as numerically, solutions to the non-linear form of the Navier-Stokes equations can be arrived at. Through numerical experiments it will be feasible to address the previously stated research questions, at least in terms of a first preliminary exploration of this topic.

Three groups of experiments will be carried out to address the three research questions and their associated sub-questions. In the first group of experiments a single TST will be deployed in a channel and the change in the harmonic analysis and asymmetry will be explored. This experiment will be repeated for a fixed- and variable-C_T turbine. For these experiments only the M_2 and its overtides will be looked at, as for a semi diurnal regime – which the focus of this thesis has been

restricted to – the M_2-M_4 interaction will have the most significant influence on asymmetry if other astronomic constituents are assumed negligible in comparison to the M_2 [van de Kreeke and Robaczemska, 1993]. The final experiment in this first group will repeat the fixed-C_T experiment including the S_2 to account for the most significant tidal beat, the spring-neap cycle. These experiments will address questions *1a), 1b), 2a)* and *2b)*.

The second group of experiments will contain three experiments. The first will deploy a single fixed-C_T turbine at multiple locations along the channel to address questions *1c)* and *2c)*, as the ambient asymmetry conditions will differ at different locations along the channel. The next two experiments will look at multiple TSTs deployed in lines and rows. These two experiments will look to address questions *1d)* and *2d)*.

The final group of experiments will look to address questions *3a)* and *3b)*. To look at the impact of TSTs on the technically exploitable resource, question *3a)*, will not require any further simulations, simply for additional analysis of the single TST experiments to be performed. Looking at the impact of TSTs on sediment transport, question *3b)*, will require additional simulations as the model will need to be expanded to include calculations of sediment transport processes. For simplicity and brevity, the impact of only single turbines will be investigated in this group of experiments.

Chapter 3

Model Description

In this chapter, the modelling system used to carry out the numerical experiments to address the research questions developed in the previous chapter is introduced (§3.1) along with the model geometry used (§3.2). The model output is verified against analytical solutions (§3.3) found in the literature and sensitivity tests are performed to explore how the results of the analysis change with varying model parameters (§3.4).

3.1 The Modelling System

The modelling system employed in this work is DHI's MIKE21 FM, a two-dimensional, Flexible Mesh (FM) modelling system, which solves the depth-integrated incompressible Reynolds-averaged Navier-Stokes equations [DHI, 2016a]. MIKE21 FM is comprised of a number of modules; those used here are the hydrodynamic and sediment transport modules. More detail on these modules is given in the proceeding subsections.

3.1.1 The Hydrodynamic Module

The two-dimensional version of MIKE, MIKE21, which will be the version used in this work solves the following two-dimensional equations [DHI, 2016b]:

$$\frac{\partial H}{\partial t} + \frac{\partial (H\overline{u})}{\partial x} + \frac{\partial (H\overline{v})}{\partial y} = HS \qquad (3.1.1)$$

$$\frac{\partial(H\overline{u})}{\partial t} + \frac{\partial(H\overline{u}^2)}{\partial x} + \frac{\partial(H\overline{uv})}{\partial y} - fH\overline{v} = -gH\frac{\partial\eta}{\partial x} - \frac{H}{\rho_0}\frac{\partial p_a}{\partial x} - \frac{gH^2}{2\rho_0}\frac{\partial\rho}{\partial x} + \frac{\tau_{sx}}{\rho_0}$$
$$- \frac{\tau_{bx}}{\rho_0} - \frac{1}{\rho_0}\left(\frac{\partial s_{xx}}{\partial x} + \frac{\partial s_{xy}}{\partial y}\right) + \frac{\partial}{\partial x}(HT_{xx}) + \frac{\partial}{\partial y}(HT_{xy}) + Hu_sS \quad (3.1.2)$$

$$\frac{\partial(H\overline{v})}{\partial t} + \frac{\partial(H\overline{vu})}{\partial x} + \frac{\partial(H\overline{v}^2)}{\partial y} - fH\overline{u} = -gH\frac{\partial\eta}{\partial y} - \frac{H}{\rho_0}\frac{\partial p_a}{\partial y} - \frac{gH^2}{2\rho_0}\frac{\partial\rho}{\partial y} + \frac{\tau_{sy}}{\rho_0}$$
$$- \frac{\tau_{by}}{\rho_0} - \frac{1}{\rho_0}\left(\frac{\partial s_{yx}}{\partial x} + \frac{\partial s_{yy}}{\partial y}\right) + \frac{\partial}{\partial x}(HT_{xy}) + \frac{\partial}{\partial y}(HT_{yy}) + Hv_sS \quad (3.1.3)$$

where:

$$\overline{u} = \frac{1}{H}\int_{-h}^{\eta} u\ dz, \qquad \overline{v} = \frac{1}{H}\int_{-h}^{\eta} v\ dz \qquad (3.1.4)$$

are the depth averaged u and v velocity components, $H = h + \eta$ is the total depth:

$$T_{xx} = 2A_H\frac{\partial\overline{u}}{\partial x}, \quad T_{xy} = A_H\left(\frac{\partial\overline{u}}{\partial y} + \frac{\partial\overline{v}}{\partial x}\right), \quad T_{yy} = 2A_H\frac{\partial\overline{v}}{\partial y} \qquad (3.1.5)$$

are the lateral stresses (including viscous and turbulent friction and differential advection):

$$A_H = c_s{}^2 l^2 \sqrt{2S_{ij}S_{ij}} \qquad (3.1.6)$$

is the horizontal eddy viscosity, c_s is the Smagorinsky constant, l is a characteristic length of eddies:

$$S_{ij} = \frac{1}{2}\left(\frac{\partial u_i}{\partial x_j} + \frac{\partial u_j}{\partial x_i}\right), \quad i,j = 1,2 \qquad (3.1.7)$$

is the deformation rate, s_{ij} are components of the radiation stress tensor, p_a is atmospheric pressure, ρ_0 is the reference density of water, τ_{si} and τ_{bi} are the surface and bottom components of the radiation stress tensor, S is the magnitude of discharge due to point sources and u_s and v_s are the velocity that water is discharged into the ambient. The above apply for a barotropic model using the Smagorinsky [1963] formulation, which will always be the case considered in this work.

If no sources, wind stress, Coriolis forcing or wave radiation stress are used in the model then (3.1.1)–(3.1.3) become:

$$\frac{\partial H}{\partial t} + \frac{\partial (H\overline{u})}{\partial x} + \frac{\partial (H\overline{v})}{\partial y} = 0 \qquad (3.1.8)$$

$$\frac{\partial (H\overline{u})}{\partial t} + \frac{\partial (H\overline{u}^2)}{\partial x} + \frac{\partial (H\overline{vu})}{\partial y} = -gH\frac{\partial \eta}{\partial x} - \frac{H}{\rho_0}\frac{\partial p_a}{\partial x} - \frac{gH^2}{2\rho_0}\frac{\partial \rho}{\partial x} - \frac{\tau_{bx}}{\rho_0}$$
$$+ \frac{\partial}{\partial x}(HT_{xx}) + \frac{\partial}{\partial y}(HT_{xy}) \quad (3.1.9)$$

$$\frac{\partial (H\overline{v})}{\partial t} + \frac{\partial (H\overline{vu})}{\partial y} + \frac{\partial (H\overline{v}^2)}{\partial y} = -gH\frac{\partial \eta}{\partial y} - \frac{H}{\rho_0}\frac{\partial p_a}{\partial y} - \frac{gH^2}{2\rho_0}\frac{\partial \rho}{\partial y} - \frac{\tau_{by}}{\rho_0}$$
$$+ \frac{\partial}{\partial x}(HT_{xy}) + \frac{\partial}{\partial y}(HT_{yy}) \quad (3.1.10)$$

In most cases the effect of density gradients in 2D models is small and so the density gradient terms can be neglected [DHI, 2016a]. With this in mind, and if the model is designed in such a way that $\overline{v} \approx 0$ and $\partial \eta / \partial y \approx \partial \overline{u} / \partial y \approx 0$, then (3.1.8)–(3.1.10) become:

$$\frac{\partial \eta}{\partial t} + h\frac{\partial \overline{u}}{\partial x} + \frac{\partial (\eta \overline{u})}{\partial x} = 0 \qquad (3.1.11)$$

$$\frac{\partial (H\overline{u})}{\partial t} + \frac{\partial (H\overline{u}^2)}{\partial x} = -gH\frac{\partial \eta}{\partial x} - \frac{H}{\rho_0}\frac{\partial p_a}{\partial x} - \frac{\tau_{bx}}{\rho_0} + \frac{\partial}{\partial x}\left(H2A\frac{\partial \overline{u}}{\partial x}\right) \qquad (3.1.12)$$

$$0 = -\frac{H}{\rho_0}\frac{\partial p_a}{\partial y} \qquad (3.1.13)$$

The momentum equation for the y-direction disappears leaving only the x momentum equation. For constant atmospheric pressure and $\tau_{bx} = \rho_0 C_F \overline{u}|\overline{u}|$, (3.1.12) is almost identical to (2.2.6) with $N = 0$ (the 1D momentum equation with no turbines), with the difference being the additional stress terms. The continuity equation is the same as the 1D continuity equation (2.2.5) if $\hat{u} = \overline{u}$. If one were to set the Smagorinsky coefficient $c_s = 0$ (alternatively when setting up the model the user can select the no eddy option under the eddy viscosity menu), then (3.1.12) becomes:

$$\frac{\partial \overline{u}}{\partial t} + \frac{\partial (\overline{u}^2)}{\partial x} = -g\frac{\partial \eta}{\partial x} - \frac{C_F}{h + \eta}\overline{u}|\overline{u}| \qquad (3.1.14)$$

which is identical to (2.2.6) if $\hat{u} = \overline{u}$ and $\partial(\overline{u}^2)/\partial x \approx \overline{u}\partial\overline{u}/\partial x$ and $N = 0$.

In summary, MIKE21 can be used to model (2.2.5) and (2.2.6) if the following conditions are met:

1. no sources are included in the model,

2. wind stress is not included in the model,

3. Coriolis forcing is not included in the model,

4. density gradients are negligible,

5. the lateral components of the velocity are negligible,

6. the lateral gradients of the surface elevation and longitudinal velocity component are negligible,

7. a quadratic friction law is used,

8. the cross-sectionally averaged longitudinal velocity is equal to the depth averaged longitudinal velocity,

9. eddy viscosity is not included in the model,

10. the gradient of the xx stress tensor is negligible

11. and $\partial(\overline{u}^2)/\partial x \approx \overline{u}\partial\overline{u}/\partial x$.

MIKE21 employs a quadratic friction law using the depth averaged velocity [DHI, 2016b] which satisfies condition 7. The conditions 1, 2, 3, 9 and 10 can be satisfied by choosing the correct options in the respective menus in the model set-up. The conditions 5 and 6 can be met in a uniform rectangular channel if uniform-along-the-boundary surface elevation or velocity (longitudinal component only, no lateral component) is input at the open boundaries, and the land boundaries use the full slip boundary condition (additionally conditions 1-3 will also be needed). If conditions 5 and 6 are met then condition 8 will also be met. Finally, conditions 4 and 11 will be assumed.

It is noted here that, whereas in an unoccupied channel the hydrodynamics will be essentially 1D if eddy viscosity is neglected (since $L \ll \lambda$), when turbines are added to the channel this will no longer be the case. The deployment of turbines will interrupt the 1D nature of the hydrodynamics because flow is accelerated as it is forced around the turbines, or slowed as it passes through the turbines. This will also introduce strong lateral velocity gradients and sub-grid scale turbulence, necessitating the inclusion of the eddy viscosity turbulence parameterisation. Therefore, the lateral stress term (the last term on the right-hand side of (3.1.12)) is retained despite this not being included in the equations in the previous chapter. In addition, note that a more accurate representation of the turbines would also include source and sink terms in the turbulence model (e.g. Roc et al. [2013]).

The model area is sub divided into triangular or quadrilateral elements and the governing equations solved using the finite volume method. The governing equations are converted into integral form, with the integral evaluated over each cell. The user has the option of a first or second order solution. Here, the second order solution will be used; this is obtained using an approximate Riemann solver – Roe's scheme [Roe, 1981] – to calculate fluxes across cell interfaces. A linear gradient-reconstruction technique is then used to achieve second order accuracy using the approach of Jawahar and Kamath [2000]. Finally, the van Leer 2nd order TVD slope limiter [Hirsch, 1990, Darwish and Moukalled, 2003] is used to avoid numerical oscillations [DHI, 2016b].

Based on the discussion above, the hydrodynamic model parameters to be used throughout this thesis are summarised in Table 3.1. The higher order solution methods are described above. MIKE uses a variable time-step in the solution of the governing equations, within the bounds of the maximum and minimum time-step, and less than the critical CFL number [DHI, 2016a]. Elements of the hydrodynamic module not included in the table, namely the depth correction, flooding and drying, Coriolis forcing, wind forcing, ice coverage, tidal potential, precipitation – evaporation, infiltration, wave radiation and sources elements, were not included in the model. The reasons for their exclusion were discussed previously. The maximum and minimum time-step, critical CFL number, Manning number and Smagorinsky coefficient were all left at their default values. More information on

each of the elements in MIKE21's Hydrodynamic Module is given by DHI [2016a].

The boundary forcing setting to be used is a water surface elevation that is constant along the boundaries and varying in time. A single elevation time-series was used for each boundary. These were synthesised using MATLAB, and the equation:

$$\eta(t) = \sum_{i=1}^{n} \eta_{0,i} \cos(\sigma_i t - \phi_i) \qquad (3.1.15)$$

where n is the number of constituents supplied at the boundaries, $\eta_{0,i}$ is the amplitude of constituent i, σ_i is the frequency of constituent i and ϕ_i is the phase of constituent i at the boundary in question.

3.1.2 The Sediment Transport Module

Sediment transport as bedload, and suspension of sediment into the water column are driven by shear stresses resulting from the flow of water over the bed. In the sediment transport simulations carried out in this work the shear stresses from the hydrodynamic module were used. This is given by a quadratic friction law as:

$$\tau_{bx} = \rho_0 C_F \overline{u} |\overline{u}| \qquad (3.1.16)$$

$$\tau_{by} = \rho_0 C_F \overline{v} |\overline{v}| \qquad (3.1.17)$$

where $\vec{\tau_b} = (\tau_{bx}, \tau_{by})$ is the bed shear stress and C_F is the friction coefficient, which is given by:

$$C_F = \frac{g}{(Mh^{1/6})^2} \qquad (3.1.18)$$

where M is the Manning number.

The flow shear stress, τ, may be split into two components, the form drag, τ'', and the skin friction, τ', where $\tau = \tau' + \tau''$. In this work, the van Rijn [1984a,b] (VR84) sediment transport model was used for both bed- [van Rijn, 1984a] and suspended-load transport [van Rijn, 1984b]. In the derivation of the equations in this model the non-dimensional form of the shear stress, or the Shield's parameter, Θ, was used, defined as:

Table 3.1: Model parameters for hydrodynamic module. † – Parameter kept at default value, ∗ – Parameter varied in sensitivity tests (Section 3.4), constant otherwise.

Module Element	Parameter	Setting / Value
Solution Technique	Time Integration	Higher Order
	Space Discretisation	Higher Order
	Minimum Time-Step†	0.01 s
	Maximum Time-Step†	30 s
	Critical CFL Number†	0.8
Density	Density Type	Barotropic
Eddy Viscosity	Eddy Type	Smagorinsky Formulation
	Format	Constant
	Constant Value†∗	0.28
	Minimum Eddy Viscosity†	1.8×10^{-6} m^2/s
	Maximum Eddy Viscosity†	1.0×10^{10} m^2/s
Bed Resistance	Resistance Type	Manning Number
	Format	Constant
	Constant Value†∗	32 M$^{1/3}$/s
Initial Conditions	Type	Constant
	Surface Elevation	0 m
	u-Velocity	0 m/s
	v-Velocity	0 m/s
Boundary Conditions: Open Boundaries	Type	Specified Level
	Format	Varying in Time, Constant Along Boundary
	Soft Start: Type	Sinus Variation
	Soft Start: Time Interval	86400 s
	Soft Start: Reference Value	0 m
	Interpolation Type: In Time	Linear
Boundary Conditions: Land Boundary	Type	Land (Zero Normal Velocity)

$$\Theta = \frac{\tau}{\rho_0 g(s-1)d_{50}} \tag{3.1.19}$$

where $s = \rho_0/\rho_s$ is the relative density of the sediment, ρ_s is the density of the sediment and d_{50} is the median sediment grain diameter. Beyond a critical value of the Shield's parameter, Θ_c, transport of sediment will be initiated. In the VR84 model Θ_c varies with the non-dimensional sediment diameter:

$$D_{ast} = d_{50}\left(\frac{(s-1)g}{\nu^2}\right)^{\frac{1}{3}} \tag{3.1.20}$$

where ν is the kinematic viscosity, taken here as 10^{-6} m^2/s. The values of Θ_c for the VR84 model are given in Table 3.2.

Table 3.2: Critical Shield's parameter as a function of D_{ast} for various ranges of D_{ast} used in the VR84 model.

D_* Range	Θ_c
$D_* < 4$	$0.24/D_*$
$4 < D_* < 10$	$0.14D_*^{-0.64}$
$10 < D_* < 20$	$0.04D_*^{-0.1}$
$20 < D_* < 150$	$0.013D_*^{0.29}$
$D_* > 150$	0.055

Should the conditions in Table 3.2 be met, then bed-load transport will commence, with the bed-load volumetric transport rate given in the VR84 model by:

$$q_{s,bl} = 0.053\frac{T^{2.1}}{D_*^{0.3}}\sqrt{(s-1)gd_{50}^3} \tag{3.1.21}$$

where:

$$T = \left(\frac{u_f'}{u_{f,c}}\right)^2 - 1 \tag{3.1.22}$$

is the non-dimensional transport stage parameter, u_f' is the effective friction velocity, estimated by:

$$u_f' = \underline{\boldsymbol{v}}\frac{\sqrt{g}}{C'} \tag{3.1.23}$$

where C' is the Chézy number originating from skin friction and is given by:

$$C' = 18 \log \left(\frac{4h}{d_{90}} \right) \tag{3.1.24}$$

where d_{90} is the grain diameter for which 90% of grains are finer, and $u_{f,c}$ is the critical friction velocity given by:

$$u_{f,c} = \sqrt{\Theta_c (s-1) g d_{50}} \tag{3.1.25}$$

If the shear stress is large enough then suspended-load transport of the sediment will occur. The conditions for suspended-load transport and the suspended-load volumetric transport rate are given by:

$$u_f > \begin{cases} \frac{4w_s}{D_{ast}}, & \text{for } D_{ast} < 10 \\ 0.4w_s, & \text{for } D_{ast} > 10 \end{cases} \tag{3.1.26}$$

and:

$$q_{s,sl} = f c_a \underline{v} h \tag{3.1.27}$$

respectively, where u_f is the friction velocity, w_s, is the settling velocity, given by:

$$w_s = 10 \frac{\nu}{d} \left(\sqrt{1 + \frac{0.01(s-1)gd^3}{\nu^2}} - 1 \right) \tag{3.1.28}$$

for particles with a diameter, 100 μm $\leq d \leq$ 1,000 μm, and by:

$$w_s = 1.1\sqrt{(s-1)gd} \tag{3.1.29}$$

for particles with $d > 1,000$ μm [van Rijn, 1984b], $\underline{v}$ is the current velocity, c_a is the volumetric bed concentration, given by:

$$c_a = 0.015 \frac{d_{50} T^{1.5}}{a D_{ast}^{0.3}} \tag{3.1.30}$$

where a is a reference level at which the bed concentration is determined and is given by:

$$a = \max \begin{pmatrix} 0.01h \\ 2d_{50} \end{pmatrix} \tag{3.1.31}$$

and f is a correction factor, given by:

$$f = \frac{\left(\frac{a}{h}\right)^Z - \left(\frac{a}{h}\right)^{1.2}}{\left(1 - \frac{a}{h}\right)^Z (1.2 - Z)} \tag{3.1.32}$$

where Z is the Rouse suspension parameter given by:

$$Z = \frac{w_s}{\beta \kappa u_f} + \varphi' \tag{3.1.33}$$

where $\kappa = 0.4$ is the von Karman constant, and β and φ' are correction factors applied to the hydrodynamic diffusion coefficient (in order to convert it into a diffusion coefficient for sediment) and concentration profile respectively, and are given by:

$$\beta = 1 + 2 \left(\frac{w_s}{u_f}\right)^2 \tag{3.1.34}$$

and:

$$\varphi' = \frac{5}{2} \left(\frac{w_s}{u_f}\right)^{0.8} \left(\frac{c_a}{0.65}\right)^{0.4} \tag{3.1.35}$$

For suspended-load transport, if the concentration of sediment in suspension is greater than an equilibrium concentration then sediment will begin to settle out of suspension. Conversely, if the concentration of sediment in suspension is less than an equilibrium concentration, the bed will erode as sediment is brought into suspension. In the VR84 model, the equilibrium concentration, c_e, is given by:

$$c_e = \begin{cases} c_a(((2.21Z - 6.41)Z - 3.95)Z + 0.97) & Z \leq 1 \\ c_a(((0.007Z - 0.06)Z - 0.347)Z + 0.22) & 1 \leq Z \leq 3 \\ c_a(((4.10 - 6Z - 1.2 \times 10^{-4})Z - 7.67 \times 10^{-3})Z + 0.018) & Z > 3 \end{cases} \tag{3.1.36}$$

Within MIKE the movement of sediment in suspension is described by a standard advection-dispersion equation, which uses as a boundary condition at the bed c_a, as given by (3.1.30). Neither the transport equation, or its derivation are presented here in the interest of brevity. Further information can be found in DHI [2016c].

The above models for the bed-load and suspended-load transport give the respective volumetric transport rates as vectors. In the case that the hydrodynamics

are 1D following the discussion in §3.1.1 the transport of sediment will also be 1D, with transport in the x-direction only. Positive and negative values of $q_{s,bl}$ and $q_{s,sl}$ therefore indicate transport of sediment in the positive and negative x-directions respectively.

3.1.3 Turbine Implementation

In MIKE, tidal-stream turbines are "...modelled as sub-grid structures using a simple drag-law to capture the increasing resistance imposed by the turbine blades as the flow speed increases..." with the turbines assumed to "...always have their axis aligned with the flow direction..." (DHI [2016a], pp. 96). The turbine drag and lift forces are calculated as [DHI, 2016a]:

$$\vec{F}_D = \frac{1}{2}\rho_0 C_D A \vec{V}_0 |\vec{V}_0| \tag{3.1.37}$$

$$\vec{F}_L = \frac{1}{2}\rho_0 C_L A \vec{V}_0 |\vec{V}_0| \tag{3.1.38}$$

where C_D and C_L are the turbine drag and lift coefficients respectively, A is the turbine swept area, $\vec{V}_0 = (\underline{u_0}, \underline{v_0})$ is the upstream velocity, $\underline{u_0}$ and $\underline{v_0}$ are its x- and y-components.

Equations (3.1.37) and (3.1.38) and be derived through actuator disk theory, e.g. Appendix B. So although implemented as a momentum sink in a model element, the sink term has a physical basis. The derivation of these forces uses the upstream velocity. However, in the model, as the size of the element reduces the velocity within the element, $\vec{V}_{\text{local}}$, diverges from the upstream velocity. Kramer et al. [2014] proposed a correction factor to address this issue, defined as:

$$\vec{V}_0 = \alpha \vec{V}_{\text{local}} = \frac{2}{1 + \sqrt{1-\gamma}}\vec{V}_{\text{local}} \tag{3.1.39}$$

where:

$$\gamma = \frac{C_D A}{H \Delta y} \tag{3.1.40}$$

where Δy is the width of the element perpendicular to the flow.

For the 1D case $\vec{V}_0$ and $\vec{V}_{\text{local}}$ will reduce to u_0 and u_{local}, and in the present work the lift force will not be considered, so that the thrust force is equal but opposite to the drag force. The 1D thrust force is therefore:

$$F_T = -\frac{1}{2}\rho_0 C_T A u_0 |u_0| \tag{3.1.41}$$

To add (3.1.41) to the 1D momentum equation, (3.1.14), one must divide (3.1.41) by $\rho_0 E$, where $E = b(h + \eta)$ as (3.1.14) has been divided through by this factor. The resulting equation is then:

$$\frac{\partial \overline{u}}{\partial t} + \frac{\partial (\overline{u}^2)}{\partial x} = -g\frac{\partial \eta}{\partial x} - \frac{C_F}{h + \eta}\overline{u}|\overline{u}| - \frac{\varepsilon_0 C_T}{2(1 + \eta/h)}u_0 |u_0| \tag{3.1.42}$$

where $\varepsilon_0 = NA/bh$ is the blockage ratio for $\eta = 0$ m, which is the same form as the momentum equation in Chapter 2, (2.2.6), if one assumes that $u_0 = \overline{u}$.

Turbines are implemented in the model though the turbine structure element of the hydrodynamic module. The parameter settings used in this element are summarised in Table 3.3. The turbine location, and therefore the turbine correction factor (which is a function of the local element area (3.1.39) & (3.1.40)) vary on a turbine-by-turbine basis. In the case of the variable-C_T turbine the drag (C_D) and lift (C_L) coefficient values used in the C_D and C_L look-up tables are given in Table 3.4. Values are given for two current directions (relative to the turbine), and lift forces are neglected by supplying $C_L = 0$ for all speeds and directions. The C_D value from Table 3.4 are plotted in Figure 2.9.

3.2 Model Geometry

Section 3.1.1 discussed how one might use MIKE 21 FM to reach numerical approximations of solutions to (2.2.5) and (2.2.6). So that the lateral components of the velocity and the lateral gradients of the surface elevation and longitudinal velocity component might be considered negligible, a uniform, rectangular geometry is employed, as the derivation of (2.2.5) and (2.2.6) make this assumption about the channel (see Appendix C). Additionally, in going from the 3D to the 1D forms of (2.2.5) and (2.2.6) it is assumed that the shallow water and narrow basin approximations hold for the channel, that is:

Table 3.3: Model parameters in turbine structure element of MIKE21's hydrodynamic module. ∗ – Parameters vary on a turbine-by-turbine basis.

Turbine Type	Parameter	Setting / Value
Fixed C_T	Position	Variable∗
	Diameter	20 m
	Description	Fixed Drag Coefficent
	Current Correction Factor: Format	Constant
	Current Correction Factor: Constant Value	Variable∗
Variable C_T	Position	Variable∗
	Diameter	20 m
	Description	Tabulated Drag and Lift Coefficient
	Orientation	90°
	Current Correction Factor: Format	Constant
	Current Correction Factor: Constant Value	Variable∗

$$D_0 \ll B_0, L_0 \tag{3.2.1}$$

and:

$$B_0 \ll L_0 \tag{3.2.2}$$

where D_0, B_0 and L_0 are the length scales of the depth, width and length of the channel respectively. Given that tidal-stream turbines will be deployed in the channel, this will impose limits on the depth. The absolute minimum depth, h, that can be employed, so that a turbine of radius, R, may be deployed in a region where the tidal elevation is η_0, is:

Table 3.4: Drag (C_D) and lift (C_L) coefficient values used in look up tables for variable-C_T turbine runs.

Current Speed [m/s]	C_D Current Direction		C_L Current Direction	
	0°	360°	0°	360°
1.00	0.850	0.850	0.000	0.000
1.25	0.850	0.850	0.000	0.000
1.50	0.850	0.850	0.000	0.000
1.75	0.850	0.850	0.000	0.000
2.00	0.850	0.850	0.000	0.000
2.25	0.850	0.850	0.000	0.000
2.50	0.850	0.850	0.000	0.000
2.75	0.635	0.635	0.000	0.000
3.00	0.490	0.490	0.000	0.000
3.25	0.385	0.385	0.000	0.000
3.50	0.308	0.308	0.000	0.000
3.75	0.250	0.250	0.000	0.000
4.00	0.205	0.205	0.000	0.000

$$h > 2R + \eta_0 \tag{3.2.3}$$

In this case the turbine would be deployed with the lower-most extent of the turbine swept area grazing the bed, and at the lowest tide, the upper-most extent of the turbine swept area grazing the water surface. So that there is more realistic clearance of the swept area from the bed and the tidal wave from the swept area, the condition:

$$h > 3R + \eta_0 \tag{3.2.4}$$

is employed. The dimensions related to this condition are illustrated in Figure 3.1

If it is assumed that if X is 10 times larger than Y, then $X \gg Y$, then according to (3.2.1) and (3.2.2), the width, b, and length, L, must satisfy:
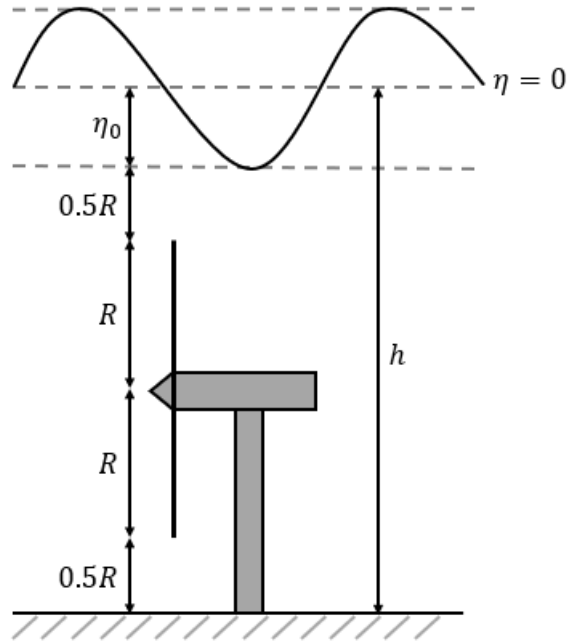
Figure 3.1: Schematic illustration of depth condition upon which model geometry design is based.

$$b \geq 10(3R + \eta_0) \tag{3.2.5}$$

$$L \geq 100(3R + \eta_0) \tag{3.2.6}$$

In the derivation of (2.2.5) and (2.2.6), so that the Coriolis force could be neglected, a more stringent condition on the width-length-ratio was imposed (see Appendix C). However, since the Coriolis force may simply be switched off in MIKE, this condition will not be imposed on the model geometry. One might simply imagine the channel to be located exactly along the equator.

For a turbine radius of 10 m, and a tidal amplitude of 5 m, the channel dimensions:

$$h = 36 \text{ m}, \quad b = 1.08 \text{ km}, \quad L = 32.4 \text{ km} \tag{3.2.7}$$

are used. This value of the depth satisfies (3.2.4) allowing the turbine to be deployed with a hub height of 20 m, so that there is 10 m clearance between the swept area and the bed, and 1 m clearance between the swept area and the water surface at

low tide. The width is then 30 times larger than the depth, and the length 30 times larger than the width, so that both (3.2.5) and (3.2.6) are comfortably satisfied.

MIKE 21 allows the user to fit the model domain with a uniform quadrilateral mesh or an unstructured triangular mesh with multiple scales. Both of these mesh options will be discussed in §3.4.

3.3 Model Verification

The numerical experiments that will be discussed in the preceding chapters will be carried out in the hypothetical channel described in §3.2. As such, validation of the output against observations is not possible. Instead, the model output is verified through comparison with analytical results. As the hypothetical channel has been designed so that the tidal dynamics are approximately one-dimensional, profiles of the model output may be compared to analytical solutions to the 1D Navier-Stokes equations.

At the time of writing no analytical solutions for the harmonics of the fundamental in an open channel have been identified in the literature. However, Kabbaj and Le Provost [1980] give an analytical solution to the one-dimensional equations of the form (2.2.5) and (2.2.6) for a channel closed at one end. Souza and Hill [2006] do present an analytical solution for an open channel. However, their solution is presented for a non-linear form of the governing equations and as such does not include the harmonics (M_4 & M_6) of the fundamental tide (M_2). Given the interest in the shallow water tides in this thesis, the M_4 in particular, the Kabbaj and Le Provost [1980] will be used as the verification case to test MIKE21's ability to represent harmonics in a channel, albeit a channel closed at one end.

Kabbaj and Le Provost [1980] (KLP) solve the set of equations (2.2.5) and (2.2.6) with the number of turbines set to zero, i.e.:

$$\frac{\partial \hat{u}}{\partial t} + \frac{\partial \hat{u}}{\partial x} = -g\frac{\partial \eta}{\partial x} - \frac{1}{1 + \eta/h}\frac{C_F}{h}\hat{u}|\hat{u}| \qquad (3.3.1)$$

Through the method of characteristics, KLP obtained the boundary conditions:

$$\hat{u} = 0, \quad \text{at } x = L \qquad (3.3.2)$$

$$\hat{u} + \sqrt{g(h + \eta)} = 2 + 2A\cos(\sigma t), \quad \text{at } x = 0 \tag{3.3.3}$$

where (3.3.3) corresponds to "an incident wave of frequency $\widetilde{\omega}$ [sic, here σ] coming from deep water where nonlinearities are assumed negligible" and "$\widetilde{A}$ [sic, here A] characterises the order of magnitude of this incident wave" (Kabbaj and Le Provost [1980], pp. 144). Non-dimensionalising the variables in the equation by; $x^* = x/L$, $t^* = tc/L$, $c = \sqrt{gh}$, $\eta^* = \eta/h$, $\hat{u}^* = \hat{u}/c$, $\sigma^* = \sigma L/c$, $A^* = A/c$ and $k = C_F L/h$ the dimensionless form of the equations to be solved and the boundary conditions are:

$$\begin{cases} \begin{cases} \frac{\partial \eta^*}{\partial t^*} + \frac{\partial \hat{u}^*}{\partial x^*} + \frac{\partial(\eta^* \hat{u}^*)}{\partial x^*} = 0 \\ \frac{\partial \hat{u}^*}{\partial t^*} + \hat{u}^* \frac{\partial \hat{u}^*}{\partial x^*} + \frac{\partial \eta^*}{\partial x^*} = -k\frac{\hat{u}^*|\hat{u}^*|}{1+\eta^*} \end{cases} \\ \begin{cases} \hat{u}^* = 0, & \text{at } x^* = 1 \\ \hat{u}^* + 2\sqrt{1+\eta^*} = 2A^*\cos(\sigma^* t^*) + 2, & \text{at } x^* = 0 \end{cases} \end{cases} \tag{3.3.4}$$

By assuming that $A^* \ll 1$, KLP approximated the solution to (3.3.4) using linearised equations obtained by the perturbation method. Substituting:

$$\begin{cases} \eta^*(x,t) = \sum A^{*j}\eta_j^*(x,t) \\ \hat{u}^*(x,t) = \sum A^{*j}\hat{u}_j^*(x,t) \quad \text{with } j = 1,2,\ldots,n \\ F = \sum A^{*j}F_j \end{cases} \tag{3.3.5}$$

and:

$$\sqrt{1+\eta^*} = 1 + A^*\frac{\eta_1^*}{2} + A^{*2}\left(\frac{\eta_1^{*2}}{2} - \frac{\eta_1^{*2}}{8}\right) + A^{*3}\left(\frac{\eta_3^*}{2} - \frac{\eta_1^*\eta_2^*}{4} + \frac{\eta_1^{*3}}{16}\right) + \ldots \tag{3.3.6}$$

where $F = k(1+\eta^*)^{-1}\hat{u}^*|\hat{u}^*|$, into (3.3.4) and arranging according to powers of A^*, KLP found:

$$\begin{cases} \begin{cases} \frac{\partial \eta_j^*}{\partial t^*} + \frac{\partial \hat{u}_j^*}{\partial x^*} = -\sum_{k+l=j}\frac{\partial(\eta_k^* \hat{u}_l^*)}{\partial x^*} \\ \frac{\partial \hat{u}_j^*}{\partial t^*} + \frac{\partial \eta_j^*}{\partial x^*} = -\sum_{k+l=j}\hat{u}_k^*\frac{\partial \hat{u}_l^*}{\partial x^*} + F_j \end{cases} \\ \begin{cases} \hat{u}_j^* = 0 & \text{at } x^* = 1 \\ \hat{u}_j^* + \eta_j^* = L_j & \text{at } x^* = 0 \end{cases} \end{cases} \tag{3.3.7}$$

where:

$$\begin{cases} L_1 = 2\cos(\sigma^* t) \\ L_2 = \frac{\eta_1^*(0,t)}{4} \\ L_3 = \frac{\eta_1^*(0,t)\eta_2^*(0,t)}{2} - \frac{\eta_1^{*3}(0,t)}{8} \\ \quad\vdots \end{cases} \tag{3.3.8}$$

They then solved (3.3.7) for each order of j with:

$$F = \lambda A^* \hat{u}_1^* - \lambda A^{*2} \hat{u}_1^* \eta_1^* + \lambda' A^{*2} \hat{u}_2^* + \lambda_{32} A^{*2} \hat{u}_{11}^{*2} \cos(3(\sigma^* t^* + \psi_{11}))$$
$$+ \lambda_{52} A^{*2} \hat{u}_{11}^{*2} \cos(5(\sigma^* t^* + \psi_{11})) + \ldots + \mathcal{O}(A^{*3}) \quad (3.3.9)$$

where:

$$\lambda = \frac{8k}{3\pi} A^* \hat{u}_{11}^*, \quad \lambda' = \frac{4k}{\pi} A^* \hat{u}_{11}^*, \quad \lambda_{32} = \frac{8k}{15\pi}, \quad \lambda_{52} = -\frac{8k}{105\pi} \tag{3.3.10}$$

The first order solution is obtained from (3.3.7) for $j = 1$, F_1 is simply the $\mathcal{O}(A^*)$ terms from F with $A^* \hat{u}_{11}^*$ set to its mean value so that λ is constant and the system of equations is linear. The solutions to this system of equations are:

$$\begin{cases} \eta_1^* = \overline{\alpha}_{11} = \eta_{11}^* \cos(\sigma^* t^* + \phi_{11}) \\ \hat{u}_1^* = \overline{\mu}_{11} = \hat{u}_{11}^* \cos(\sigma^* t^* + \psi_{11}) \end{cases} \tag{3.3.11}$$

where:

$$\begin{cases} \eta_{11}^* = 2\sqrt{\mathrm{Re}(\alpha_{11})^2 + \mathrm{Im}(\alpha_{11})^2} \\ \hat{u}_{11}^* = 2\sqrt{\mathrm{Re}(\mu_{11})^2 + \mathrm{Im}(\mu_{11})^2} \\ \phi_{11} = \tan^{-1}\left(\frac{\mathrm{Im}(\alpha_{11})}{\mathrm{Re}(\alpha_{11})}\right) \\ \psi_{11} = \tan^{-1}\left(\frac{\mathrm{Im}(\mu_{11})}{\mathrm{Re}(\mu_{11})}\right) \end{cases} \tag{3.3.12}$$

$$\begin{cases} \alpha_{11} = iB\sqrt{1 - i\frac{\lambda}{\sigma^*}} \cos\left(\sigma^*\sqrt{1 - i\frac{\lambda}{\sigma^*}}(x^* - 1)\right) \\ \mu_{11} = B\sin\left(\sigma^*\sqrt{1 - i\frac{\lambda}{\sigma^*}}\right) \end{cases} \tag{3.3.13}$$

where B is a constant set by the open boundary condition.

The second order solution is obtained from (3.3.7) for $j = 2$, F_2 is the $\mathcal{O}(A^{*2})$ terms from F. The solutions (3.3.11) may be substituted into the sets of differential equations for terms of zero frequency, frequency σ^*, $2\sigma^*$ and $3\sigma^*$, which can then

be solved. The solutions for the terms of frequency $2\sigma^*$ and $3\sigma^*$ are of the same form as (3.3.11) and (3.3.12) with:

$$
\begin{cases}
\mu_{22} = E\sin\left(2\sigma^*\sqrt{1 - j\frac{\lambda'}{2\sigma^*}}(x^* - 1)\right) \\
\qquad\qquad +\frac{3}{2}\frac{\sigma^*}{2\lambda - \lambda'}B^2\left(1 - i\frac{\lambda}{\sigma^*}\right)^{\frac{3}{2}}\sin\left(2\sigma^*\sqrt{1 - i\frac{\lambda}{\sigma^*}}(x^* - 1)\right) \\
\alpha_{22} = iE\sqrt{1 - i\frac{\lambda'}{2\sigma^*}}\cos\left(2\sqrt{1 - i\frac{\lambda'}{2\sigma^*}}(x^* - 1)\right) \\
\qquad\qquad +i\frac{\sigma^*}{2\lambda - \lambda'}B^2\left(\frac{3}{2} - i\frac{\lambda + \lambda'}{2\sigma^*}\right)\left(1 - i\frac{\lambda}{\sigma^*}\right)\cos\left(2\sigma^*\sqrt{1 - i\frac{\lambda}{\sigma^*}}(x^{ast} - 1)\right)
\end{cases}
\tag{3.3.14}
$$

$$
\begin{cases}
\mu_{33} = Le^{+Arg} + Me^{-Arg} + P + Q\cos\left(2\sigma^*\sqrt{1 - i\frac{\lambda}{\sigma^*}}(x^* - 1)\right) \\
\alpha_{33} = \sqrt{1 - i\frac{\lambda'}{3\sigma^*}}[-Le^{Arg} + Me^{-Arg}] \\
\qquad\qquad -j^{\frac{3}{2}}Q\sqrt{1 - i\frac{\lambda}{\sigma^*}}\sin\left(2\sigma^*\sqrt{1 - i\frac{\lambda}{\sigma^*}}(x^* - 1)\right)
\end{cases}
\tag{3.3.15}
$$

where E, L and M are constants set by the open boundary condition and:

$$
\begin{cases}
Arg = 3i\sigma^*\sqrt{1 - i\frac{\lambda}{\sigma^*}}(x^* - 1) \\
P = \frac{3\sigma^*e^{i\Omega}}{9\sigma^{*2} + \lambda'^2}\lambda_{32}B^2\left(1 + i\frac{\lambda'}{3\sigma^*}\right) \\
Q = \frac{3e^{-i\Omega}}{25\sigma^{*2} + (4\lambda - 3\lambda')^2}\lambda_{32}B^2(5\sigma^* - i(4\lambda - 3\lambda'))
\end{cases}
\tag{3.3.16}
$$

with $\psi_{11} = \tan^{-1}(\cot(\sigma^*)) = \Omega$ coming from the first order solution for the case with no friction, an approximation used to make the frequency $3\sigma^*$ set of equations analytically solvable.

A test model run was carried out for a channel, closed at one end, with the dimensions matching those used for the numerical illustration in KLP. The test model had a length of 495 km, a depth of 50 m, a width of 16.5 km (factor of 30 smaller than length, the example in KLP is one-dimensional so has no width) and used a Manning number $M = 29.79$ m$^{\frac{1}{3}}$/s (approximately equivalent to $C_F = 3 \times 10^{-3}$ used in KLP). The open end of the channel was forced using velocity values at the boundaries. A velocity curve was constructed with an amplitude of 0.6671 m/s and a phase value of 9.444^o, derived from the analytical solution at $x = 0$ from KLP. Other than the above, the model parameters remained the same as outlined in Table 3.1. Harmonic analysis of the output of this test run was analysed as described in §3.2. The results from this analysis are presented in Figures 3.2 & 3.3, along with values digitised from the figures in KLP.
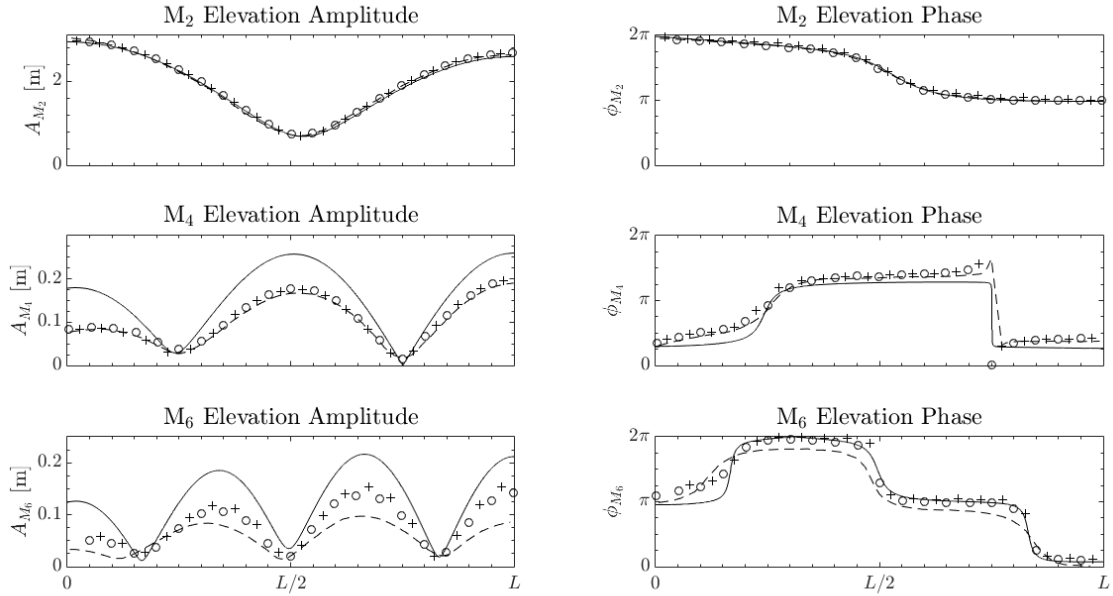
Figure 3.2: Profiles of the M_2 (top panels), M_4 (middle panels) and M_6 (bottom panels) of the surface elevation (amplitude left panels & phase right panels) along the channel from the test run (solid line), along with the analytical solution (dashed line), analytical-numerical solution (circles) and numerical solution (pluses) from Kabbaj and Le Provost [1980].

For the M_2, the agreement between the 3 KLP solutions and the model is almost exact. For both harmonics, the pattern of both phase and amplitude is repeated in all 4 solutions. There is a slight difference between the analytical solution and the other two KLP solutions for M_4; this difference increases for M_6 and in the M_6 amplitudes there is also a difference between the analytical-numerical and numerical solutions of KLP. The amplitudes of both the velocity and surface elevation are larger in the test model than in all three solutions from KLP. A possible cause of this difference could be the bed resistance used in the test model being too small, however the M_2 amplitudes agree well.

The reproduction in the model output of the analytical, analytical-numerical and numerical solutions of KLP gives confidence in MIKE's ability to correctly simulate the harmonics of a fundamental and harmonic generation in a similar model geometry, at least in terms of the pattern of harmonics along the channel length.
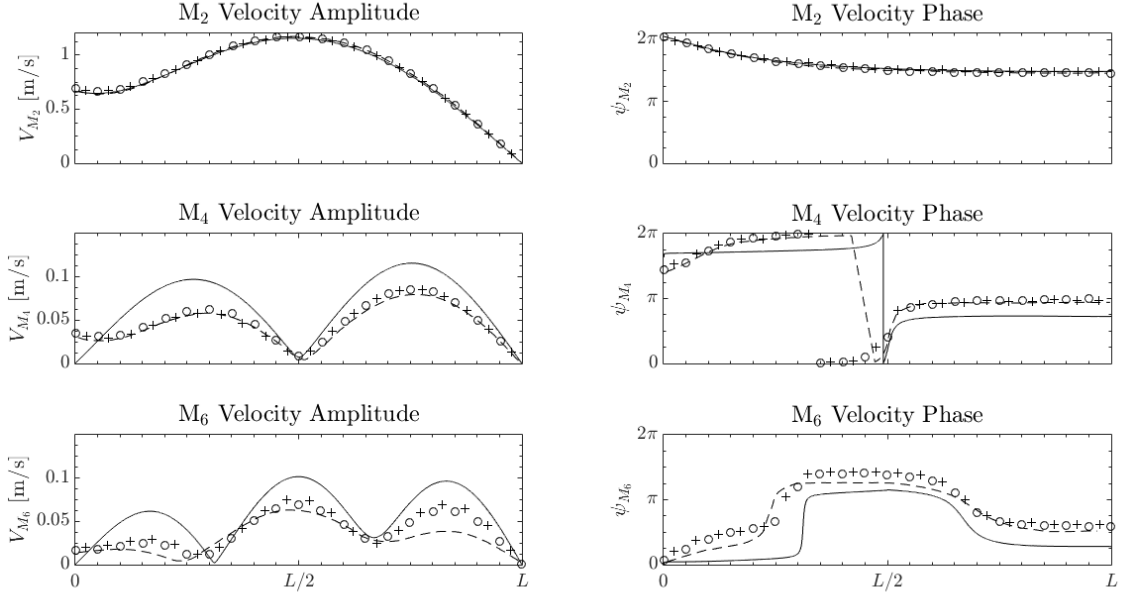
Figure 3.3: Profiles of the M_2 (top panels), M_4 (middle panels) and M_6 (bottom panels) of the current velocity (amplitude left panels & phase right panels) along the channel from the test run (solid line), along with the analytical solution (dashed line), analytical-numerical solution (circles) and numerical solution (pluses) from Kabbaj and Le Provost [1980].

3.4   Sensitivity Tests

In this section the sensitivity of three aspects of the model will be explored: first, the effect of changing model parameters on the harmonics generated within the model; second, the sensitivity of the elevation and velocity at the boundary to the deployment of turbines, to ensure the effect of the turbines is not felt at the model boundary; and finally, the sensitivity of the turbine wake to the model turbulence parameters.

The model parameters outlined in Table 3.1 and the geometry (3.2.7) will be used throughout these tests. Those parameters marked with a ∗ in Table 3.1 are parameters which will be tested in these sensitivity tests. When not being tested the value stated in Table 3.1 will be used. In the turbine sensitivity tests fixed-C_T turbines will be tested, using the parameters outlined in Table 3.5.

In these tests the model will be forced at the boundary by only the M_2. Forcing elevation time-series were synthesised using equation (3.1.15) with $n = 1$, $\eta_{0,1} = 5$

m for both boundaries, $\sigma_1 = 1.9323$ cycles per day, $\phi_1 = 0°$ at the left hand boundary, and $\phi_1 = 60°$ at the right hand boundary. Finally, a uniform 30x30 m structured square mesh will be employed.

3.4.1 Sensitivity of Harmonics to Model Parameters

The harmonic sensitivity tests that were carried out can be divided into two categories. The first are tests of what will be termed "physical model parameters", such as the Manning number, and second are tests of "numerical model parameters", such as mesh element size.

In (3.1.11) and (3.1.12) there are four non-linear terms: the Continuity Term (CT) (in (3.1.11)), the Advection Term (AT), Friction Term (FT) and Lateral Stress Term (LST) (all in (3.1.12)), provided eddy viscosity is not switched off. The sizes of CT and AT are dictated by size of η_0 and $\overline{u}_0$ (the amplitudes of the surface elevation and longitudinal component of the depth averaged velocity respectively), the size of FT is dictated by both C_F (the friction coefficient) and $\overline{u}_0$, and the size of LST will be dictated by c_s, l and $\overline{u}_0$. The MIKE user has control of η_0, $\overline{u}_0$, c_s and C_F through M, where:

$$C_F = \frac{g}{(Mh^{\frac{1}{6}})^2} \tag{3.4.1}$$

The values of η_0 and $\overline{u}_0$ are set through the definition of new forcing time-series at the boundary and are altered simultaneously given their inter-dependence, whereas the values of c_s and M are set in the eddy viscosity and bed resistance menus respectively. The parameters that will make up the physical tests will be M (Test-1), c_s (Test-2) and η_0 (as only η will set at the boundary) (Test-3).

Xing et al. [2011] found that for adjacent cells in shallow regions of their model there was significant spatial variability in the size of the non-linear momentum advection terms (AT here). They took this to suggest insufficient grid resolution at this location to accurately resolve the non-linear terms. The numeric parameter that will be tested will therefore be the model mesh grid-size (Test-4).

The values used in each of the 5 tests discussed above are given in Table 3.5. Also presented in Table 3.5 is the Relative Percentage Range, RPR, of each set of parameter values. Where:

$$RPR = 100 \times \frac{\max(X) - \min(X)}{\overline{X}} \qquad (3.4.2)$$

X is one of the parameters from Table 3.5 and $\overline{X}$ is the mean of X.

Table 3.5: Values of the parameters altered in each of the 5 sensitivity tests.

Test	Parameter	Values							RPR
1	M [m$^{1/3}$s^{-1}]	8	16	24	32	40	48	56	148.02
2	c_s	0.07	0.14	0.21	0.28	0.35	0.42	0.49	150
3	η_0 [m]	1	2	3	4	5			133.33
4	Δx [m]	15	40	65	90	115	140	165	166.67

3.4.1.1 Physical Model Parameter Tests

Elevation and current time series were calculated by the model for each run. Harmonic analysis of this output was carried out and the standard deviation across each set of runs calculated at each element. This data is presented as patch plots for the amplitude and phase of the surface elevation and current velocity for Test-1 in Figures 3.4–3.7, for Test-2 in Figures 3.8–3.11, and for Test-3 in Figures 3.12–3.15. Tables 3.6 and 3.7 presents statistics, minimum, maximum, mean and standard deviation, of the standard deviation, for each parameter, for each test.

For Test-1 the standard deviation over the channel retains a 1D character. The effect of varying the bottom roughness is quite large. For η, the standard deviation is $\mathcal{O}(10^{-2})$ m in the fundamental and $\mathcal{O}(10^{-3})$ m in the harmonics for $\mathcal{O}(10^{-2})$ standard deviation in C_F ($RPR_M = 150\%$, and via (3.4.1), $RPR_{C_F} = 450\%$). For ϕ, the standard deviation is $\mathcal{O}(10^0)^\circ$ for M$_2$ and M$_4$ and $\mathcal{O}(10^1)^\circ$ for M$_6$. As one might expect when altering friction, the effect on the current velocity was much greater. A standard deviation of $\mathcal{O}(10^0)$ m/s was seen in the amplitude of the M$_2$ current velocity, and $\mathcal{O}(10^{-2})$ m/s and $\mathcal{O}(10^{-1})$ m/s standard deviations were seen for the M$_4$ and M$_6$ respectively. For ψ, the standard deviations were $\mathcal{O}(10^1)^\circ$ for all constituents. These results imply that the model is quite sensitive to the choice of M. When building a model of a real-world site, therefore, it will be important to use the correct value for M. Greater accuracy might also be obtained if M is

allowed to vary over the model area as may be the case in nature (e.g. Nicolle and Karpytchev [2007]).

For Test-2 the variation in the standard deviation of η over the channel area was not as one-dimensional as for Test-1, but could be approximated as such. However, for $\hat{u}$ this approximation is much less appropriate. A $\mathcal{O}(10^{-1})$ variation in c_s ($RPR_{c_s} = 150\%$) was used in this test, the result being very small, essentially negligible variation in η ($\mathcal{O}(10^{-8})$–$\mathcal{O}(10^{-7})$ m), ϕ ($\mathcal{O}(10^{-6})$–$\mathcal{O}(10^{-3})^\circ$), $\hat{u}$ ($\mathcal{O}(10^{-8})$–$\mathcal{O}(10^{-7})$ m/s) and ψ ($\mathcal{O}(10^{-7})$–$\mathcal{O}(10^{-5})^\circ$). This implies that variation in the LST has little impact on the harmonics, therefore for the unoccupied channel the LST could be neglected. However, as discussed previously, the LST will be retained as it will become more important when turbines are deployed in the channel.

For Test-3 the variation in standard deviation was again one-dimensional, but larger standard deviations were seen. For the M_2 η, the largest standard deviations (~ 1.55 m) were seen at either end of the channel, as one would expect given this parameter was varied at the boundaries. Near the centre of the channel the variation reduced to ~ 1.3 m. The opposite was true for ϕ. Near the boundaries, the standard deviation was almost zero, whilst at the centre it was at its maximum. However, the standard deviation remained negligible throughout the channel at $< 0.7^\circ$. Variations in the M_4 and M_6 η were $\mathcal{O}(10^{-3})$–$\mathcal{O}(10^{-2})$ m, with the largest standard deviations near the channel centre and the smallest near the boundaries. For ϕ, standard deviations of $\sim 10^\circ$ were seen in the immediate vicinity of either boundary for the M_4 with much smaller values over most of the model area, whilst for the M_6, standard deviations of between 10–20° were seen over much of the model area. For $\hat{u}$, standard deviations of up to ~ 1.2 m/s, ~ 1.6 cm/s and ~ 2.1 cm/s were seen for the M_2, M_4 and M_6 respectively, and between $\sim 9.7^\circ$ and $\sim 9.95^\circ$, between $\sim 1^\circ$ and $\sim 7^\circ$, and $\sim 39^\circ$ for the M_2, M_4 and M_6 ψ respectively. The variation in η_0 was $\mathcal{O}(10^0)$ or $RPR = 133.\dot{3}\%$. This resulted in standard deviations comparable to those seen in Test-1. However, in Test-1 $RPR = 450\%$ for C_F, much larger than the RPR of η_0 in Test-3. This is taken to suggest a greater sensitivity of the harmonics to η_0 than to C_F. Variation in η_0 will lead to variation in $\overline{u}_0$, and therefore changes in all non-linear terms directly, which may be why the harmonics are most sensitive to η_0. Whilst C_F only affects the FT, the FT will affect both η_0

and $\overline{u}_0$, so variation in C_F directly changes the FT and indirectly all other terms, so the results are also sensitive to C_F.
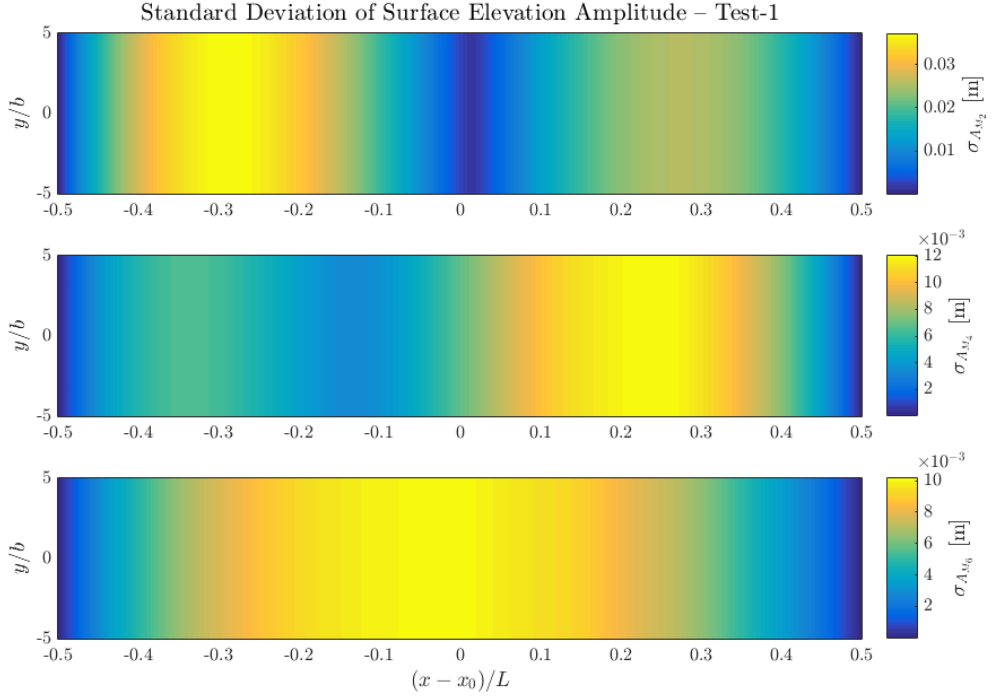
Figure 3.4: Standard deviation in the amplitude of the M_2 (top), M_4 (middle), M_6 (bottom) harmonics of the surface elevation across the runs in Test-1.

3.4.1.2   Numerical Model Parameter Tests

For Test-4 the grid-size was changed as part of the experiment. Therefore, in order to compare the results from the different runs, the output from each of the runs was interpolated / extrapolated onto a 15x15 m uniform grid, which may impact on the results. This extra step for Test-4 aside, the analysis of Test-4 was the same as described for the physical tests above. Contour plots for the amplitude and phase of the surface elevation and current velocity for Test-4 are presented in Figures 3.16–3.19. Table 3.7 presents statistics for the standard deviation, for each parameter.

In Test-4 the standard deviation in the channel was one-dimensional, however, this may be a product of interpolating onto the uniform grid. The standard deviation in the M_2 η was small, up to $\mathcal{O}(10^{-3})$ m, and similar values, $\mathcal{O}(10^{-4})$–$\mathcal{O}(10^{-3})$ m, were seen for the M_4 and M_6 η. For the M_6 this is considered negligible

Table 3.6: Minimum, maximum, mean and standard deviation of the standard deviation of the amplitude and phase of the surface elevation and current velocity across the runs in the physical parameter tests, Test-1 and Test-2, over the whole channel.

		Test-1				Test-2			
		Min	Max	Mean	σ	Min	Max	Mean	σ
A [m]	M_2	1.2×10^{-4}	3.7×10^{-2}	2.0×10^{-2}	1.0×10^{-2}	4.9×10^{-10}	3.86×10^{-8}	1.0×10^{-8}	5.2×10^{-9}
	M_4	8.0×10^{-5}	1.2×10^{-2}	6.9×10^{-3}	$3.2 \times^{-3}$	5.0×10^{-10}	4.65×10^{-8}	1.3×10^{-8}	7.0×10^{-9}
	M_6	1.6×10^{-5}	$1.0 \times^{-2}$	$7.1 \times^{-3}$	$2.9 \times^{-3}$	$8.7 \times^{-10}$	3.64×10^{-8}	$9.9 \times^{-9}$	5.1×10^{-9}
ϕ [º]	M_2	3.4×10^{-3}	2.3	1.5	0.7	1.1×10^{-8}	6.94×10^{-7}	2.0×10^{-7}	1.3×10^{-7}
	M_4	3.3	7.4	5.7	1.1	$2.9 \times^{-7}$	1.60×10^{-3}	9.6×10^{-6}	3.5×10^{-5}
	M_6	17.2	55.8	21.2	3.5	1.2×10^{-6}	9.4×10^{-3}	4.8×10^{-5}	2.0×10^{-4}
V [m/s]	M_2	2.0	2.0	2.0	1.5×10^{-2}	9.3×10^{-10}	6.8×10^{-8}	1.3×10^{-8}	9.0×10^{-9}
	M_4	2.5×10^{-2}	9.5×10^{-2}	4.9×10^{-2}	2.0×10^{-2}	6.8×10^{-10}	3.7×10^{-8}	7.0×10^{-9}	3.3×10^{-9}
	M_6	0.1	0.1	0.1	3.3×10^{-3}	4.6×10^{-10}	2.3×10^{-8}	5.9×10^{-9}	2.6×10^{-9}
ψ [º]	M_2	12.0	13.3	12.3	0.3	7.5×10^{-9}	3.7×10^{-7}	8.2×10^{-8}	4.6×10^{-8}
	M_4	2.3	20.0	11.7	6.3	2.0×10^{-7}	1.5×10^{-5}	2.6×10^{-6}	1.4×10^{-6}
	M_6	48.4	51.6	49.4	1.0	7.4×10^{-8}	5.3×10^{-6}	8.3×10^{-7}	4.2×10^{-7}
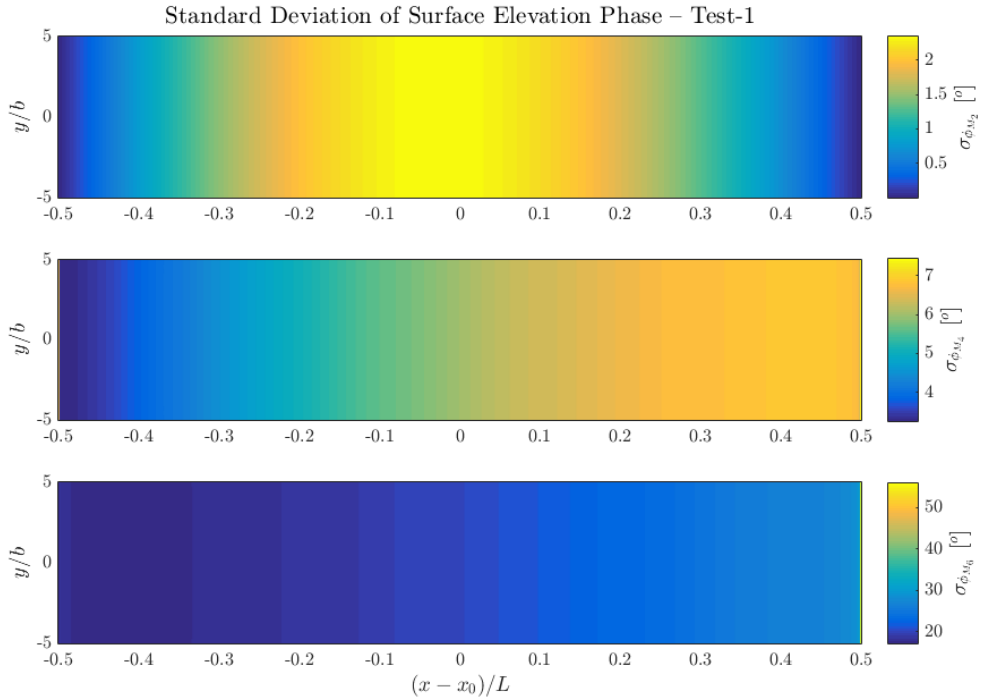
Figure 3.5: Standard deviation in the phase of the M_2 (top), M_4 (middle), M_6 (bottom) harmonics of the surface elevation across the runs in Test-1.

as it is two orders of magnitude smaller than the amplitude of the harmonic; for the M_4 this variation will be considered appreciable, but small.
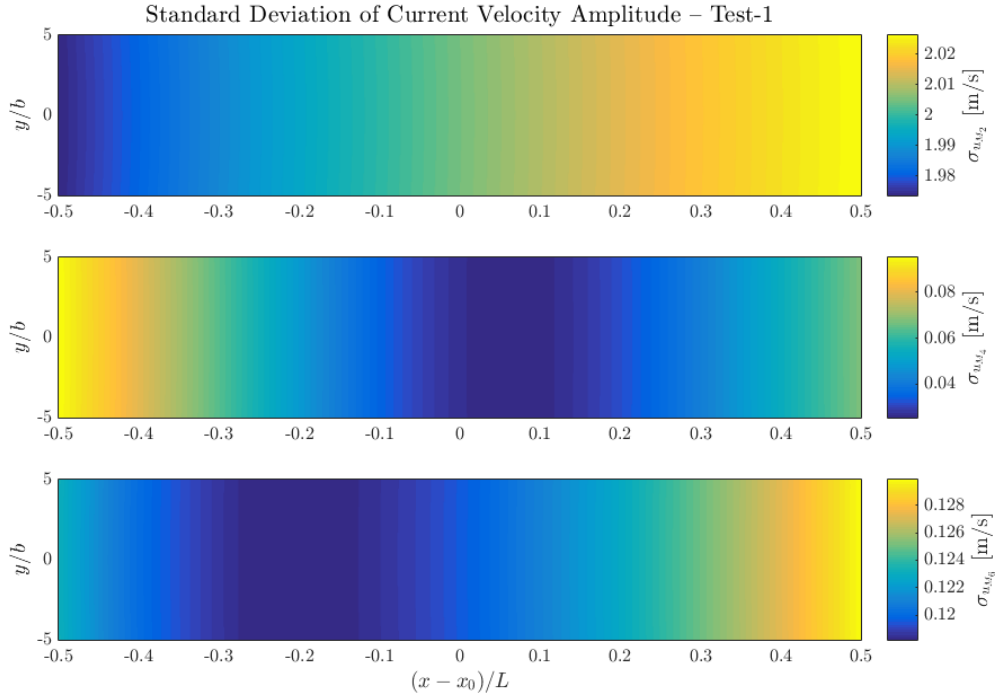
Figure 3.6: Standard deviation in the amplitude of the M_2 (top), M_4 (middle), M_6 (bottom) harmonics of the current velocity across the runs in Test-1.
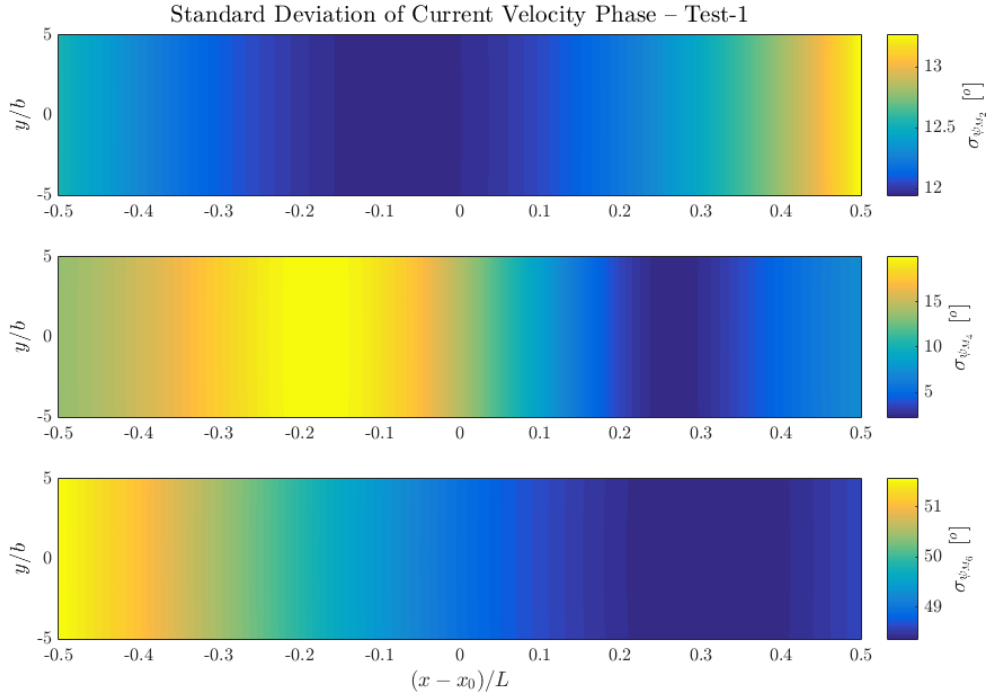
Figure 3.7: Standard deviation in the phase of the M_2 (top), M_4 (middle), M_6 (bottom) harmonics of the current velocity across the runs in Test-1.
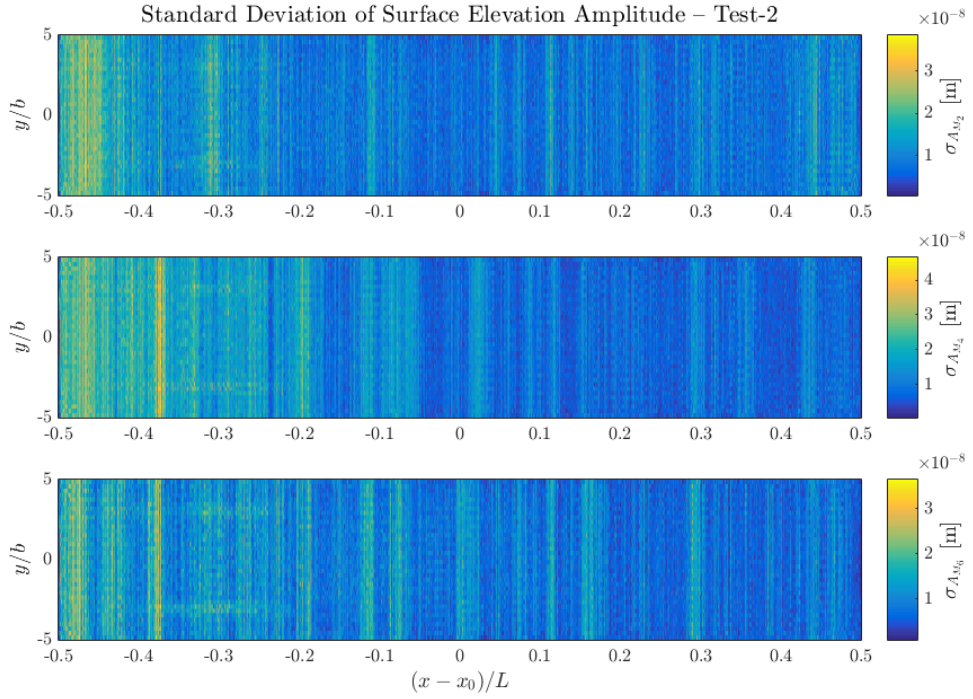
Figure 3.8: Standard deviation in the amplitude of the M_2 (top), M_4 (middle), M_6 (bottom) harmonics of the surface elevation across the runs in Test-2.
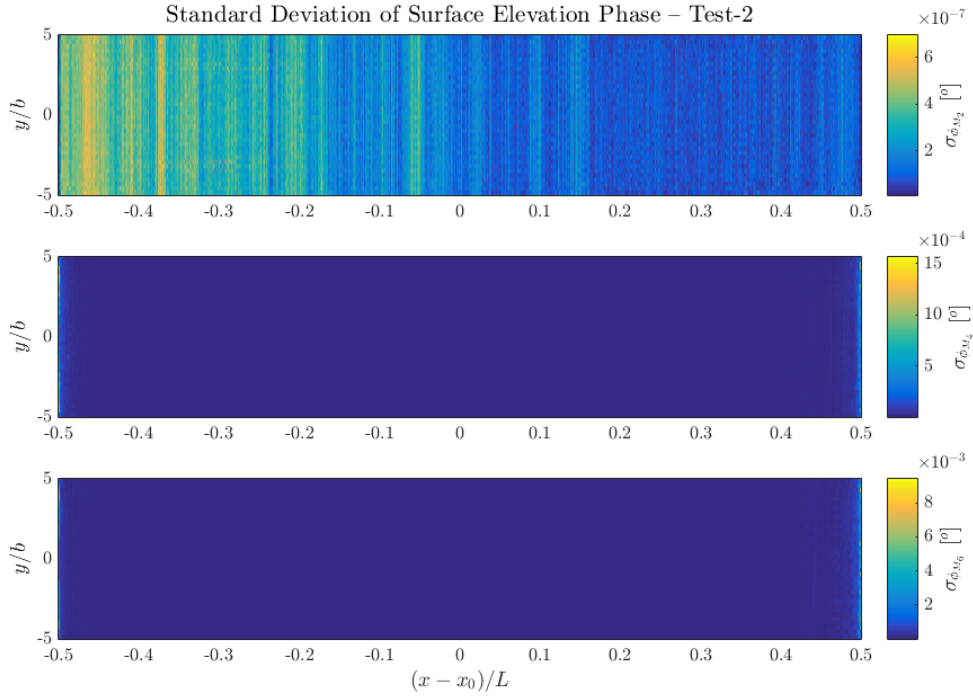
Figure 3.9: Standard deviation in the phase of the M_2 (top), M_4 (middle), M_6 (bottom) harmonics of the surface elevation across the runs in Test-2..
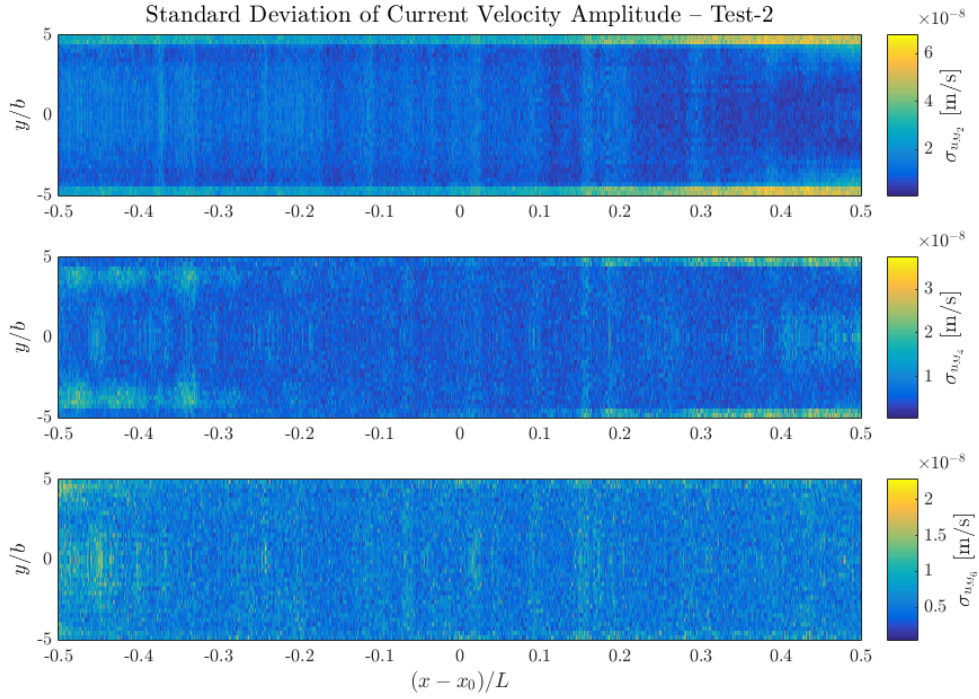
Figure 3.10: Standard deviation in the amplitude of the M_2 (top), M_4 (middle), M_6 (bottom) harmonics of the current velocity across the runs in Test-2.
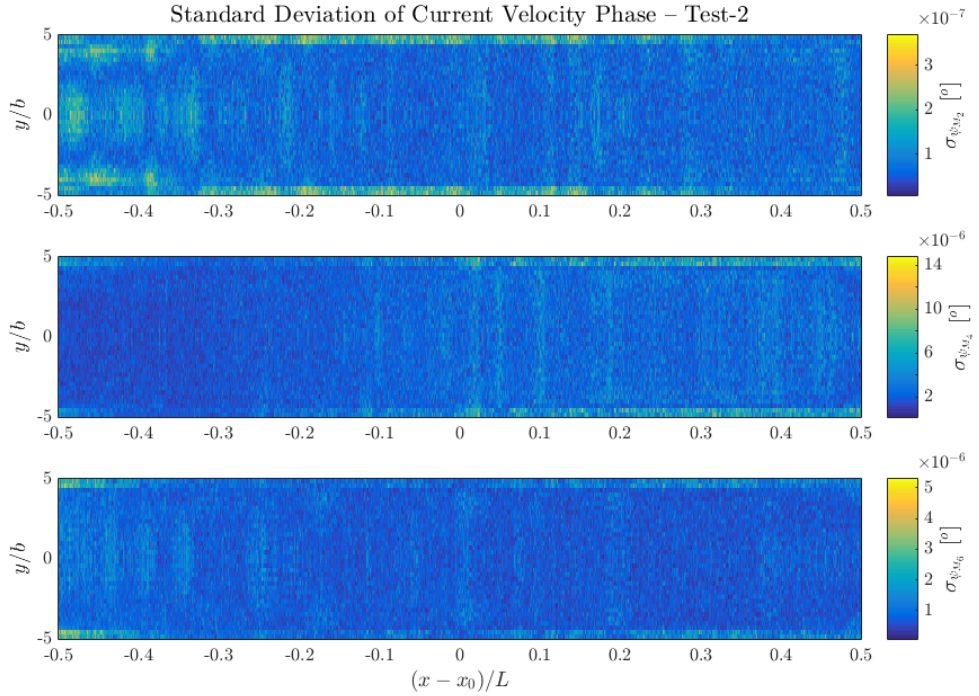
Figure 3.11: Standard deviation in the phase of the M_2 (top), M_4 (middle), M_6 (bottom) harmonics of the current velocity across the runs in Test-2.
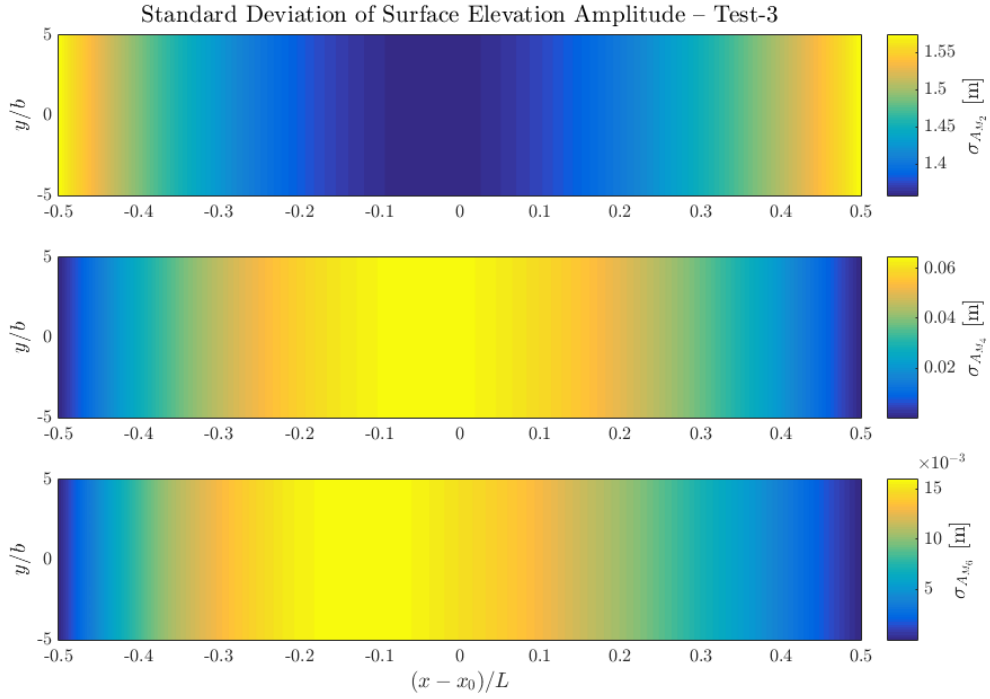
Figure 3.12: Standard deviation in the amplitude of the M_2 (top), M_4 (middle), M_6 (bottom) harmonics of the surface elevation across the runs in Test-3.
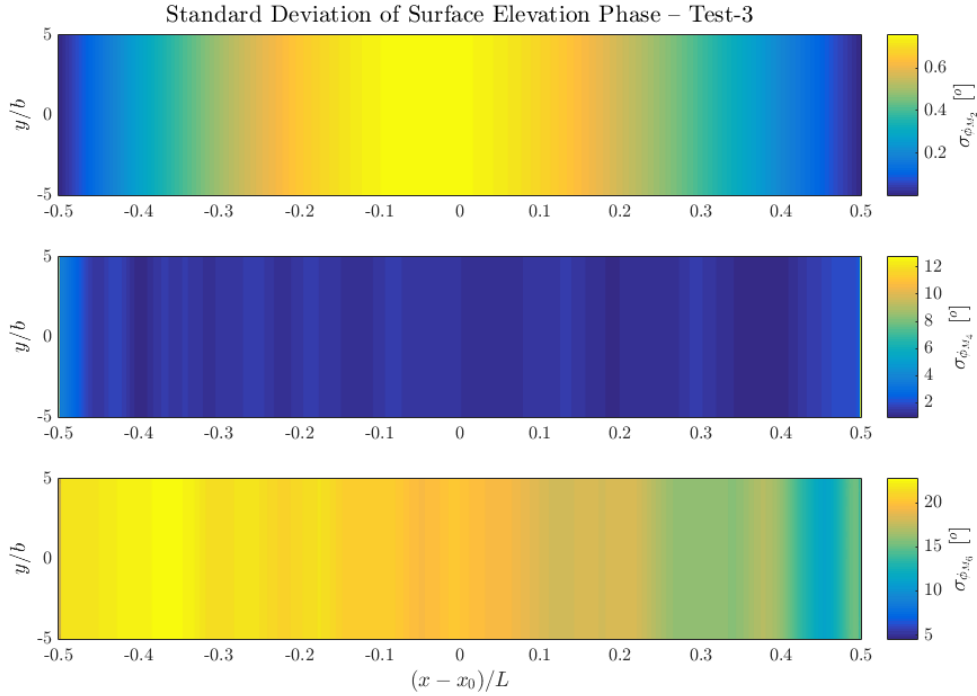
Figure 3.13: Standard deviation in the phase of the M_2 (top), M_4 (middle), M_6 (bottom) harmonics of the surface elevation across the runs in Test-3.

Standard Deviation of Current Velocity Amplitude – Test-3
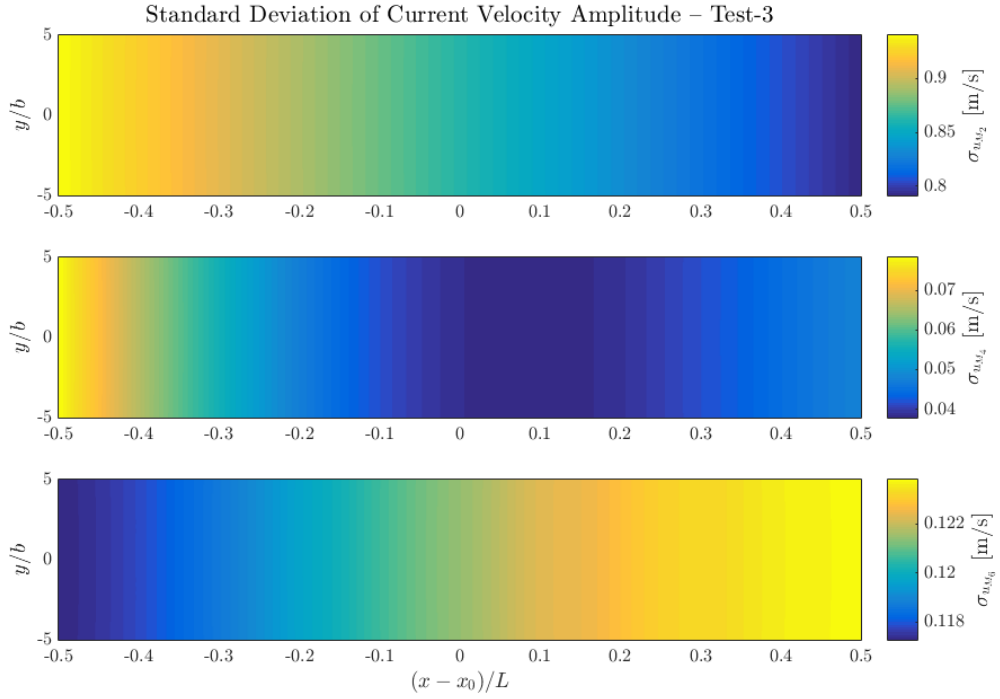
Figure 3.14: Standard deviation in the amplitude of the M_2 (top), M_4 (middle), M_6 (bottom) harmonics of the current velocity across the runs in Test-3.

Standard Deviation of Current Velocity Phase – Test-3
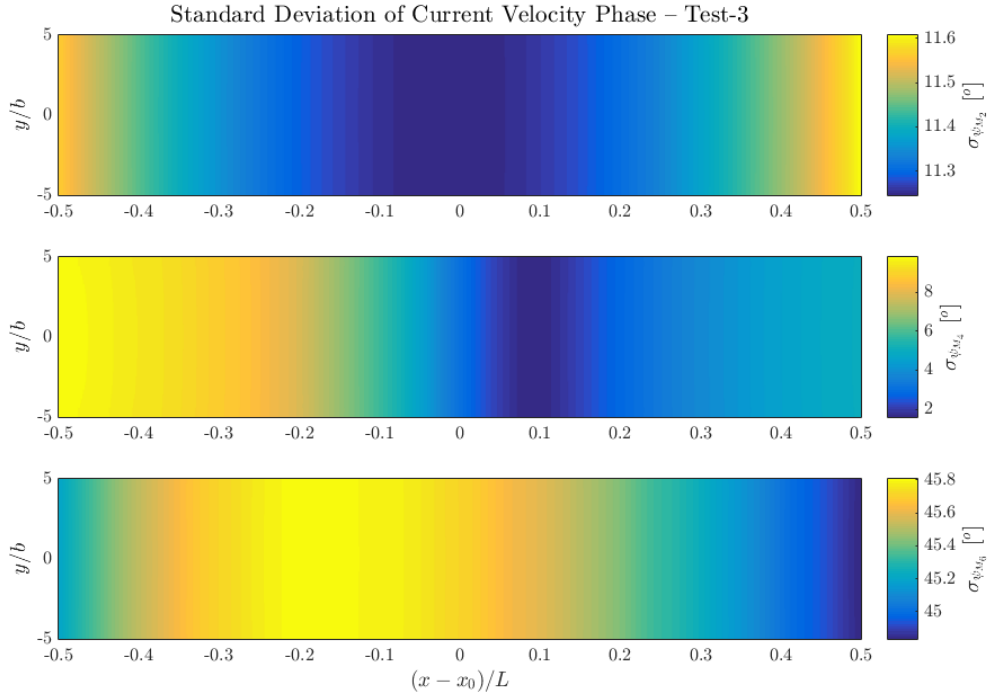
Figure 3.15: Standard deviation in the phase of the M_2 (top), M_4 (middle), M_6 (bottom) harmonics of the current velocity across the runs in Test-3.
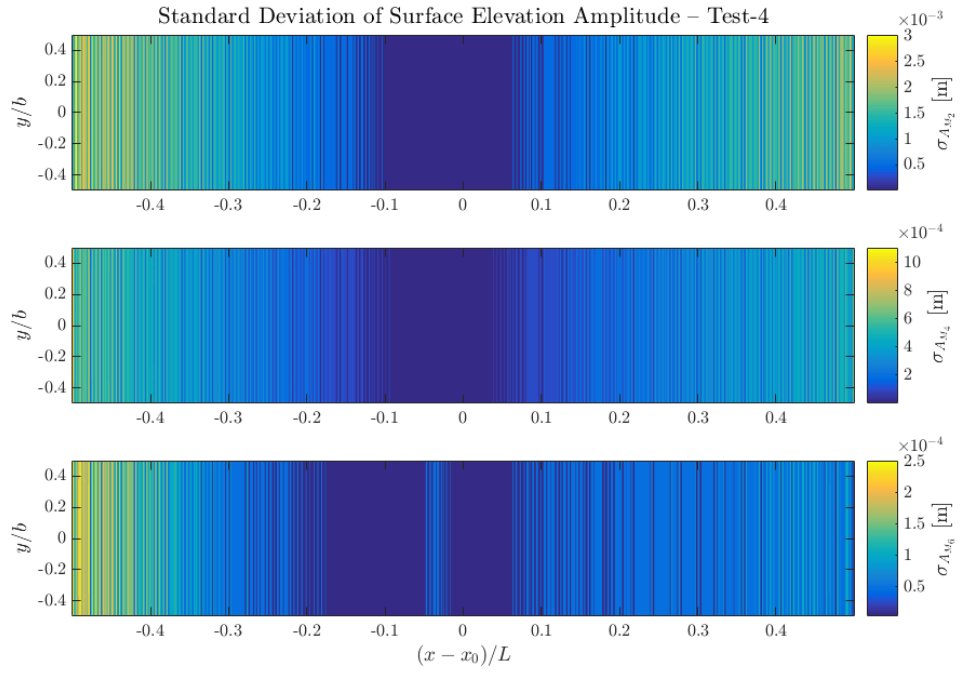
Figure 3.16: Standard deviation in the elevation of the M_2 (top), M_4 (middle), M_6 (bottom) harmonics of the surface elevation across the runs in Test-4.
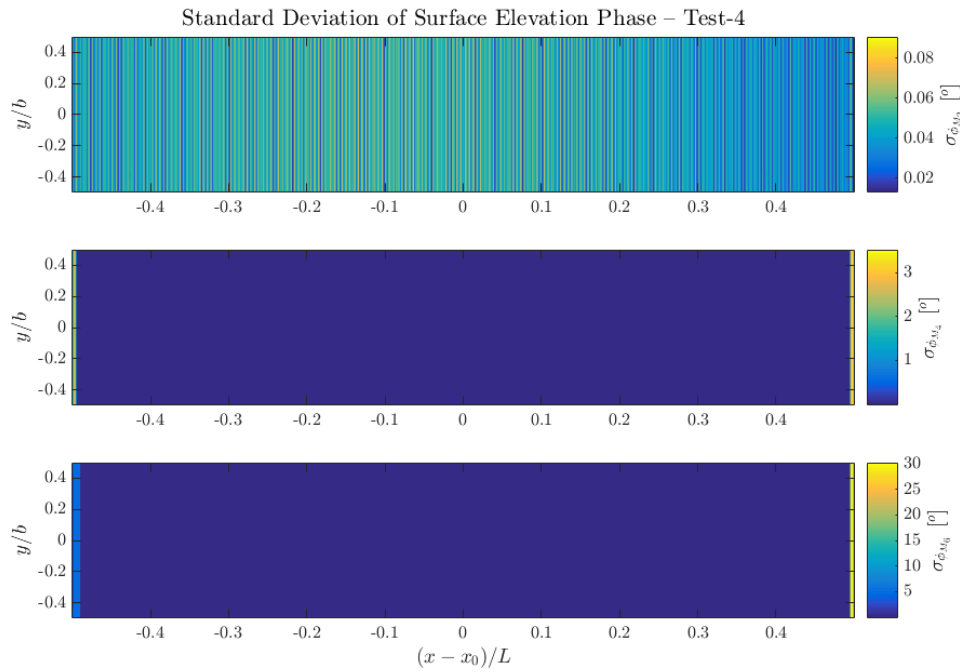
Figure 3.17: Standard deviation in the phase of the M_2 (top), M_4 (middle), M_6 (bottom) harmonics of the surface elevation across the runs in Test-4.
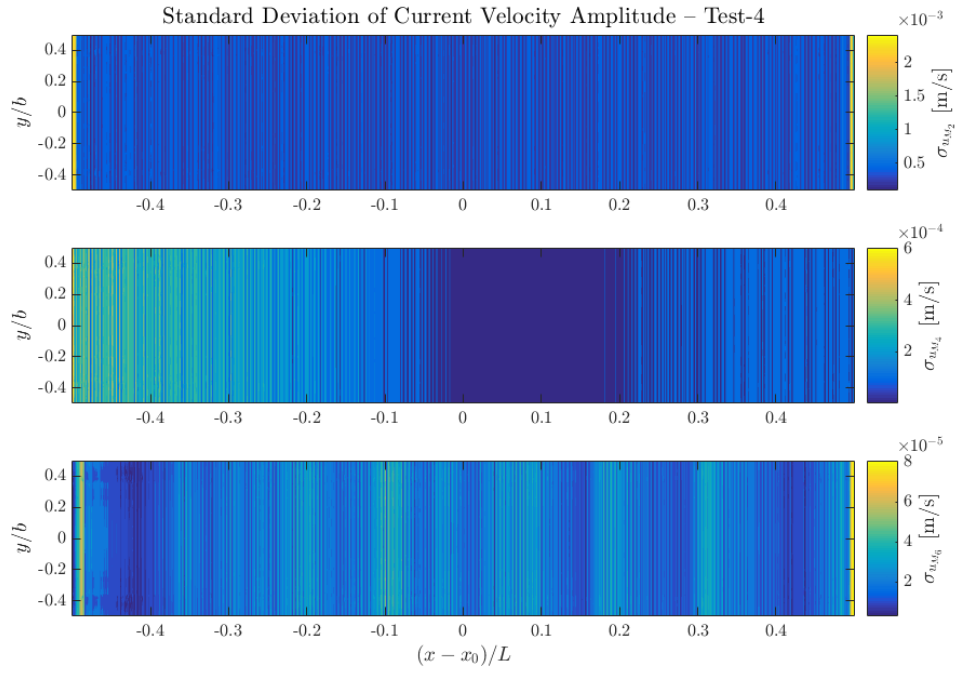
Figure 3.18: Standard deviation in the elevation of the M_2 (top), M_4 (middle), M_6 (bottom) harmonics of the current velocity across the runs in Test-4.
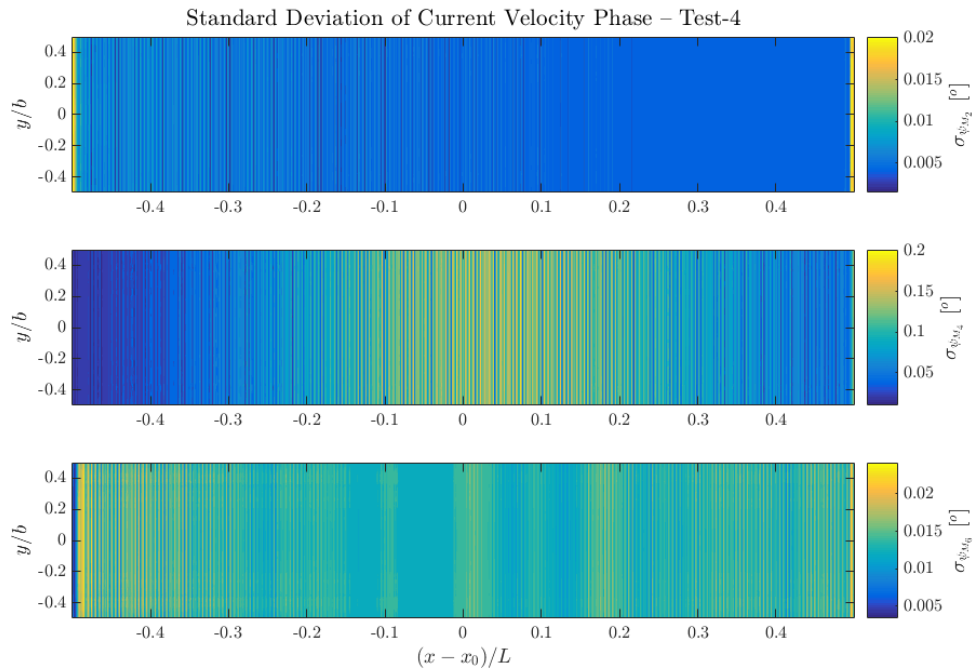
Figure 3.19: Standard deviation in the phase of the M_2 (top), M_4 (middle), M_6 (bottom) harmonics of the current velocity across the runs in Test-4.

The standard deviation of the M_2 ϕ, $\mathcal{O}(10^{-2})$, was considered negligible, whilst for the M_4 the standard deviation, up to $\mathcal{O}(10^0)$, was small but appreciable near the boundary, and negligible elsewhere. Similarly, the variation of the M_6 was important, $\mathcal{O}(10^1)^\text{o}$, near the boundary, and negligible elsewhere, $\mathcal{O}(10^{-1})$–$\mathcal{O}(10^{-2})$.

The standard deviation of ψ for M_2, M_4 and M_6, up to $\mathcal{O}(10^{-1})$, was considered negligible. For $\hat{u}$ the standard deviation of the M_2 was up to $\mathcal{O}(10^{-3})$, and for the M_4 and M_6 the standard deviations were $\mathcal{O}(10^{-5})$–$\mathcal{O}(10^{-4})$ m/s. As these are at least two orders of magnitude smaller than the amplitudes of these constituents they were again considered negligible.

These results imply that changes to mesh grid-size has an appreciable effect on the amplitude of the harmonics of the surface elevation and the phase of the M_6 near the boundaries, and a negligible effect on the remaining terms elsewhere. This is something that should be considered when designing a mesh as variation in grid-size across the mesh may result in small changes in the amplitude of the harmonics of elevation and velocity, which may be important when looking for small changes relating to turbines. However, these changes were seen near the boundaries and good modelling practice dictates that turbines should not be deployed near the boundaries (see §3.4.2).

3.4.2 Sensitivity of Boundaries to Turbines

As a rule of thumb, the boundaries of a model should be far enough away from the turbine(s) simulated in the model so that the turbine(s) have "a negligible effect on the boundary conditions and that perturbations resulting from the turbine array are not amplified by the boundary" (Adcock et al. [2015], pp. 10). The model used in the experiments undertaken in this work employed a boundary with the variation in M_2 surface elevation set at the boundary. However, in this work the harmonics of the tide generated within the model are of interest, with only the M_2 tidal elevation input at the boundary, therefore changes in the M_4 and M_6 elevation will be examined along with the M_2, M_4 and M_6 for the current velocity.

These tests started with the same mesh as used in the previous subsection (30 m structured mesh for a channel with dimensions (3.2.7)). The change in the M_4 and M_6 amplitude and phase for the surface elevation and the M_2, M_4

and M_6 amplitude and phase for the current velocity at the elements along both boundaries are presented in Figure 3.20. Changes to the velocity following the deployment of a turbine at both boundaries appeared to be acceptably small: $< 2\%$ in amplitude and $< 4°$ for the phase. However, for the harmonics of the elevation, very large changes were seen, approaching 20% and 100% for the amplitude at the $x/L = 1$ boundary for the M_6 and M_4 respectively, along with large phase changes. Approaching the boundary, the amplitude of the M_4 and M_6 tends to zero as these tides are not input at the boundary, therefore small changes to the amplitude of the tides will appear as large percentage changes. However, even when their expression as percentages is considered, these changes are due to just a single turbine, and seem unphysically large $\mathcal{O}(10)$ km from the turbine.

Figure 3.20: Changes to amplitude (left column) and phase (right column) of the M_4 and M_6 surface elevation (first and second rows respectively) and the M_2, M_4 and M_6 current velocity (third, fourth and fifth rows respectively) at the $x/L = 0$ (dashed line) and $x/L = 1$ (dotted line) boundaries following the addition of a single turbine (extent shown by vertical grey lines) using the structured mesh.

Table 3.7: Minimum, maximum, mean and standard deviation of the standard deviation of the amplitude and phase of the surface elevation and current velocity across the runs in the physical parameter test, Test-3, and the numerical parameter test, Test-4, over the whole channel.

		Test-3				Test-4			
		Min	Max	Mean	σ	Min	Max	Mean	σ
	M_2	1.4	1.6	1.4	6.5×10^{-2}	2.8×10^{-5}	3.4×10^{-3}	1.1×10^{-3}	4.2×10^{-7}
A [m]	M_4	1.5×10^{-4}	6.4×10^{-2}	4.3×10^{-2}	1.9×10^{-2}	4.8×10^{-6}	1.1×10^{-3}	2.7×10^{-4}	3.0×10^{-7}
	M_6	$1.0 \times^{-5}$	$1.6 \times^{-2}$	1.0×10^{-2}	4.8×10^{-3}	4.5×10^{-6}	2.9×10^{-4}	7.1×10^{-5}	2.1×10^{-7}
	M_2	6.5×10^{-4}	0.8	0.5	0.2	1.4^{-2}	9.1×10^{-2}	4.9×10^{-2}	7.6×10^{-6}
ϕ [^{o}]	M_4	1.0	12.7	1.5	0.5	1.6×10^{-3}	3.6	4.6×10^{-2}	5.9×10^{-4}
	M_6	4.6	22.7	19.1	2.8	1.1×10^{-2}	33.5	0.3	8.2×10^{-3}
	M_2	0.8	0.9	8.6	4.3×10^{-2}	1.1×10^{-4}	2.5×10^{-3}	4.2×10^{-4}	3.2×10^{-6}
V [m/s]	M_4	3.8×10^{-2}	7.8×10^{-2}	4.7×10^{-2}	1.1×10^{-2}	4.7×10^{-6}	6.5×10^{-4}	1.5×10^{-4}	2.1×10^{-6}
	M_6	0.1	0.1	0.1	2.1×10^{-3}	3.3×10^{-6}	8.3×10^{-5}	2.5×10^{-5}	3.1×10^{-7}
	M_2	11.3	11.6	11.4	0.1	1.6×10^{-3}	2.1×10^{-2}	5.9×10^{-3}	2.2×10^{-5}
ψ [^{o}]	M_4	1.6	9.8	5.5	2.7	1.08×10^{-2}	0.2	8.9×10^{-2}	2.9×10^{-4}
	M_6	44.8	45.1	45.49	0.3	3.6×10^{-3}	2.6×10^{-2}	1.4×10^{-2}	7.2×10^{-5}

The effect of the turbine appeared to be largely localised to the elements sharing the same y-value as the element containing the turbine. This effect then extends all the way to the boundary as seen in Figure 3.20. This result was seen when using a structured 30×30 m mesh. An unstructured run was also undertaken using the same model geometry (3.2.7) but with a multi-scale unstructured mesh where the central 10 km had a target element area of 750 m^2, increasing to 1,600 m^2 for the 5 km either side of the central region then increasing further to 6,300 m^2 for the final 6.2 km either side. The changes at the boundary between the no turbine and turbine runs for this mesh are presented in Figure 3.21.

As before, for the velocity, the changes at the boundary for all tides and both amplitude and phase were acceptably small ($< 0.2\%$ and $< 0.1^o$ respectively). The effect of the turbine was also no longer localised to the y-values where the turbine was deployed. The impact on the harmonics of the tide was also reduced with changes of up to ~2.5% and ~25% in the amplitude of the M_4 and M_6 respectively and up to ~ 3° and ~ 12° in the phase of the M_4 and M_6 respectively. The smaller changes at the boundary indicate the unstructured mesh is more suitable for the future experiments than the structured mesh, the changes were however

still considered too large, so the model domain was extended.
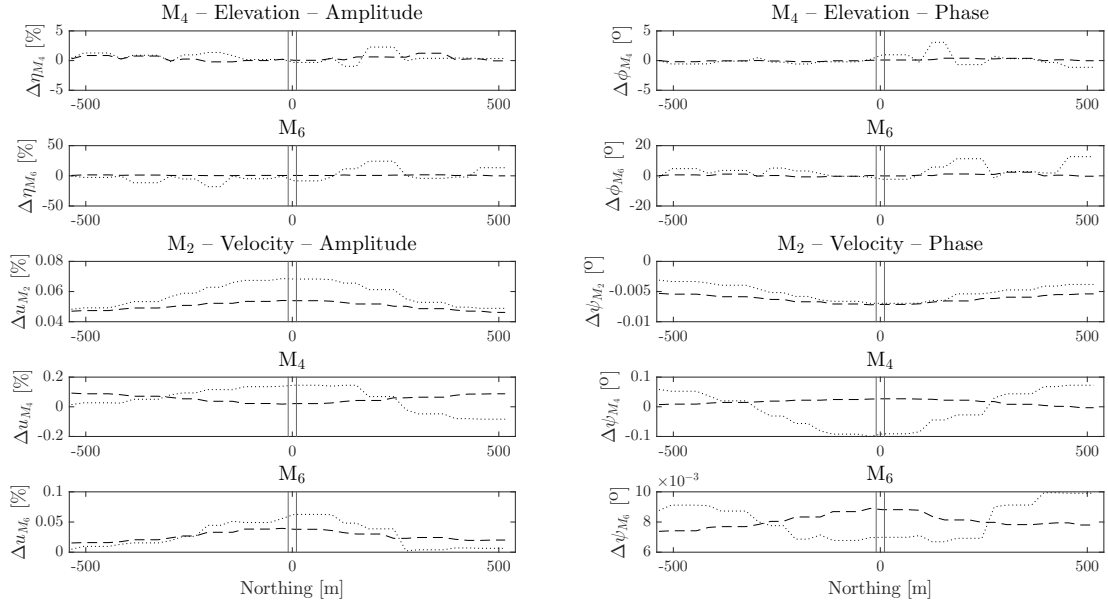
Figure 3.21: Changes to amplitude (left column) and phase (right column) of the M_4 and M_6 surface elevation (first and second rows respectively) and the M_2, M_4 and M_6 current velocity (third, fourth and fifth rows respectively) at the $x/L = 0$ (dashed line) and $x/L = 1$ (dotted line) boundaries following the addition of a single turbine (extent shown by vertical grey lines) using the multi-scale unstructured mesh.

A further model geometry was designed, the length of the channel was increased to 80 km. A multi-scale unstructured grid was again used with the same distribution of scale as described in the previous paragraph, with the additional 23.8 km added to either side having a target element area of 25,000 m^2. A schematic illustration of the model geometry and target mesh areas is presented in Figure 3.22, and summarised in Table 3.8. To achieve similar velocities in the extended mesh the value of phase of the tide input at the right hand boundary was changed to $\phi_1 = 100°$. This value was reached through trial and error.

The changes at the boundaries between the no turbine and turbine runs for this extended geometry are presented in Figure 3.23. For this extended geometry the effect of a single turbine was negligible at the boundary with $< 0.1\%$ change in amplitude and $< 0.1°$ change in phase of the harmonics of surface elevation and

$< 0.03\%$ change in amplitude and $< 0.01°$ change in phase for the fundamental and harmonics of velocity.
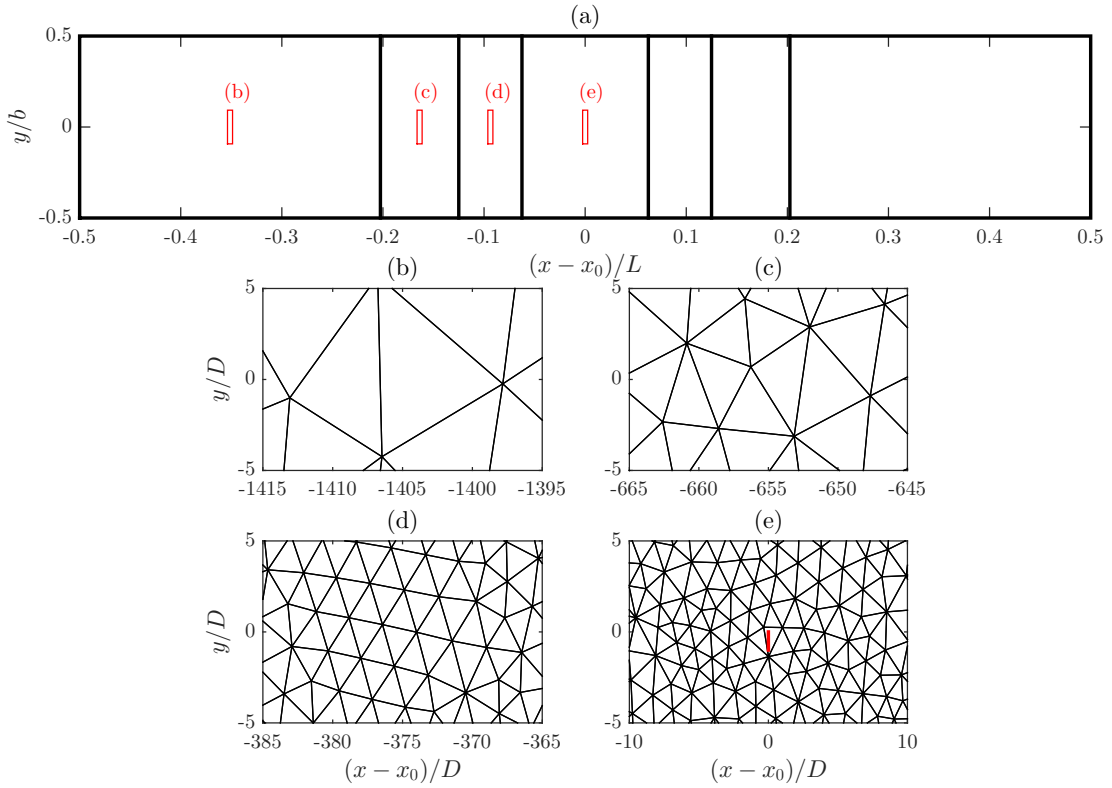
Figure 3.22: Outline of model geometry, (a), with snap-shots of the mesh at the central 10 km (central region), (e), for the 5 km either side (inner regions), (d), for the next 6.2 km either side (intermediate regions), (c) and for the final 23.8 km either side (outer regions), (b). The red boxes in (a) outline the location of the snap-shots (b), (c), (d), (e) in the model domain, and the bold red line in (b) indicates the location of the turbine in the turbine runs.

With sufficiently small changes seen at the boundary for a single turbine in the extended channel additional turbines were added to the channel as a single row. A run where 26 turbines were added to the channel with a spacing of approximately 1 turbine diameter was carried out. The changes at either boundary for this run are presented in Figure 3.24. The changes to the amplitude and phase of the harmonics of elevation are $< 4\%$ and $< 2.5°$ respectively and changes to the amplitude and phase of the fundamental and harmonics of the current velocity are all $< 1\%$ and $< 0.25°$ respectively. These changes were all considered acceptably small, and, as

no more than 26 turbines will be deployed in future experiments, the mesh was therefore considered suitable.

Table 3.8: Mesh generation parameters. Region marked with $*$ only present in extended mesh.

Region	Maximum Element Area [m²]	Target Element Length [m]
Central	750	~ 40
Inner	1600	~ 60
Intermediate	6300	~ 120
Outer$*$	25000	~ 240

3.4.3   Sensitivity of Turbine Wake to Model Turbulence Settings

The turbulence characteristics of a flow will dictate the characteristics of the turbine wake, such as the velocity deficit, wake recovery and size of the wake [Blackmore et al., 2014], and through these characteristics the impact of the turbine on the wider hydrodynamics. The turbulence parameterisation employed in this work is that of Smagorinsky [1963], which expresses sub-grid scale turbulence by an effective eddy viscosity, A, (3.1.6). In MIKE 21 the user has control of the expression of A through the Smagorinsky constant, c_s, and setting upper and lower bounds on A [DHI, 2016a]. In this sensitivity test, Test-5, the effect of varying c_s, using the values from Table 3.5, on a turbine wake will be explored.

The aim of this test was not to gain an understanding of the effect of ambient turbulence on the turbine wake (e.g. Blackmore et al. [2014]) but to understand how the choice of c_s influences the simulated effect of the turbine. In Figures 3.25 and 3.26 the standard deviation in the difference in the amplitude and phase (respectively) of the velocity constituents between runs with and without (without turbine minus with turbine) a single turbine at the channel centre are plotted. For this test the extended unstructured mesh and the single turbine from §3.4.3 were used.
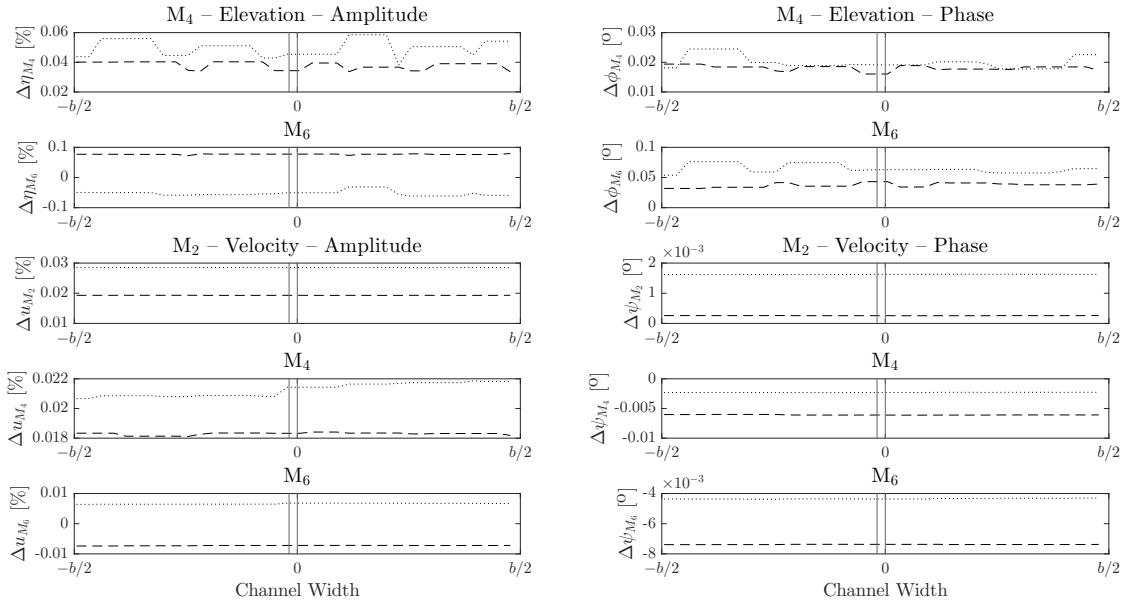
Figure 3.23: Changes to amplitude (left column) and phase (right column) of the M_4 and M_6 surface elevation (first and second rows respectively) and the M_2, M_4 and M_6 current velocity (third, fourth and fifth rows respectively) at the $x/L = 0$ (dashed line) and $x/L = 1$ (dotted line) boundaries following the addition of a single turbine (extent shown by vertical grey lines) using the extended multi-scale unstructured mesh.

The largest variation in both the amplitude and phase across all constituents was in the vicinity of the turbine. With the maximum values in the region closest to the turbine, the near-wake. The variation in the current amplitude was $\mathcal{O}(10^{-4})$–$\mathcal{O}(10^{-3})$ m/s, four to five orders of magnitude larger than the variations seen in Test-2 (the previous c_s experiment). For the M_2 and M_6 this may be considered negligible as it is two orders of magnitude smaller than the amplitude of the constituent, however, this variation may be appreciable at the scale of changes to these constituents resulting from the turbine operation. For the M_4, variation of this size may be appreciable given its only around an order of magnitude smaller than the amplitude of the constituent itself. Again, this may be important at the order of the changes to this harmonic resulting from the operation of the turbine. The variation in the current phase was $\mathcal{O}(10^{-3})^\circ$, $\mathcal{O}(10^{-2})^\circ$ and $\mathcal{O}(10^0)^\circ$ for the M_2, M_6 and M_4 respectively. As for the amplitudes, the variation to the M_2 and

M_6 phase may be considered negligible, whilst appreciable variation to the M_4 phase was seen. For the M_4 this variation will likely be important when it comes to changes to the phase due to the turbine. For the other two constituents these variations may remain negligible.
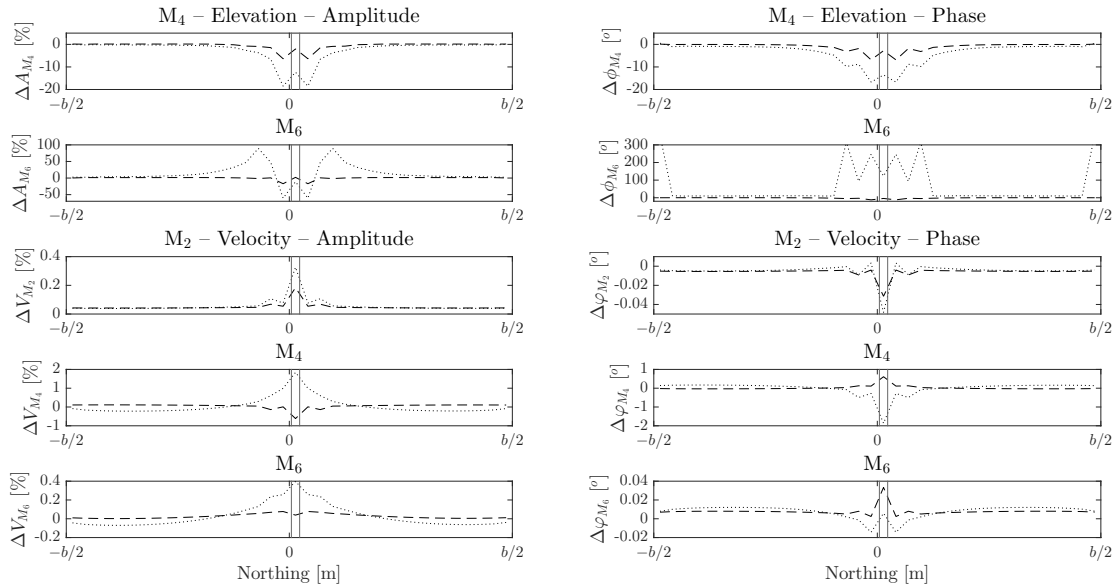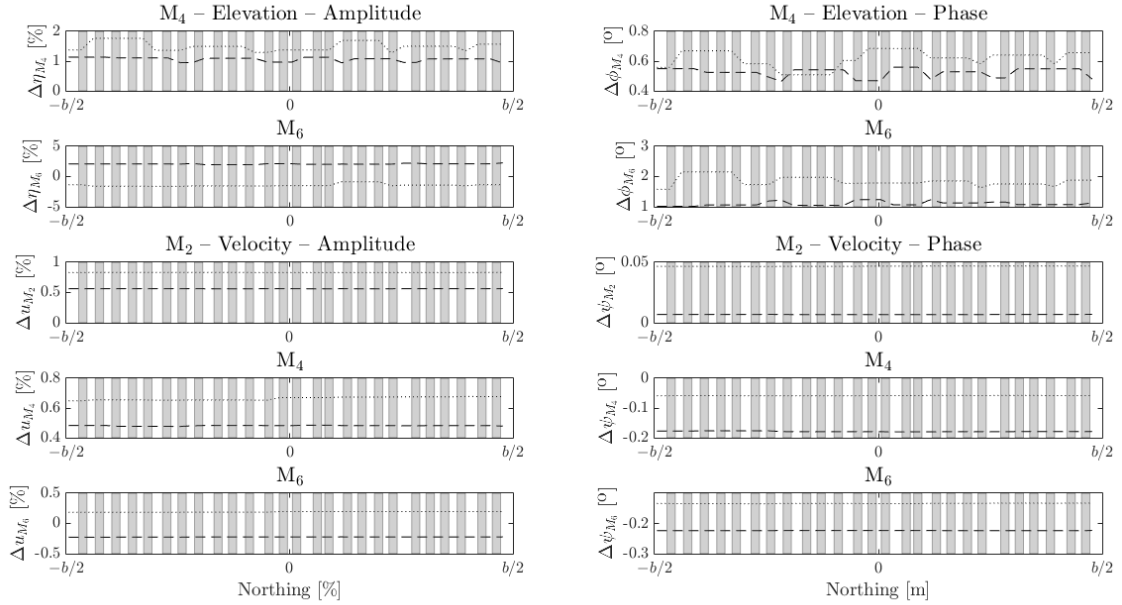

Figure 3.24: Changes to amplitude (left column) and phase (right column) of the M_4 and M_6 surface elevation (first and second rows respectively) and the M_2, M_4 and M_6 current velocity (third, fourth and fifth rows respectively) at the $x/L = 0$ (dashed line) and $x/L = 1$ (dotted line) boundaries following the addition of 26 turbines with an approximate 1 diameter spacing turbine (extent shown by shaded grey areas) using the extended multi-scale unstructured mesh.

These results suggest that the parameterisation of the turbulence is indeed something that should be considered when exploring the effect of the turbine on the hydrodynamics, with even the value of c_s influencing the results. For a real-world site one should take care to ensure that ambient turbulence conditions are reproduced so that the impact of the turbine may be properly understood. In fact, one might look to account for the way in which the turbine operation will interfere with the ambient turbulence in the very definition of the model, such as through source and sink terms in the turbulence closure scheme [Roc et al., 2013]. The luxury afforded by the hypothetical modelling scenario is that a real-world

site is not being recreated, as such MIKE's default value of $c_s = 0.28$ will be used and will remain fixed throughout all experiments. It will be recognised however that a different choice may change the results.
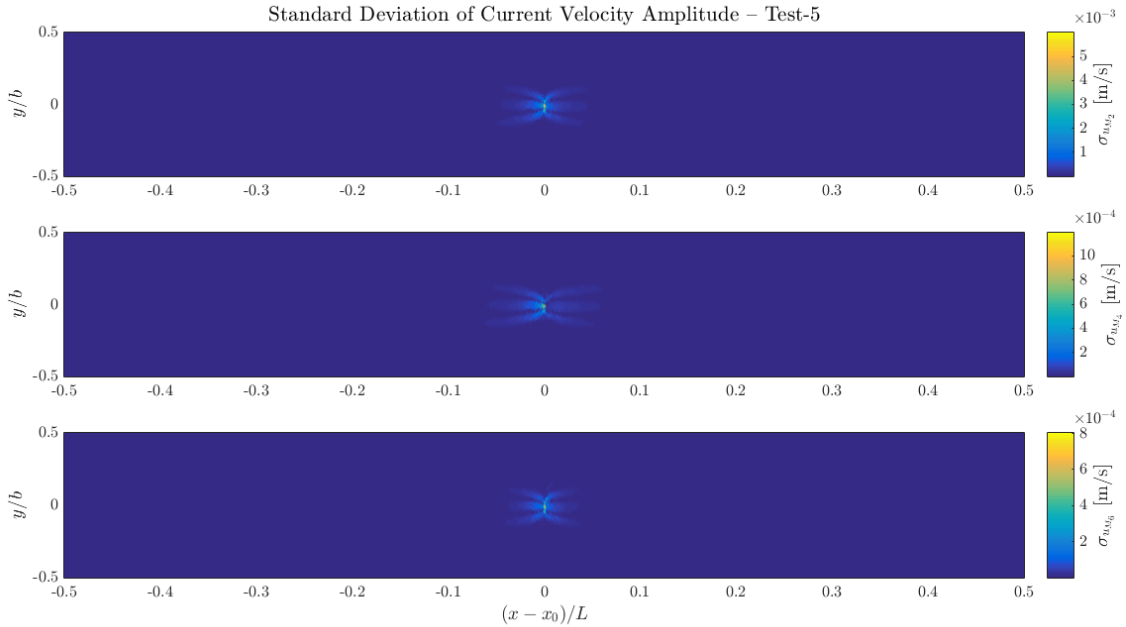
Figure 3.25: Standard deviation of the difference in amplitude of the M_2 (top), M_4 (middle), M_6 (bottom) constituents of the current velocity between runs with and without (with minus without) a turbine at the channel centre, across the runs in Test-5.

3.5   Summary

This chapter has laid out and discussed (i) the assumptions required to model (2.2.5) and (2.2.6) using MIKE21; (ii) the model geometry design to be employed in proceeding chapters; (iii) a comparison of MIKE21 results with analytical solutions to the one-dimensional governing equations; (iv) tests of the sensitivity of model output to variations in input parameter values, (v) tests of the sensitivity of the boundary conditions to turbine deployments and (vi) a sensitivity test of turbine effect to choice of Smagorinsky constant.

The model compared well with analytical solutions for the fundamental tide, but less well for the harmonic tides. The model did however reproduce the patterns

of amplitude and phase of the harmonics giving some confidence in the modelling system's ability to simulate the physics of harmonic generation. Future work might look at the simulation of a real-world site which might be validated against observations. For this work however, an idealised channel was employed so as to minimise the influence of bathymetry on the harmonic tides, simplifying the analysis of the impact of the turbine.
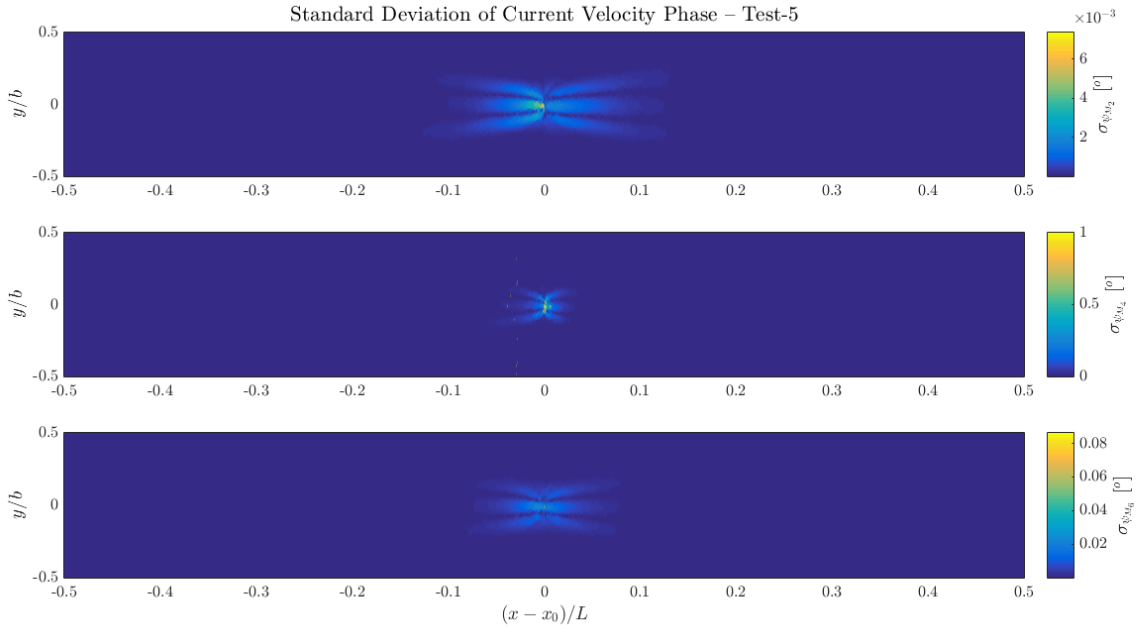
Figure 3.26: Standard deviation of the difference in phase of the M_2 (top), M_4 (middle), M_6 (bottom) constituents of the current velocity between runs with and without (with minus without) a turbine at the channel centre, across the runs in Test-5.

Sensitivity tests for input parameters showed the solution to be sensitive to the Manning number and amplitude of elevation input at the boundaries, but not the Smagorinsky constant. However, when it comes to the effect of the turbine, the results may be sensitive to the choice of Smagorinsky constant, the M_4 in particular. Also, there was suggestion from the results of the test of a non-negligible effect on the solution of grid-size. However, it must be noted that this experiment involved the interpolation of the output to the same structured grid for comparison, which will have impacted on the results. For simulations of real-world sites the correct tides at the boundaries and Manning number across the domain would be very

important for the accuracy of the model. However, in the hypothetical scenario considered in this work the default value for M and the 5 m tide used at the boundary will suffice.

Finally, the channel dimensions (3.2.7) were shown in a boundary sensitivity test to be not suitable for turbine deployments and the effect of the turbines was seen at the boundary. A larger model geometry of:

$$h = 30 \text{ m}, \quad b = 1,080 \text{ m}, \quad L = 80 \text{ km} \tag{3.5.1}$$

was shown to be large enough for a row of 26 turbines to be deployed in the channel with only a small change seen at the boundary. Another finding to come from this test was that the structured grid did not seem to be suitable for the turbine study as the effect of the turbine appeared to be localised in the y-direction to the near turbine region along the length of the channel, resulting in larger effects in this region compared to the unstructured case (cf. Figures 3.20 & 3.21).

To address this a multi-scale unstructured mesh was employed. The target element sizes used in the generation of this mesh are summarised in Table 3.8, and a schematic of the model geometry, along with snapshots of the mesh are presented in Figure 3.22. In this mesh the element length scale is similar to the turbine length scale. As such the correction to the turbine term (3.1.39) & (3.1.40) will be applied.

Chapter 4

Effect of Single Turbine on Overtides and Compound Tides

This chapter will introduce a set of experiments undertaken to address research questions *1a)*, *1b)*, *2a)* and *2b)*, presented in Chapter 2. The experiments will be introduced along with the reasoning behind them in §4.1. In §4.2–§4.4 the results from the experiments will be presented and discussed. Finally, in §4.5 the findings from these experiments will be summarised.

4.1 Introduction

This first set of experiments consisted of five model runs. First the channel free of tidal turbines, forced by only the M_2 tide, was simulated. For the next two runs, a single turbine was deployed at the centre of the channel. In the first of these two runs, the turbine had a fixed thrust coefficient and in the second the thrust coefficient varied with flow velocity using the generic thrust coefficient curve from Bastón et al. [2014] (Figure 2.9). For the next two model runs, the channel was forced by both the M_2 and S_2 tides. In the first of the two runs the channel remained unoccupied, in the second a single fixed thrust coefficient turbine was deployed in the channel.

The above model runs were numbered as follows: Run-1 – unoccupied channel forced by M_2, Run-2 – single fixed-C_T turbine in M_2 forced channel, Run-3 – single variable-C_T turbine in M_2 forced channel, Run-4 – unoccupied channel forced by

M_2 and S_2 and Run-5 – single fixed-C_T turbine in M_2 and S_2 forced channel. These five runs made up 3 experiments. The first using Run-1 and Run-2 looked at the effect of a fixed-C_T turbine on the overtides of the M_2. The second used Run-1, Run-2 and Run-3 and looked at the difference in effect of a fixed- and variable-C_T turbine. The final experiment used Run-4 and Run-5 and looked at the effect of a fixed-C_T turbine on the compound tides of the M_2 and S_2. Turbine implementation in the model is as outlined in Tables 3.3 and 3.4. The run labelling described above is summarised in Table 4.1.

Table 4.1: Chapter 4 model runs.

Run Name	Experiment	No. Turbines	C_T Type	Forcing Constituents
Run-1	1 & 2	0	N/A	M_2
Run-2	1	1	Fixed	M_2
Run-3	2	1	Variable	M_2
Run-4	3	0	N/A	M_2 & S_2
Run-5	3	1	Fixed	M_2 & S_2

The model geometry used for all the above runs was identical, (3.5.1), and the mesh presented in Table 3.8 and Figure 3.22 was used. The turbine was deployed in a location as close to the channel centre as possible whilst only occupying a single element, the turbine hub location was $x = 40{,}010$ m, $y = -10$ m (channel centre at $x = 40{,}000$ m, $y = 0$ m). The channel spans from 0 to 80,000 m in the x-direction and -540 m to 540 m in the y-direction. In the figures throughout this work the x- and y-coordinates will be normalised by either $(x - x_0)/L$ and y/b or $(x - x_0)/D$ and y/D where $x_0 = 40{,}000$ m, L is the channel length ($= 80$ km) and D is the turbine diameter ($= 20$ m).

For the runs forced only by the M_2 tide, a M_2 amplitude of 5 m was used (3.1.15). The model run time was 4 days, including a 24-hour model spin-up time. For the runs where the S_2 was added the model run time was increased to 17 days. This was done so that the length of the time-series output from the model (minus the spin-up period) was greater than the synodic period[1] for the M_2 and S_2, 14.8

---

[1] The interval between two consecutive conjunctions of phase of two tidal constituents (Parker [2007], p 84)

days. This is a condition required for the two frequencies to be resolved in the harmonic analysis. The M_4 and M_6 for example have a synodic period of 0.5 days with respect to the M_2 and M_4 respectively, whilst the MS_4 and S_4 both also have a synodic period of 14.8 days with respect to the M_4 and MS_4 respectively. For both the M_2 and S_2 phases of $\phi_1 = \phi_2 = 0°$ at the left boundary and $\phi_1 = \phi_2 = 100°$ at the right hand boundary was used. Amplitudes of $\eta_1 = 3.25$ m and $\eta_2 = 1.75$ m in (3.1.15) so that $\eta_{S2} \sim \eta_{M2}/2$ and spring peak floods at the boundary were 5 m. All other model parameters are as outlined in Table 3.1.

The model output time-series of surface elevation, η, and easterly and northerly velocity components, u and v respectively, at each mesh element. These time-series underwent harmonic analysis using the *t_tide* MATLAB® function [Pawlowicz et al., 2002] so that the model output was converted into a set of harmonic constituents for each time-series at each mesh element. For the channel forced by only the M_2 the set of harmonic constituents comprised the M_2, M_4 and M_6; and for the channel forced by the M_2 and S_2, the set of harmonic constituents comprised the M_2, S_2, MS, M_4, S_4, MS_4, M_6, $2MS_6$ and $2SM_6$.

4.2 Experiment 1: Effect of Fixed-C_T Turbine on Overtides

4.2.1 Run-1 Results

The results of the harmonic analysis of Run-1 are presented in Figure 4.1. The first thing that one takes from these results is the lack of cross-channel variation. The channel was designed so that the hydrodynamics were one-dimensional. Therefore, the results from Figure 4.1 can be represented by a profile along the channel with little loss of information. This is also why the v-component of the velocity is not included in this figure, as it is negligible.

The profiles of the results from Figure 4.1 along $y = -10$ m (which will be the y position of the turbine hub in Run-2, Run-3 and Run-5) are presented in Figure 4.2. The profile of the M_2 for the surface elevation amplitude (Figure 4.2a) took the form of a parabola (u-shaped) with a minimum near the channel centre.

The profiles of the M_4 and M_6 surface elevation (Figure 4.2a & 4.2c) were also parabola-like but with a maximum near the channel centre (n-shaped). The M_2 and M_6 surface elevation phase (Figure 4.2d & 4.2f) increased from west to east along the channel whilst for the M_4 (Figure 4.2e) it took an n-shaped parabola form. The profile of the M_2 current velocity amplitude (Figure 4.2g) decreased monotonically from west to east, the M_6 profile (Figure 4.2i) decreased monotonically from west to east, and the M_4 profile (Figure 4.2h) took the form of a u-shaped parabola with a minimum near the channel centre, and an eastern maximum 27% smaller than its western maximum. The patterns seen in the current velocity phase profiles are more complicated. The M_2 and M_6 profiles (Figures 4.2j & 4.2l) took on skewed positive and negative parabola shapes and the M_4 profile (Figure 4.2k) took on an arctangent-like shape which might still be described as a monotonic west-east decrease.

4.2.2 Run-1 − Run-2 Comparison Results

The changes in the results of the harmonic analysis of the u-velocity component, between Run 1 (no turbine) and Run 2 (fixed C_T-turbine) along the $y = -10$ m profile are shown in Figure 4.3. For the amplitude of the M_2 and M_6 (Figures 4.3a & 4.3e), sharp peaks of decrease of up to 7.92% and 7.91% respectively were seen around the turbine. Within 10 km either side this change fell to 0.1% for the M_2 or within 6 km for the M_6. For the M_4 (Figure 4.3c) an increase of up to 38% was seen to the west of the turbine, and a decrease of up to 12% was seen to the east of the turbine. Within 12 km either side of the turbine the size of the change fell to less than 0.5%. The largest phase change was seen for the M_4 (Figure 4.3d), with a decrease to the phase of up to 19º to the west of the turbine and an increase in phase of up to 46º to the east of the turbine. The changes to the phase of the M_2 and M_6 were less severe (Figures 4.3b & 4.3f), with decreases to the phase of both tides of at most 0.17º for the M_2, just to the west of the turbine, and ~ 1º either side of the turbine for the M_6.

The addition of the turbine to the channel caused the one-dimensional form of the hydrodynamics to break down as flow was accelerated around the turbine, or slowed as it passed through the turbine, introducing lateral velocity gradients.

As such, though informative, profiles along the channel showing changes in the results of the harmonic analysis do not give the full picture. Therefore, area plots of changes to the harmonic analysis are presented in Figure 4.4. One can see from this figure that there is lateral variation in the effect on current velocity with wake-like structures seen extending in either direction, originating at the turbine.
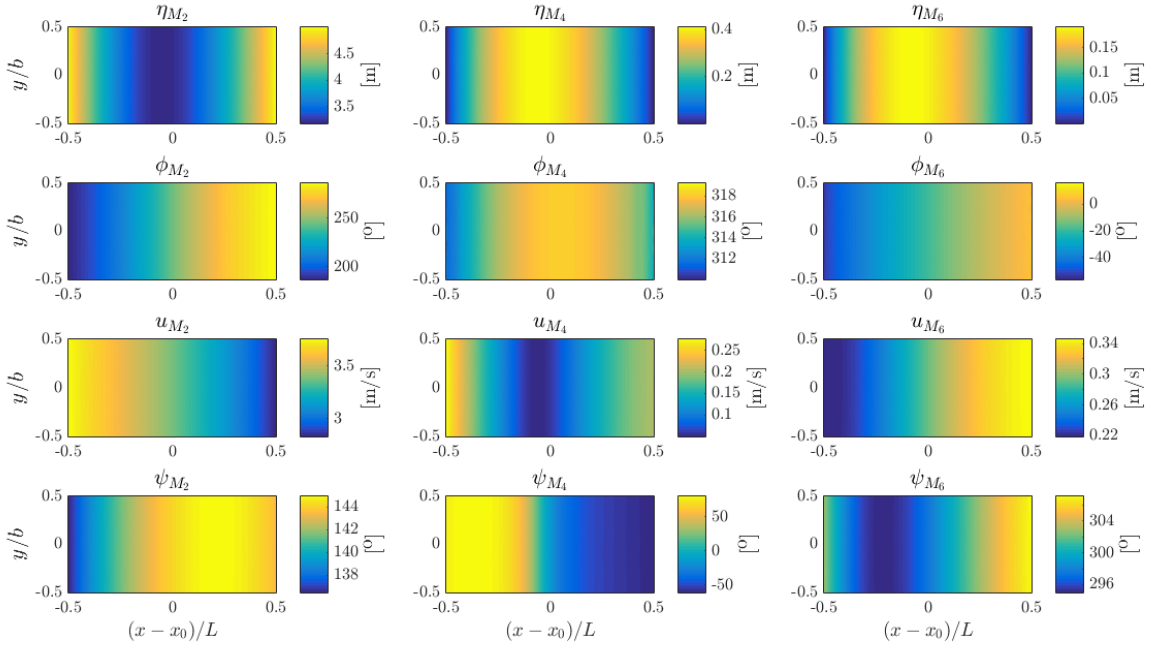
Figure 4.1: Results of harmonic analysis of the surface elevation and u-velocity component (v-component negligible) for Run-1. Along channel distances normalised by channel length, L, and subtracted by $L/2$ so that channel centre is at 0. Across channel distances normalised by channel width b, channel centre naturally at 0, see Figure 3.24. First row – amplitude of surface elevation, second row – phase of surface elevation, third row – amplitude of velocity, fourth row – phase of velocity, first column – M_2, second column – M_4, third column – M_6.

4.2.3   Discussion

The effect of the turbine on the M_6 tide was similar to the effect on the M_2 whilst different patterns of change, and much larger changes, to the M_4 tide were seen. This is an important finding as it is the M_4 tide which dictates flood-ebb asymmetry, which in turn dictates net sediment transport pathways and may also affect the

tidal resource itself (Chapter 2, §2.4). The flood-ebb magnitude asymmetry (FVA) in the model output was quantified using two different measures. The first was introduced in §2.3:

$$A_{S,1} = \frac{u_{\mathrm{M}_4}}{u_{\mathrm{M}_4}} \cos(2\psi_{\mathrm{M}_2} - \psi_{\mathrm{M}_4}) = r_u \cos(\Psi) \qquad (4.2.1)$$

where u_{M_2} and ψ_{M_2} are the amplitude and phase of the M_2 u-velocity, u_{M_4} and ψ_{M_4} are the amplitude and phase of the M_4 u-velocity, r_u is the ratio of the M_4–M_2 u-velocity amplitudes and Ψ is the relative phase of the M_2 and M_4. The second measure comes from Neill et al. [2014]:

$$A_{S,2} = 100 \times \frac{u_f - |u_e|}{\langle |u| \rangle} \qquad (4.2.2)$$

where u_f is the magnitude of the current at maximum flood, $|u_e|$ is the absolute value of the magnitude of the current at maximum ebb and $\langle |u| \rangle$ is the mean current speed over a tidal cycle.

In the top panel of Figure 4.5 the transition from ebb-dominated FVA near the western boundary, west (left) of $(x - x_0)/L \approx -0.2$, to flood-dominated FVA, east (right) of $(x - x_0)/L \approx -0.2$, can be seen. In Run-2 the turbine increased the strength of flood domination to the west and reduced it to the east, almost to the point of magnitude symmetry. The middle panel in Figure 4.5 plots the difference between the runs along the profile, focusing on the region between $(x - x_0) = \pm L/10 = \pm 400D$, where change is most apparent. This plot echoes the discussion above. However, it is interesting when compared with the profile in the bottom panel, in which the profile of the change in $A_{S,1}$ is plotted across the same region. The patterns seen in the two profiles were identical but with slightly different absolute values. This indicates that $A_{S,1}$ is a suitable predictor of regions of a/symmetry and flood/ebb dominance. It does not however give a percentage measure of the asymmetry as is the case with $A_{S,2}$. It does however require less information: $A_{S,2}$ requires a time-series, whilst $A_{S,1}$ requires only the amplitude and phase of the M_2 and M_4 which is more likely to be known over a wide area. For example, using the co-range and co-phase charts of a region, the flood/ebb a/symmetry for that region could be estimated with relative ease. The measure $A_{S,2}$ is however considered a direct measure of asymmetry.
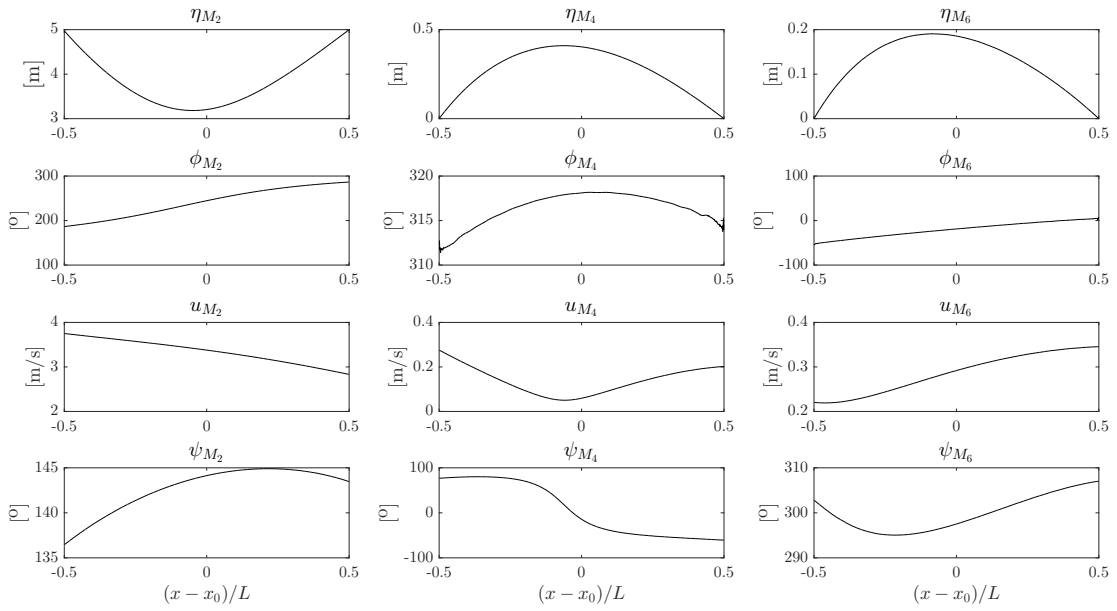
Figure 4.2: Results of harmonic analysis of the surface elevation and u-velocity component (v-component negligible) as profiles along $y = -10$ m. Along channel distances normalised by the channel length, L, and subtracted by $L/2$ so that channel centre is at 0. First row – amplitude of surface elevation, second row – phase of surface elevation, third row – amplitude of velocity, fourth row – phase of velocity, first column – M_2, second column – M_4, third column – M_6.

Figure 4.6 plots $A_{S,2}$ against $A_{S,1}$ for each element in the model. For Run-1 there is a strongly linear relationship with a correlation coefficient of 0.9974. The addition of the turbine in Run-2 appeared interfere somewhat with the relationship between $A_{S,1}$ and $A_{S,2}$, reducing slightly the overall correlation to 0.9965. This apparent change should be borne in mind if one were to use $A_{S,1}$ to make an initial estimate of the effect of a turbine on the flood-ebb-asymmetry of a region. The equation of the line of best fit to the Run-1 plot was:

$$A_{S,2} = \frac{A_{S,1} - 0.02}{0.24} \tag{4.2.3}$$

which allows for an approximate conversion from $A_{S,1}$ to $A_{S,2}$. However, given the changes caused by the deployment of a turbine, conversion between the two measures may not be suitable in this situation. It is not clear that this change to the $A_{S,1}$-$A_{S,2}$ relationship has a physical origin. It being model related cannot be

ruled out at this stage and may warrant future investigation.

The significance of the sensitivity of the effect of the turbine to the choice of c_s identified in §3.4.3 is explored in Figure 4.7. This figure plots the range of differences in the M_2, M_4 and M_6 current across Test-5, where the effect of the turbine was tested for different values of c_s, normalised by changes when $c_s = 0.28$, the default value, and the value used in the experiment above, $R'_{\Delta u_X}$. Where:

$$R'_{\Delta u_X} = \frac{\max(|\Delta u_X|) - \min(|\Delta u_X|)}{|\Delta u_{X,E}|}$$

$X = M_2$, M_4 or M_6 and $\Delta u_{X,E}$ is the change in u_X with $c_s = 0.28$, as seen in the experiment above.
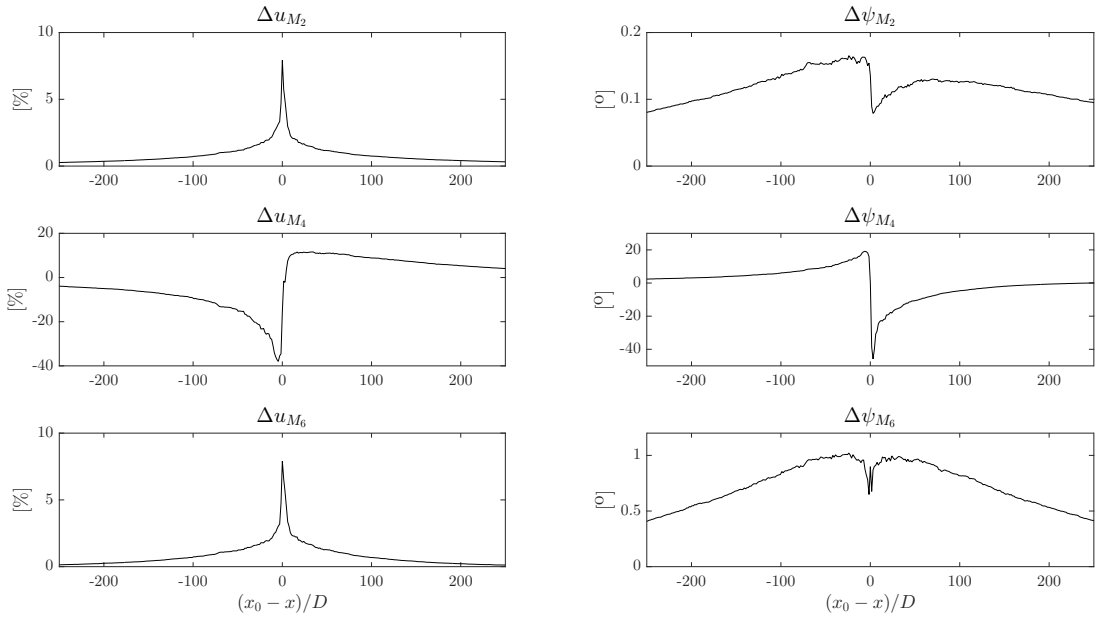
Figure 4.3: Profiles of change in the results of the harmonic analysis of the current velocity between Run-1 and Run-2 (Run-1 minus Run-2) along $y = -10$ m, i.e. through the centre of the turbine. Along channel distances normalised by the turbine diameter D and defined so that 0 is the channel centre. Left column – change to amplitude of current velocity constituents, right column – change to phase of the current velocity constituents, top row – M_2, middle row – M_4, bottom row – M_6.
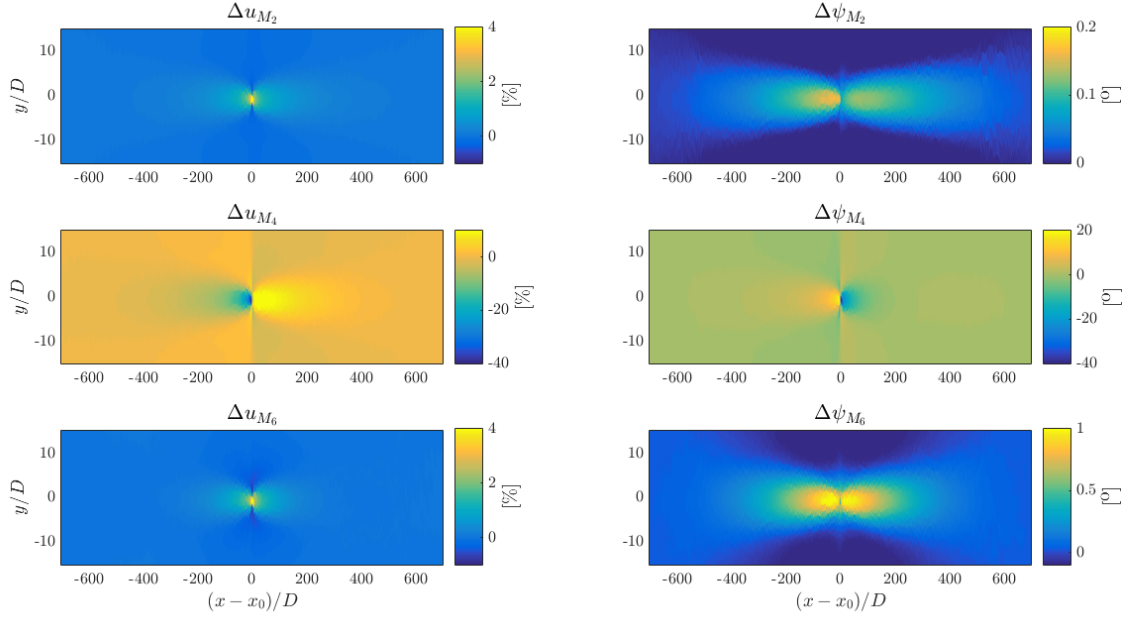
Figure 4.4: Plots of change in the results of the harmonic analysis of the current velocity between Run-1 and Run-2 (Run-1 minus Run-2) over the area surrounding the turbine. The along channel and across channel distances are normalised by the turbine diameter, D and the along channel normalisation designed in such a way that the centre of the channel lies at 0. The area covered spans 14 km $(700D)$ east and west of the channel centre along the channel (left and right) and 300 m $(15D)$ either north and south of the channel centre across the channel (up and down). Left column – change to current velocity amplitude, right column – change to current velocity phase, top row – M_2, middle row – M_4, bottom row – M_6.

Across the majority of the model domain the ratio is small to negligible suggesting little significance in the choice of c_s. However, near the edge of the turbine wake the ratio becomes larger indicating an increased significance of the choice of c_s. Also, for the M_4 there is a band at approximately $(x - x_0)/L \sim 0.35$ where the ration is large. This is is causes by M_4 being approximately zero. Overall Figure 4.7 shows that the choice of c_s has little significance to the conclusions above.
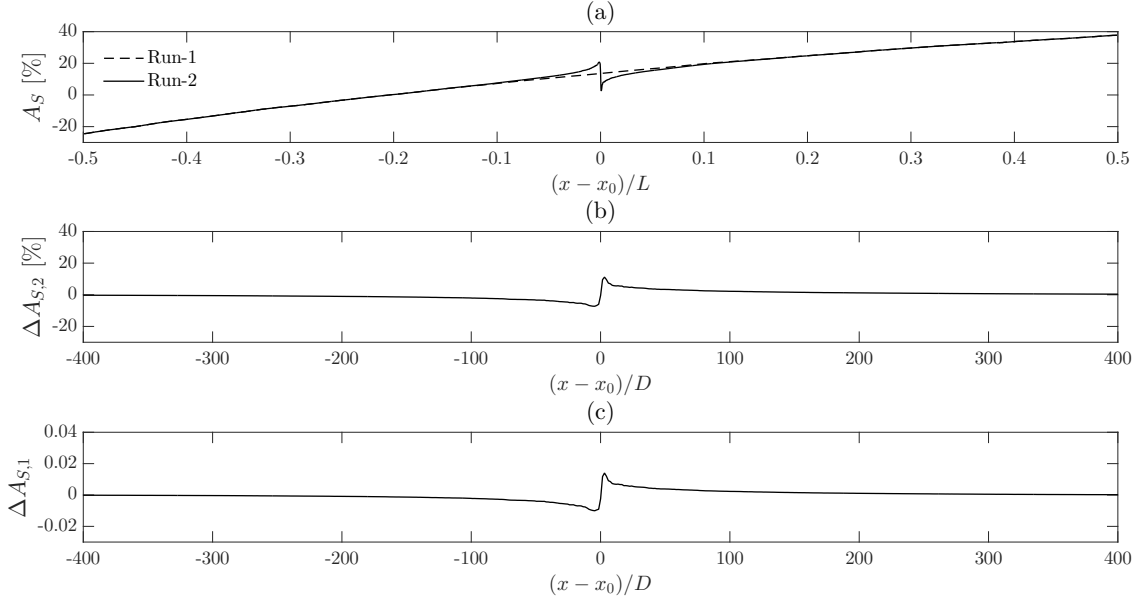
Figure 4.5: (a): flood-ebb-asymmetry measured by $A_{S,2}$ for Run-1 (solid) and Run-2 (dashed) along $y = -10$ m, (b): change in $A_{S,2}$ between Run-1 and Run-2 (Run-1 minus Run-2) along $y = -10$ m between $(x - x_0) = \pm L/10$, (c): change in $A_{S,1}$ between Run-1 and Run-2 (Run-1 minus Run-2) along $y = -10$ m between $(x - x_0) = \pm L/10$. Along channel distances normalised by the turbine diameter D and defined so that 0 is the channel centre.

4.3   Experiment 2: Difference in Effect of Fixed- and Variable-C_T Turbines on Overtides

4.3.1   Results

In Figure 4.8 profiles of the difference in the harmonic analysis of the current velocity between Run-1 and Run-3 (solid line) are plotted, with reference to the change between Run-1 and Run-2 (dashed line). The peak amplitude changes for the M_2 and M_4 (both peaks) were smaller in the variable-C_T experiment (Run-1 minus Run-3: R13 hereinafter) than the fixed-C_T experiment (Run-1 minus Run-2: R12 hereinafter). In the variable-C_T experiment (R13) the peak M_2 amplitude reduction was 30% smaller, and the peak M_4 amplitude reduction and augmentation were 61% and 15% smaller respectively, compared to the fixed-C_T experiment (R12). Conversely, the peak reduction to the M_6 amplitude was 35% larger in R13 than

R12. As for the phase, larger changes to the M_2 phase were seen in R13 than R12. Here the runs aren't so easily compared, but the maximum value of M_2 phase change in R13 was 48% larger than the maximum value for R12. For the change to the M_6 phase in R13 the pattern of change was completely reversed compared to R12. In R12 reduction to the M_6 was seen local to the turbine, but for R13 large augmentation to the M_6 phase was seen. Finally, for the M_4 phase both the augmentation and reduction peaks were smaller in R13 than R12, 87% and 54% respectively.
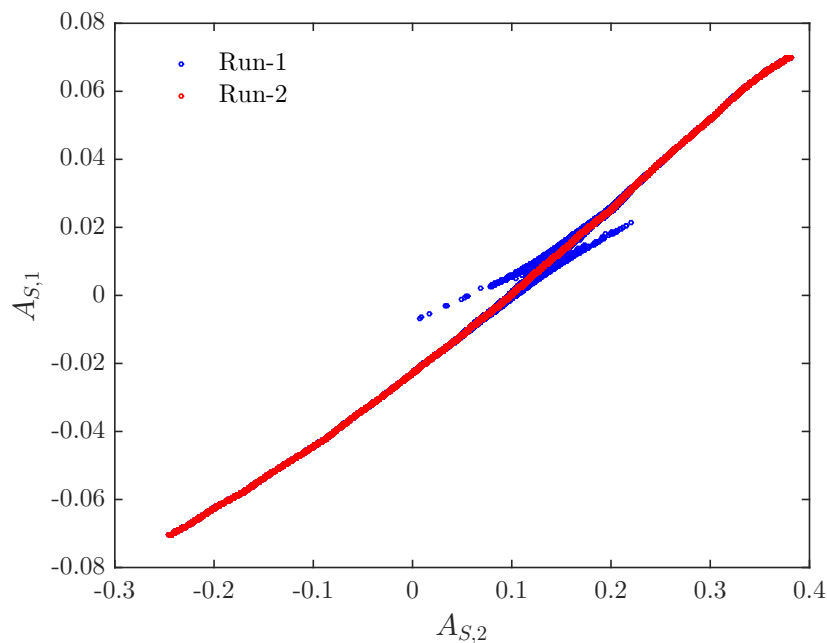
Figure 4.6: $A_{S,1}$ against $A_{S,2}$ at each model element Run-1 (blue) and Run-2 (red).

4.3.2   Discussion

Figure 4.9a shows the change in $A_{S,2}$ between Run-1 and Run-3 along with the change between Run-1 and Run-2 for reference. One can see that the variable-C_T turbine has a much smaller effect on the local flood-ebb asymmetry than does the fixed-C_T turbine. Figure 4.9b shows the change in $A_{S,2}$ between Run-2 and Run-3 (Run-2 minus Run-3). In terms of the amount of difference between the two runs the largest differences are seen at the two peaks (augmentation and reduction peaks), the $A_{S,2}$ augmentation peak was 41% smaller for the variable-C_T turbine and the reduction peak is 59% smaller.
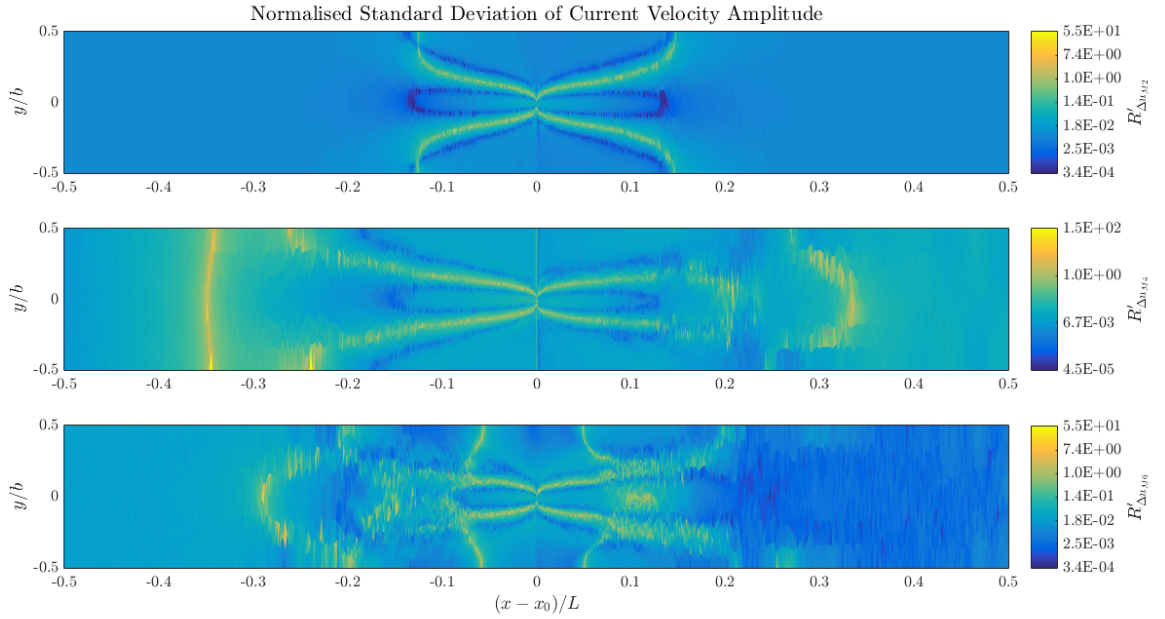
Figure 4.7: Standard deviation of the effect of the turbine on the current amplitude from sensitivity test-5 (Figure 3.25) normalised by the change caused by turbine using default $c_s = 0.28$ (Figure 4.4).

These changes can be understood through the changes to the M_2 and M_4 seen in Figures 4.8a–4.8d, using (4.2.1) and the relationship between $A_{S,1}$ and $A_{S,2}$ (Figure 4.6 & (4.2.3)). As seen through most of the results in Figure 4.8, the majority of the difference between the effect of the fixed- and variable-C_T turbines was that the variable-C_T turbine has a smaller effect. Physically, the reason for this is most likely that the fixed-C_T turbine is extracting energy from the flow continuously whilst the variable-C_T turbine only cuts in when the flow velocity is above 1 m/s, meaning the turbine is only operational for 44% of the tidal cycle, as opposed to 100% for the fixed-C_T turbine. Additionally, when the current is above 2.5 m/s (63% of operational time) there is a polynomial relationship between C_T and $\hat{u}$, and reduced turbine efficiency, which may go some way towards explaining the changes in pattern seen in, for example, the phase of the M_6 current velocity. According to the expansions in §2.2, only the elevation element of the friction and turbine terms introduce the M_6 harmonic, making changes to the elevation turbine term, through changes to C_T at speeds above $\hat{u} = 2.5$ m/s the most obvious source of this change.
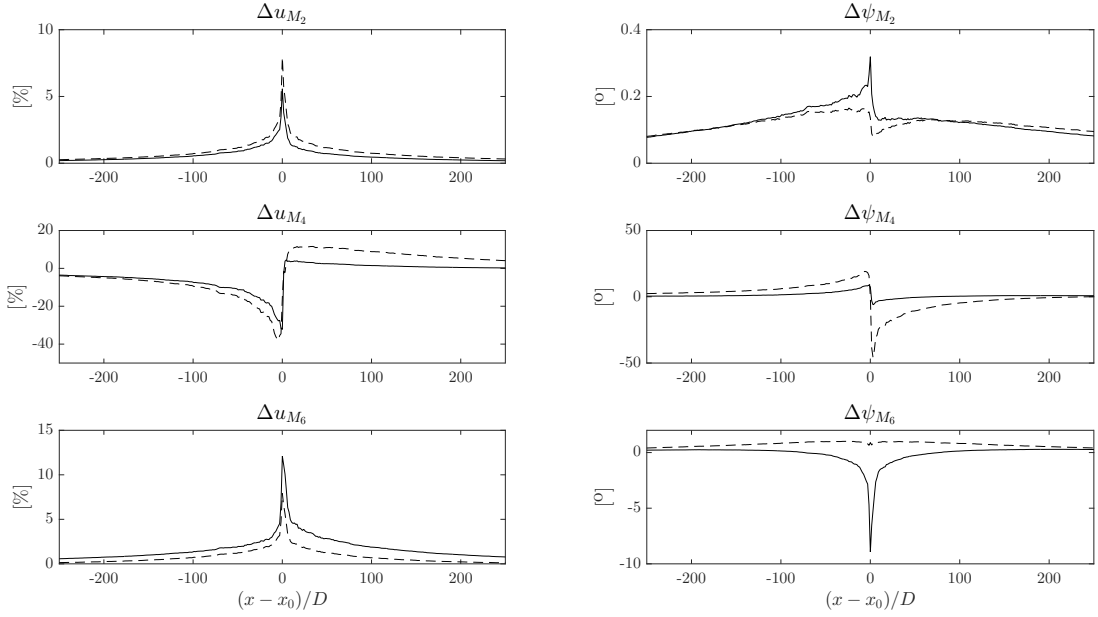
Figure 4.8: Profiles of change in the harmonic analysis between Run-1 and Run-3 (Run-1 minus Run-3) (solid line) and between Run-1 and Run-2 (dashed line), along $y = -10$ m, i.e. through the centre of the turbine. Along channel distances normalised by the turbine diameter D and defined so that 0 is the channel centre. Left column – change in amplitude of current velocity, right column – change in phase of current velocity, top row – M_2, middle row – M_4, bottom row – M_6.

In order to look at this in more detail, estimates of the size of the non-linear terms from the 1D governing equations were made using the model output. Figure 4.10 shows the mesh in the immediate vicinity of the turbine. The turbine location is denoted by the bold red line, located within the element highlighted in red. The two elements highlighted in blue were used in the calculation of the size of the Continuity Term (CT) and Advection Term (AT) east and west of the turbine. These calculations used the x-locations of the element centres, x_1, x_2 and x_T, and the values of $\hat{u}$ and η in these elements, $\hat{u}_1$, $\hat{u}_2$, $\hat{u}_T$, η_1, η_2 and η_T, also given at the element centres. The two terms were estimated as follows:

$$\frac{\partial(\eta\hat{u})}{\partial x} \sim \frac{\eta_T u_T - \eta_{1,2} u_{1,2}}{x_T - x_{1,2}} \tag{4.3.1}$$

$$\hat{u}\frac{\partial\hat{u}}{\partial x} \sim u_T \frac{u_T - u_{1,2}}{x_T - x_{1,2}} \tag{4.3.2}$$
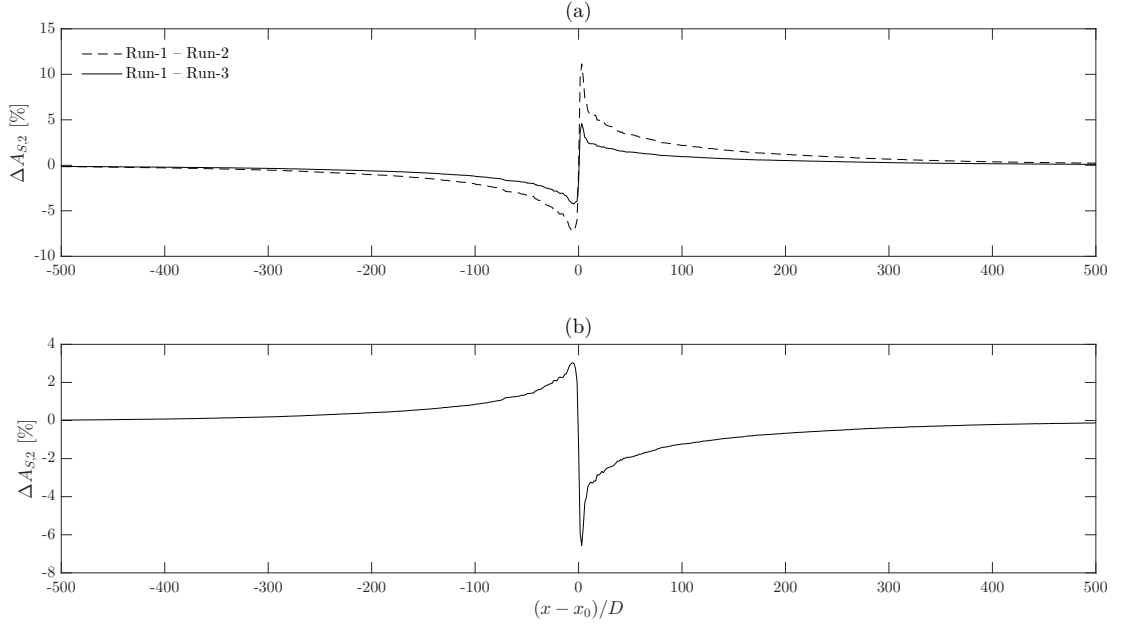
Figure 4.9: (a): profiles of change in $A_{S,2}$ between Run-1 and Run-2 (dashed line) and Run-1 and Run-3 (solid line) along $y = -10$ m between $(x - x_0) = \pm L/8$. (b): profile of change in $A_{S,2}$ between Run-2 and Run-3 (Run-2 minus Run-3) along same profile. Along channel distances normalised by the turbine diameter D and defined so that 0 is the channel centre.

Time-series of these estimates over the model run, for Run-1 (R1), Run-2 (R2) and Run-3 (R3) are plotted in Figure 4.11. The quadratic and elevation parts of the friction and turbine terms were estimated in a similar fashion, except none of these terms involved a gradient, and as such they were calculated only in the element containing the turbine. These terms were estimated as follows:

$$\frac{C_F}{h}\hat{u}|\hat{u}| \sim \frac{C_F}{h}u_T|u_T| \tag{4.3.3}$$

$$\frac{C_F}{h^2}\eta\hat{u}|\hat{u}| \sim \frac{C_F}{h^2}\eta_T u_T|u_T| \tag{4.3.4}$$

$$\frac{1}{2}\varepsilon_0 C_T\hat{u}|\hat{u}| \sim \frac{1}{2}\varepsilon_0 C_T u_T|u_T| \tag{4.3.5}$$

$$\frac{\varepsilon_0 C_T}{2h}\eta\hat{u}\hat{u} \sim \frac{\varepsilon_0 C_T}{2h}\eta_T u_T|u_T| \tag{4.3.6}$$

Time-series of the estimates of these terms over the model run time are presented in Figure 4.12 for R1, R2 and R3.
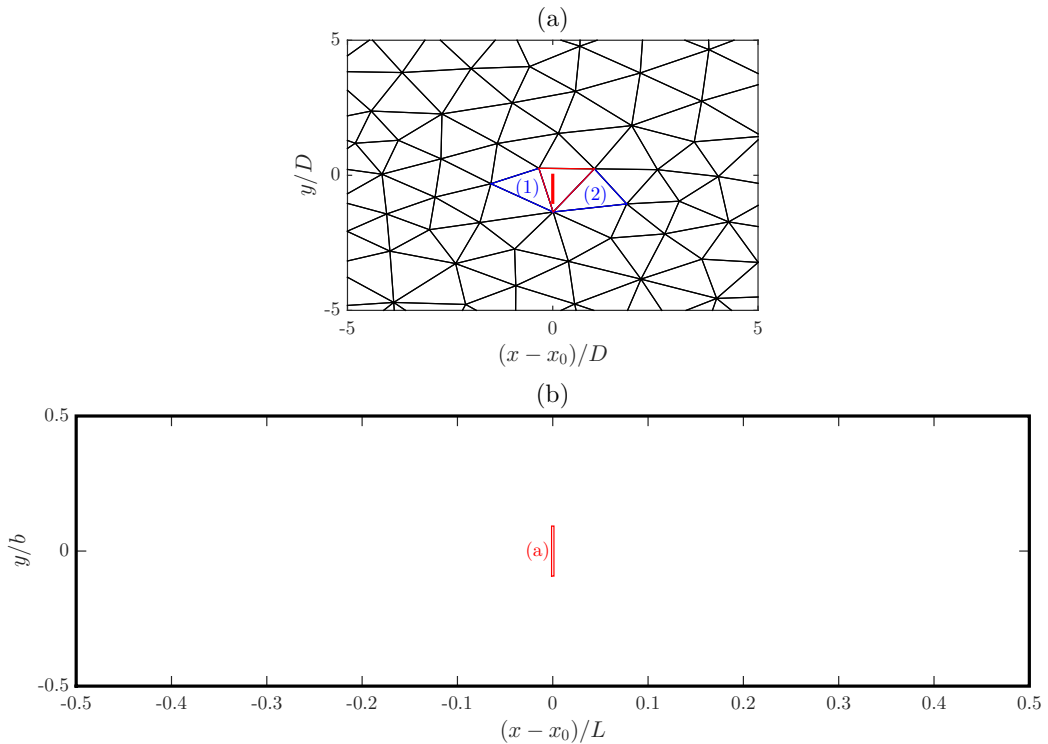
Figure 4.10: (a): Elements used in the estimation of the non-linear terms. Red element contains the turbine (location denoted by bold red line) and blue elements used in the calculations of spatial gradients in advection and continuity terms. (b): Location of snapshot of mesh in the channel, red box is the extent of (a).

The first thing apparent from Figure 4.11 is that in the two runs containing the turbine term both the AT and CT were much larger. This was most likely the result of the velocity gradients resulting from the operation of the turbine. In the expansions of these terms, (2.2.11) and (2.2.12), the first even overtide was introduced, in this case the M_4, meaning that indirectly the turbine was resulting in the generation of the M_4, i.e. the turbine operation impacted the AT and CT which impacted the M_4. Secondly, to the west of the turbine both the AT and CT grow large during the flood tide, and to the east they grow large during the ebb tide. This offers a potential explanation for the pattern of increases in asymmetry to the west and decreases to the east seen in the profiles of $\Delta A_{S,2}$ and $\Delta A_{S,1}$.
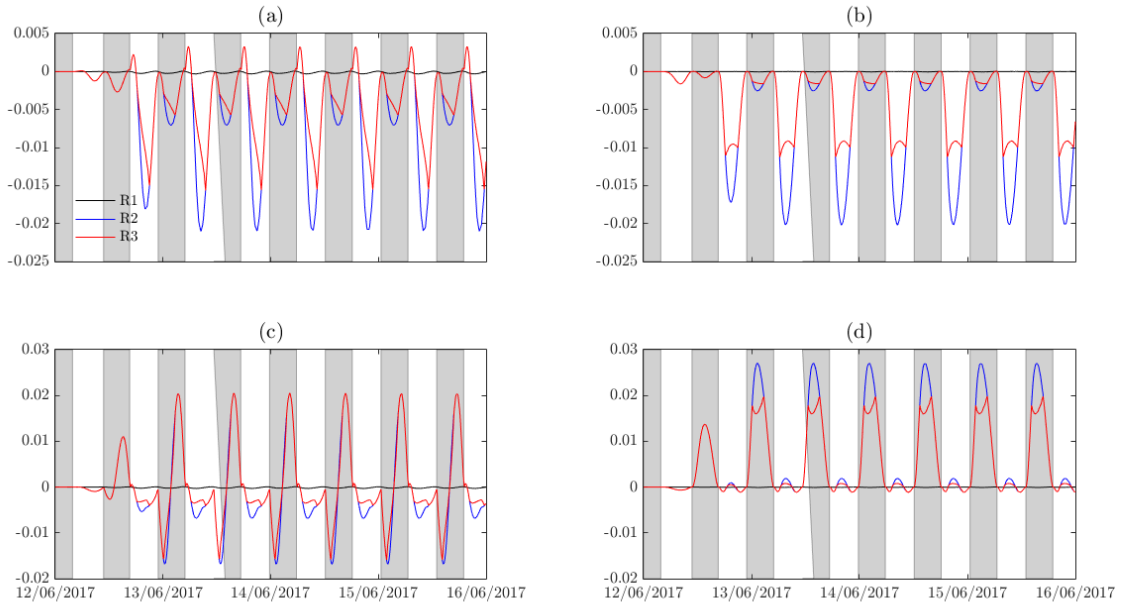
Figure 4.11: Time-series of estimates of size of advection term (right column) and continuity term (left column) to the west (top row) and east (bottom row) of turbine for Run-1 (black), Run-2 (blue) and Run-3 (red). Shaded areas mark times of ebb and unshaded areas times of flood

In Figure 4.12 attention shifts to the friction and turbine terms. When the turbine was deployed, both the quadratic and elevation elements of the friction term were reduced with less effect when a variable-C_T turbine was deployed. This was the result of the reduction in the velocity due to the turbine, and the smaller effect for the variable-C_T turbine was due to the turbine not operating at low velocities, and operating less efficiently at higher velocities, as discussed previously. This smaller effect can be seen in the time-series for the Quadratic Friction Term (QFT) where the peaks for Run-3 are larger than for Run-2. The flood-ebb shading has also been included in this figure despite the sign indicating flood and ebb cycles for the QFT and Quadratic Turbine Term (QTT) as the directionality of the Elevation Friction Term (EFT) and Elevation Turbine Term (ETT) deviates from the flood-ebb cycle (see Chapter 3 for definition of these terms).
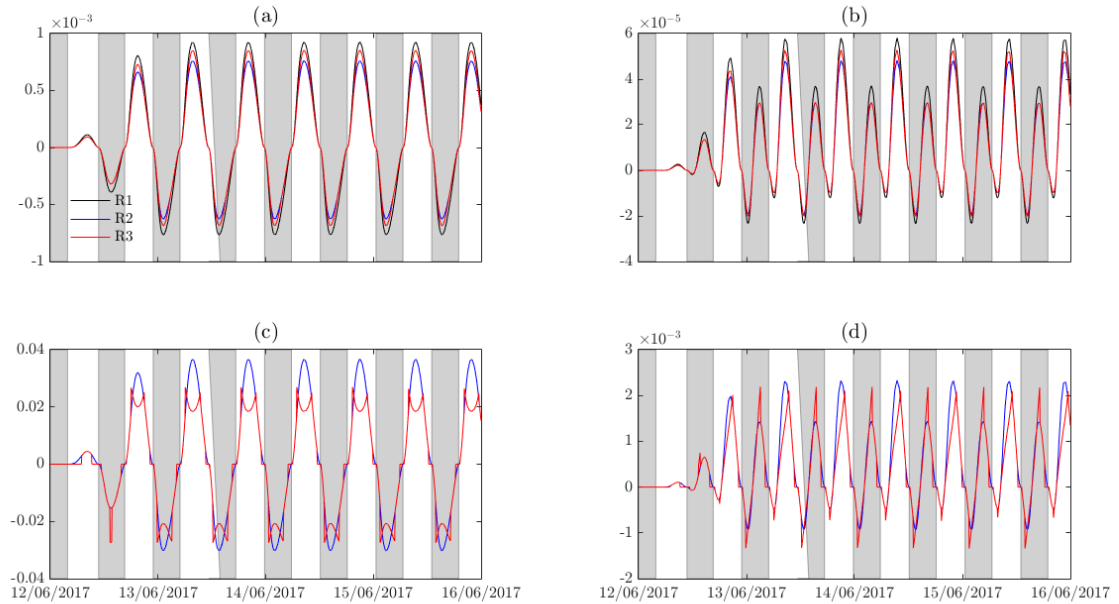
Figure 4.12: Time-series of estimates the quadratic friction term (a), elevation friction term (b), quadratic turbine term (c) and elevation friction term (d) for Run-1 (black), Run-2 (blue) and Run-3 (red) in the element containing the turbine. Shaded areas mark times of ebb and unshaded areas times of flood.

The peaks for the EFT and ETT were also larger in Run-3 compared to Run-2 which is of significance as these terms introduce even overtides. However, the difference was small, and these terms remain at least an order of magnitude smaller than the AT and CT which also introduce the first, even overtide. Also, the ETT, the larger of the two terms only exists in the presence of turbines, and so will only exist in the cell containing the turbine. Given the extent of the changes to the M_2 and its overtides, it is physically intuitive that the turbine indirectly causes these changes by introducing a wake, and therefore steep velocity gradients, rather than directly generates these overtides. The QFT was larger for Run-3 than Run-2 at its peak values which may explain the larger M_6 amplitude seen in this run (Figure 4.8e). In Run-1 there is no QFT or EFT as there are no turbines in the channel, thus with the addition of the turbines these terms grew from 0 to $\mathcal{O}(10^{-2})$ and $\mathcal{O}(10^{-3})$ respectively. The growth of the QFT is of the same order as the growth in the AT and , with the growth in the EFT an order of magnitude smaller. Therefore, it is the QFT to which the local change to the M_2 and M_6 tides is attributed, as

the expansion of this term, (2.2.13), shows it is these tides that the QFT impacts upon.
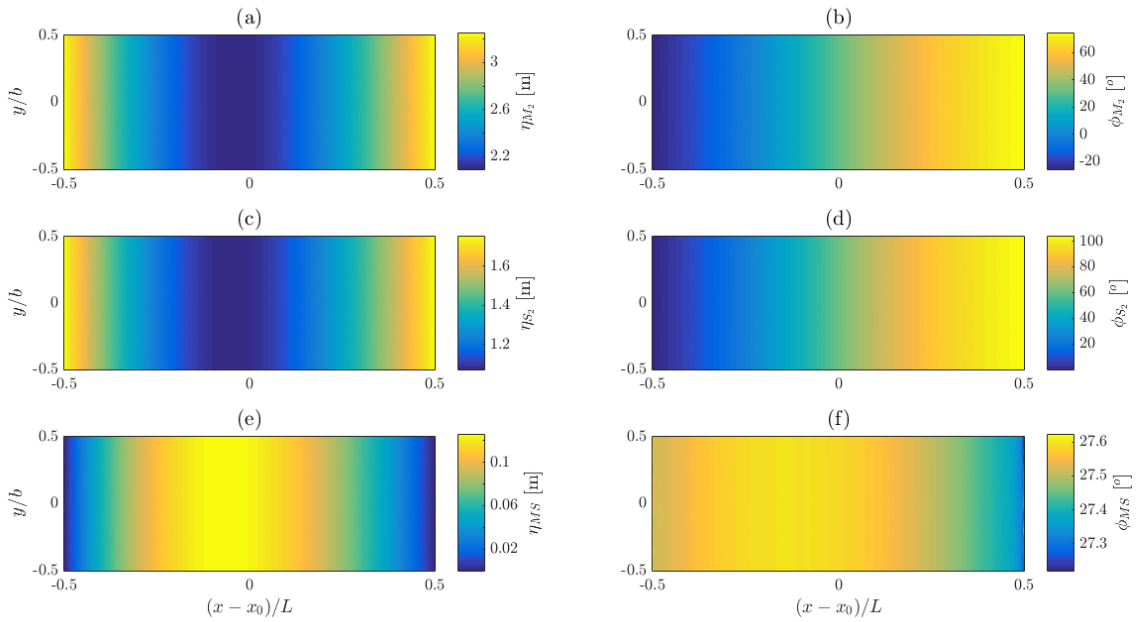
Figure 4.13: Results of harmonic analysis of the surface elevation for Run-4. Distances normalised as in Figure 3.24. First row – M_2, second row – S_2, third row – MS, first column – amplitude, second column – phase.
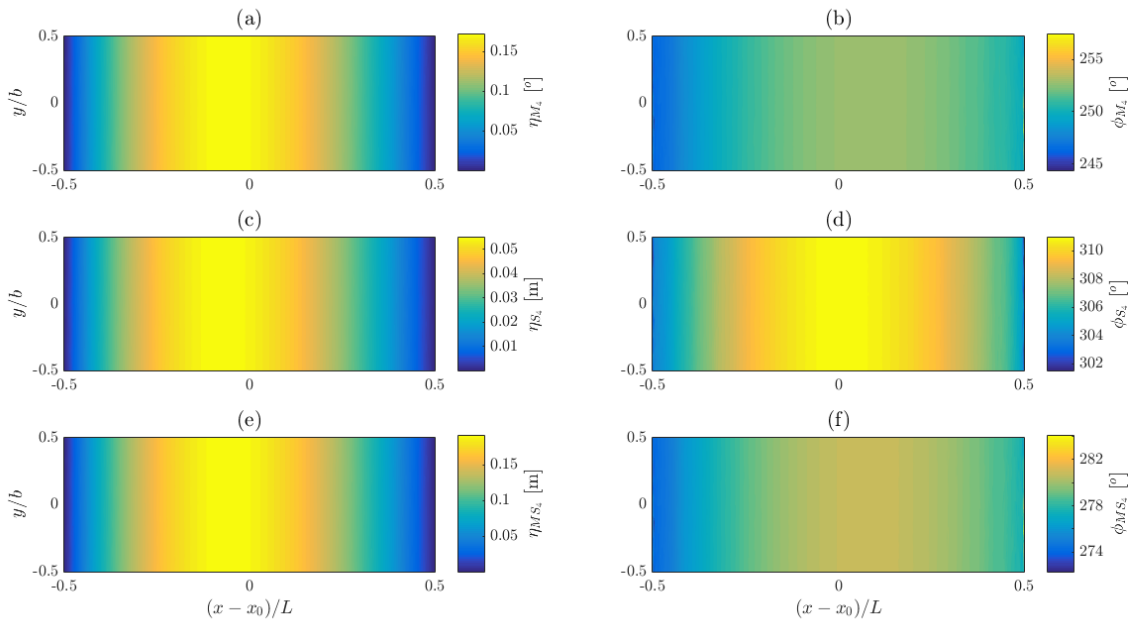
Figure 4.14: As Figure 4.13 but first row – M_4, second row – S_4, third row – MS_4.
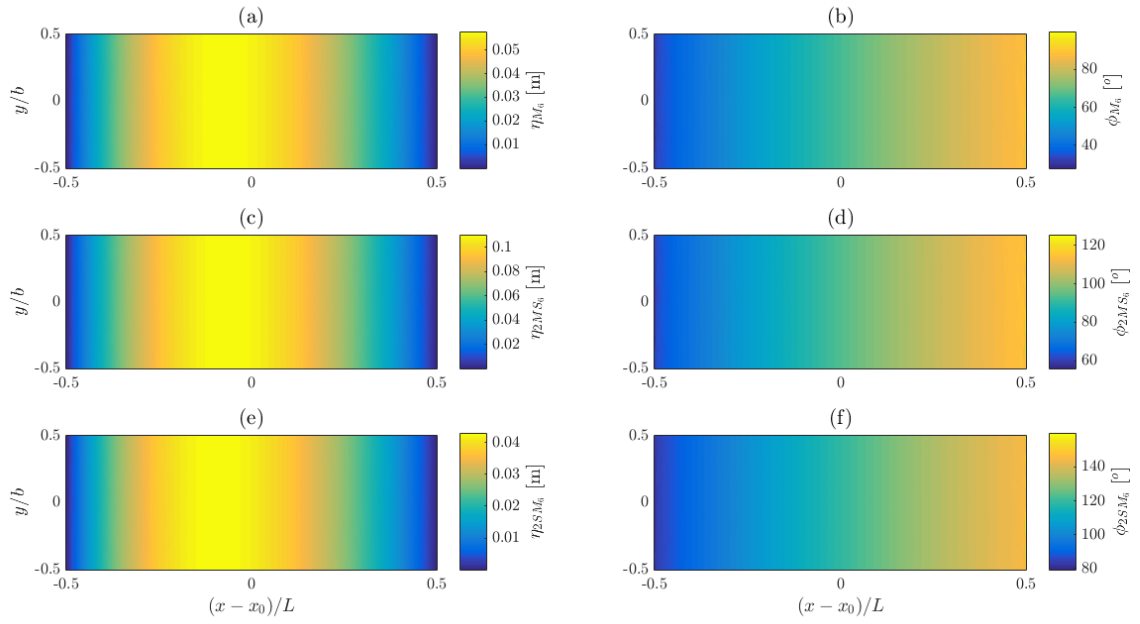
Figure 4.15: As Figure 4.13 but first row – M_6, second row – $2MS_6$, third row – $2SM_6$.
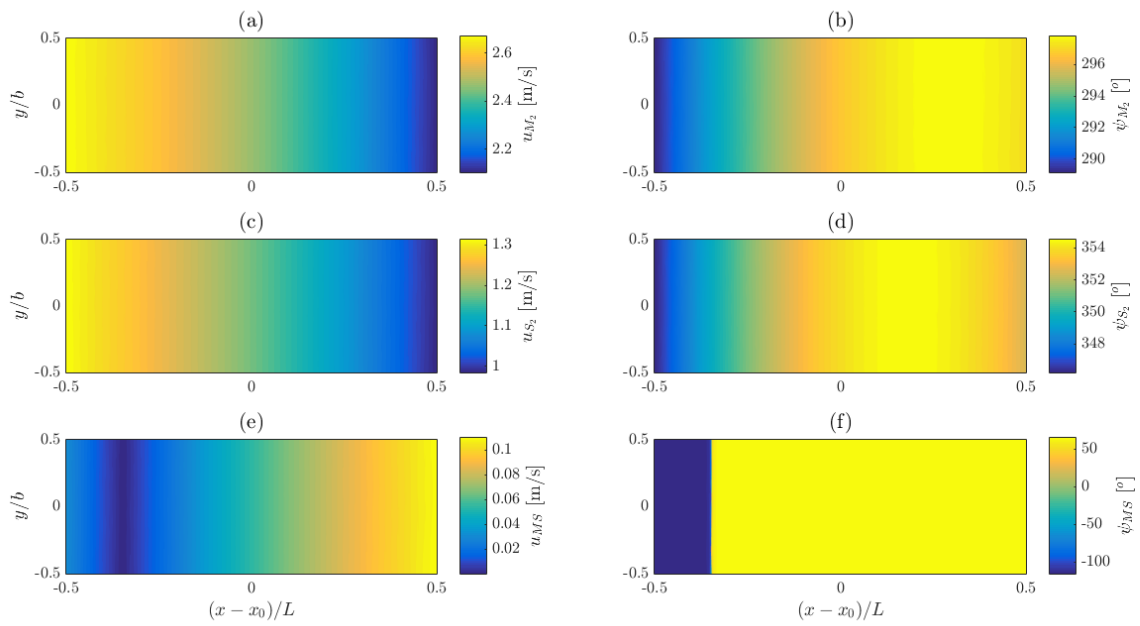
Figure 4.16: As Figure 4.13 but for u-velocity.
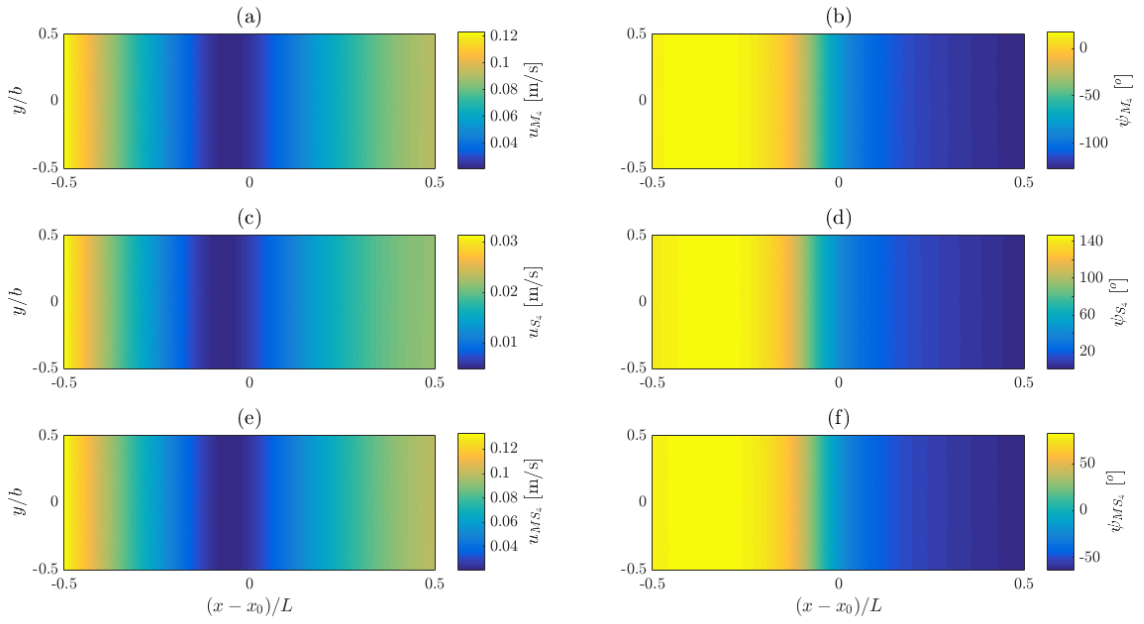
Figure 4.17: As Figure 4.14 but for u-velocity.
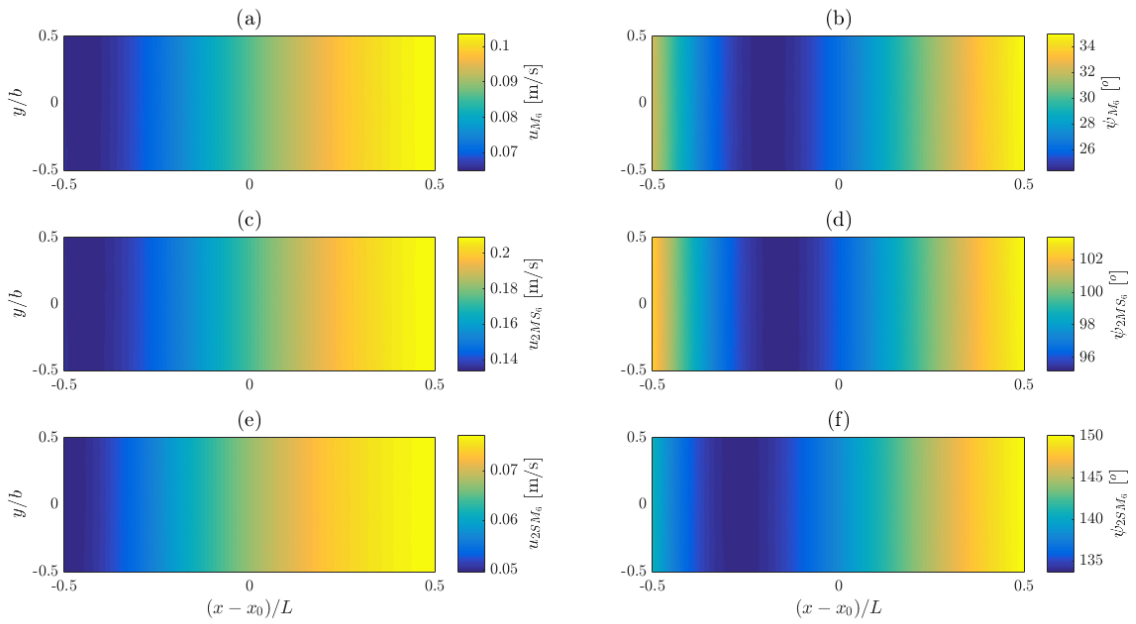
Figure 4.18: As Figure 4.15 but for u-velocity.

4.4   Experiment 3: Effect of Variable-C_T Turbine on Compound Tides

4.4.1   Results

The results of the harmonic analysis of the output from Run-4, an unoccupied channel forced by the M_2 and S_2 tides are presented in Figures 4.13–4.18. In the analysis of Run-4 (and Run-5) output, 9 constituents were identified: the M_2, M_4 and M_6, as seen in the previous runs, the S_2, the second forcing tide, and the S_4, MS_4, MS, $2MS_6$ and $2SM_6$. The first of these is an overtide of S_2 and the remainder are compound tides of the M_2 and S_2. These constituents have been grouped according to frequency for plotting, the quarter-diurnal tides (M_4, S_4 & MS_4: Figures 4.14 & 4.17) together and the sixth-diurnal tides (M_6, $2MS_6$ & $2SM_6$: Figures 4.15 & 4.18) together and the low-frequency MS tide together with the two forcing diurnal tides (M_2 & S_2: Figures 4.13 & 4.16). The latter of these groupings is a grouping of convenience rather than a grouping chosen because the results are expected to be comparable.

Figures 4.13–4.15 present the results of the harmonic analysis of the surface elevation. In terms of the pattern of the results, for the amplitude, the two forcing tides showed a similar pattern, maxima at either boundary and minima near the centre, and the remaining tides showed a similar pattern of minima at either boundary and maxima near the centre. There was a slight phase difference between the three tides. For the two forcing tides and the three sixth-diurnal tides, phase increases from west to east were seen. For the remaining tides there were phase minima either side and maxima towards the channel centre, although the variation of phase along the channel was small.

Figures 4.16–4.18 present the results of the harmonic analysis of the current velocity. As for the surface elevation, similar patterns of amplitude and phase across the channel were seen for the diurnal, semi-diurnal, quarter-diurnal and sixth-diurnal constituents, as described above.

The change to the amplitude and phase of the constituents of the current velocity with the addition of a turbine are presented in Figures 4.19–4.21 as profiles

along $y = -10$ m between $(x - x_0) = \pm L/16 = \pm 250D$, and in Figures 4.22–4.24 as $2D$ plots covering the area surrounding the turbine.
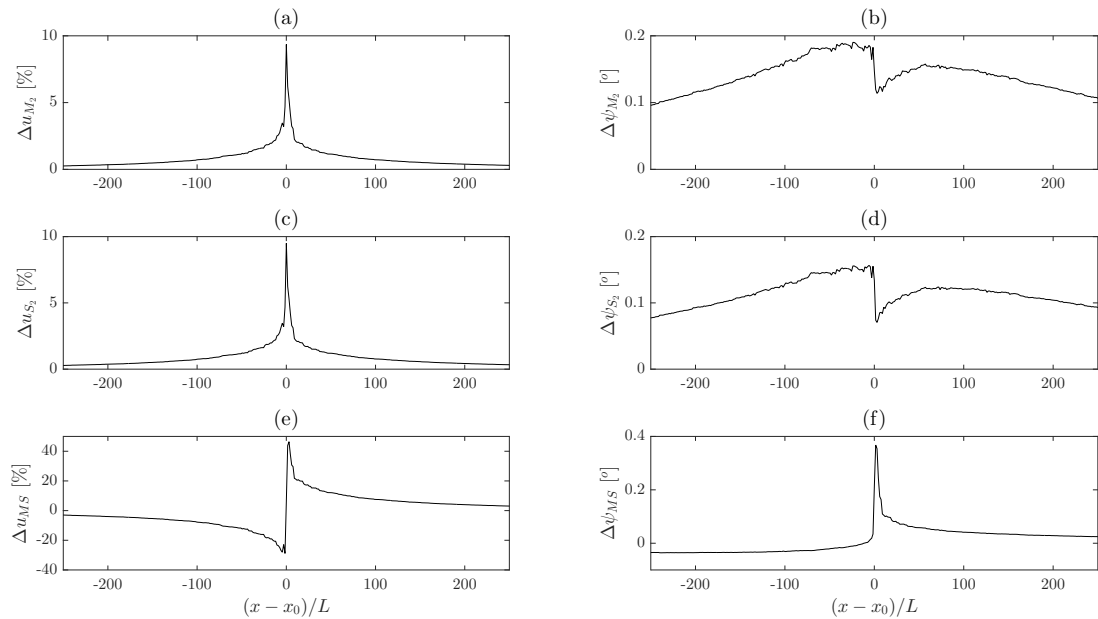
Figure 4.19: Profiles of change in the harmonic analysis between Run-4 and Run-5 (Run-4 minus Run-5) along $y = -10$ m. Distances normalized as in Figure 4.3. First row – change in amplitude of current velocity, second row – change in phase of current velocity, first column – M_2, second column – S_2, third column – MS.

The patterns of change in Figures 4.19–4.21 again show similarity between tides, as in the contour plots from Run-4 (Figures 4.13–4.18). Both the forcing tides had a sharp reduction peak for the amplitude, centred around the turbine, with a similar sized peak, in percentage terms, for each of the tides (Figures 4.19a & 4.19c). The pattern of change to the phase was also similar for both tides, as was the size of the change (Figures 4.19b & 4.19d). The pattern of change to the amplitude of the MS (Figure 4.19e) more closely resemble the patterns seen for the M_4 and MS_4 tides (Figures 4.20a & 4.20e) than the diurnal tides, with larger changes nearer the turbine and smaller changes moving away from the turbine in either direction. The pattern of change to the phase of the MS was unique to this tide, with a sharp reduction peak centred around the turbine, with a small overall increase to the west and a small overall decrease to the east (Figure 4.19f). The M_4 and MS_4 tides showed similar patterns of change for the amplitude and

phase (Figures 4.20a, 4.20b, 4.20e & 4.20f). For the S_4 amplitude there was an augmentation peak centred around the turbine (Figure 4.20b). The phase of the S_4 (Figure 4.20d) follows a more similar pattern to the other phase changes but with greater symmetry between the augmentation and reduction (whereas the M_4 and MS_4 phase changes saw much larger augmentation than reduction). Finally, the pattern of change to both the amplitude and the phase of the sixth-diurnal tides was very similar across all tides (Figure 4.21). The2D plots of change to the current constituents (Figure 4.22–4.24) tell a similar story to the proiles (Figures 4.19–4.21).
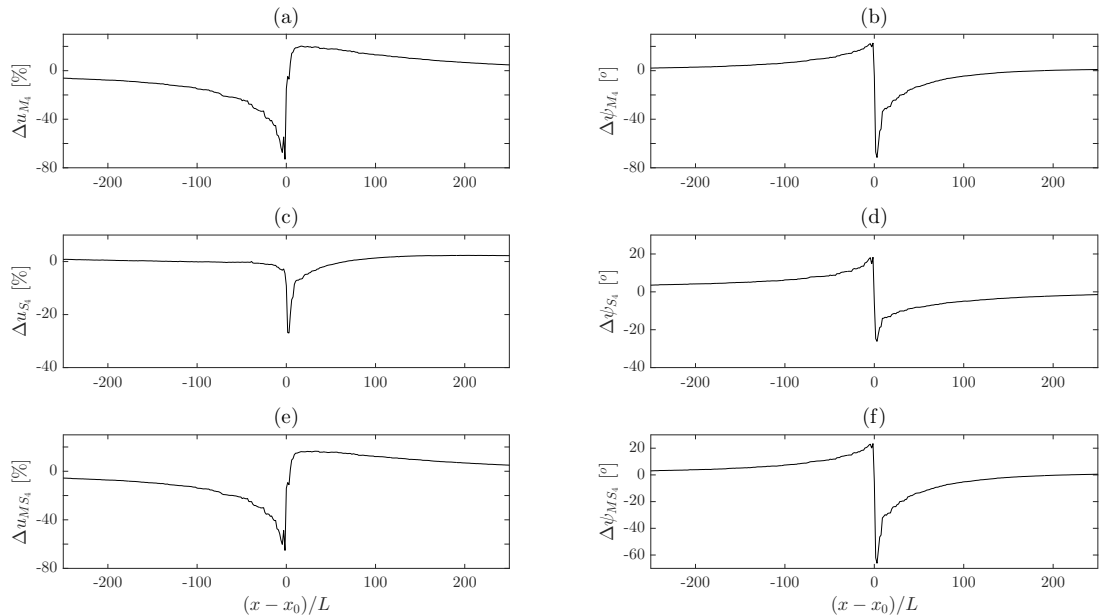
Figure 4.20: As Figure 4.19 but first column – M_4, second column – S_4, third column – MS_4.

4.4.2   Discussion

The primary finding of this experiment is that there is some similarity in the effect of the interaction between the turbine and the tides within the same frequency bands, i.e. the pattern of change to the M_2 is similar to the pattern of change to the S_2 and the pattern of change to the M_4 is similar to the MS_4. However, the pattern of change to the S_4 differed from the pattern of change to the M_4. This means that inference of the kind of change one might see in tides not included in

the experiment above, e.g. N_2, K_2 MN_4, $2MN_6$, etc. may not be possible. There was however a high degree of similarity across the M_4 and MS_4 and the M_6, $2MS_6$ and $2SM_6$.
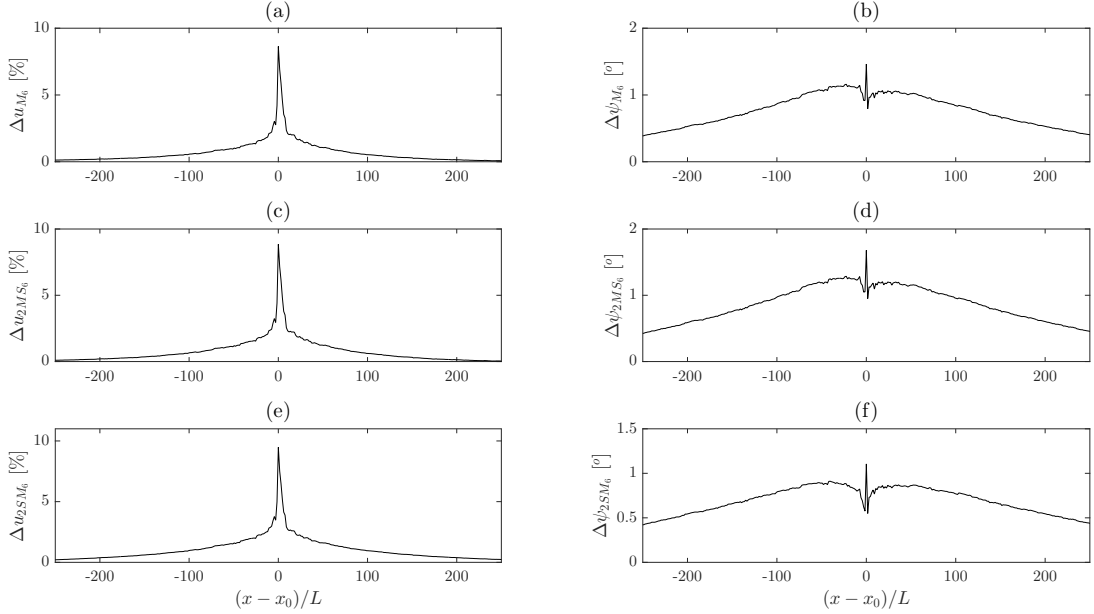
Figure 4.21: As Figure 4.19 but first column – M_6, second column – $2MS_6$, third column – $2SM_6$.

This similarity is most likely an indication of the similar origins of these changes. In expansion (2.2.26) (Chapter 2, §2.2) it was seen that the QFT and QTT introduce the M_6, $2MS_6$ and $2SM_6$, and the change in these three constituents, with the addition of a turbine, was similar, along with the change to the M_2 and S_2, which is also accounted for in these expansions. Additionally, the change was local to the turbine. These two facts, along with Figure 4.12, which shows the change in the QTT to be the larger than the change in the QFT between Run-1 and Run-2 are good evidence that it is the change in the QTT that accounts for the change in these constituents.

In expansions (2.2.24), (2.2.25) and (2.2.27) (Chapter 2, §2.2) it was seen that the CT, AT, EFT and ETT all introduce the M_4, S_4, MS_4 and MS constituents. The effect of the ETT will be local to the turbine and the changes seen to these constituents are further reaching than the changes to the M_6, $2MS_6$ and $2SM_6$ (compare Figure 4.20 and Figure 4.21). The change in the ETT between Run-1

and Run-2 was negligible compared to the change in the AT and CT (compare Figure 4.11 and 4.12). This is good evidence that it is the change to the AT and CT resulting from the introduction of steep velocity gradients in the turbine wake is the cause of the change to the M_4, S_4, MS_4 and MS.
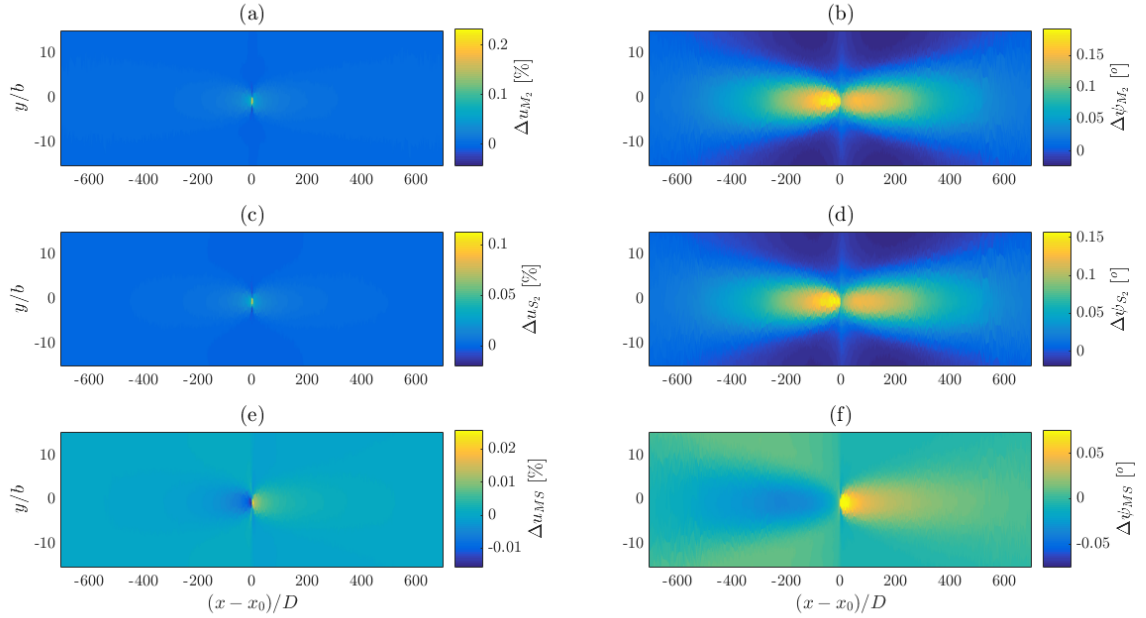
Figure 4.22: Plots of the change in the results of the harmonic analysis of the current velocity between Run-4 and Run-5 (Run-4 minus Run-5) across the area surrounding the turbine. Distances normalised as in Figure 4.4 and area spans that of Figure 4.4. First row – M_2, second row – S_2, third row – MS, first column – amplitude, second column – phase.

The addition of the S_2 introduced the spring-neap cycle to the system. This leads one to question whether there is a difference in the flood-ebb asymmetry between spring and neap tides, and, whether there is a difference in the effect of the turbine on the asymmetry between spring and neap tides. From Figure 4.25 one can see that the answer to both of these questions is yes. The asymmetry was smaller towards the neap tide and larger towards the spring tide (Figure 4.25a), and likewise the effect of the turbine on the asymmetry (Figure 4.25c). In this figure the time-series was split into 1-day bins and the asymmetry calculated using (4.2.1) for Run-4 and Run-5. From inspection of the time-series one can see that due to the spring neap cycle the amplitude of the tide reduces/increases from one

day to the next, this effect will also occur from one tidal cycle to the next, and even from flood to ebb, which will impact on the asymmetry. As for the difference in the effect of the turbine, if one considers that the effect of the turbine depends on u, and that u is smaller at neap tides and larger at spring tides, then it follows that the effect of the turbine will also be smaller at neap tides and larger at spring tides.
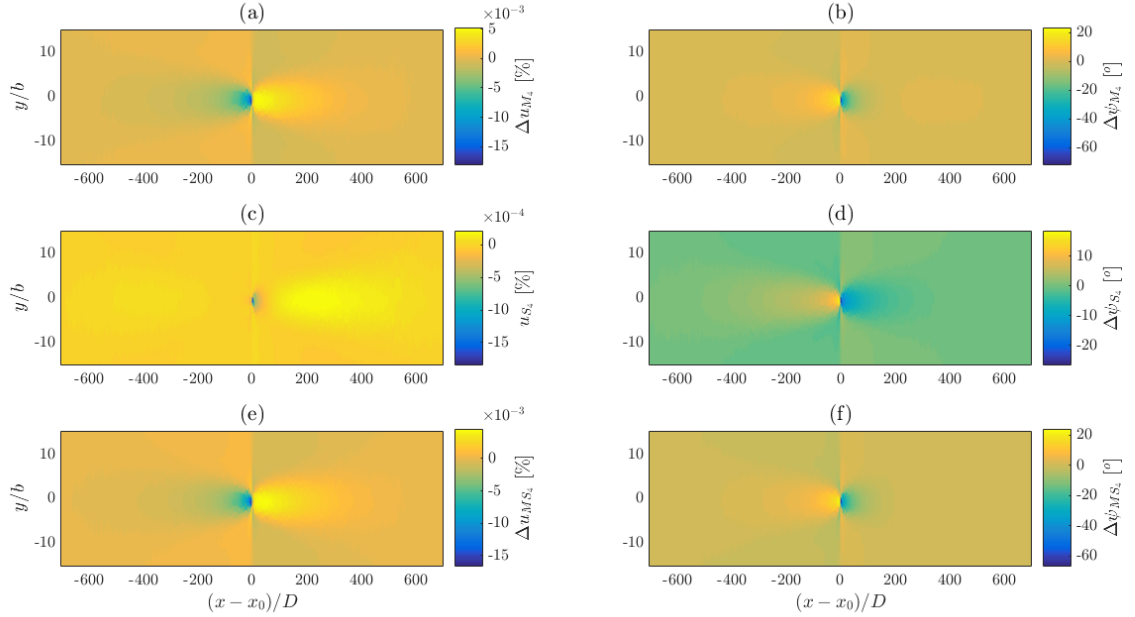
Figure 4.23: As Figure 4.22 but first row – M_4, second row – S_4, third row – MS_4.

The calculation of flood-ebb asymmetry for the 1-day bins was repeated for the whole model area. In Figure 4.26a the profile of the average of the asymmetry across these 1-day bins along the channel length is presented, along with the standard deviation, which is given by the amplitude of the envelope. The width of the envelope therefore indicates the spring-neap variability of ambient tidal asymmetry, (a), and impact the turbine has on the asymmetry, (b). The mean of $A_{S,2}$ in this figure looks very much like $A_{S,2}$ from Figure 4.5a, i.e. the average $A_{S,2}$ over the spring neap cycle for Run-4 is similar to Run-1. The variability of the envelope, or the magnitude of the temporal variation, along the channel shows the largest variability to be near either boundary and the smallest variability at around $(x - x_0) = -L/8$. Figure 4.26b presents the mean and standard deviation of the change to $A_{S,2}$ with the deployment of a turbine in a similar fashion. In this

case, the largest temporal variation was seen near the turbine where the largest mean changes were seen.
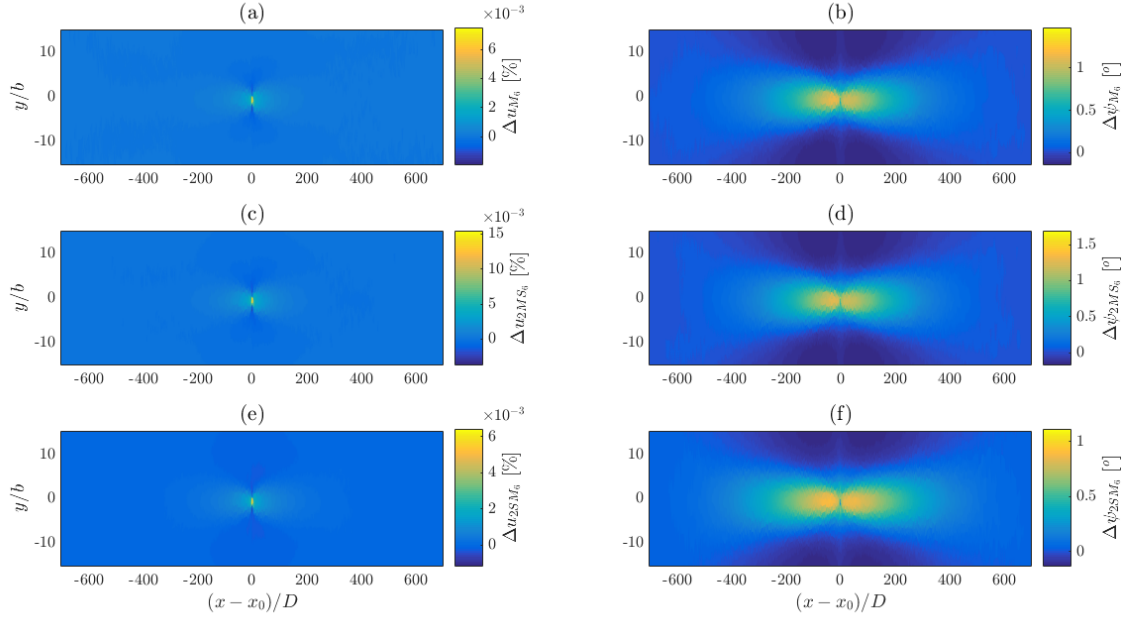
Figure 4.24: As Figure 4.22but first row – M_6, second row – $2MS_6$, third row – $2SM_6$.

The inclusion of the S_2 in the model and therefore the introduction of S_4, MS_4, and the spring-neap cycle means that $A_{S,1}$ will no longer be as good a representation of the asymmetry as in the M_2-only runs as none of these new elements are included in $A_{S,1}$, whilst all will impact on the asymmetry. As an illustration, profiles of mean $A_{S,2}$ and mean $\Delta A_{S,2}$ are presented along with profiles of $A_{S,1}$ and $\Delta A_{S,1}$ in Figure 4.27. The patterns of mean $A_{S,2}$ (Figure 4.27a) and mean $\Delta A_{S,2}$ (Figure 4.27c) are no longer reproduced in $A_{S,1}$ (Figure 4.27b) and $\Delta A_{S,1}$ (Figure 4.27d) as was the case in the M_2-only runs. Equation (4.2.1) requires modification to include the impact of S_2, S_4, and MS_4. Equation (4.2.1) was modified as follows:

$$A_{S,1}{}^* = \frac{u_{M_4}}{u_{M_2}} \cos(2\psi_{M_2} - \psi_{M_4}) + \frac{u_{S_4}}{u_{S_2}} \cos(2\psi_{S_2} - \psi_{S_4})$$
$$+ \frac{2u_{MS_4}}{u_{M_2} + u_{S_2}} \cos(\psi_{M_2} + \psi_{S_2} - \psi_{MS_4})$$
$$+ \frac{2u_{M_6}}{u_{M_2} + u_{M_4}} \cos(\psi_{M_2} + \psi_{M_2} - \psi_{M_6}) \quad (4.4.1)$$
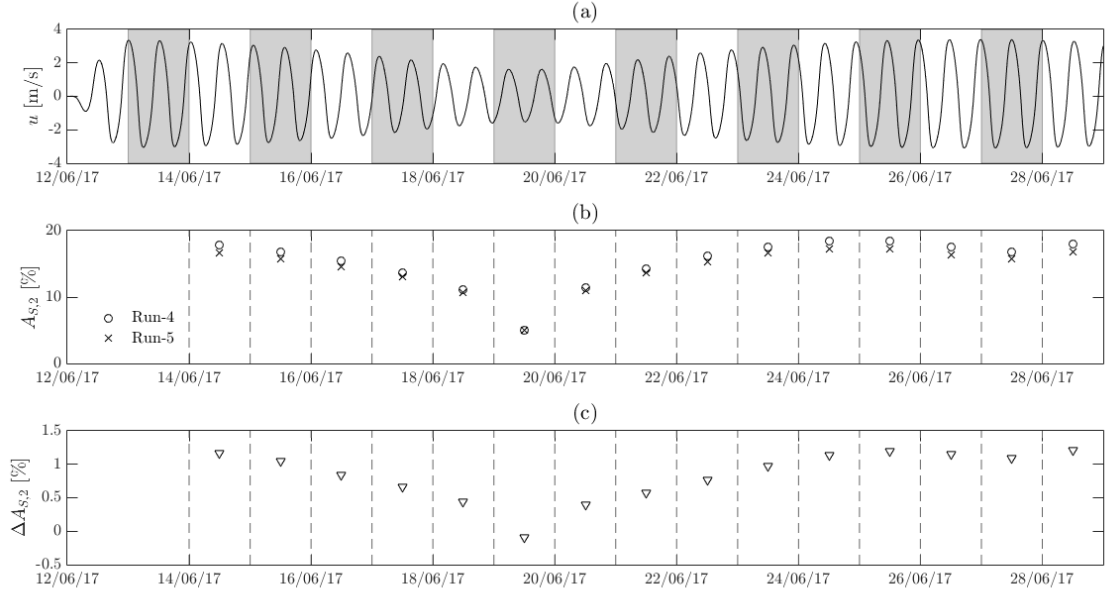
Figure 4.25: (a): Time-series of u from the element containing the turbine for Run-4. Intermediate white and grey shading delineate successive days. (b): Flood-ebb asymmetry calculated using (4.2.2) for a single day, dashed grey lines delineate days, circles are asymmetries calculate for Run-4 and crosses are asymmetries calculated for Run-5. (c): Change in flood-ebb asymmetry between Run-4 and Run-5 for given one-day period.

(in this extension of (4.2.1) the M_2-M_4-M_6 triplet interaction was also included along with the S_2-S_4 pair and M_2-S_2-MS_4 triplet interaction)[2]. Figure 4.28 shows profiles of mean $A_{S,2}$ (Figure 4.28a) and mean $\Delta A_{S,2}$ (Figure 4.28c) along with profiles of $A_{S,1}{}^*$ (Figure 4.28b) and $\Delta A_{S,1}{}^*$ (Figure 4.28d). From a comparison of Figures 4.27 & 4.28 one can see that the modified relationship (4.4.1) gives a more accurate representation of the temporal mean of the asymmetry. This relationship

---

[2]This extension includes all the tidal constituent interactions from the harmonic analysis satisfying the frequency conditions $2\sigma_A = \sigma_B$ and $\sigma_A + \sigma_B = \sigma_C$, and therefore contributing to asymmetry (c.f. Song et al. [2011]). Information on the relative contributions to asymmetry isn't given directly from (4.4.1). One could however repeat the plots in Figures 4.27 & 4.28 for various combinations of the interactions to determine their importance. Given the sizes of the constituents, Figures 4.16 & 4.17, the M_2-S_2-MS_4 interaction will most likely contribute the most to asymmetry after the M_2-M_4. Additionally the role of the M_2-M_4-M_6 triplet interaction is known to be minimal given the reproduction of the $A_{S,2}$ by $A_{S,1}$.

does not however give an indication of temporal variation as seen in Figure 4.26.

Equation (4.4.1) may be written more generally as:

$$A_{S,1}{}^{\dagger} = \sum^{N} \frac{u_j}{u_i} \cos(2\psi_i - \psi_j) + \sum^{M} \frac{2u_m}{u_k + u_l} \cos(\psi_k + \psi_l - \psi_m) \qquad (4.4.2)$$

where N is the total number of cases where the frequency condition $2\sigma_i = \sigma_j$ is satisfied, M is the total number of cases where the frequency condition $\sigma_k + \sigma_l = \sigma_m$, u_i and ψ_i are the amplitude and phase of the constituent i and likewise for the constituents j, k, l and m (cf. Song et al. [2011])[3]. With this form of the expression the effect on the flood-ebb asymmetry of additional semi-diurnal tides that may be of importance, for example the N_2 and K_2, and their related overtides and compound tides may be considered. Likewise, the asymmetry introduced through the interaction of diurnal and semi-diurnal constituents in a mixed tidal regime may also be considered through (4.4.2).

4.5 Summary

In this chapter the results from three experiments have been described. These experiments investigated the effect of a fixed-C_T and variable-C_T turbine on the overtides in a channel forced by the M_2 only and the effect of a fixed-C_T turbine on the overtides and compound tides in a channel forced by both the M_2 and S_2.

These experiments offer confirmation that both augmentation as well as reduction of the quarter-diurnal tides is possible, as predicted from the analytical discussion in Chapter 2 (question *1a)*). The pattern and size (in percentage terms) of the effect was similar for the M_2 and M_6, hinting that the effect on odd tides (i.e. harmonics with odd integer multiples) may be similar. In order to confirm this the analysis would have to look at further odd and even tides, up to M_{12} for 3 odd and 3 even overtides. In practice, however, it is unlikely that tides beyond the sixth-diurnal band will have an important effect on the overall tide. The size of the change to the M_4 was considerably larger than for the other tides which

---

[3]In theory both N and M will equal infinity. In practice however a finite number of interactions will accurately describe the asymmetry.

is important given the dominant role of this tide in flood-ebb asymmetry. The variable-C_T tide had a considerably (up to 59%) smaller effect, which is suspected to be a result of the turbine only operating for 44% of the tidal cycle due to the cut-in speed introduced, compared to 100% for the fixed-C_T turbine.
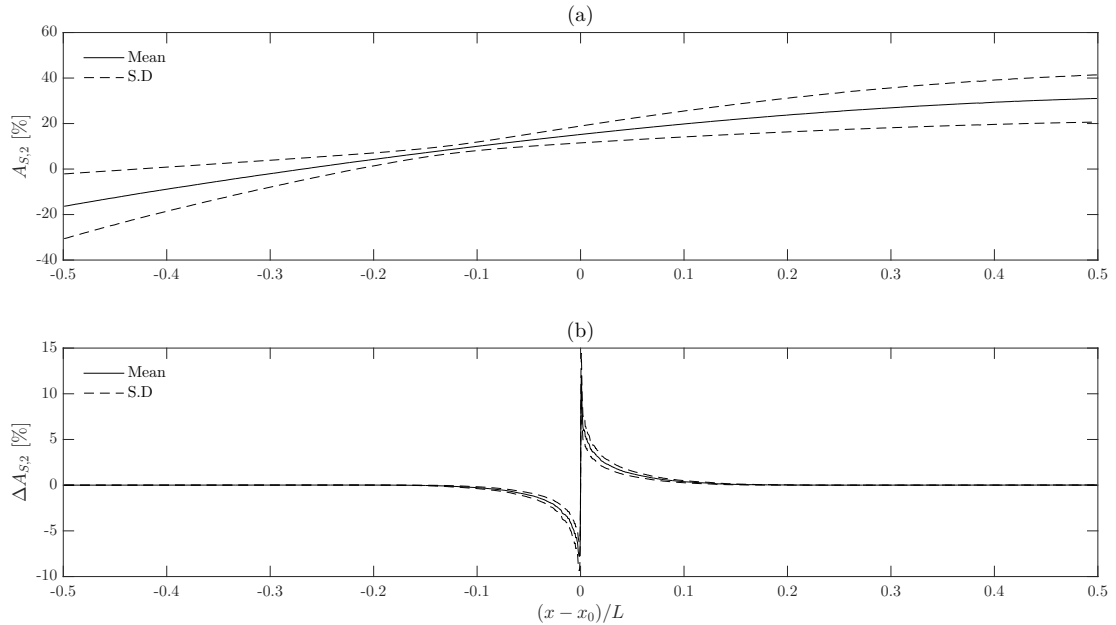
Figure 4.26: (a): Profile of the average flood-ebb asymmetry in current velocity across 1-day bins along channel length (solid line) with an envelope whose amplitude is given by the standard deviation. (b): as above for change to flood-ebb asymmetry. Distance normalised as in Figure 4.3.

From estimations of the non-linear terms in the vicinity of the turbine it is suspected that changes to the advection and continuity term, resulting from the velocity gradients introduced by the turbine wake cause the larger effect on the M_4 compared to the other tides. The changes to the friction terms were negligible and the elevation turbine term introduced in the turbine runs, which would also introduce the M_4 tide, was an order of magnitude smaller than the advection and continuity terms. Also, these two terms are many orders of magnitude larger in Run-2 and Run-3 than in Run-1. Additionally, the turbine terms only exist in the presence of turbines and therefore would only lead to highly local generation (not seen) or reduction (seen for M_2 and M_6). The much larger extent of the changes seen further supports the idea that it is the turbine wakes that lead to the changes

seen to the M_4.

With the addition of the S_2 forcing tide, a further overtide and compound tides were introduced to the discussion. The addition of the S_2 also introduced the spring-neap cycle and with this a variation in the asymmetry over time in the natural case. As a result, a difference in the effect of the turbine over time was seen, namely less asymmetry and a smaller effect of the turbine at the neap tide and more asymmetry and a larger effect of the turbine at spring tide.
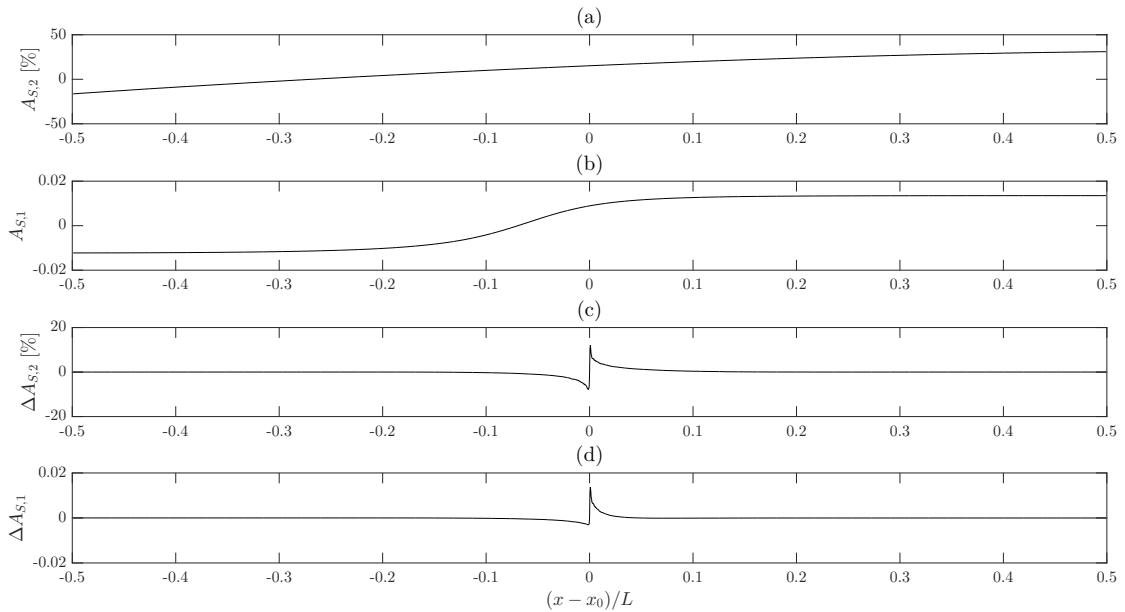
Figure 4.27: (a): Profile of averaged asymmetry from Figure 4.26, (b): profile of (4.2.1) along channel, (c): Profile of change in averaged asymmetry from Figure 4.26, (d): profile of change to (4.2.1) between Run-4 and Run-5 along channel. Distance normalised as in Figure 4.3.

The similarity in the changes to the M_2, S_2, M_6, $2MS_6$ and $2SM_6$ across the runs, along with the estimations of the sizes of the terms that effect these constituents led to the conclusion that it is the introduction of the turbine to the channel that was responsible for the changes to these constituents, through the QTT. Likewise, for the M_4, S_4, MS_4 and MS, it was concluded that it was the changes to the AT and CT resulting from the turbine wake that was responsible for the changes to these constituents. This also explains why the effect was not localised to the turbine.
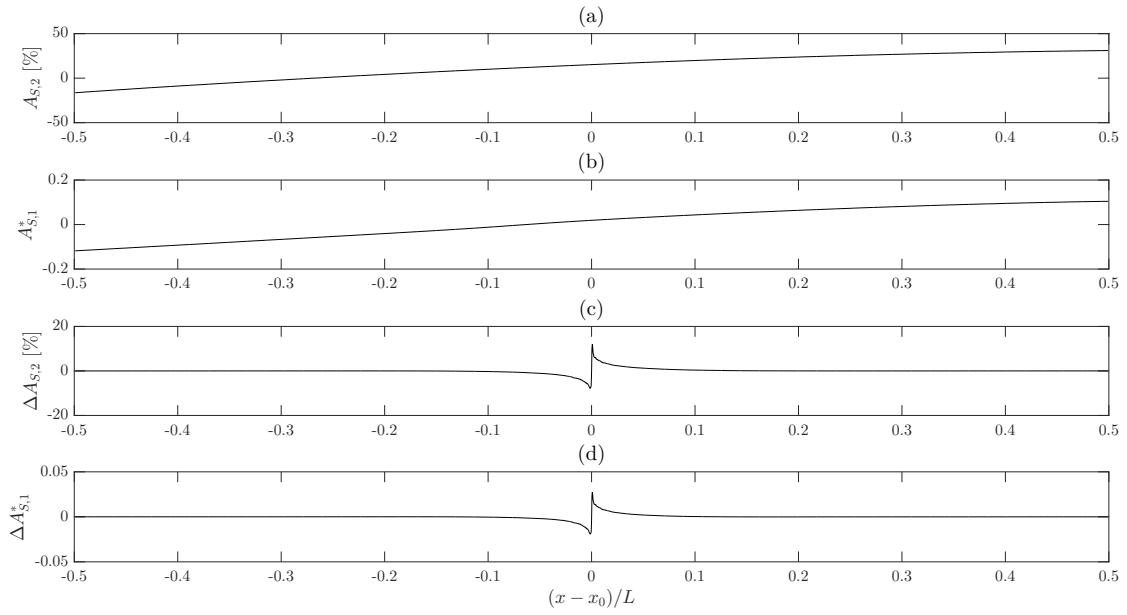
Figure 4.28: (a): Profile of averaged asymmetry from Figure 4.26, (b): profile of (4.4.1) along channel, (c): Profile of change in averaged asymmetry from Figure 4.26, (d): profile of change to (4.4.1) between Run-4 and Run-5 along channel. Distance normalised as in Figure 4.3.

Finally, for the M_2 only runs $A_{S,1}$, given by (4.2.1), was seen to be a useful indicator of flood/ebb dominance and could also indicate the size of the asymmetry through (4.2.3). With the addition of the S_2 equation (4.2.1) may be modified to (4.4.1) to account for the effect of this new tide and its overtides and compound tides, and further generalised to (4.4.2), allowing consideration of forcing due to additional semi-diurnal tides, such as N_2 and K_2, and diurnal tides.

Chapter 5

Effect of Multiple Turbines on Overtides

This chapter introduces the second set of experiments undertaken to address research questions *1c)* and *2c)*, presented in Chapter 2. The experiments are introduced along with the reasoning behind them in §5.1. In §5.2–§5.4 the results from the experiments are presented and discussed. Finally, in §5.5 the findings from these experiments are summarised and conclusions drawn.

5.1 Introduction

Given that a single turbine alters the nature of the tide in an extended area around, and particularly downstream of itself (see Chapter 4), there are likely to be interactions between the effects of multiple turbines. This chapter, therefore, investigates the effects on the tides of multiple turbines arrayed in lines (along the length of a channel) and rows (across the width of a channel). However, the nature of the tides (particularly their asymmetry) varies along the channel length even in the absence of turbines (see Figures 4.1, 4.2 & 4.5a). Firstly, therefore, differences in the impact of single turbines on the tides due to their position along the channel (and therefore the nature of the tidal forcing they experience) are investigated.

Three experiments, which between them explore the effects on tides of multiple turbines, are discussed in this chapter. The first investigates interactions between a single turbine and the tide when the turbine is placed at different positions

along the channel, and therefore experiences different natural tidal forcing. This experiment has been undertaken to address research questions *1c)* and *2c)*. The second considers the effects of multiple turbines deployed in a line along the length of the channel on the tides, and interactions between the effects of each turbine. The third considers the effects of multiple turbines deployed in a row across the width of the channel. Together, these two experiments look to address research questions *1d)* and *2d)*.

In the first experiment, four model runs were carried out. In each one, a single turbine was deployed at the $A_{S,2} = 0$, $A_{S,2} = 0.1$, $A_{S,2} = 0.2$ and $A_{S,2} = 0.3$ contours[1] (see Chapter 4, Figure 4.5). In all four of these runs, the channel was forced by only the M_2 tide and the turbine had a fixed-C_T. The differences amongst these four runs and Run-1, from Chapter 4 (the unoccupied channel), have been calculated to assess the differing effects of the turbine at the four locations.

In the second experiment, nine model runs were carried out. Three of these runs had three turbines deployed in a line along the channel with longitudinal spacings of $\sim 120D$, $\sim 60D$ and $\sim 20D$. The other six runs used only the westernmost and easternmost turbines from the arrays. The largest of these spacings, $120D$, was chosen as at this distance from a turbine, its effect on tidal asymmetry falls below 2% (see Chapter 4). The smallest spacing, $20D$, was chosen as an approximation of the distance of wake recovery based on Malki et al. [2011]. The $60D$ spacing was chosen as an intermediate value. The additional six runs, along with Run-2, from Chapter 4 (the single fixed-C_T run), allowed for comparison between the turbines' individual effects, and their effects within an array.

In the final experiment, five further runs were undertaken with turbines deployed in a row across the channel, with different numbers of turbines and therefore different across-channel spacings. Spacings of approximately $5D$, $4D$, $3D$, $2D$ and $1D$ were used, which correspond to channel width-filling arrays of 9, 10, 13, 17 and 26 turbines respectively. The $1D$ spacing was considered the minimum realistic spacing, and the further spacings were simply integer multiple (of D) increases to the spacing.

---

[1]Where $A_{S,2}$ is a measure of the Flow Velocity Asymmetry (FVA), calculated via (4.2.2) following Neill et al. [2014].

The runs described above a summarised in Table 5.1. Across all runs the model parameters are as outlined in Table 3.1. All runs including turbines use fixed-C_T turbines, implemented as outlined in Table 3.3. Unless stated otherwise the same mesh was uses as illustrated in Figure 3.22, and summarised in Table 3.8. Boundary forcing was M$_2$ only for all runs, using $\eta_1 = 5$ m in (3.1.15) at both boundaries, and $\phi_1 = 0°$ at the left boundary and $\phi_1 = 100°$ at the right boundary.

Table 5.1: Chapter 5 model runs. Line runs marked with a $*$ are runs that simulate turbines from the line runs operating individually.

Run Name	Experiment	No. Turbines	Array Configuration	Turbine Spacing	$A_{S,2}$ Contour
Run-1	1, 2 & 3	0	N/A	N/A	N/A
Run-2	2	1	Line*	N/A	N/A
Run-6	1	1	N/A	N/A	0
Run-7	1	1	N/A	N/A	0.1
Run-8	1	1	N/A	N/A	0.2
Run-9	1	1	N/A	N/A	0.3
Run-10	2	3	Line	$120D$	N/A
Run-11	2	1	Line*	$120D$	N/A
Run-12	2	1	Line*	$120D$	N/A
Run-13	2	3	Line	$60D$	N/A
Run-14	2	1	Line*	$60D$	N/A
Run-15	2	1	Line*	$60D$	N/A
Run-16	2	3	Line	$20D$	N/A
Run-17	2	1	Line*	$20D$	N/A
Run-18	2	1	Line*	$20D$	N/A
Run-19	3	9	Row	$5D$	N/A
Run-20	3	10	Row	$4D$	N/A
Run-21	3	13	Row	$3D$	N/A
Run-22	3	17	Row	$2D$	N/A
Run-23	3	26	Row	$1D$	N/A

5.2   Experiment 1: Effect of Natural Asymmetry Conditions on Turbine Impact

5.2.1   Results

In this experiment, a single turbine was deployed approximately on the contour lines of asymmetry (FVA) from the unoccupied channel run (Run-1), $A_{S,2} = 0, 0.1,$

0.2 and 0.3. However, in order to conduct this experiment a new mesh was required, so that the flow-facing element width, Δy, for the western-most and eastern-most turbine deployments more closely resembled Δy at the more central deployments. The reasoning for the new mesh is discussed further in Appendix F.

The y-coordinates of the turbine deployments remained constant for all turbine placements, at $y = -10$ m, and the x-coordinates used were, $(x - x_0)/L \approx -0.2041$, -0.0790, 0.0660 and 0.2338 $((x - x_0) = -816.5D, -316D, 264D, 935D)$. These coordinates correspond approximately to the $A_{S,2} = 0$, 0.1, 0.2 and 0.3 contours, respectively. The changes to the amplitude and phase of the M_2, M_4 and M_6 along-channel velocity component are presented in Figures 5.1 and 5.2 respectively, and the changes to the FVA ($\Delta A_{S,2}$) presented in Figure 5.3. The changes to the along channel current amplitude in Figure 5.1 are given by the normalized along channel current amplitude change, $\Delta \widetilde{u}$, defined as:

$$\Delta \widetilde{u} = 100 \times \frac{u_0 - u_T}{u_0} \tag{5.2.1}$$

where u_0 is the along channel current amplitude in Run-1 and u_T is the along channel current amplitude in any of the turbine runs. The changes to the phase and FVA are given by:

$$\Delta X = X_0 - X_T \tag{5.2.2}$$

The profiles of change to the M_2 and M_6 amplitude and phase (Figures 5.1a & 5.1c and 5.2a & 5.2c respectively) each show the same pattern as was seen in the fixed-C_T experiment in Chapter 4. The size of the change to the M_2 and M_6 phases appeared reasonably constant across the deployment, with the deployment on the $A_{S,2} = 0.3$ contour perhaps seeing a slightly larger change. Similarly, there was only a small difference in the percentage change to the M_2 and M_6 amplitudes across the 4 deployments. Crucially, there did not appear to be a consistent pattern in the variation of the size of the turbine effect on the M_2 and M_6 amplitude and phase across the 4 deployments.
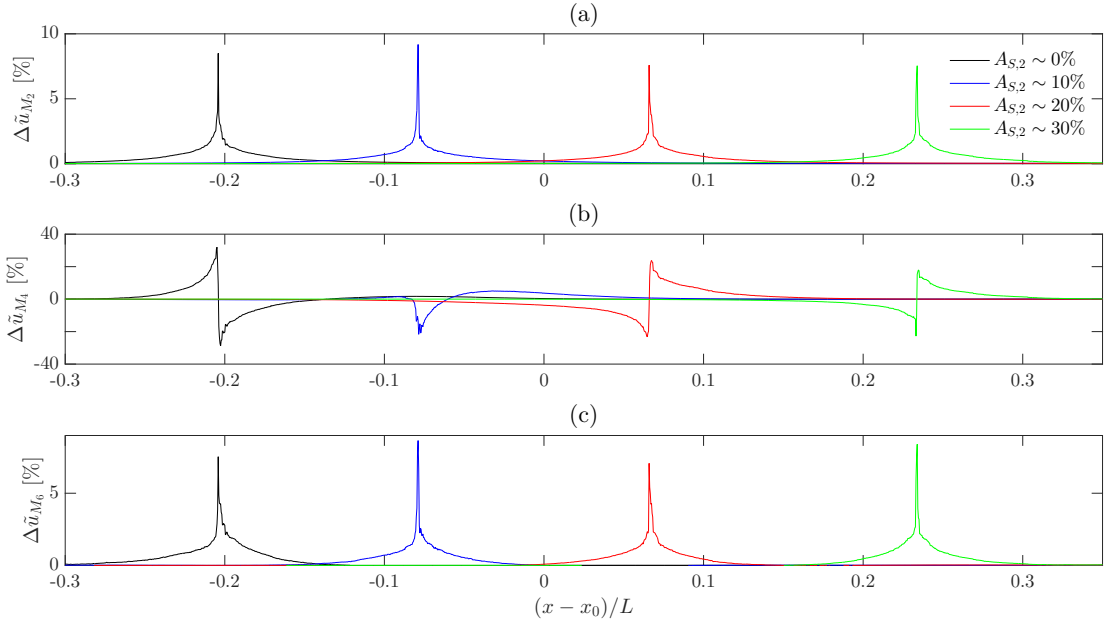
Figure 5.1: Changes to the M_2 [(a)], M_4 [(b)] and M_6 [(c)] current amplitude with the turbine located at the $A_{S,2} = 0$ contour (black), the $A_{S,2} = 0.1$ contour (blue), the $A_{S,2} = 0.2$ contour (red) and the $A_{S,2} = 0.3$ contour (green). Along channel direction normalised by length of channel, L, in such a manner that the channel centre value is 0.

A much more prominent variation in the M_4 amplitude and phase (Figures 5.1b & 5.2b) can be seen across the 4 deployments. The pattern of change to the M_4 amplitude varies across the deployments, with augmentation seen to the east (positive x-direction) and reduction to the west (negative x-direction) for the deployment on the $A_{S,2} = 0$ contour, opposite to the deployments on the $A_{S,2} = 0.2$ and 0.3 contours, and what was seen in the experiments in Chapter 4. For the deployment on the $A_{S,2} = 0.1$ contour the pattern is that of almost entirely reduction. The variation to the pattern of change to the phase of the M_4 across the 4 deployments is much less extreme. In all cases reduction is seen to the west and augmentation to the east, as was the case in the experiments in Chapter 4. In the deployments to the west of the channel centre, on the $A_{S,2} = 0$ & 0.1 contours, the reduction peak is larger than the augmentation peak, and vice-versa for the deployments to the east of the channel centre, on the $A_{S,2} = 0.2$ & 0.3 contours. In terms of the overall size of the changes to the phase the largest change was seen for the deployment on the $A_{S,2} = 0.1$ contour, smaller but roughly

similar sized changes for the deployments on the $A_{S,2} = 0$ & 0.2 contours, and the smallest overall change for the deployment on the $A_{S,2} = 0.3$ contour. The overall size of the change to the M_4 amplitude showed a different pattern, with the smallest and largest changes seen for the deployments on the $A_{S,2} = 0.1$ & 0 contours respectively, with roughly similar sized intermediate changes seen for the deployments on the $A_{S,2} = 0.2$ & 0.3 contours.
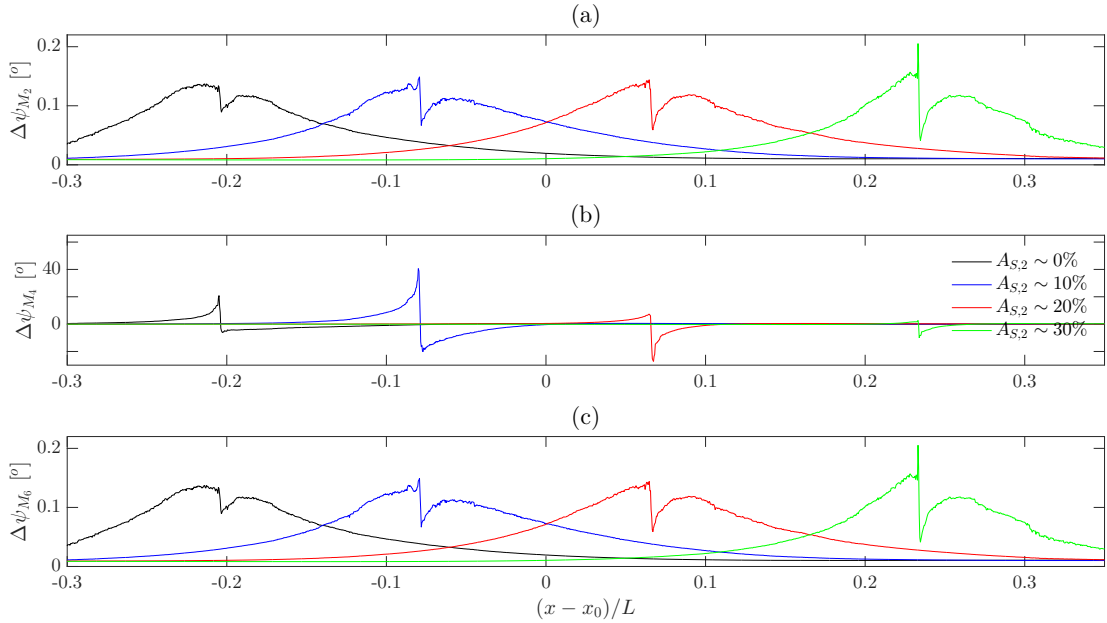
Figure 5.2: As Figure 5.1, but for phase of M_2, [(a)] M_4, [(b)] and M_6 [(c)].

Finally, the changes seen to the FVA (Figure 5.3) were all similar in overall size across the 4 deployments with all having the same east/west reduction/augmentation pattern. The change seen for the deployments on the $A_{S,2} = 0$ and 0.3 contours were almost identical, with larger augmentation than reduction peaks. The deployment on the $A_{S,2} = 0.1$ contour also had a larger augmentation peak than reduction peak. The augmentation peak for this deployment is of a similar size to the $A_{S,2} = 0$ contour deployment but the reduction peak was smaller than both the $A_{S,2} = 0$ and 0.3 deployments. This pattern appears almost exactly opposite to the $A_{S,2} = 0.2$ contour deployment, with a reduction peak similar in size to the augmentation peaks of the other deployments, and an augmentation peak of a similar size to the reduction peak of the $A_{S,2} = 0.1$ deployment.
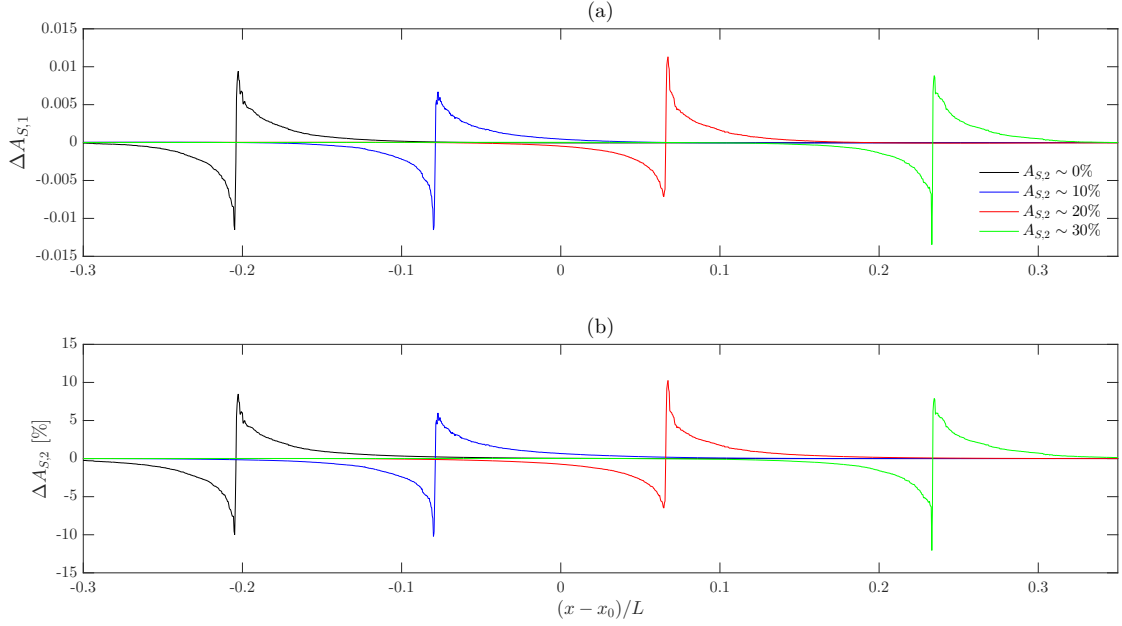
Figure 5.3: Changes to the FVA with the turbine located at the $A_{S,2} = 0$ contour (black), the $A_{S,2} = 0.1$ contour (blue), the $A_{S,2} = 0.2$ contour (red) and the $A_{S,2} = 0.3$ contour (green). Measured by $A_{S,1}$ [(a)] and $A_{S,2}$ [(b)]. Along channel length normalised as in Figure 5.1.

5.2.2 Discussion

Two things are clear from inspection of Figures 5.1–5.3; (i) the relationship between the natural tidal asymmetry and the change to the natural asymmetry due to the turbine does not exist and (ii) no consistent pattern is seen in the variation of change to the considered parameters across the four deployments. In Figure 5.4 profiles of some physical parameters from the unoccupied channel run (Run-1) are plotted to look for hints of potential physical causes for the variation that is seen across the 4 deployments.

These parameters are; the amplitudes of the M_2 current, u_{M_2}, and surface elevation, η_{M_2}, which are proxies for the overall tidal amplitudes of the current and surface elevation, the phase difference between high water and maximum flood, γ, which indicates whether the tide is standing or progressive, and the FVA, given by $A_{S,2}$. Both u_{M_2} and η_{M_2} are normalised by their maximum values, i.e.

$$\widetilde{u}_{M_2} = \frac{u_{M_2}}{\max(u_{M_2})} \tag{5.2.3}$$

and

$$\widetilde{\eta}_{M_2} = \frac{\eta_{M_2}}{\max(\eta_{M_2})} \tag{5.2.4}$$

A normalisation was also devised for γ, given by:

$$|\widetilde{\gamma}| = \left| \frac{2\gamma + \pi}{\pi} \right| \tag{5.2.5}$$

This normalisation is based on the fact that tide is a standing tide when $\gamma = \pm\pi/2$ ($\pm90^{\circ}$), a progressive tide when $\gamma = 0$, and the range of values of γ encountered in the channel was between around -50° to -150°. When $|\widetilde{\gamma}| = 0$, the tide is a standing tide, when $|\widetilde{\gamma}| = 1$, the tide is a progressive tide. The negative values of γ seen in the channel indicate peak flood (ebb) occurs before max high (low) water in the channel. When the modulus is not taken, $\widetilde{\gamma}$ may take both positive and negative values, with positive values indicating that max flood occurs before the surface elevation returns to mean-sea-level ($\eta = 0$) following max high water ($\eta = \eta_0$), and negative values indicating that max flood occurs after $\eta = 0$ following $\eta = \eta_0$. In Figure 5.4 only $|\widetilde{\gamma}|$ is plotted, but values of $\widetilde{\gamma}$ to the west of $\widetilde{\gamma} = 0$ are negative, and values to the east are positive.

Finally, $A_{S,2}$ is normalised by definition, (4.2.2), the absolute value is plotted in Figure 5.4, but from Figure 4.5, one can see that the values of $A_{S,2}$ to the west of $A_{S,2} = 0$ are negative, and values to the east are positive, with negative values indicating a larger ebb than flood and positive values indicating a larger flood than ebb.

It is not obvious from of Figures 5.1 & 5.2 that the changes to the M_2 and M_4 current constituents lead to the changes to FVA seen in Figure 5.3. For example, the change to the M_4 amplitude for the $A_{S,2} = 0$ deployment sees reduction to the west and augmentation to the east, the change to the FVA for this deployment shows the opposite pattern. To illustrate that the changes to the harmonics do indeed lead to the changes to the FVA, the values of u_{M_2}, u_{M_4}, ψ_{M_2}, ψ_{M_4} and $A_{S,2}$ at the points of peak augmentation/reduction to $A_{S,2}$ are presented in Table 5.2, along with the associated $r_u = u_{M_4}/u_{M_2}$ and $\cos(\Psi)$ values, for the $A_{S,2} = 0$, 0.1, 0.2 turbine deployments, and the changes between Run-1, and the turbine runs.
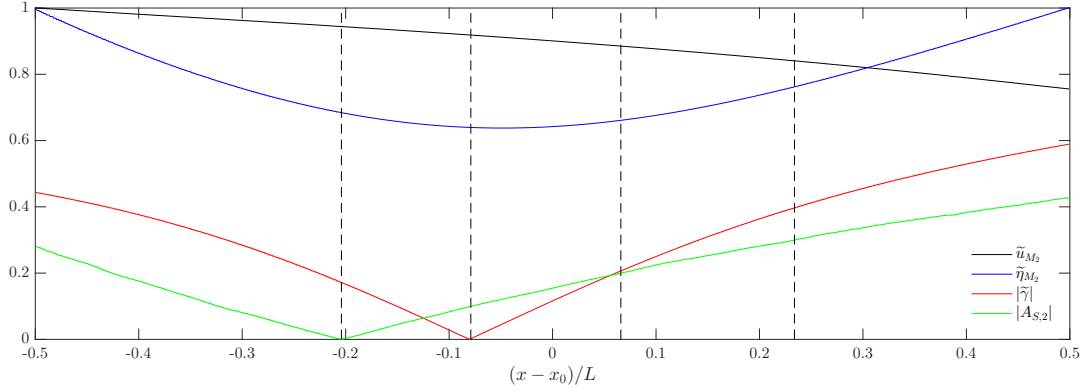
Figure 5.4: Profiles of the normalised M_2 surface elevation (blue line), $\widetilde{\eta}_{M_2}$, normalised M_2 current (black line), $\widetilde{u}_{M_2}$, absolute FVA (green line), $|A_{S,2}|$, and a parameter indicating the point on standing/progressive spectrum of the tide, at that point along the profile (red line), $|\widetilde{\gamma}|$. Along channel distance normalised as in Figure 5.1.

Forgetting the changes to the M_4 constituent for a moment, the findings above are that the ambient FVA conditions do not have much influence on the magnitude of the change to the FVA (in percentage terms) resulting from the turbine. Similarly, whether the tide is standing or progressive also seems to have little influence on the resulting effect of the turbine. Variation in the change to the M_4 tide across the deployments was seen, a variation that possibly coincides with the variation of γ along the channel. However, given the changes to the M_2 constituent and the FVA are similar across the four deployments, and it is these parameters that have the most physical significance (the M_2 is a proxy for the tidal current and the FVA indicates is flood-ebb magnitude asymmetry in this current, the M_4 and M_6 simply indicate distortions to the M_2 tide, and not propagating tidal waves).

One can then be confident that the difference in the effect of turbines seen when multiple turbines are deployed, compared to the effect of a single turbine, will be mostly due to the interaction of the multiple turbine effects, rather than the result of a variation in initial conditions due to the different turbine locations. As the model geometry has been designed so that the hydrodynamics in the unoccupied channel are approximately one-dimensional, the variation in $A_{S,2}$, and γ, with turbine position, will only be of importance when the along channel position is varied considerably, as in the next experiment.

5.3 Experiment 2: Effect of Multiple Turbines on Turbine Impact – Lines of Turbines

5.3.1 Results

The second experiment consisted of three sets of runs for a line of three turbines with three different spacings. In the first set of runs a spacing of $120D$, or 2.4 km was used; in the second set, the spacing was $60D$, or 1.2 km, and in the final set the spacing was $20D$, or 400 m. In each of the sets of runs the three turbines were deployed together, then the outermost turbines were run individually (central turbine deployed at the same location as runs in Chapter 4), thus there are three runs in total, per set. The coordinates the turbines were deployed at are given in Table 5.3. From the turbine locations one can see that in all cases the turbines will be deployed within 5 km $(250D)$ of the channel centre, and thus are all within the central region of the channel where the element will have the same target element size, 750 m^2 (see Figure 3.22). Therefore, the potential influence of grid-size on the effect of the turbine, identified in the previous section, should be lesser, and the mesh used for the experiments in Appendix F will again be used.

As was seen in the previous section, the variation of the turbine position (and therefore ambient conditions) will have little influence on the magnitude of the effect that the turbine has on the M$_2$ and the FVA. The variation in element size may however still be an issue. The variability of the flow-facing width, $\Delta y_{\text{Elem}} = \max(y_{\text{Elem}}) - \min(y_{\text{Elem}})$, of the elements containing the turbines across the $120D$, $60D$ and $20D$ lines was 3%, 22% and 14% respectively. Where these values are expressed as a relative percentage range, $RPR_{\Delta y} = 100 \times (\max(\Delta y) - \min(\Delta y))/\overline{\Delta y}$, where $\overline{\Delta y}$ is the mean of Δy. This suggests, as per Appendix F, that there will indeed be some numeric influence on the results as they are transposed to profiles. These values compare to $RPR_{\Delta y} = 148\%$ and $RPR_{\Delta y} = 2\%$ for the uncorrected and corrected meshes used in the previous experiment. To minimise any numeric influence on the results, runs where the outermost turbines are deployed individually were also carried out (Run-11, Run-12, Run-14, Run-15, Run-17 and Run-18). Therefore, the difference in the effect of the turbine operating alone and as part of an array, deployed longitudinally, can be explored.

Table 5.2: Values of M_2 and M_4 current amplitude and phase, and the associated $r_u = u_{M_4}/u_{M_2}$, $\cos(2\psi_{M_2} - \psi_{M_4}) = \cos(\Psi)$ and $A_{S,1} = r_u \cos(\Psi)$ at the locations of peak augmentation / reduction to $A_{S,2}$ resulting from the $A_{S,2} = 0$, 0.1 & 0.2 turbine deployments. Changes to each of these parameters is also presented to illustrate how the changes to the harmonics lead do in fact describe the changes to the FVA seen. *change not given as percent, but as $X_{\text{Run}-1} - X_{\text{Run}-2)}$

$A_{S,2}$	Run	Peak	u_{M_2} [m]	u_{M_4} [m]	r_u	ψ_{M_2} [°]	ψ_{M_4} [°]	$\cos(\Psi)$	$A_{S,1}$
0	1	+ve	3.5408	0.0969	0.0274	142.0225	71.2908	-0.8410	-0.0230
		-ve	3.5393	0.0959	0.0271	142.0505	70.9654	-0.8374	-0.0227
	2	+ve	3.4100	0.0660	0.0194	141.8908	50.4144	-0.5967	-0.0116
		-ve	3.4345	0.1235	0.0356	141.9561	77.1025	-0.8925	-0.0318
	Δ [%]	+ve	3.6940	31.8885	29.1970	0.1317*	20.8764*	29.0488	-0.0114*
		-ve	2.9610	-28.7800	-31.3653	0.0944*	-6.1371*	-6.5799	0.0091*
0.1	1	+ve	3.4423	0.0514	0.0149	143.5003	26.9145	-0.1722	-0.0026
		-ve	3.4448	0.0517	0.0150	143.4706	28.6227	-0.2025	-0.0030
	2	+ve	3.3706	0.0620	0.0184	143.4218	47.0283	-0.5028	-0.0093
		-ve	3.3202	0.0588	0.0177	143.3259	-12.0127	0.4797	0.0085
	Δ [%]	+ve	2.0829	-20.6226	-23.4899	0.0785*	-20.1138*	-191.9861	0.0067*
		-ve	3.6170	-13.7331	-18	0.1447*	40.6354*	336.8889	-0.0115*
0.2	1	+ve	3.3178	0.0820	0.0247	144.5355	-33.6840	0.7961	0.0197
		-ve	3.3203	0.0810	0.0244	144.5217	-33.2017	0.7906	0.0193
	2	+ve	3.1927	0.0624	0.0195	144.4708	-6.3526	0.4273	0.0083
		-ve	3.2442	0.0997	0.0307	144.3776	-40.4465	0.8590	0.0264
	Δ [%]	+ve	3.7706	23.9024	20.9547	0.0647*	-27.3314*	46.3258	0.0114*
		-ve	2.2920	-23.0864	-25.8197	0.1441*	7.2448*	-8.6517	-0.0071*

Figures 5.5–5.7 show differences in the current amplitude, phase and flood-ebb magnitude asymmetry between cases where the turbines were deployed as an array with a spacing of $120D$, and individually, respectively. Figure 5.8–5.10 show the same differences for the $60D$ spacing case, and Figure 5.11–5.13 for the $20D$ spacing case.

For the M_2 and M_6 amplitudes the reduction peaks were larger when the turbines were deployed as an array, with a larger difference between the individual deployments and the array the closer together the turbines were deployed (Figures 5.5a, 5.5c, 5.8a, 5.8c, 5.11a & 5.11c). In the regions between the turbines the amplitude reduction levelled-off, but not at zero, and the value appeared to increase

with reduced turbine spacing, implying less wake recovery between the turbines. For the M_4, the difference between the array and individual turbine cases changed depending on the turbine in question (Figures 5.5b, 5.8b & 5.11b). For the central turbine the reduction and augmentation peaks were both smaller in the array deployment. For the west-most turbine the augmentation peak was larger and the reduction peak smaller in the array deployment, whilst for the east-most turbine the opposite was true. The differences between the peaks appeared to increase as the turbines were more closely spaced. However, this is not immediately clear from inspection of Figures 5.5, 5.8 and 5.11 and a more detailed analysis is required. This can be found in §5.3.2.
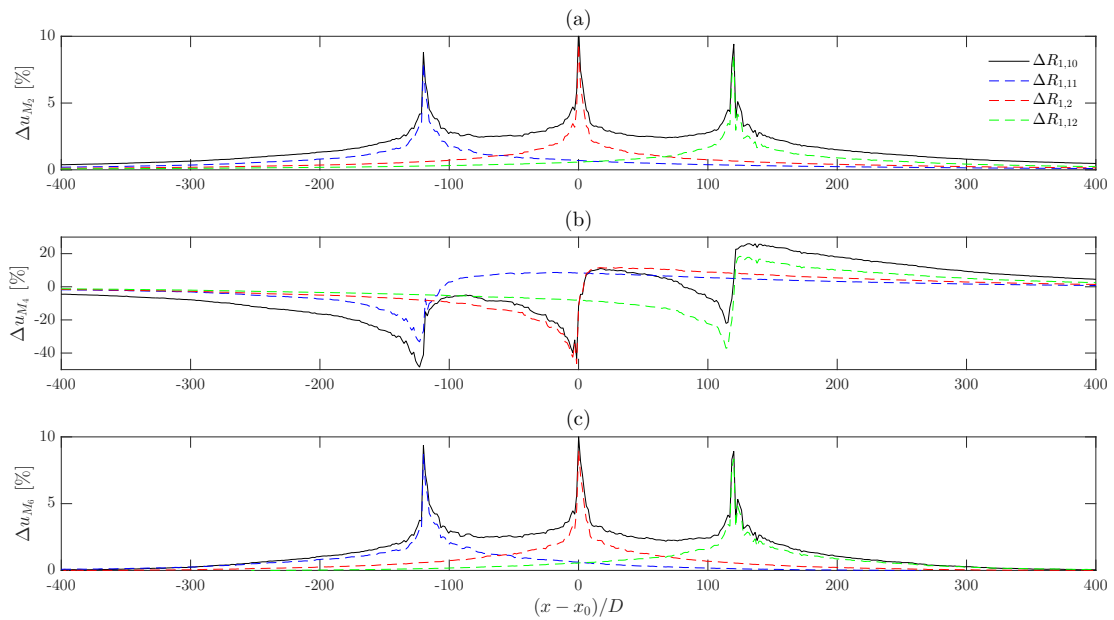
Figure 5.5: Change to the amplitude of the M_2 [(a)], M_4 [(b)] and M_6 [(c)] currents for $120D$ spaced array (solid black) and the turbines individually (coloured dashed lines). Along channel distance normalised by the turbine spacing, D, with the normalisation defined in such a way that the channel centre lies at 0.

The patterns of change to the phase for the M_2 and M_6 tides were somewhat similar (Figure 5.6a, 5.6c, 5.9a, 5.9c, 5.12a & 5.12c). For both tides and for each of the spacings, the change to the phase due to the array was much larger than for individual turbines. The array phase change appeared to be almost the superposition of each of the individual phase changes. For closer turbine spacing

the overall effect was large, and therefore the difference between the overall change and the individual changes was larger. For the M_4 phase the pattern was very similar to the M_4 amplitude, but reversed (Figure 5.6b, 5.9b & 5.12b). In the case of the central turbine, the reduction peak was slightly smaller for the array than for the individual turbine, but the augmentation peak was the same. For the west-most turbine the reduction peak was larger for the array and the augmentation peak smaller, and vice-versa for the east-most turbine. This difference again appeared to grow for smaller turbine spacings, but closer analysis is needed, and can be found in §5.3.2.
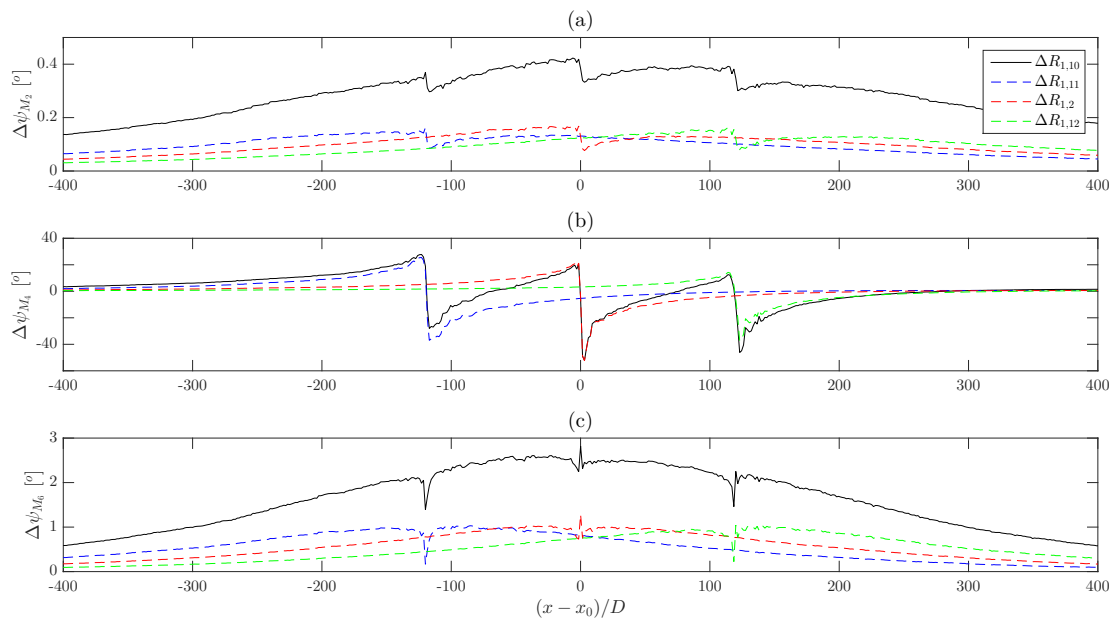
Figure 5.6: As Figure 5.5 but for the phase of the M_2 [(a)], M_4 [(b)] and M_6 [(c)].

The changes to asymmetry showed similar patterns to the changes to the M_4 tide (Figures 5.7, 5.10 & 5.13), due to the important role that the M_4 plays in describing asymmetry. The difference between the array and individual central turbine changes was small regardless of spacing. The main difference was seen in the region between the turbines where the difference between the array run and the individual runs were large, growing larger as the turbine spacing was reduced and the opposing peaks of the adjacent turbines moved closer. For the west-most turbine the augmentation peak was larger and the reduction peak smaller for the array run than the individual run, and vice-versa for the east-most turbine. Again,

the difference seemed to grow larger as the spacing reduced. Also, the combined effect of the array reached further east and west than the east-most/west-most effect of the east-most/west-most turbine. This effect also appeared to grow with reduced turbine spacing.

Table 5.3: Coordinates of turbines in line arrays.

	Run-10			Run-11	Run-12
$(x_T - x_0)/D$	-119.5	0.5	199.6	-119.5	119.6
y/D	-0.5	-0.5	-0.5	-0.5	-0.5
	Run-13			Run-14	Run-15
$(x_T - x_0)/D$	-59.65	0.5	60.5	-59.65	60.5
y/D	-0.5	-0.5	-0.5	-0.5	-0.5
	Run-16			Run-17	Run-18
$(x_T - x_0)/D$	-19.5	0.5	20.95	-19.5	20.95
y/D	-0.5	-0.5	-0.5	-0.5	-0.5
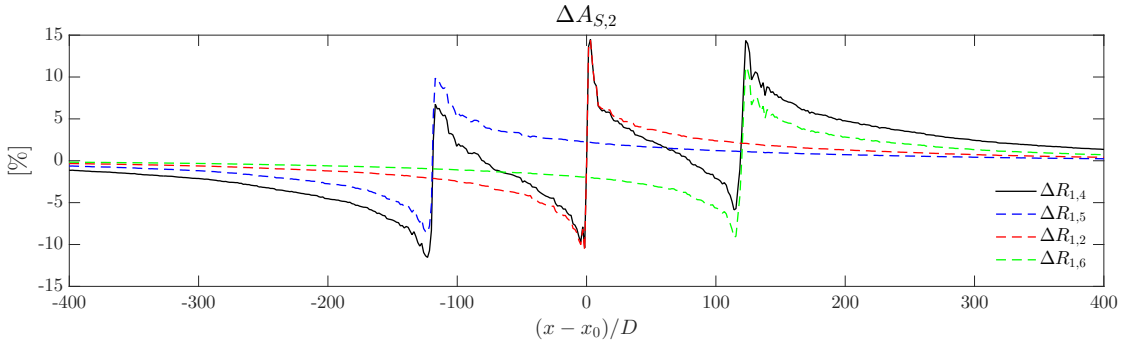
Figure 5.7: Change to the FVA for $120D$ spaced array (solid black) and the turbines individually (coloured dashed lines). Along channel distance normalised as in Figure 5.5.

5.3.2 Discussion

From inspection of Figures 5.5–5.13, a pattern of larger overall impact when turbines are deployed closer together was seen. In this sub-section a more detailed quantitative analysis of the results is carried out to either confirm or deny this initial, subjective interpretation. In Table 5.4 the values of the peaks, both positive

and negative (or reduction and augmentation respectively), from Figures 5.5–5.13, are given for the array runs and individual runs, along with the difference between the peaks values for the array and individual runs (array difference minus individual difference). These differences are calculated as:
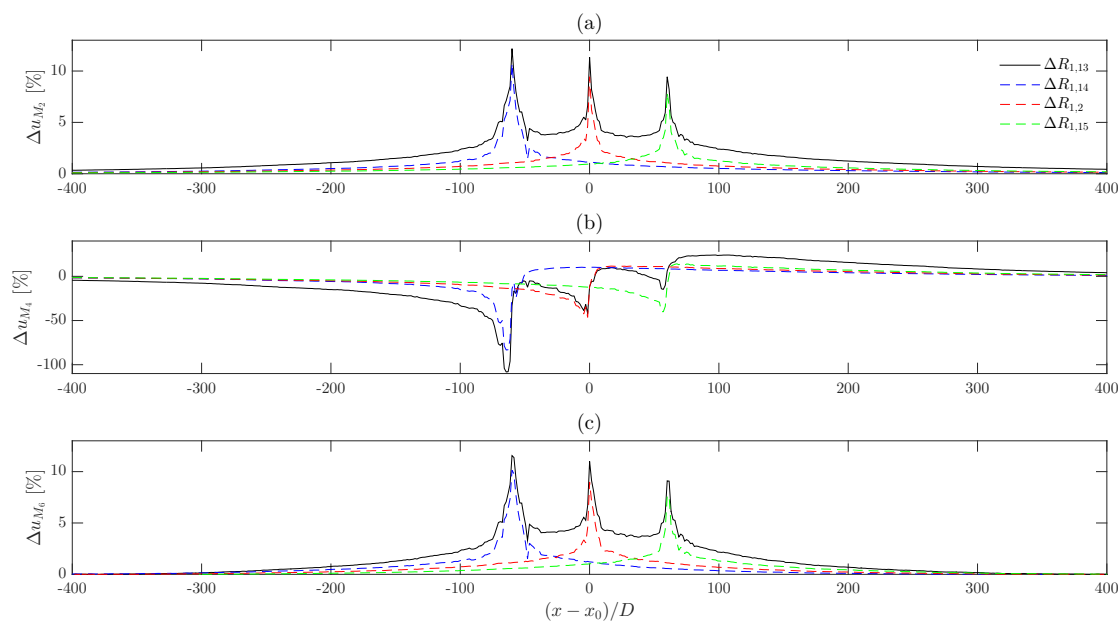
Figure 5.8: As Figure 5.5, but for $60D$ spaced array.
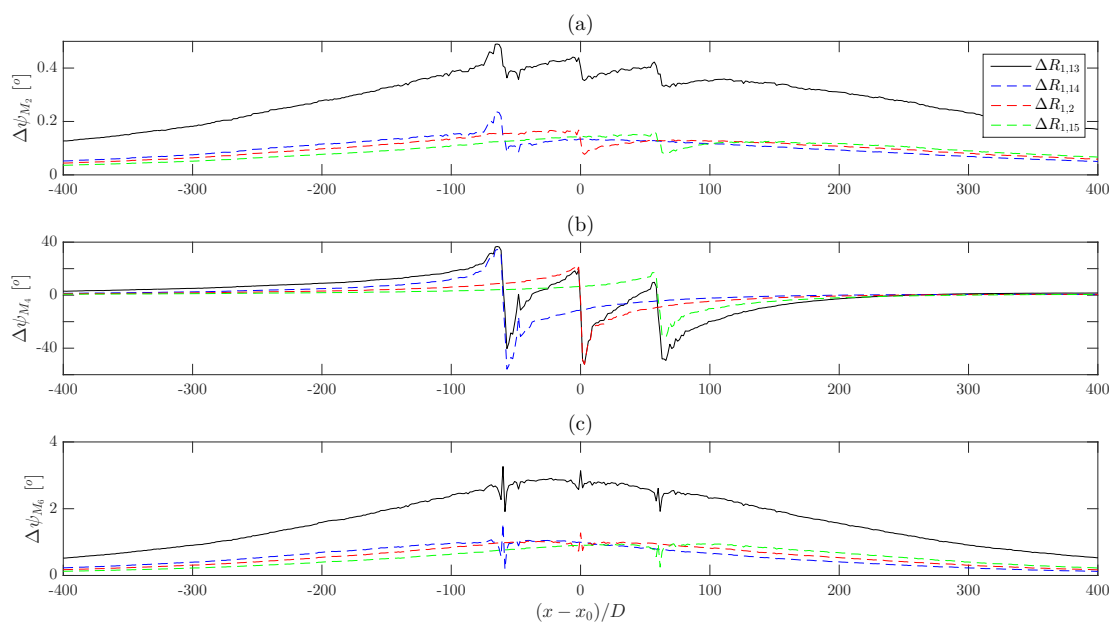
Figure 5.9: As Figure 5.6, but for $60D$ spaced array.

$$\Delta(\Delta X) = \Delta X_A - \Delta X_I \tag{5.3.1}$$

for all parameters, X, where the subscripts A and I denote parameters pertaining to the array and individual runs respectively and ΔX is as defined in (5.2.2).
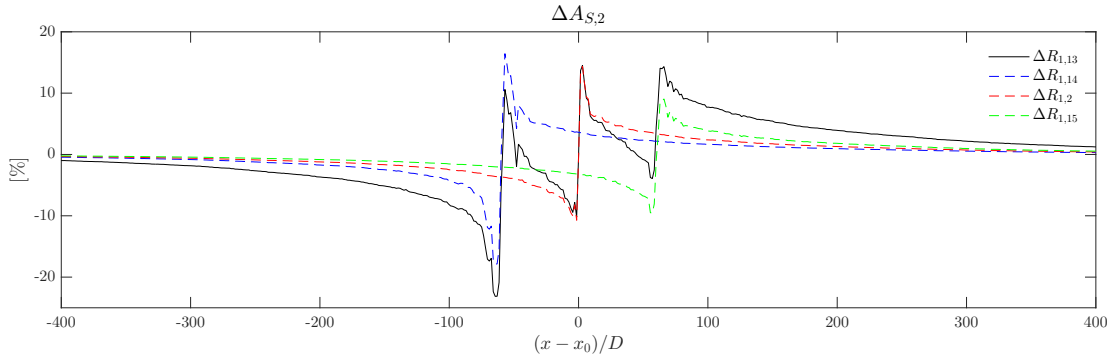
Figure 5.10: As Figure 5.7, but for $60D$ spaced array.
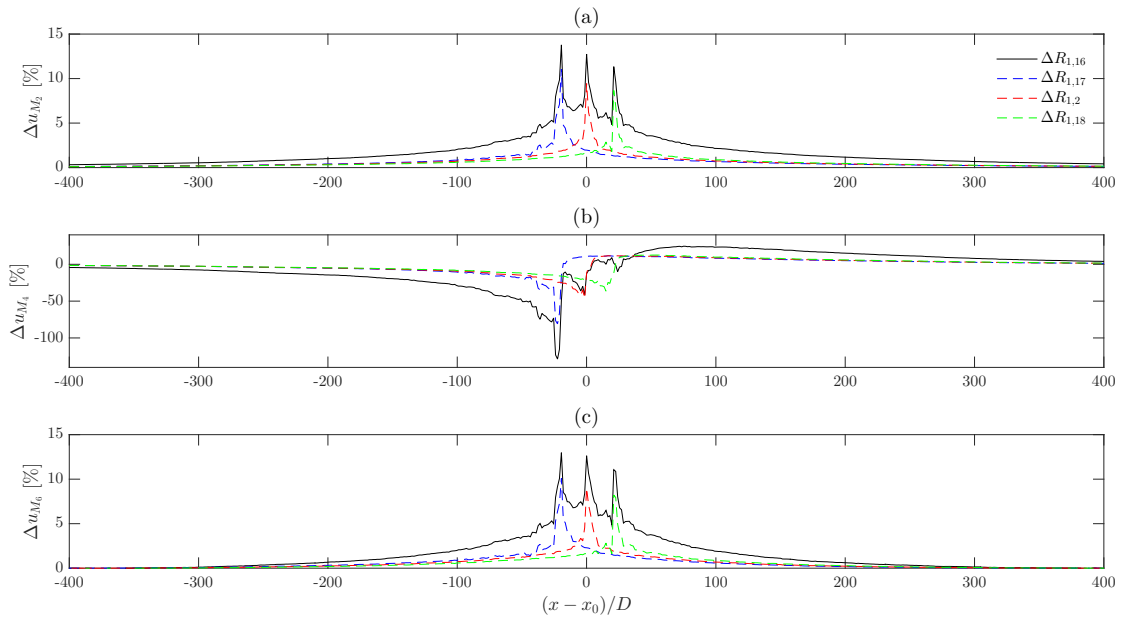
Figure 5.11: As Figure 5.5, but for the $20D$ spaced array.

In Figure 5.14 the differences in the peak changes to the amplitudes and phase of all tides between the individual and array runs are plotted against the inter-turbine spacing. In this plot the absolute changes to Δu_{M_4} and $\Delta \psi_{M_4}$ are considered (Figures 5.14b & 5.14e). A trend of increasing difference in the peak change to the tides between the individual and array runs with decreasing turbine spacing can be

seen across all parameters except ψ_{M_2}. Figure 5.15 shows the equivalent plot for the FVA metric $A_{S,2}$. This figure shows little variation in the impact of the central turbine on $A_{S,2}$, whilst for the easternmost turbine a larger difference is seen with smaller turbine spacing, likewise for the augmentation peak for the westernmost turbine.
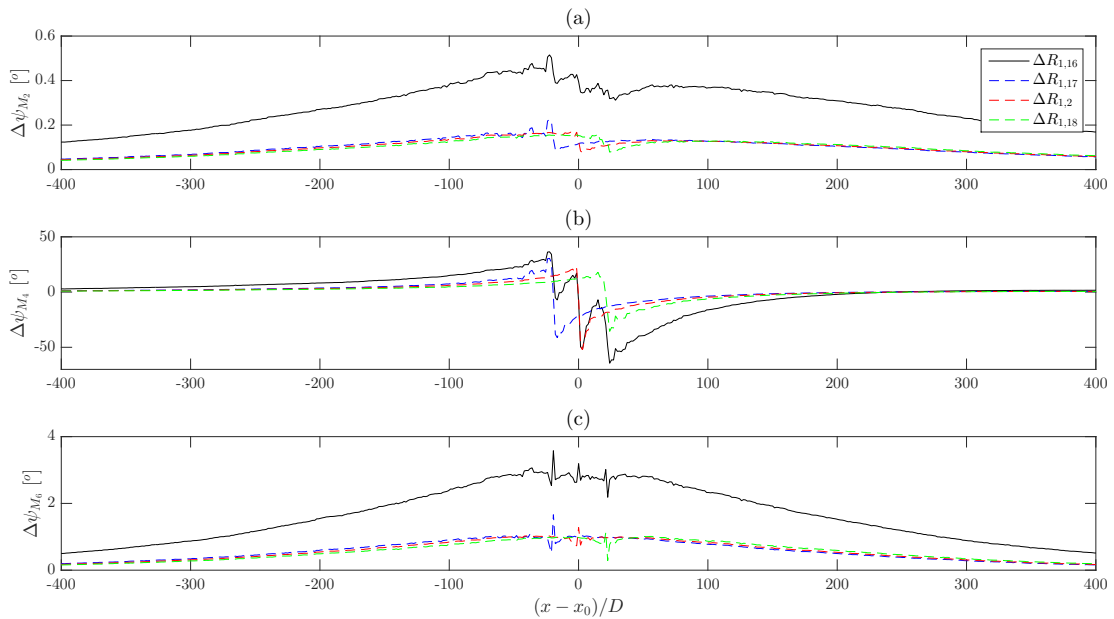
Figure 5.12: As Figure 5.6, but for the $20D$ spaced array.

Summarising what is shown by this analysis; there is a suggestion that closer longitudinal turbine spacing leads to an increased impact on the asymmetry as the impacts of the individual turbines interact within the array. Much larger effects on both the amplitude and phase of all tides were seen when the turbines were more closely spaced. However, for each of the plots the number of data-points was small, meaning more runs, covering a larger number of inter-turbine spacings and possibly more turbines would be required to better understand any trends.

For the smallest turbine spacing, the difference in the change to the asymmetry between the array and individual runs for the east most turbine becomes very large. The introduction of a longitudinal array of turbines causes step-like changes to asymmetry. The augmentation peak of the west most turbine is larger and the reduction peak smaller, and vice-versa for the east-most turbine. This is an indication of an additive effect of each turbine to the overall effect of the array.

The augmentation peaks for asymmetry are consistently larger than the reduction peaks, and the peak values of the effect of the west-most turbine individually has been larger than the east-most turbines. Combined, these effects lead to this larger difference between the individual and array effects for the east-most turbines compared to the west-most turbine.
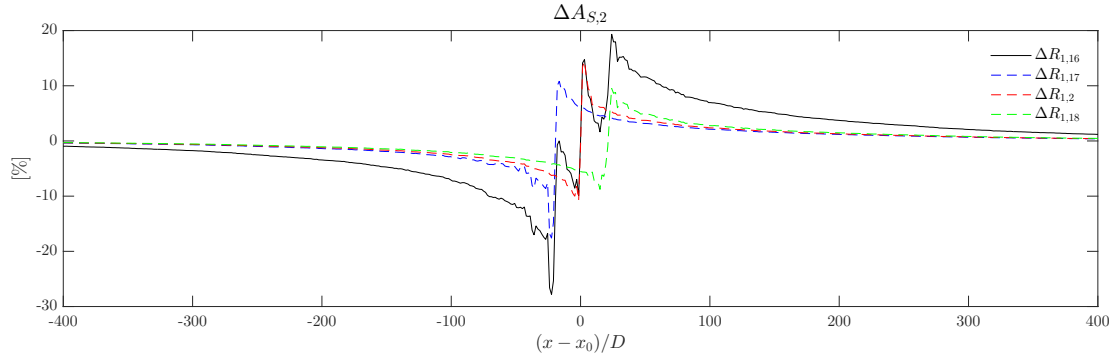
Figure 5.13: As Figure 5.7, but for the $20D$ spaced array.
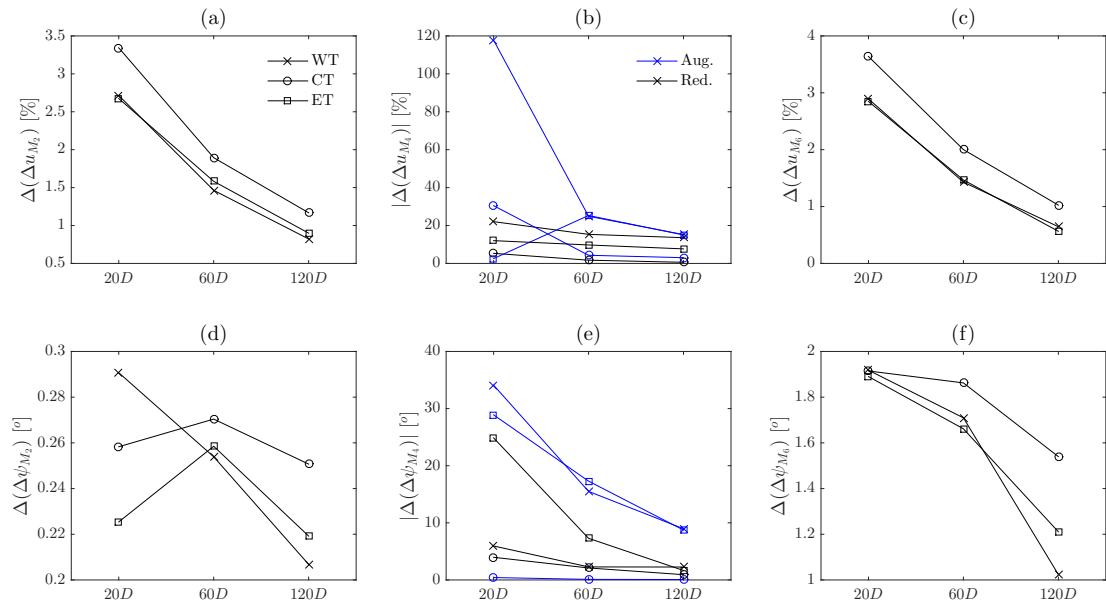
Figure 5.14: Difference in the change in the amplitude, (top row), and phase, (bottom row), of the M_2 (left column), M_4 (middle column) and M_6 (right column), between the array and individual runs, against turbine spacing.
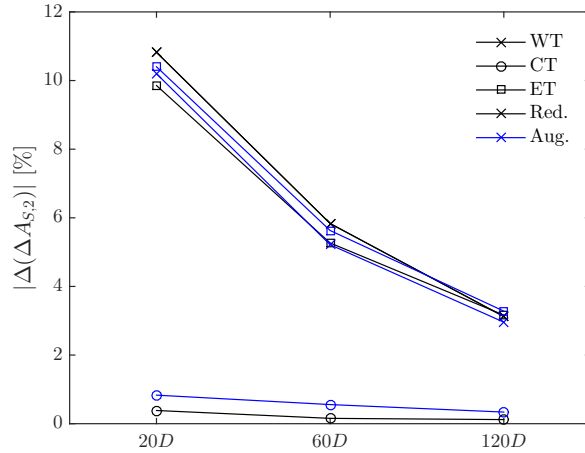
Figure 5.15: Difference in the change to the flood-ebb amplitude asymmetry between the array and individual runs, against turbine spacing.

5.4 Experiment 3: Effect of Multiple Turbines on Turbine Impact – Rows of Turbines

5.4.1 Results

In the third set of experiments, five additional model runs were undertaken, the first with 9 turbines deployed in a row across the channel, the second with 10 turbines, then 13, 17 and 26 turbines. These deployments correspond to rows with an inter-turbine spacing of $5D$, $4D$, $3D$, $2D$ and $1D$ respectively. These five runs are assigned the row numbers Run-19, Run-20, Run-21, Run-22 and Run-23 respectively. The spacings were not exact as all turbines were deployed so that they only occupied a single mesh element. The coordinates of the turbines are given in Table 5.5, and Figure 5.16 shows their locations.

For this experiment the results are presented differently from the form adopted in the previous sections since, in that form, up to 26 profiles of the change to the harmonic analysis would be required. The up to 26 profiles running the length of the channel through each of the turbines in the row were calculated. Then, at each point along the profile, the average across all profiles for that run was calculated, along with the maximum and minimum values across the profiles, at that point. In Figures 5.17–5.21 the mean profiles of the change to the M_2, M_4

and M_6 amplitude and phase are plotted along with the envelope given by the maximum and minimum values, along with the single turbine (Run-2) profile, for Run-19, Run-20, Run-21, Run-22 and Run-23 respectively. In addition to these plots, Figures 5.22–5.26 show $2D$ plots of the change to the harmonic analysis between Run-1 (the no-turbine case) and Run-19, Run-20 and Run-21 respectively. Figures 5.17–5.21 use the same axis for each of the parameters of the harmonic analysis between the three figures for comparison, likewise Figures 5.22–5.26 use the same colour-axis for each parameter between the three figures. Finally, the mean and envelope of the asymmetry change profiles are given in Figure 5.27, and the $2D$ plots of asymmetry change are given in Figure 5.28.

For the $5D$ (Figure 5.17), $4D$ (Figure 5.18) and $3D$ (Figure 5.19) spaced rows the mean profiles retained approximately the same pattern as seen for a single turbine, for each parameter. In each case however the magnitude of peak change along the mean profile was considerably smaller than for the single turbine profile. From the envelope in these figures one can also see that the magnitude of the peaks for all profiles in for the $5D$, $4D$ and $3D$ rows were also smaller than single turbine profile, and the pattern of change along the profiles was reasonably consistent, as indicated by the narrow envelope.

As the number of turbines in the row is increased, the envelope widens and the magnitude of the peak changes in the mean profile becomes smaller. This widening of the envelope indicates a greater variation in the pattern of change seen in the individual profiles, which also explains the flattening out of the mean profiles. The mean profiles for the $2D$ row (Figure 5.20) still show the pattern of change seen in the single turbine profile, but for the $1D$ row, most of this pattern is lost for the M_2 phase and M_4 amplitude and phase (Figures 5.21b–5.21d). A more detailed analysis of these subjectively-identified trends will be undertaken in §5.4.2.
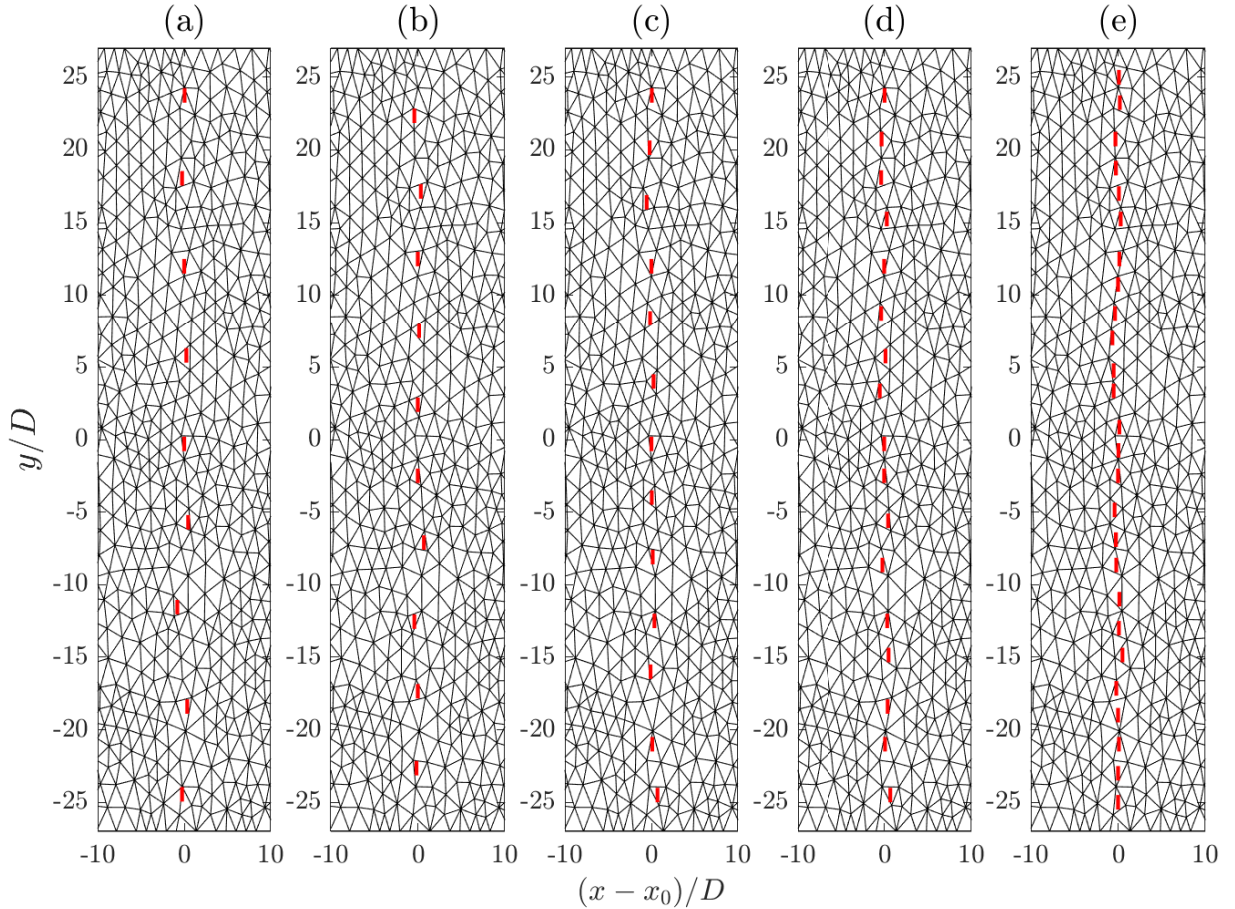
Figure 5.16: Turbine locations for Run-19 [(a)], Run-20 [(b)], Run-21 [(c)], Run-22 [(d)] and Run-23 [(e)]. The along and across channel distances have been normalised by the turbine diameter, D. The definition of the along channel normalisation defined in such a way that the channel centre lies at zero, in the across channel the channel centre naturally lies at 0.

In the contour plots for the $5D$ (Figure 5.22), $4D$ (Figure 5.23), $3D$ (Figure 5.24) and $2D$ (Figure 5.25) rows one can see repeating patterns of change, further indicating a regular pattern of change across the array for these greater inter-turbine spacing runs. This pattern was less clear for the $1D$ row (Figure 5.26) which used the smallest inter-turbine spacing. If one compares the turbine locations in Figure 5.16 with the patterns of change in Figure 5.26, one can see that the largest changes appeared to coincide with the larger gaps in the row of turbines. This seems to imply that for smaller inter-turbine spacings, uniformity of the inter-turbine spacing is important for the uniformity of the pattern of turbine impact.

Table 5.4: Peak values from Figure 5.5–5.13 and the normalised differences between these peak values in the array and individual runs (grey shaded). Red. – Reduction peak, Aug. – Augmentation peak.

Spacing	Turbine(s)		Δu_{M_2} [%]	Δu_{M_4} [%]		Δu_{M_6} [%]	$\Delta\psi_{M_2}$ [°]	$\Delta\psi_{M_4}$ [°]		$\Delta\psi_{M_6}$ [°]	$\Delta A_{S,2}$ [%]	
			Red.	Red.	Aug.	Red.	Red.	Red.	Aug.	Red.	Red.	Aug.
120D	Array	West-Most	8.7974	-4.9323	-48.4918	9.3676	0.3696	27.7451	-28.0469	2.0541	6.748	-11.539
		Centre	10.6094	11.0079	-43.3522	10.0199	0.4191	20.3665	-52.1714	2.8187	14.4928	-10.4071
		East-Most	9.4252	26.0109	-22.1073	8.9176	0.382	12.6093	-46.1983	2.2526	14.3532	-5.8795
	Single	West-Most	7.9749	8.6499	-33.2737	8.7221	0.1628	25.4837	-37.0072	1.0305	9.8715	-8.5805
		Centre	9.4415	11.6045	-46.388	8.9946	0.1684	21.2909	-52.2483	1.279	14.373	-10.7458
		East-Most	8.5259	18.3383	-37.1434	8.3522	0.1628	14.267	-37.4686	1.0419	11.1889	-9.16
	$\Delta(\Delta X)$	West-Most	0.8225	-13.5822	-15.2181	0.6455	0.2068	2.2614	8.9603	1.0236	-3.1235	-2.9585
		Centre	1.1679	-0.5966	3.0358	1.0253	0.2507	-0.9244	0.0769	1.5397	0.1198	0.3387
		East-Most	0.8993	7.6726	15.0361	0.5654	0.2192	-1.6577	-8.7297	1.2107	3.1643	3.2805
60D	Array	West-Most	12.1811	-4.9321	-108.2076	11.5555	0.49	36.7363	-40.4294	3.2678	10.6134	-23.137
		Centre	11.3359	9.8932	-42.0833	10.9961	0.4388	19.191	-52.1482	3.1414	14.5285	-10.1885
		East-Most	9.4389	24.1376	-14.7833	9.1023	0.4228	9.7303	-49.2743	2.6143	14.3287	-3.93
	Single	West-Most	10.7171	10.4057	-83.3286	10.1268	0.2361	34.4536	-55.9346	1.5583	16.4464	-17.9218
		Centre	9.4415	11.6045	-46.3888	8.9946	0.1684	21.2909	-52.2483	1.279	14.373	-10.7458
		East-Most	7.8561	14.3967	-40.073	7.6347	0.1643	17.019	-31.9769	0.9528	9.0623	-9.5597
	$\Delta(\Delta X)$	West-Most	1.464	-15.3378	-24.879	1.4287	0.2539	2.2827	15.5052	1.7095	-5.833	-5.2152
		Centre	1.8944	-1.7113	4.3055	2.0015	0.2704	-2.0999	0.1001	1.8624	0.1555	0.5573
		East-Most	1.5828	9.7409	25.2897	1.4676	0.2585	-7.2887	-17.2974	1.6615	5.2664	5.6297
20D	Array	West-Most	13.7845	-10.4145	-128.6649	12.9798	0.5154	36.4607	-7.1942	3.5817	0.022	-27.8154
		Centre	12.7845	6.2945	-41.8452	12.633	0.4267	17.3276	-51.83	3.1937	14.7576	-9.9138
		East-Most	11.343	24.5738	-9.9499	11.064	0.3878	-6.9231	-64.4921	3.0177	19.3776	1.6139
	Single	West-Most	11.0692	11.6261	-10.9418	10.0873	0.2247	30.5146	-41.2889	1.6638	10.8445	-17.6173
		Centre	9.4415	11.6045	-11.3851	8.9946	0.1684	21.2909	-52.2483	1.279	14.373	-10.7458
		East-Most	8.6685	12.5554	-12.5055	8.2162	0.1624	17.9455	-35.5933	1.1276	9.522	-8.7875
	$\Delta(\Delta X)$	West-Most	2.7153	-22.0406	-117.7231	2.8925	0.2907	5.9461	34.0947	1.9179	-10.823	-10.1981
		Centre	3.343	-5.31	-30.4601	3.6384	0.2583	-3.9633	0.4183	1.9147	0.3846	0.832
		East-Most	2.6745	12.0184	2.5556	2.8478	0.2254	-24.869	-28.8988	1.8901	9.8556	10.4014

5.4.2 Discussion

In order to give a more quantitative comparison of the similarity of the profiles of the change to parameter X due to the $5D$, $4D$, $3D$, $2D$ and $1D$ rows, the parameter Si_X will be used, defined as:

$$Si_X = \frac{1}{N} \sum_{j,k}^{N} \left(\sqrt{\sum_{i=1}^{N} \frac{(X(j,i) - X(k,i))^2}{n}} \right) \tag{5.4.1}$$

In each of the aforementioned runs, for each parameter X there are m profiles, each of length n. Therefore X has dimensions $m \times n$. Defining $i = 1, \ldots, n$, and $j, k = 1, \ldots, m$ and $N = \binom{m}{2}$. Equation (5.4.1) is therefore the root-mean-square-difference of profiles j and k, averaged over all combinations of j and k.

Figure 5.29 plots Si_X for each parameter, including the asymmetry metric $A_{S,2}$, for each experiment. Smaller values of Si indicate greater similarity between the profiles. From Figure 5.29 one can see that there is indeed a trend of less similarity between the profiles for each turbine when the inter-turbine spacing is reduced.
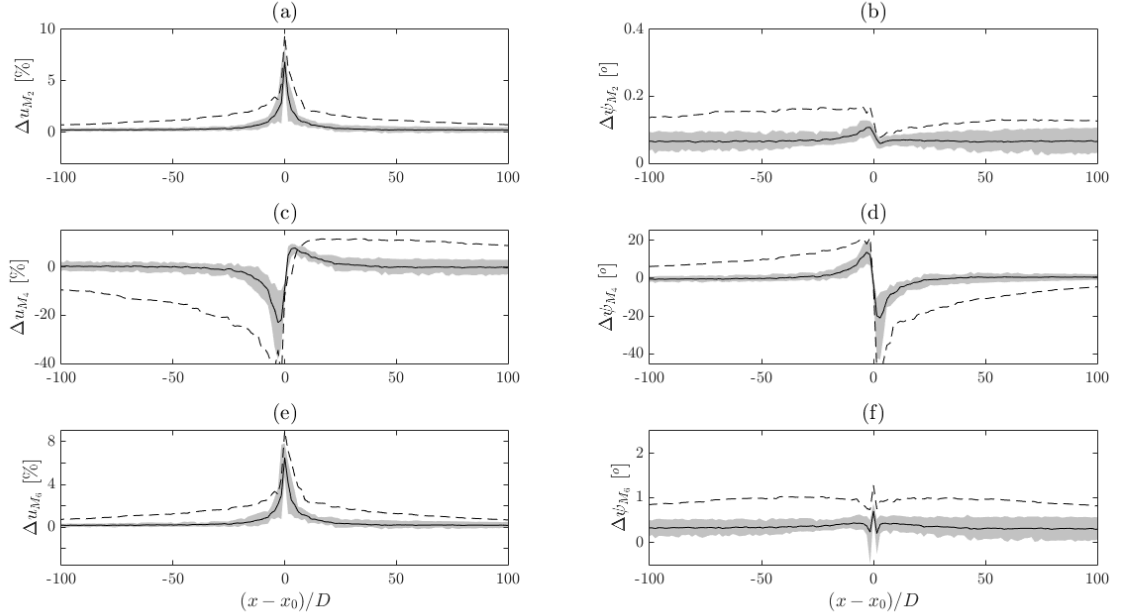
Figure 5.17: Mean (solid line) and envelope (shaded grey area) of all profiles of change in amplitudes (left column) and phases (right column) of the M_2 (top row), M_4 (middle row) and M_6 (bottom row), between Run-1 and Run-19, the $5D$ spaced row, along with the respective profiles of change between Run-1 and Run-2 (dashed black line). The along channel distance has been normalised by the turbine diameter, D, with the definition of the normalisation defined in such a way that the channel centre lies at 0.

Comparison of Figures 5.16 and 5.26, suggests that non-uniformity of the inter-turbine spacing may also play a role in the lack of conformity between profiles. From the turbine locations given in Table 5.5, a measure of the uniformity of the spacing can be calculated as:

$$Us = \sqrt{\frac{1}{N}\sum_{j}^{N}\left(\widetilde{As_j} - \frac{1}{N}\sum_{j}^{N}\widetilde{As_j}\right)^2} \qquad (5.4.2)$$
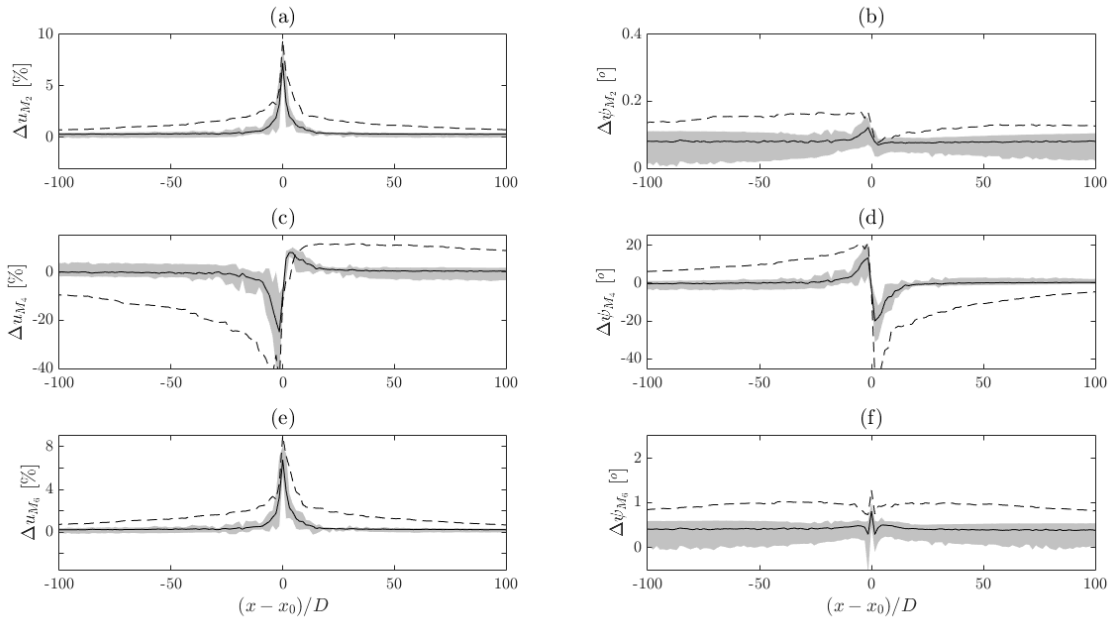
Figure 5.18: As Figure 5.17, but for the $4D$ spaced array (Run-1–Run-20 difference).
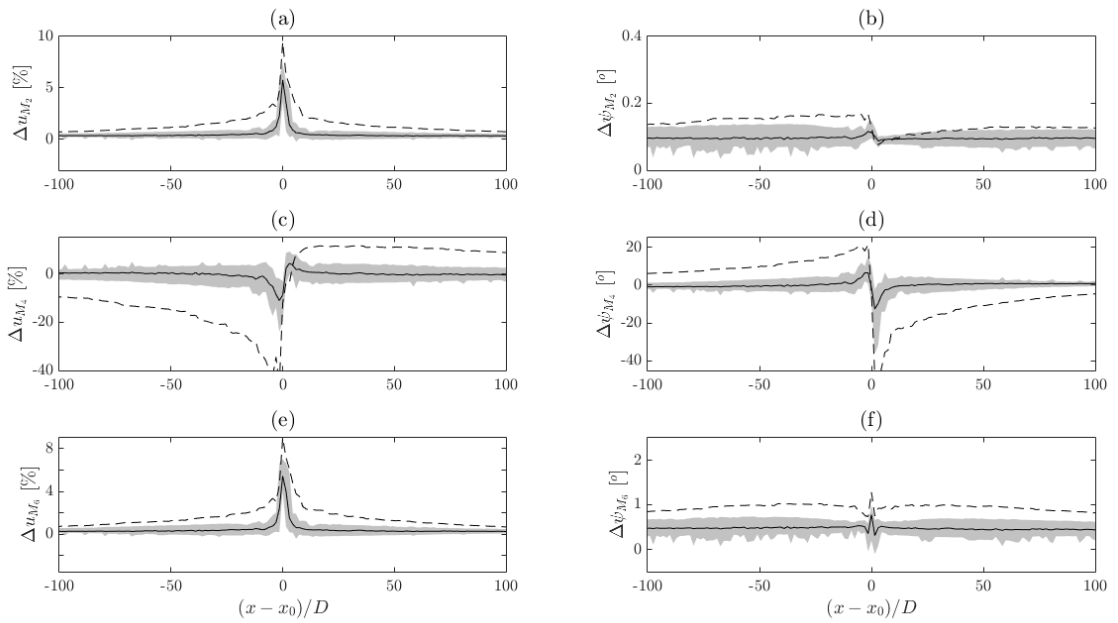
Figure 5.19: As Figure 5.17, but for the $3D$ spaced array (Run-1–Run-21 difference).
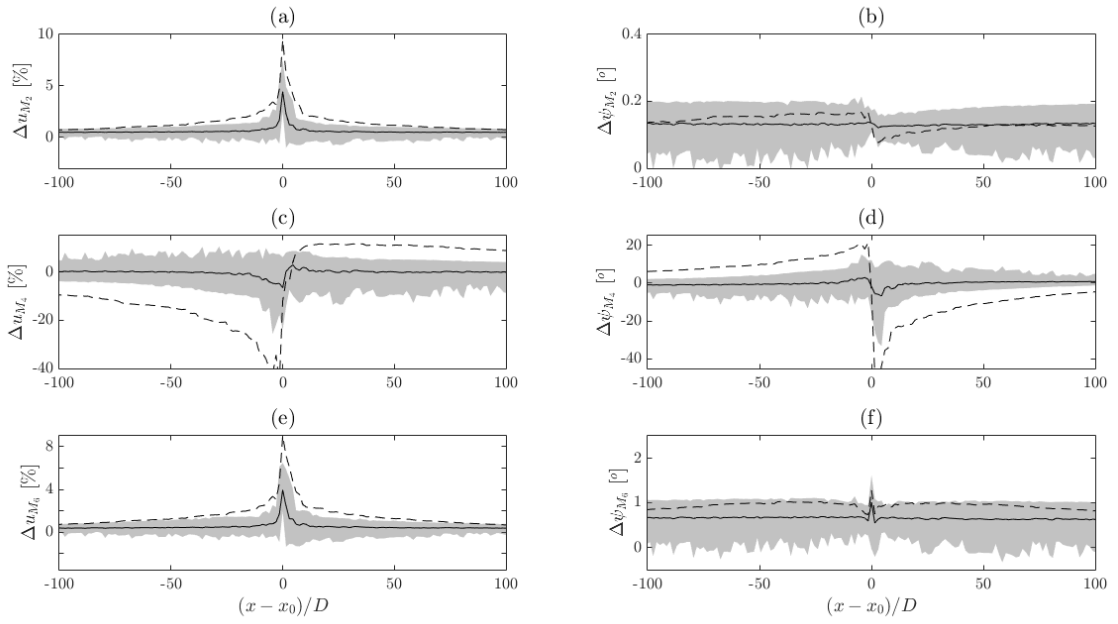
Figure 5.20: As Figure 5.17, but for the $2D$ spaced array (Run-1–Run-22 difference).
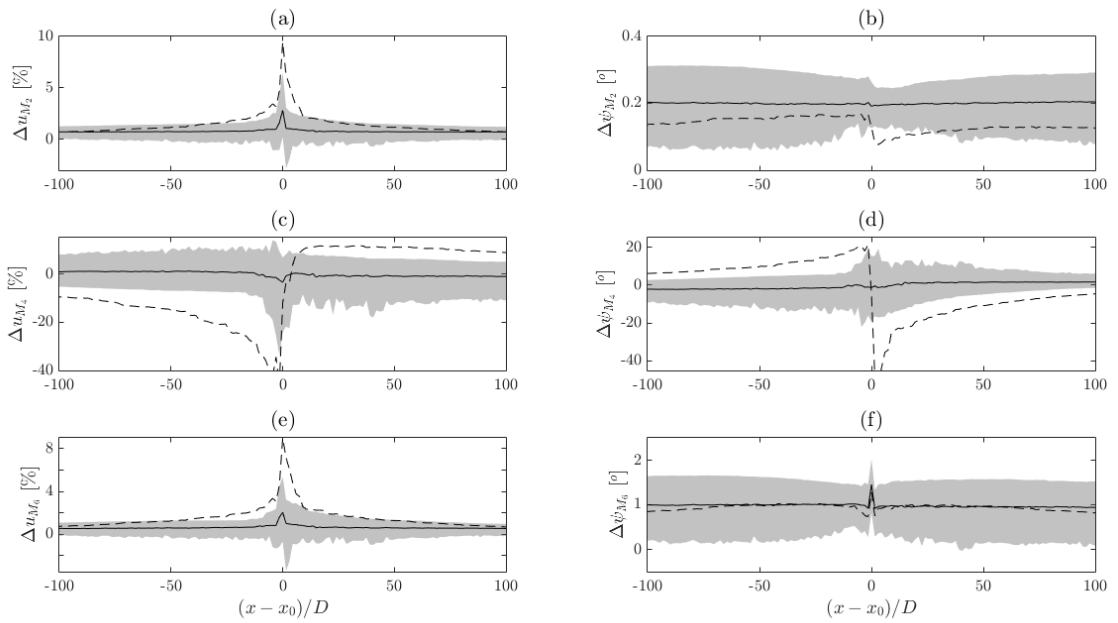
Figure 5.21: As Figure 5.17, but for the $1D$ spaced array (Run-1–Run-23 difference).

Table 5.5: Turbine locations for Run-19, Run-20, Run-21, Run-22 and Run-23.

Run-19		Run-20		Run-21		Run-22		Run-23	
$\frac{(x_T-x_0)}{D}$	$\frac{y_T}{D}$	$\frac{(x_T-x_0)}{D}$	$\frac{y_T}{D}$	$\frac{(x_T-x_0)}{D}$	$\frac{y_T}{D}$	$\frac{(x_T-x_0)}{D}$	$\frac{y_T}{D}$	$\frac{(x_T-x_0)}{D}$	$\frac{y_T}{D}$
0.05	23.75	-0.40	22.35	0.05	23.75	0.05	23.75	0.10	25.00
-0.25	15.05	0.35	17.15	-0.20	20.15	-0.30	20.75	0.20	23.25
0.00	12.00	0.00	12.50	-0.55	16.40	-0.35	18.10	-0.30	20.75
0.25	5.80	0.15	7.50	0.00	12.00	0.30	15.25	-0.25	18.75
0.00	-0.30	0.00	2.40	-0.15	8.40	0.00	12.00	0.10	17.00
0.45	-5.70	0.00	-2.50	0.25	4.00	-0.35	8.75	0.30	15.25
-0.80	-11.55	0.70	-7.10	0.00	-0.30	0.25	5.75	0.15	12.50
0.35	-18.40	-0.40	-12.35	0.05	-4.00	-0.5	3.35	0.00	10.75
-0.25	-24.45	0.00	-17.35	0.15	-8.10	0.00	-0.30	-0.35	8.75
		-0.15	-22.65	0.35	-12.50	0.00	-2.50	-0.65	7.00
				-0.10	-16.00	0.45	-5.60	-0.50	4.75
				0.10	-21.00	-0.20	-8.65	-0.50	3.35
				0.70	-24.50	0.35	-12.50	0.15	0.85
						0.50	-14.85	0.05	-0.75
						0.40	-18.40	0.00	-2.50
						0.10	-21.00	-0.40	-4.85
						0.70	-24.50	-0.25	-6.90
								-0.20	-8.65
								0.15	-11.00
								0.10	-13.00
								0.50	-14.85
								-0.20	-17.15
								0.00	-19.00
								0.10	-21.00
								0.00	-23.00
								0.00	-25.00

where $\widetilde{As}$ is the normalised actual turbine spacing, given by:

$$\widetilde{As_j} = \begin{cases} \frac{x_i - x_{i+1} - D/2}{Is} & \text{if } i = 1, N \\ \frac{x_i - x_{i+1} - D}{Is} & \text{otherwise} \end{cases} \tag{5.4.3}$$

where $i, j = 1, \ldots, N$, N is the number of turbines in the row, D is the turbine diameter and Is is the intended turbine spacing, i.e., $1D$, $2D$, $3D$, $4D$ or $5D$.

Table 5.5, gives the locations of the turbine hubs, therefore the diameter must be subtracted from the difference between these values to give the spacing between turbines. The locations of the channel walls must also be included so, $x_{i=1} = b/2$ and $x_{i=N+1} = -b/2$, and in these cases $D/2$ used. Equation (5.4.2) is then the standard deviation of $\widetilde{As}$. For the intended spacings $1D$, $2D$, $3D$, $4D$ and $5D$, the values of Us are 0.33, 0.24, 0.17, 0.06 and 0.34 respectively. These values of Us do not support the hypothesis that the variability in the inter-turbine spacing increases with reduced target inter-turbine spacing, as the variability of inter-turbine spacing for the most sparsely spaced row is in fact the largest of all the tested rows.
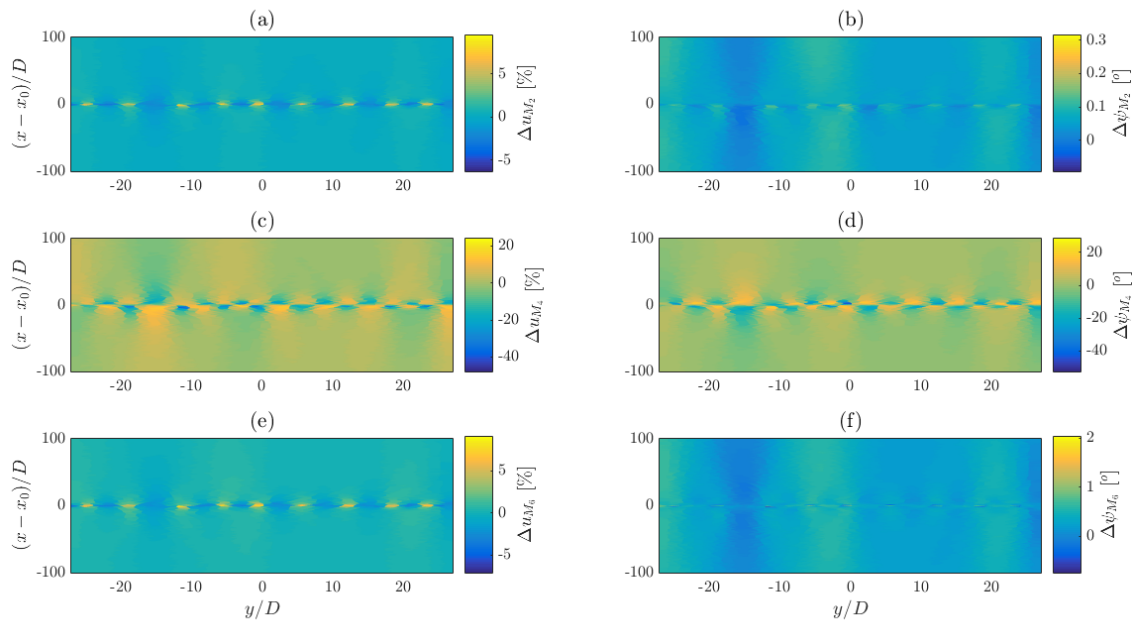
Figure 5.22: Contour plots of change to amplitudes (left column) and phases (right column) of the M_2 (top row), M_4 (middle row) and M_6 (bottom row) between Run-1 and Run-19, $5D$ spaced row. For this figure x-axis is the across channel and the y-axis is the along channel. The along channel distances have been normalised by the turbine diameter, D, and the across channel distances by the channel width, b. The definition of the along channel normalisation defined in such a way that the channel centre lies at zero, in the across channel the channel centre naturally lies at 0.
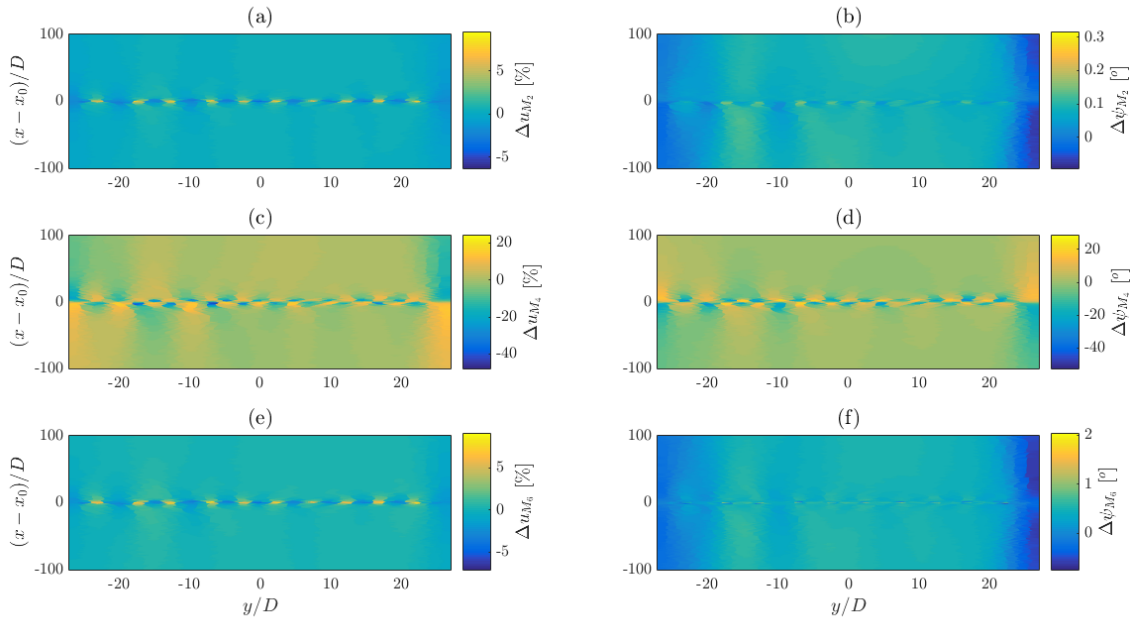
Figure 5.23: As Figure 5.22, but for the $4D$ row (Run-1–Run-20 difference).
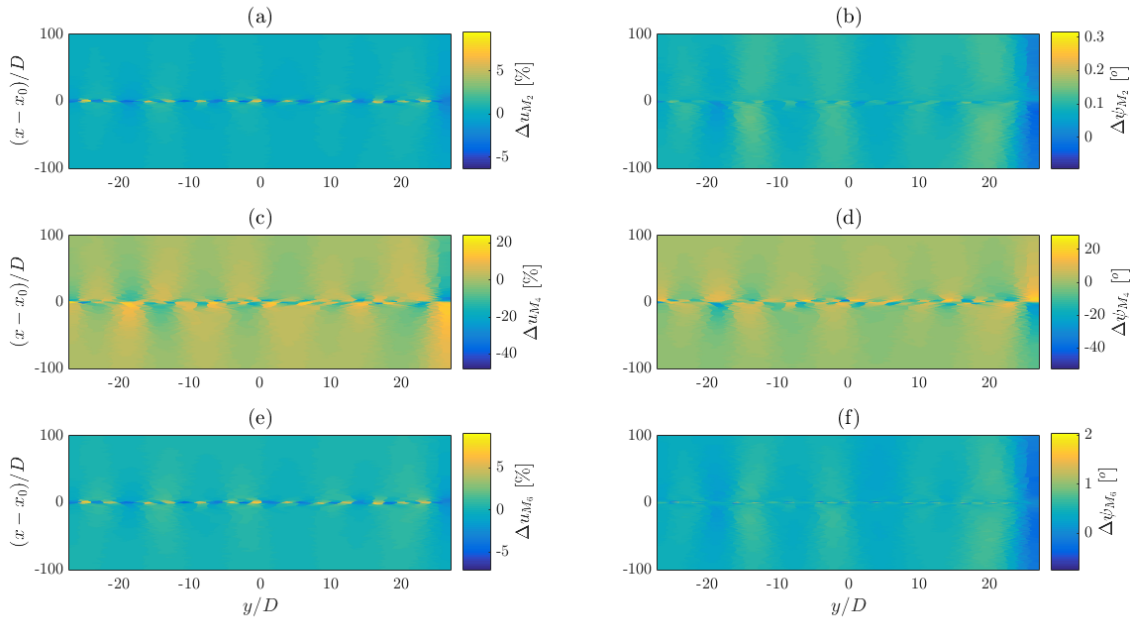
Figure 5.24: As Figure 5.22, but for the $3D$ row (Run-1–Run-20 difference).
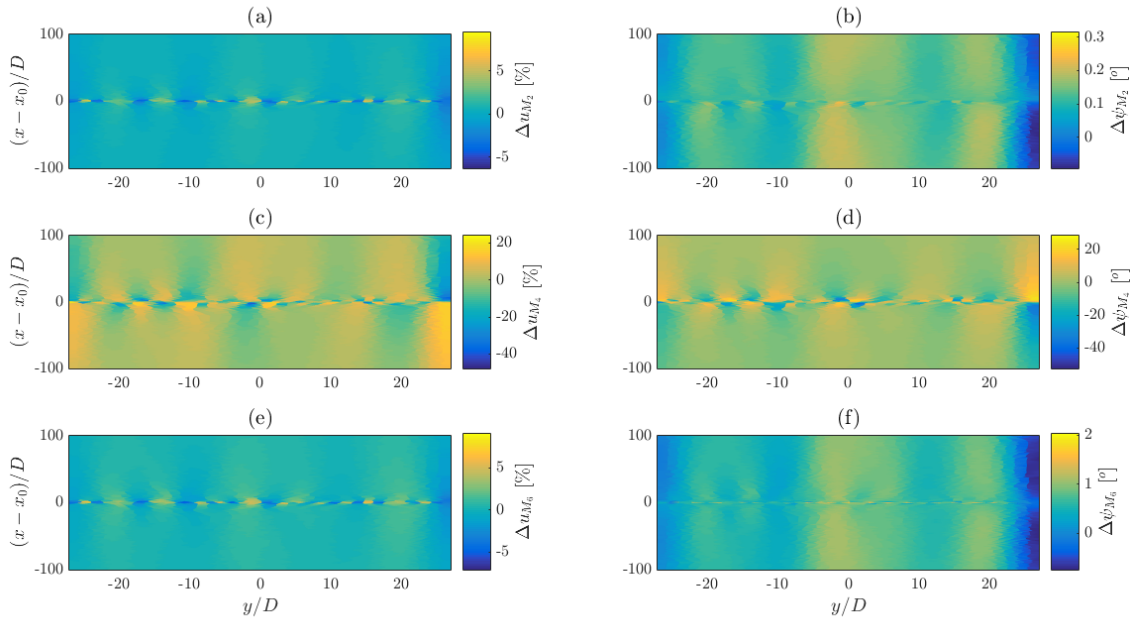
Figure 5.25: As Figure 5.22, but for the $2D$ row (Run-1–Run-20 difference).
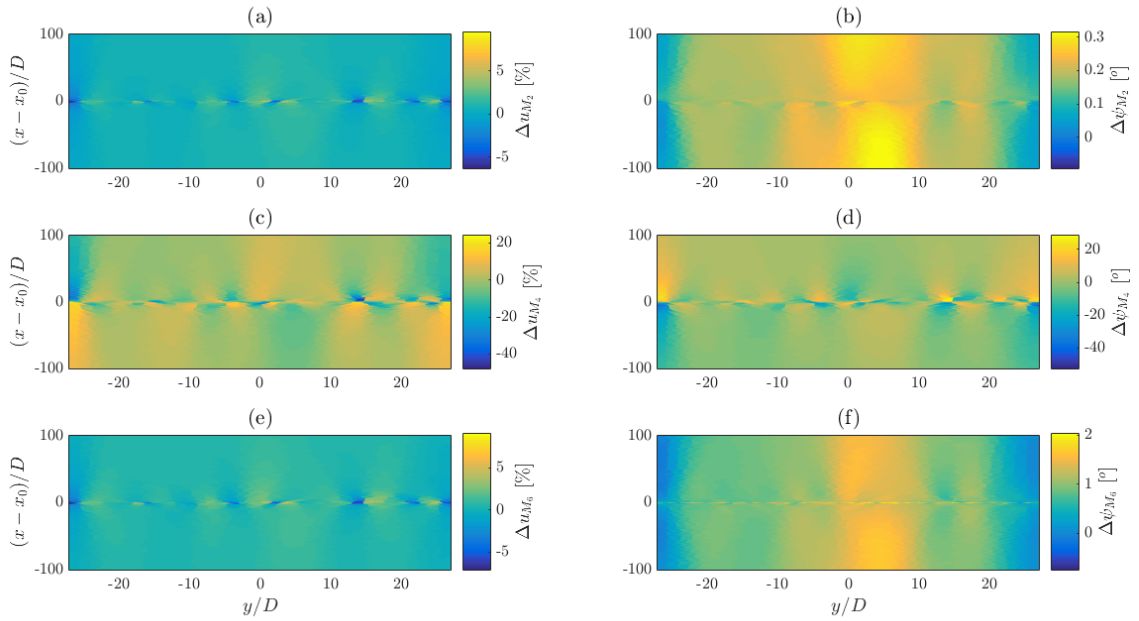
Figure 5.26: As Figure 5.22, but for the $1D$ row (Run-1–Run-20 difference).
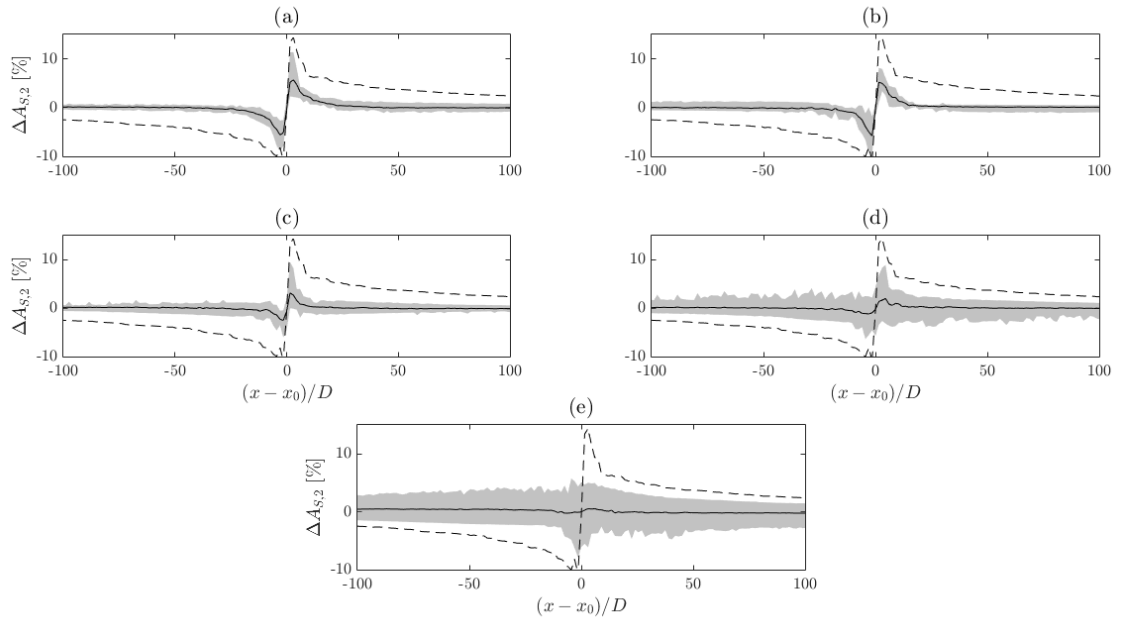
Figure 5.27: Mean (solid black line) and envelope (shaded grey area) of all profiles of change to the FVA between Run-1 and Run-19 [(a)], Run-20 [(b)], Run-21 [(c)], Run-22 [(d)] and Run-23 [(e)], along with the profiles of change between Run-1 and Run-2 (dashed black line). Along channel distances normalised as in Figure 5.17.

In Figure 5.30 the peak values of all parameters, averaged across all turbine profiles are plotted against the target turbine spacing[2]. For the M_2 and M_6 there was a clear trend of decreased peak changes in amplitude with decreasing turbine spacing and therefore more turbines (Figures 5.30a & 5.30c) and increased peak changes in phase with decreased turbine spacing (Figures 5.30d & 5.30f). Physically this can be interpreted as each turbine having a smaller effect on the current amplitude and a greater impact on the current phase per turbine when it is within a more densely packed row. For the M_4 this trend is less clear with the number of data-points available, but the indication here is that more turbines results in a smaller peak per turbine effect on both the amplitude and phase (Figures 5.30b & 5.30e). Physically, this implies less augmentation and reduction of the M_4 amplitude and phase per turbine when there are more turbines, and greater augmentation and reduction per turbine when there are more turbines. Finally, the indication from the $A_{S,2}$ plot

---

[2]These are the averages of the peak values across the profiles in each row experiment rather than the peak values of the average profiles.

(Figure 5.30g) is that more turbines in the row again results in a lower per-turbine peak change to the FVA.
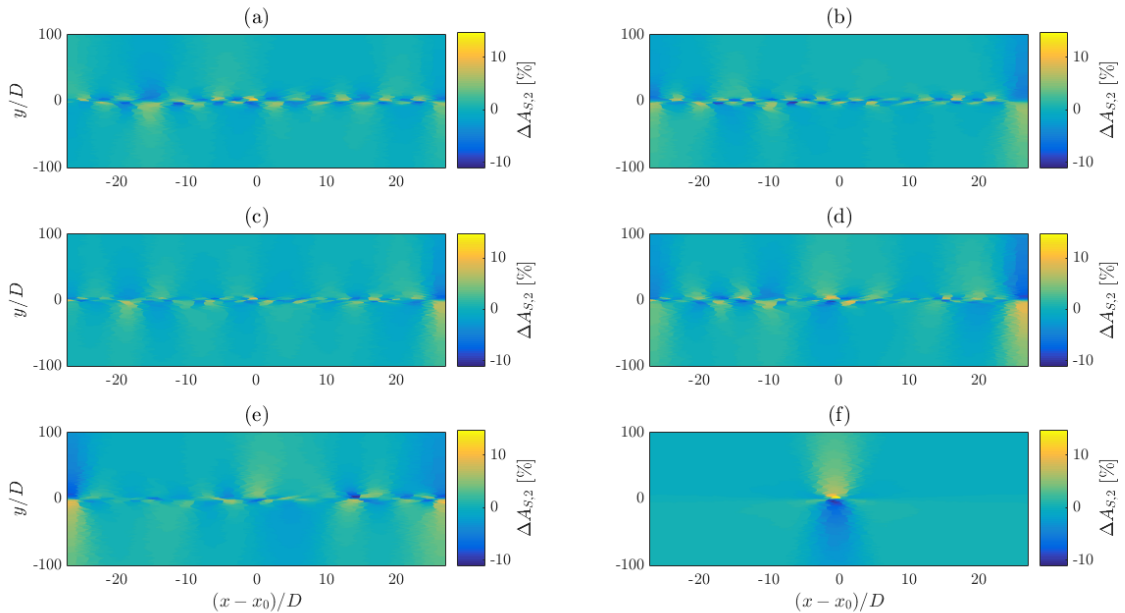
Figure 5.28: Contour plots of change to asymmetry between Run-1 and Run-2 [(a)], Run-19 [(b)], Run-20 [(c)], Run-21 [(d)], Run-22 [(e)] and Run-23 [(f)]. Axes and normalisation of along and across channel distances as in Figure 5.22.

Even if peak changes per turbine were smaller for the larger array, given that there were multiple turbines, the footprint[3] of change due to the turbine(s) would be expected to be larger for larger arrays. This is tested in Figures 5.31 & 5.32. The changes to the asymmetry, measured using the metric $A_{S,2}$ (4.2.2), and the M_2 current, were split into bins 1% wide from -11% to 15%, and from -7% to 10%, and mesh elements falling into each of these bins found. The areas of these elements were calculated and summed to give the values seen in Figure 5.31 & 5.32. In these figures the areas where the absolute change was <0–1% were not plotted, as most of the channel area falls into this category, thus this area dwarfs the areas experiencing all other ranges of change. The values used in Figures 5.31 & 5.32 are given in Tables 5.6 & 5.7, including those for the -1% to 0% and 0% to 1%.

---

[3]The total spatial area that, due to the effect of the turbine(s), experiences a change above a decided threshold.
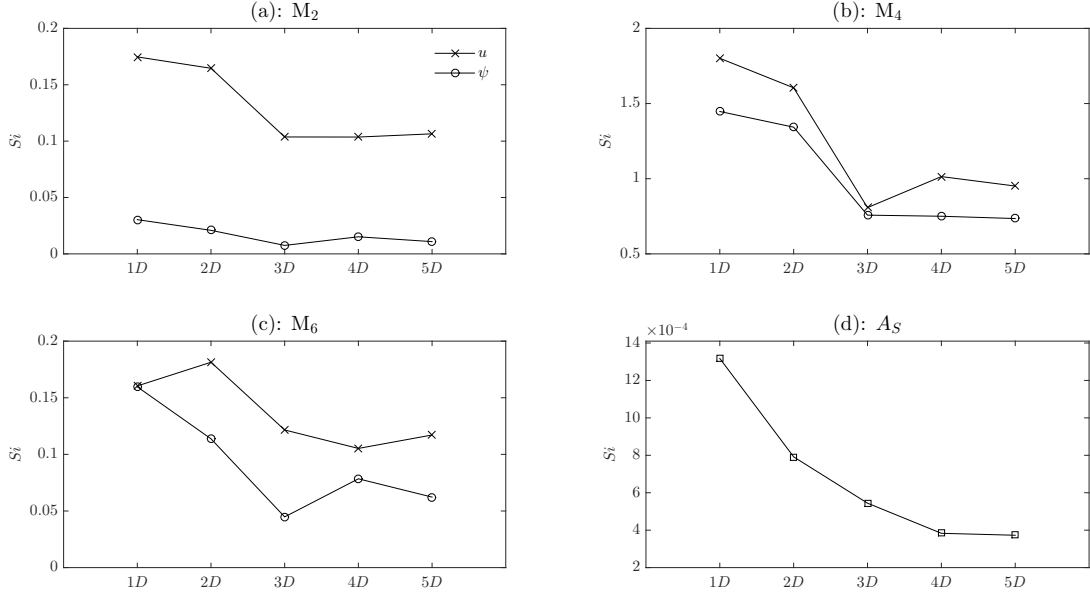
Figure 5.29: Plots of profile similarity parameter, Si, against inter-turbine spacing for the amplitude (crosses) and phase (circles) of the M_2 (a), M_4 (b), M_6 (c) and the asymmetry metric, A_S (d).

From Tables 5.6 & 5.7 and Figures 5.31 & 5.32 one can see that the smaller changes account for most of the area of the array footprint, Fp, which is the total area where the absolute change is greater than 1% (note that -1 to 0% and 0 to 1% contributions are not included in Fp). Raising the threshold used to define Fp to $|\Delta A_{S,2}| > 3\%$ would result in an order of magnitude drop in the size of Fp across all rows. Raising the threshold to $|\Delta A_{S,2}| > 6\%$ would lead to further order of magnitude drop in the size of Fp across all rows. For the $|\Delta A_{S,2}| > 1\%$, $|\Delta A_{S,2}| > 3\%$ and $|\Delta A_{S,2}| > 6\%$ thresholds the size of Fp for the five array runs was approximately $\mathcal{O}(10^6)$ m^2, $\mathcal{O}(10^5)$ m^2 and $\mathcal{O}(10^4)$ m^2, whilst the size of Fp for the single turbine runs was $\mathcal{O}(10^5)$ m^2 throughout, bringing the size of Fp for the array runs into line with the single turbine run. This highlights the importance of the choice of threshold. However, the choice of threshold is a complex issue. What is an acceptable level of change? The answer to this question is not known. Without knowing what constitutes an acceptable level of change it is not possible to set an appropriate threshold. This question lies beyond the scope of this thesis. However, the choice of threshold is not as important when the data is presented in Figures

5.31 & 5.32 and Tables 5.6 & 5.7 as all changes are presented, so any threshold may be applied the data to interrogate the results, so long as it is a change to the M_2 current and/or the FVA, expressed as a percentage change.
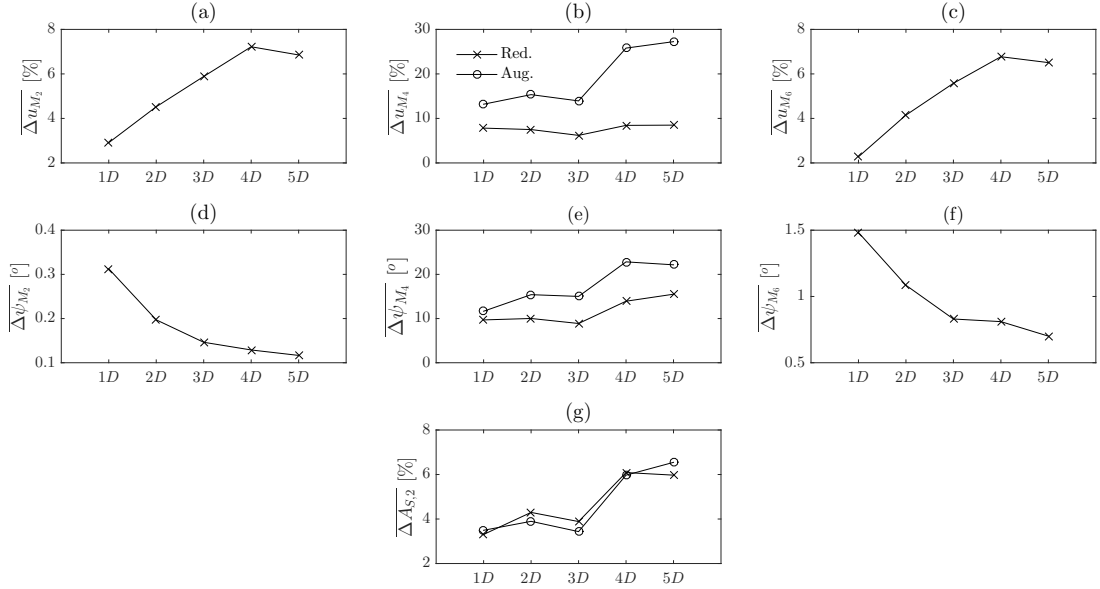
Figure 5.30: Plots of absolute peak values (crosses – positive peaks, circles – negative peaks) of the amplitude (top row) and phase (middle row) of the M_2 (first column), M_4 (middle column, top and middle rows) and M_6 (right column) and the asymmetry metric, $A_{S,2}$ (bottom row).

From Table 5.7 one can see that for the $5D$ and $4D$ spaced rows the area of -1 to -2% change is larger than the area of 1 to 2% change, and for the $5D$ and $3D$ spaced rows, the area of -2 to -3% changes is larger than the area of 2 to 3% change. The negative changes to the M_2 current represents the flow that is accelerated around the turbines, the bypass flow. For the wider spaced rows there is more area between the turbines, so naturally these negative changes were seen over a larger area. For the 13 turbine ($\varepsilon_0 \approx 0.10$) row the total area of negative change ($>1\%$) falls, before rising again for the 17 turbine ($\varepsilon_0 \approx 0.14$) row, then falling again for the 26 turbine ($\varepsilon_0 \approx 0.21$) row. For the highest blockage row the largest negative changes are seen whilst for the single turbine the largest positive changes are seen, i.e. the greatest velocity reductions occurred for the single turbine and the largest flow acceleration occurred for the highest blockage row.

Table 5.6: Areas experiencing changes of -11% to 15% to the FVA, divided into 1% bins, for each of the five row runs and the single turbine run.

N	1	9	10	13	17	26	
$\Delta A_{S,2}$			δFp [m^2]				$\delta Fp \times$
-11 to -10%	1.08	0.00	0.40	0.00	0.00	0.55	$\times 10^3$
-10 to -9%	0.93	0.00	2.04	0.00	0.36	0.77	$\times 10^3$
-9 to -8%	3.72	1.35	0.65	0.00	2.48	1.74	$\times 10^3$
-8 to -7%	0.35	0.37	0.43	0.21	0.96	1.23	$\times 10^4$
-7 to -6%	0.76	0.56	0.68	0.36	1.78	0.95	$\times 10^4$
-6 to -5%	1.34	1.81	1.25	0.95	3.43	1.45	$\times 10^4$
-5 to -4%	2.95	2.33	3.62	1.43	5.34	4.50	$\times 10^4$
-4 to -3%	0.48	0.46	0.72	0.37	1.15	1.32	$\times 10^5$
-3 to -2%	1.21	0.86	1.74	1.13	3.17	4.22	$\times 10^5$
-2 to -1%	0.39	0.47	0.71	0.43	0.89	1.36	$\times 10^6$
-1 to 0%	2.40	2.51	2.28	2.57	2.39	2.34	$\times 10^7$
0 to 1%	6.11	6.00	6.14	5.94	5.95	5.83	$\times 10^7$
1 to 2%	0.42	0.44	0.80	0.45	1.06	1.96	$\times 10^6$
2 to 3%	1.39	0.86	1.67	1.29	2.77	4.28	$\times 10^5$
3 to 4%	0.54	0.51	0.77	0.40	1.22	1.56	$\times 10^5$
4 to 5%	2.63	2.87	4.55	2.20	5.79	6.02	$\times 10^4$
5 to 6%	1.07	2.03	2.90	1.43	3.11	2.53	$\times 10^4$
6 to 7%	0.83	0.46	0.70	1.51	1.86	1.67	$\times 10^4$
7 to 8%	0.00	3.79	3.77	0.07	1.26	0.50	$\times 10^4$
8 to 9%	0.00	0.09	0.11	0.06	1.23	0.41	$\times 10^4$
9 to 10%	1.63	0.00	0.00	0.70	1.53	1.34	$\times 10^3$
10 to 11%	0.00	0.00	0.00	0.00	3.42	2.16	$\times 10^2$
11 to 12%	0.92	1.02	0.00	0.00	0.00	0.00	$\times 10^3$
12 to 13%	0.00	0.00	0.00	0.00	0.00	0.00	-
13 to 14%	3.94	0.00	0.00	0.00	0.00	0.00	$\times 10^2$
14 to 15%	6.29	0.00	0.00	0.00	0.00	0.00	$\times 10^2$
Fp [m^2]	1.28	1.29	2.15	1.28	3.04	4.66	$\times 10^6$
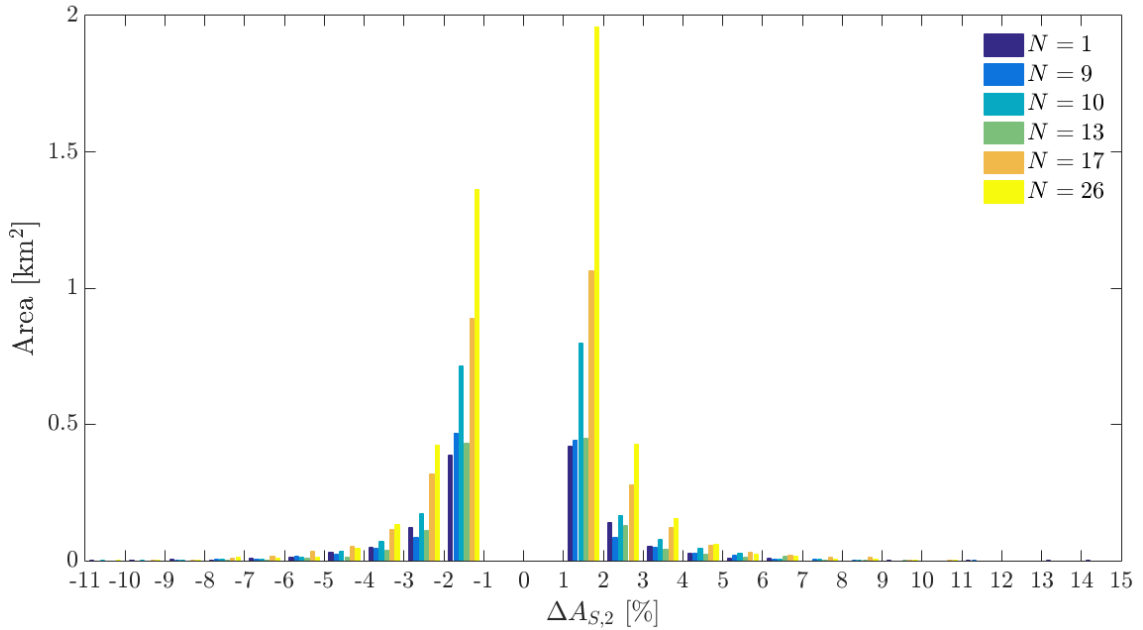
Figure 5.31: Areas of effect of percentage bins of change to FVA, measured using the asymmetry metric $A_{S,2}$, for the single turbine (navy blue bar), $5D$ spaced row (blue bar), $4D$ spaced row (cyan blue bar), $3D$ spaced row (green bar), $2D$ spaced row (orange bar) and $1D$ spaced row (yellow bar).

From Figures 5.16 & 5.26 one can see that the regions of highest flow acceleration coincided with the largest inter-turbine / turbine-wall spacing. For the higher blockage rows the pressure build up across the row will be higher, this higher pressure must then force the flow through these wider gaps leading to the larger flow accelerations. According to Garrett and Cummins [2007] and Vennell [2010] for higher blockage rows the by pass flow should have a lower velocity than in higher blockage rows. This is not seen in these results. From Figure 5.16, one can see that for the two most densely packed rows (Figures 5.16d & 5.16e) elements containing turbines are adjacent to one another, i.e. the inter-turbine spacing is not resolved. Therefore, the flow can only pass through the larger turbine spacings which are resolved, which is why larger flow acceleration is seen for these larger turbine spacings than the smaller turbine spacings.

The above raises the larger issue that rather than a row of turbines, a partial tidal fence is in-fact being simulated, and therefore the impact of these denser two rows is most likely overpredicted. This then raises questions over the steep increase

in the array footprint for these more densely packed rows. Potentially the footprint may remain at a similar level to the more sparsely packed rows. Higher resolution simulations, which adequately resolve the inter-turbine spacing of even the most densely packed rows would be required to explore this further.
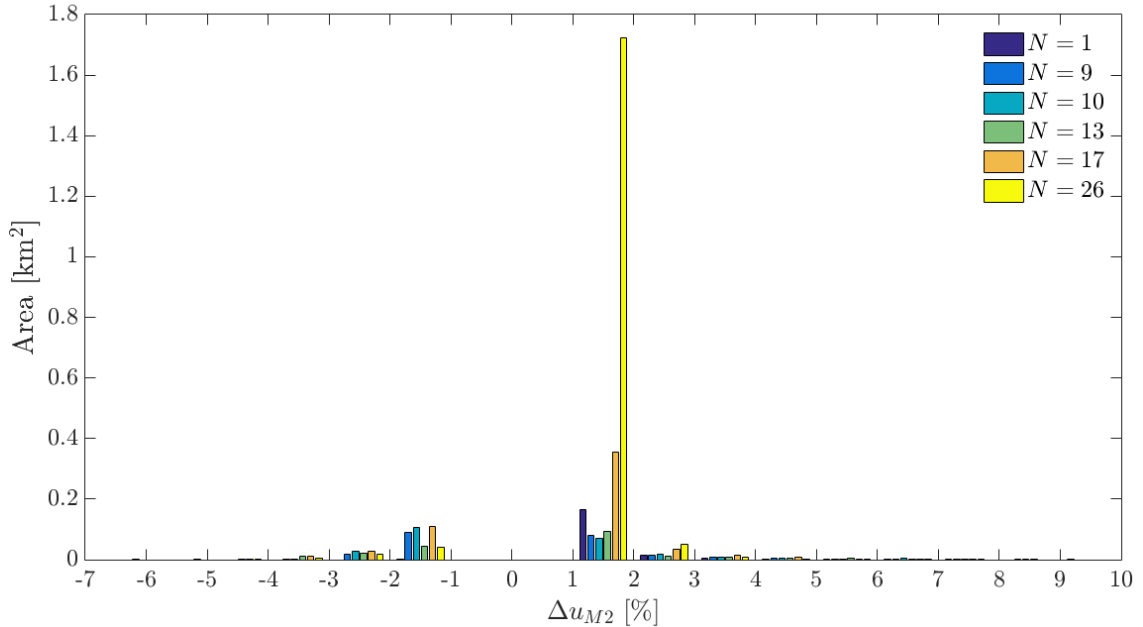
Figure 5.32: Areas of effect of percentage bins of change to u_{M2}, for the single turbine (navy blue bar), $5D$ spaced row (blue bar), $4D$ spaced row (cyan blue bar), $3D$ spaced row (green bar), $2D$ spaced row (orange bar) and $1D$ spaced row (yellow bar).

5.5   Summary

In this chapter the results from three experiments were presented, described and analysed. These experiments looked at the effect of multiple turbines and the interaction of the effects of multiple turbines. In the first experiment a single turbine was deployed in various locations based on the natural flood-ebb asymmetry of the current. In the second experiment a line of 3 turbines was deployed with longitudinal spacings $120D$, $60D$ and $20D$, and in the third experiment a single row of turbines with lateral turbine spacings of $5D$, $4D$, $3D$, $2D$ and $1D$, and therefore 9, 10, 13, 17 and 26 turbines respectively, equivalent to row blockages of $\varepsilon_0 = 0.07$,

0.08, 0.11, 0.14 and 0.21 were deployed. It is important to note that it is the effect of changing row blockage that is tested here rather than across channel spacing, for the latter to be tested the blockage would need to be fixed.

In the first experiment no trend between the ambient FVA, and the magnitude of the effect of the turbine on the FVA, was identified. In fact, little variation in the effect of the turbine on the FVA was seen. Greater variation on the impact of the turbine on the M_4 tide was seen, but these variations did not lead to a significant difference in the effect of the turbine on the FVA.

Table 5.7: Areas experiencing changes of -7% to 10% to the M_2 current, divided into 1% bins, for each of the five row runs and the single turbine run.

N	1	9	10	13	17	26	
$\Delta A_{S,2}$			δFp [m^2]				$\delta Fp\times$
-7 to -6%	0.00	0.00	0.00	0.00	0.00	7.83	$\times 10^2$
-6 to -5%	0.00	0.00	0.00	0.00	0.00	1.84	$\times 10^3$
-5 to -4%	0.00	0.00	0.00	0.45	3.27	2.70	$\times 10^3$
-4 to -3%	0.00	0.12	0.12	0.99	1.22	0.33	$\times 10^4$
-3 to -2%	0.00	1.77	2.63	2.17	2.74	1.79	$\times 10^4$
-2 to -1%	0.09	9.02	10.70	4.53	10.80	4.15	$\times 10^4$
-1 to 0%	1.52	0.08	0.16	0.05	0.09	0.05	$\times 10^7$
0 to 1%	7.11	8.53	8.45	8.57	8.50	8.41	$\times 10^7$
1 to 2%	0.16	0.08	0.07	0.09	0.36	1.72	$\times 10^6$
2 to 3%	1.59	1.56	1.88	1.03	3.29	5.15	$\times 10^4$
3 to 4%	0.43	0.76	0.75	0.80	1.33	0.70	$\times 10^4$
4 to 5%	1.28	5.41	6.12	6.20	9.38	2.53	$\times 10^3$
5 to 6%	1.12	2.89	2.49	4.94	1.35	0.38	$\times 10^3$
6 to 7%	0.39	2.95	3.61	0.92	0.49	0.35	$\times 10^3$
7 to 8%	0.93	1.03	1.46	1.28	1.32	0.00	$\times 10^3$
8 to 9%	0.00	9.02	8.17	4.88	0.00	0.00	$\times 10^2$
9 to 10%	4.36	0.00	0.00	0.00	0.00	0.00	$\times 10^2$
Fp [m^2]	0.19	0.22	0.25	0.20	0.57	1.85	$\times 10^5$

In the second experiment the results suggest that when multiple turbines are deployed along the longitudinal axis of the channel, there is an additive effect where the areas of effect interact. There was also a trend of increased overall effect when the turbines were deployed closer together. Turbines on the easternmost extremity of the line caused a greater difference in the effect on asymmetry when deployed in an array compared with their individual deployment than their westernmost counterparts. For the central and east-most turbine the reduction peak (positive peak to the east) is larger than the augmentation peak (negative peak to the west), whilst the situation is reversed for the west-most turbine. Therefore, if there is indeed an additive effect then the turbine to the east is superimposed upon the larger reduction peak to the east of the central turbine and the turbine to the west is superimposed upon the smaller augmentation peak to the west of the central turbine. In this case one would expect to see a larger difference between the turbine deployed individually and the individual turbine in the array for the east-most turbine and a smaller difference for the west-most turbine. Which is what is seen.

In the third experiment it was seen that with increased row blockage the peak per-turbine change to all parameters but the M_2 and M_6 phase was reduced (Figures 5.17–5.21 & 5.27). For the M_2 and M_6 phase an increase in row blockage led to an increase in the per-turbine phase reduction (Figures 5.17–5.21 & 5.27). Physically this means smaller velocity deficits (and increases in the case of the M_4 current) in the turbine wakes in rows compared to individual turbines, with the difference growing larger with increased row blockage (Figure 5.30). At the same time the phase lag on the M_2 and M_6 tide introduced by the row increased with increased blockage, but for the M_4 the positive and negative phase shift imparted by the row reduced with increased blockage (Figure 5.30). Of these constituents the M_2 represents the progression of the forcing tidal wave, thus the phase lag indicates an impediment to the tidal wave resulting from the row of turbines. An impediment that is increased with increased blockage. According to Vennell [2012, 2013] increased blockage leads to an increased head difference across the turbine row. The power produced by the turbines then derives from both this head difference and the momentum of the flow, which leads to reduced velocity deficits in the turbine wakes at higher row blockage values. Which is indeed what is seen in this

experiment.

The spatial extent of the changes resulting from the turbine rows were also explored in this experiment, using the footprint of the row, Fp, on the FVA and M_2 current, where the footprint is defined as the total area where the absolute change exceeds some threshold. The footprint, Fp, and the variation in Fp with N, the number of turbines in the row, was sensitive to the choice of threshold. However, what constitutes a suitable threshold is at best subjective and at worst unknown and was therefore not considered in this thesis.

Across all row runs smaller changes made up most of Fp (Figures 5.31 & 5.32 and Tables 5.6 & 5.7). When a low threshold is chosen, e.g. 1%, Fp was larger for higher blockage rows, which had larger N. The difference between the footprint of a single turbine and rows up to $N = 13$ was small (Table 5.7).

The difference between the two highest blockage rows runs and the remaining row runs may be explained by the lack of mesh resolution to adequately resolve all inter-turbine spacings in the higher blockage rows. This numerical issue means it is likely that the footprint of the row is overestimated, as the bypass flow between some turbines is not resolved, and therefore wake recovery will be underestimated. Simulations using a higher resolution mesh would be required to address this issue.

Chapter 6

Implications of Changes to Flood-Ebb Asymmetry: Turbine Power and Sediment Transport

6.1   Introduction

In the previous chapters it has been shown that turbines alter the Flow Velocity Asymmetry (FVA) and therefore the M_4 current. Such changes to the FVA may have knock on effects for sediment transport given the role FVA plays in sediment transport (see Chapter 2, §2.4). Also, the FVA will affect the technically exploitable tidal resource, and therefore energy generation (see Chapter 2, §2.4).

In §6.2, model output from Chapters 4 & 5 will be re-analysed to investigate energy conversion by the turbines, addressing research question *3a*) (§2.5.2). In §6.3, additional model runs will be carried out using the sediment transport module from MIKE 21 coupled with the hydrodynamic module. These experiments will look at the effect of changes to the asymmetry due a single turbine on sediment transport. This section addresses research question *3b*) (§2.5.2). Finally, in §6.4, the findings from this chapter will be summarised.

6.2 Flood-Ebb Asymmetry and Turbine Power

The turbine power (neglecting internal losses) is given by the product of the force on the turbine and the velocity of the flow through the turbine. Taking the turbine force from the MIKE 21 manual (see also Chapter 3, §3.1.3), the power produced by the turbine is given by:

$$P_T = \frac{1}{2}\rho C_T A \alpha^2 u_T^3 \tag{6.2.1}$$

where α is a velocity correction factor, C_T is the turbine thrust coefficient, A is the swept area of the turbine rotor and u_T is the flow velocity in the turbine element. The correction factor is required as turbine forces are defined using the free-stream velocity, but as the size of the model element is reduced the velocity value in the element diverges from the free-stream value. The correction factor is given by Kramer et al. [2014] as:

$$\alpha = \frac{2}{1 + \sqrt{1 - \gamma}} \tag{6.2.2}$$

where $\gamma = C_T A/(h\Delta y)$, h is the water depth and Δy is the width of the element perpendicular to the flow direction.

The energy conversion over the flood or ebb phases of the tide by the turbine, $E_{f,e}$, may then be calculated by:

$$E_{f,e} = \int_{f,e} |P|\ dt \tag{6.2.3}$$

i.e. the power integrated over either the flood or ebb phase of the tidal cycle. The difference between the energy converted over the flood and ebb phases, ΔE, and the energy converted over the whole tidal cycle, $E_{t.c.}$, can be calculated by:

$$\Delta E = 100 \times \frac{2(E_f - E_e)}{E_f + E_e} \tag{6.2.4}$$

and

$$E_{t.c.} = E_f + E_e \tag{6.2.5}$$

respectively.
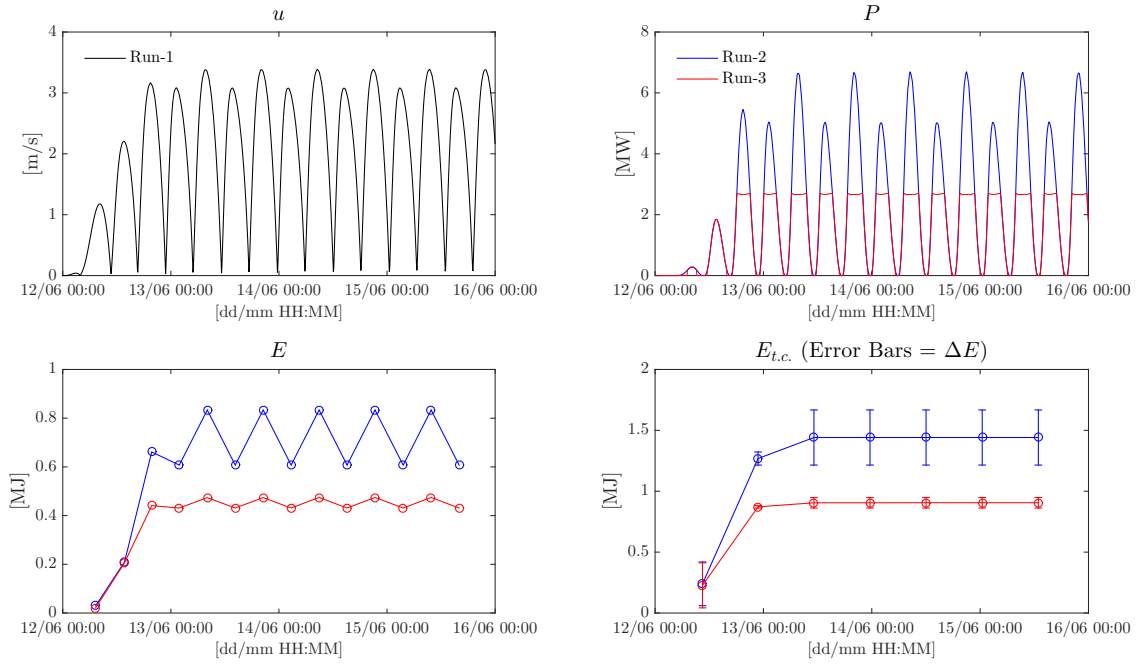
Figure 6.1: Time-series of u-velocity component, u, (top left), turbine power, P, (top right), turbine energy conversion over phases of the tide (either flood or ebb), E, (bottom left), and energy conversion over a tidal cycle, $E_{t.c.}$, and difference between energy conversion over the flood and ebb of the tide, ΔE, (bottom right). In the bottom right time-series the circles denote $E_{t.c.}$ and the amplitude of the error bars ΔE.

In the analysis in Section 6.2.1, equation (6.2.1), and the dependant equations (6.2.3) to (6.2.5), are applied to elements not containing turbines. Whilst (6.2.1) has been derived for a turbine. The aim of this was a first order investigation of the influence of the hydrodynamic changes identified in Chapter 4 on the power available to additional turbines. What is not accounted for in this analysis is the co-effect of multiple turbines. This is explored in Sections 6.2.2 and 6.2.3.

6.2.1 Single Turbine

On the way to addressing research question *3a)*, "Can the change to the technically exploitable resource be predicted from the changes to the flow asymmetry?", the intermediary question "how does the change to the hydrodynamics resulting from the turbine operation impact on the energy conversion of further turbines" will

be addressed first. To answer this, the changes between Run-1 (no-turbine run) and Run-2 (single fixed-C_T turbine run) will be revisited, along with the changes between Run-1 and Run-3 (single variable-C_T turbine (defined §2.5.2, (2.5.2) & Figure 2.9) run). In Figure 6.1, time-series of u, P, E, $E_{t.c.}$ and ΔE for the turbines in Run-2 and Run-3 are plotted. These time-series show that, once the model stabilises following the spin-up period, the values of $E_{t.c.}$ and ΔE stabilise. Therefore, the changes to these stable values between Run-1 and Run-2, and, Run-1 and Run-3, can be compared to changes to the M_2 current amplitude (u_{M_2}) and flood-ebb magnitude asymmetry (or FVA: $A_{S,2}$), both of which will also have stable values at each model element.
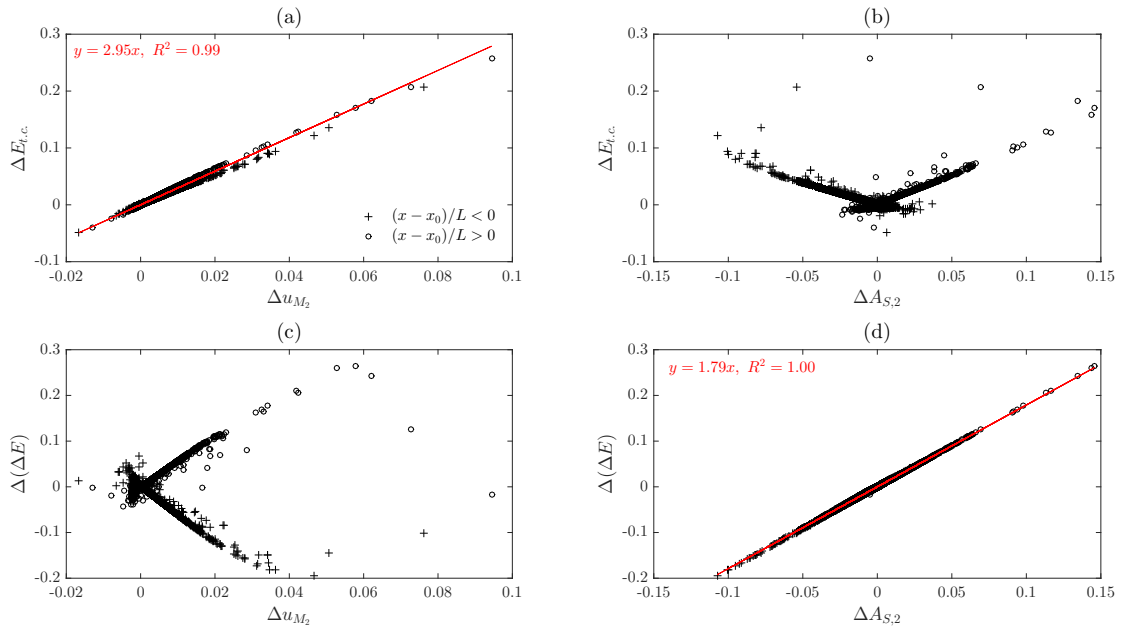
Figure 6.2: Comparisons of change in energy conversion over a tidal cycle, $\Delta E_{t.c.}$, top row, and change in the difference in energy conversion over the flood and ebb of the tide, $\Delta(\Delta E)$, bottom row, against the change in M_2 amplitude, Δu_{M_2}, left column, and the change in the asymmetry, $\Delta A_{S,2}$, right column, for a fixed-C_T turbine and additional fixed-C_T turbines. Pluses (+) denote elements in the eastern half of the channel, $(x - x_0)/L < 0$, and circles (o) denote elements in the western half of the channel, $(x - x_0)/L > 0$ (x_0 – x-coordinate of channel centre).

The changes to u_{M_2} (Δu_{M_2}) and $A_{S,2}$ ($\Delta A_{S,2}$) between these two sets of runs will be compared to the changes to ΔE ($\Delta(\Delta E)$) and $E_{t.c.}$ ($\Delta E_{t.c.}$) for further

fixed- or variable-C_T turbines added to the channel, estimated from u time-series in the elements throughout the model. The changes are defined as:

$$\Delta X = \frac{X_1 - X_{2,3}}{X_1} \tag{6.2.6}$$

for $X = u_{M_2}$, $A_{S,2}$ and $E_{t.c.}$, and

$$\Delta(\Delta E) = \Delta E_1 - \Delta E_{2,3} \tag{6.2.7}$$

where the subscripts 1, 2 and 3 denote terms related to Run-1, Run-2 and Run-3 respectively. These changes are compared in Figure 6.2 for the fixed-C_T turbine case and in Figure 6.3 for the variable-C_T turbine case.
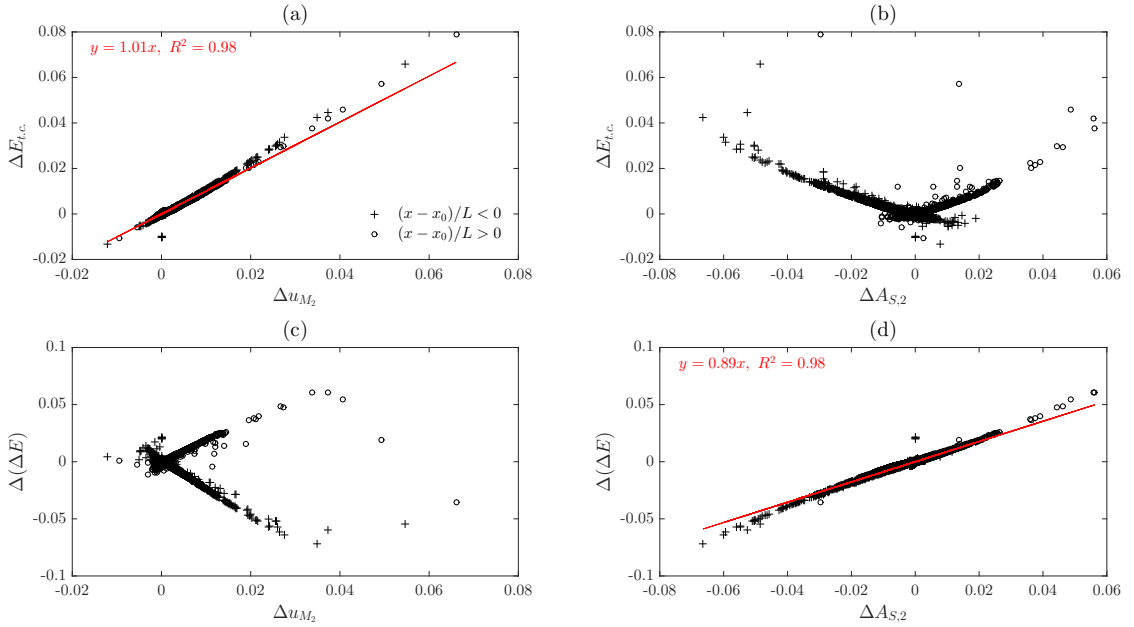
Figure 6.3: As Figure 6.2 but for a variable-C_T.

In Figures 6.2 and 6.3 the eastern $((x-x_0)/L < 0)$[1] and western $((x-x_0)/L > 0)$ halves of the channel have been plotted separately, as augmentation to $A_{S,2}$ was seen to the east of the turbine and reduction to the west (Chapter 4, Figures 4.5 and 4.8). Clear linear trends between Δu_{M_2} and $\Delta E_{t.c.}$, and between $\Delta(\Delta E)$ and $\Delta A_{S,2}$ can be seen in Figures 6.2a and 6.3a, and Figures 6.2d and 6.3d, respectively. Both these trends are simple to understand, and expected. With lower currents

---

[1]Where x_0 is the x-coordinate of the channel centre.

there will be less power, and therefore less energy conversion and, as the largest constituent of the current, the M_2 will have the greatest impact on $E_{t.c.}$. As the FVA, quantified as $A_{S,2}$, increases/decreases, one expects greater/less asymmetry in the energy conversion over the flood and ebb phases of the tide, given by ΔE.
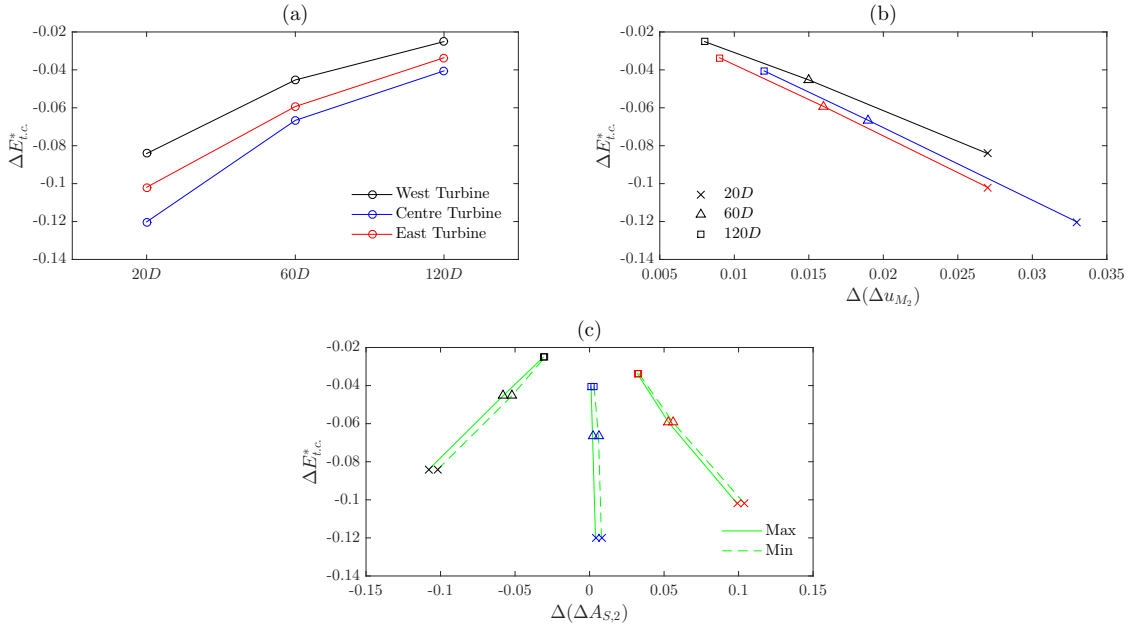
Figure 6.4: Difference in the energy conversion per tidal cycle between the turbine operating individually and as part of an array, $\Delta E_{t.c.}$, for different longitudinal turbine spacings, (a). Plots $\Delta E_{t.c.}$ against the difference in the change in M_2 current amplitude, $\Delta(\Delta u_{M_2})$, (b), the difference in the change in asymmetry, $\Delta(\Delta A_{S,2})$, (c).

In Figures 6.2b, 6.2c, 6.3b and 6.3c twin tails are seen in the plots, identified as western and eastern tails by the separate plotting of elements lying to the east and west of the channel centre. These twin tails are the result of the eastern augmentation and western reduction in $A_{S,2}$ resulting from the turbine operation. Conversely, reduction to the M_2 was seen in both directions (Chapter 4, Figures 4.3 and 4.7) as the result of the turbine operation, and is seen in Figures 6.2a, 6.2c, 6.3a and 6.3c[2]. The linear trends in Figures 6.2a and 6.3a and lack of such trends in Figures 6.2b and 6.3b imply that changes to $A_{S,2}$ do not play an important role

---

[2]In some elements an increase in u_{M_2} was seen (negative values). This is due to the acceleration of the flow around the turbine due to the pressure build up resulting from the blockage the turbine offers to the flow.

in changes to $E_{t.c.}$, compared to the changes to the M_2 current. Similarly, the linear trends in Figures 6.2d and 6.3d and lack of such trends in Figures 6.2c and 6.3c imply that changes to u_{M_2} do not play as important a role in the changes to ΔE as changes to $A_{S,2}$, which in turn implies it is the changes to the M_4 current that dictate the changes to $A_{S,2}$.

Comparing Figures 6.2 and 6.3; the gradient of the lines of best fit are shallower in Figure 6.3, suggesting that variable-C_T turbines are less sensitive to changes to the current magnitude and FVA than fixed-C_T turbines. The R^2 values show that the lines of best fit, fit less well in the variable-C_T case. From visual inspection of Figure 6.3 one can see that it is the largest changes that diverge from the trend the most. Given that these largest changes will occur closest to the turbine, and that additional turbines will not be deployed in such close proximity, the linear trends can then be considered applicable in practice.

The 95% confidence intervals of the u_{M2}-$\Delta E_{t.c.}$ and $A_{S,2}$-$\Delta(\Delta E)$ regressions from the fixed-C_T plot are 0.15% and 0.05% respectively, and 0.05% and 0.10% respectively for the variable-C_T regressions. From these linear models it is estimated that a 1% change to u_{M2} will lead to a 2.95±0.15% change to $E_{t.c.}$ for a fixed-C_T turbine or a 1.01±0.05% change for a variable-C_T turbine, and a 1% change to $A_{S,2}$ will lead to a 1.79±0.05% change to ΔE for a fixed-C_T turbine or 0.89±0.10% change for a variable-C_T turbine.

6.2.2 Lines of Turbines

The energy conversion for the turbine arrays aligned along the channel discussed in Chapter 5 §5.3 are compared against the energy conversion for those turbines had they been deployed individually in Figures 6.4 and 6.5. In these figures the behaviour of $E_{t.c.}$ and ΔE for a line of turbines are explored respectively. The differences in $E_{t.c.}$ and ΔE between the turbine, i, operating individually and as part of an array is given by:

$$\Delta E_{t.c.}{}^{*i} = \frac{E_{t.c.,A}^{i} - E_{t.c.,I}^{i}}{E_{t.c.,A}^{i}} \qquad (6.2.8)$$

and

$$\Delta(\Delta E^i)^* = \Delta E_A^i - \Delta E_I^i \tag{6.2.9}$$

where the subscripts A and I denote parameters pertaining to the array and individual runs respectively.
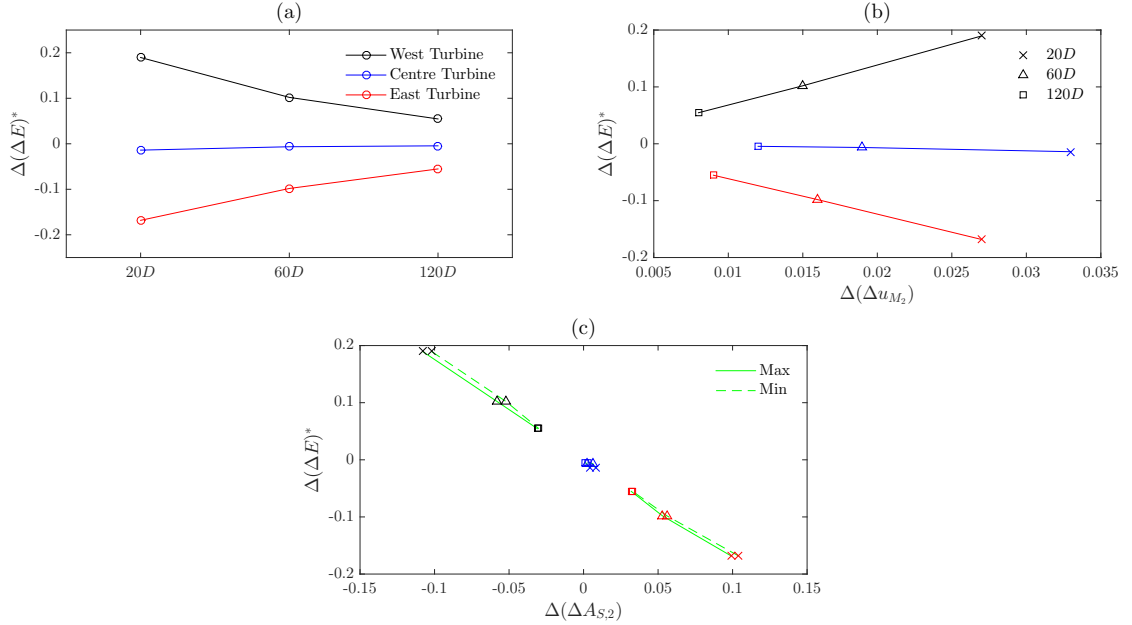
Figure 6.5: Difference in the flood-ebb energy conversion asymmetry between the turbine operating individually and as part of an array, $\Delta(\Delta E)$, for different longitudinal turbine spacings, (a). Plots $\Delta(\Delta E)$ against the difference in the change in M_2 current amplitude, $\Delta(\Delta u_{M_2})$, (b), and the difference in the change in asymmetry, $\Delta(\Delta A_{S,2})$, (c).

In Figure 6.4a, one can see that for all spacings, and for all turbines, $E_{t.c.}$ is smaller in the array run than the individual run. As the inter-turbine spacing decreases, the smaller $E_{t.c.}$ becomes compared to the individual case. In Figure 6.4b, $\Delta E_{t.c.}^*$ is plotted against $\Delta(\Delta u_{M_2})$, where:

$$\Delta(\Delta u_{M_2}^i) = \frac{\Delta u_{M_2,A}^i - \Delta u_{M_2,I}^i}{\Delta u_{M_2,A}^i} \tag{6.2.10}$$

From this plot one can see that there was a strong linear trend between $\Delta(\Delta u_{M_2})$ and $\Delta E_{t.c.}^*$ across all turbines. Physically this may be interpreted as the turbine in the array having a larger impact on the M_2 current than the turbine individually, with the difference increasing with reduced spacing. The knock-on effect of this is

then less energy conversion per tidal cycle for the turbines. Finally, in Figure 6.4c, $\Delta E_{t.c.}{}^{*}$ is plotted against $\Delta(\Delta A_{S,2})$, where:

$$\Delta(\Delta A_{S,2}{}^{i}) = \Delta A_{S,A} - \Delta A_{S,I} \qquad (6.2.11)$$

No apparent trend between $\Delta(\Delta A_{S,2})$ and $\Delta E_{t.c.}{}^{*}$ is seen in this plot. This, along with what was seen in Figures 6.2 and 6.3, was taken to suggest that it was the impact of the surrounding turbines on the M_2 current that caused the differences in the energy conversion per tidal cycle between the turbine operating as an individual and as part of an array rather than the impact of the surrounding turbines on $A_{S,2}$. These findings for the the line of turbines are in-line with the predictions made from the single turbine analysis.
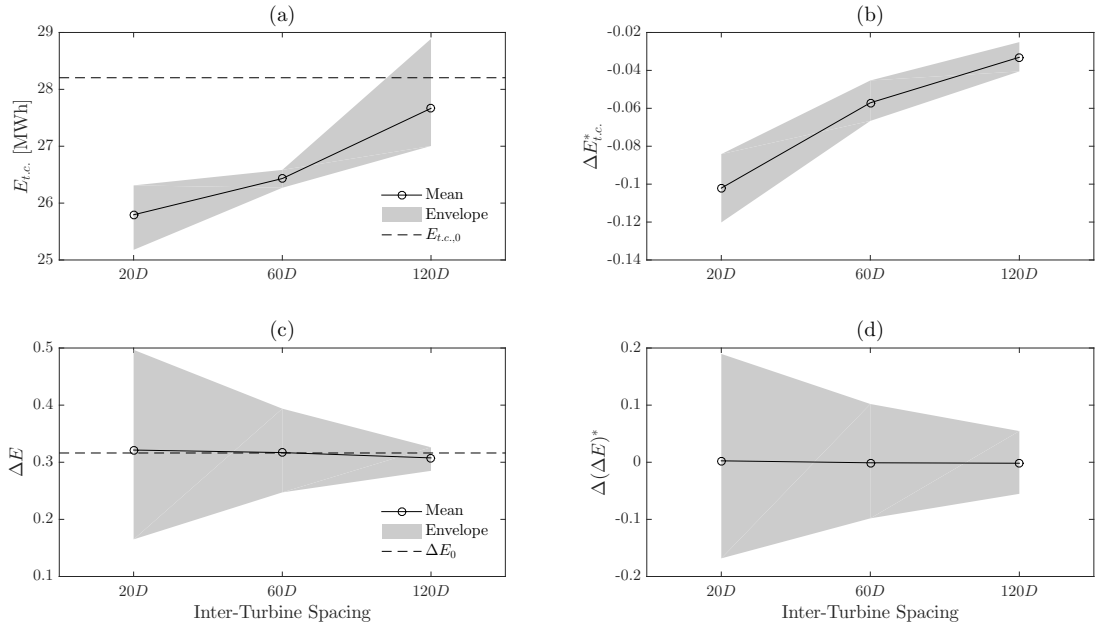
Figure 6.6: (a): Mean (across all turbines in array) energy conversion per tidal cycle for various inter-turbine spacings. (b): Mean difference in energy conversion per tidal cycle between the turbine operating as part of an array or individually. (c): Mean difference in energy conversion over the flood and ebb of the tide. (d): Mean absolute difference in the flood-ebb energy conversion asymmetry between the turbine operating individually and as part of an array. Envelope given by maximum and minimum values.

Figure 6.5 presents a similar set of plots to Figure 6.4, but for $\Delta(\Delta E)^*$ rather than $\Delta E_{t.c.}{}^*$. From Figure 6.5a, one can see that, as the inter-turbine spacing of the array reduced, $\Delta(\Delta E)^*$ increases for all turbines (in absolute terms). The differences for the easternmost and westernmost turbines are similar. However, in the case of the westernmost turbine, ΔE was larger for the individual turbine, whilst the opposite is true for the other two turbines. For the central turbine the difference is small. The plot of $\Delta(\Delta E)^*$ against $\Delta(\Delta u_{M_2})$ tells a similar story to the plot of $\Delta E_{t.c.}{}^*$ against $\Delta(\Delta A_{S,2})$. The suggestion from this subplot and Figures 6.2 and 6.3 is that it is not the effect of the surrounding turbine on the M_2 current that is of the most importance to $\Delta(\Delta E)^*$, but the effect on $\Delta(\Delta A_{S,2})$. This is seen in Figure 6.5c. In this figure $\Delta(\Delta E)^*$ is plotted against $\Delta(\Delta A_{S,2})$ and a linear trend between $\Delta(\Delta E)^*$ and $\Delta(\Delta A_{S,2})$ can be seen. This, along with Figures 6.2 and 6.3, is taken to imply that the changes to asymmetry due to the surrounding turbines lead to changes to ΔE for each turbine in the array, compared to that turbine operating individually.

In the final figure relating to the line array experiment, Figure 6.6, the averages of $E_{t.c.}$, ΔE, $\Delta E_{t.c.}{}^*$ and $\Delta(\Delta E)^*$ across all turbines in the array are plotted against the inter-turbine spacing, along with an envelope given by the maximum and minimum values. From this set of figures ((a)–(d)) one can see that, on average, each turbine will convert more energy per tidal cycle if the inter-turbine spacing is larger, and as seen previously, the turbines will convert less energy than if they were deployed individually. The mean of ΔE remains similar regardless of the inter-turbine spacing. However, with reduced spacing the spread of ΔE increases.

6.2.3 Rows of Turbines

Finally, the energy conversion of turbines deployed in rows across the channel is explored. In Figure 6.7 the difference between the peak values of profiles of Δu_{M_2} and $\Delta A_{S,2}$ for each individual turbine that makes up the rows discussed in Chapter 5 (§5.4) are plotted against the respective difference in $E_{t.c.}$ and ΔE between array and individual runs, defined as in (6.2.8) and (6.2.9). The mean values across all turbines in the row are also plotted in red and connected by a line. Of these plots, only that of $\Delta(\Delta u_{M_2})$ against $\Delta E_{t.c.}{}^*$ hints at any trend. The positive values of

$\Delta E_{t.c.}$ mean there is greater energy conversion per tidal cycle for the turbines in the array than an individual turbine, and the negative values of $\Delta(\Delta u_{M_2})$ mean there is less impact, per turbine, on the M_2 current by the turbines when they are part of the array. The trend is that of larger $\Delta E_{t.c.}{}^*$ with larger $|\Delta(\Delta u_{M_2})|$, and larger $|\Delta(\Delta u_{M_2})|$ for denser arrays. The modulus sign is used here as $\Delta(\Delta u_{M_2})$ is negative due to the per turbine Δu_{M_2} being smaller in the array than individually.
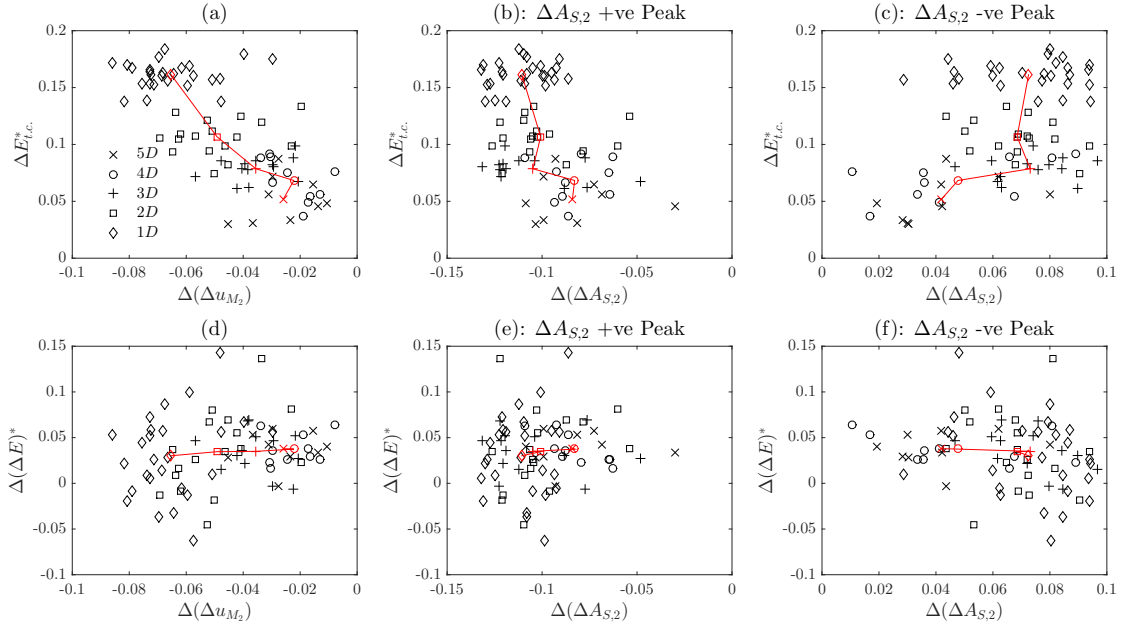
Figure 6.7: Plots of peak values of change to M_2 current, Δu_{M_2}, (left column) and absolute change to positive (centre column) and negative (right column) $\Delta A_{S,2}$ peaks, against the change to energy conversion per tidal cycle, $\Delta E_{t.c.}$, (top row) and change to the energy conversion asymmetry, $\Delta(\Delta E)$, (bottom row).

For $\Delta(\Delta A_{S,2})$ the positive and negative $\Delta A_{S,2}$ peaks (see Chapter 4, Figures 4.5 and 4.8 and Chapter 5, Figure 5.23) have been plotted separately against $\Delta E_{t.c.}{}^*$ and $\Delta(\Delta E)^*$ in Figure 6.7. The comparisons of $\Delta E_{t.c.}{}^*$ and $\Delta(\Delta E)^*$ against the positive and negative $\Delta A_{S,2}$ peaks appear similar, somewhat symmetric about the y-axis. The positive $\Delta A_{S,2}$ peaks are smaller in the array runs, and the negative $\Delta A_{S,2}$ peak is larger in array runs, compared to the individual run. Therefore, similar but opposite patterns are seen in the $\Delta(\Delta A_{S,2})$ plots (Figure 6.7b, 6.7c, 6.7e and 6.7f). On average, the difference in ΔE is small between the array runs and the individual run, $\sim$4%, but as seen in Figure 6.7 the variation between turbines

is large, increasingly so for the denser rows[3]. This variation could be caused by the increased variability of the inter-turbine spacing, longitudinal turbine location and element size, as discussed in Chapter 5 (§5.4.2), shown in Table 5.5 and discussed in Appendix F respectively. A clear trend between $\Delta(\Delta E)^*$ and $\Delta(\Delta A_{S,2})$ is not apparent from Figure 6.7, and likewise for $\Delta(\Delta E)^*$ and $\Delta(\Delta u_{M_2})$. Figures 6.2 and 6.3 suggest that it should be changes to $\Delta A_{S,2}$ that lead to changes to ΔE, but this is not what is seen in Figure 6.7. It may be that the differences seen in ΔE between the array runs and the individual run is due to a combination of the change to Δu_{M_2}, $\Delta A_{S,2}$ and variability of the location of the turbine / inter-turbine spacing / element size, and as such no simple trend between $\Delta(\Delta E)^*$ and the change in any one other parameter is identifiable.

In Figure 6.8 the mean values of $E_{t.c.}$, $\Delta E_{t.c.}{}^*$, ΔE and $\Delta(\Delta E)^*$ are plotted against the inter-turbine spacing along with an envelope defined by the maximum and minimum values. From this figure one can see that as the inter-turbine spacing is reduced there is a greater difference between the mean $E_{t.c.}$ per turbine in the array and an individual turbine, with the mean values of $E_{t.c.}$ increasing with reduced inter-turbine spacing (Figure 6.8a). This can be attributed to a number of factors, first, with increased blockage the turbine wakes have less opportunity to mix with the bypass flow due to their closer proximity [Garrett and Cummins, 2007, 2008, Vennell, 2010]. Second, with the increased blockage there is increased impediment to the flow, thus a head difference across the row of turbines develops, and the turbines produced their energy from this head difference in addition to the momentum of the flow which leads to a reduced velocity deficit in the turbine wakes [Vennell, 2012, 2013]. With this reduced velocity defect mixing of the wake with the bypass flow is again reduced leading to more efficient energy conversion by the turbines. Figure 6.8b echoes what is seen in Figure 6.8a. Turbines convert more energy per turbine when deployed in a row compared to deployed individually.

---

[3]One sees this even more clearly in Figure 6.8.

6.3 Flood-Ebb Asymmetry and Sediment Transport

The driver of sediment transport is bed shear stress, τ, resulting from the flow of water over the sea-bed. The bed shear stress is given by:

$$\vec{\tau} = \rho_0 C_F \vec{\overline{V}} |\vec{\overline{V}}| \qquad (6.3.1)$$

where C_F is the friction coefficient and $\vec{\overline{V}} = (\overline{u}, \overline{v})$ is the depth averaged current velocity vector and $\overline{u}$ and $\overline{v}$ are the depth averaged velocity components in the x- and y-directions respectively. Many models of sediment transport exist based on empirical and deterministic principals. The methodology used to describe sediment transport in this thesis was that of van Rijn [1984a,b]. A summary of that methodology is given in Chapter 3 (§3.1.2), and will not be repeated here.

The rates of bed-load and suspended-load transport are both functions of the size and density of the grains of sediment, the water depth and the current velocity (see §3.1.2). In the experiments throughout this thesis the water depth was kept constant. To simplify the sediment transport experiment the same grain density is used throughout, namely a density relative to that of water of 2.65. Of the two remaining variables, in the experiments in this chapter, the mean grain diameter was altered, whilst the current velocity magnitude was kept constant, with the only other change being the addition of turbines to the channel.

For this experiment, eight additional runs are carried out, four where the channel is unoccupied, and four where a single fixed-C_T turbine is deployed in the channel. Each of the four runs in the two groups uses a different mean grain diameter, classifying the sediment as very coarse, coarse, medium and fine sand according to the Wentworth [1922] scale. The model run numbers and details are given in Table 6.1. These model runs (Table 6.1) will be used to explore the impact of the changes to the hydrodynamics due to the turbine on sediment transport, and how this impact differs for various sediment grain sizes.

The model parameters in the hydrodynamic module remain as described in Table 3.1. The mesh depicted in Figure 3.22 and summarised in Table 3.8 was applied to geometry (3.5.1). Fixed-C_T turbines were implemented as outlined in

Table 3.3.

In these additional runs the pure current (i.e. no waves), non-equilibrium (i.e. sediment transport phase lag included) form of the sediment transport model was employed. Varying bed layer thickness was not turned on. However, the morphodynamic module was included, with the feedback between morophology, hydrodynamics and sediment transport also switched on.
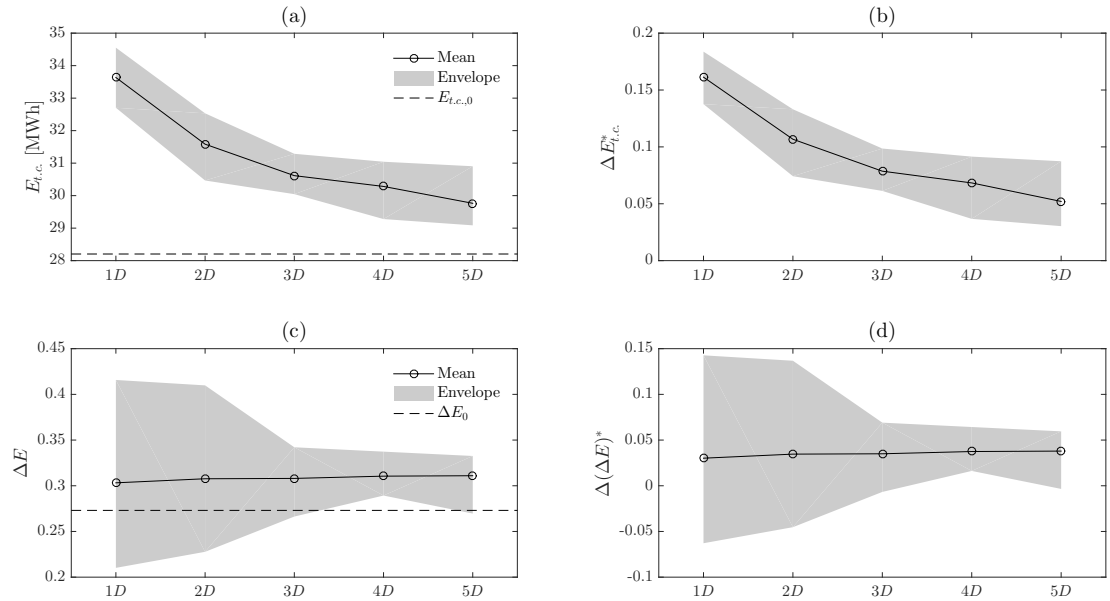
Figure 6.8: Plots of mean energy conversion per tidal cycle per turbine (top left), mean difference in energy conversion per tidal cycle between single turbine and array per turbine (top right), mean difference in energy conversion over the flood and ebb of the tide per turbine (bottom left) and mean difference in the difference between energy conversion over the flood and ebb of the tide between a single turbine and a turbine in the array per turbine (bottom right) (circles). Means are over all turbines in array. Envelope given by maximum and minimum values in array (shaded area).

At the two open boundary the "zero gradient" boundary condition was used for the sediment transport, and the "zero sediment flux gradient for outflow, zero bed change for inflow" condition was used for morphology module. The initial concentration of sediment in suspension was set to a constant value of 0 g/m^3 across the model.

Table 6.1: Run numbers and description for sediment transport experiment.

No. Turbines	Grain Size [mm]	Grain Size [ϕ]	Grain Classification	Run Numbers
0	1.5	-0.585	Very Coarse Sand	Run-24
0	0.75	0.415	Coarse Sand	Run-25
0	0.375	1.415	Medium Sand	Run-26
0	0.1875	2.415	Fine Sand	Run-27
1	1.5	-0.585	Very Coarse Sand	Run-28
1	0.75	0.415	Coarse Sand	Run-29
1	0.375	1.415	Medium Sand	Run-30
1	0.1875	2.415	Fine Sand	Run-31

A single sediment fraction was defined using the default bedload and suspended load factors of 1, and maximum concentration of 1×10^4 g/m^3. The solution methods for time-integration and space-discretisation were both set to higher order. The time parameters for the sediment transport module, "start time" and "time step factor" were set to 0 and 1 respectively.
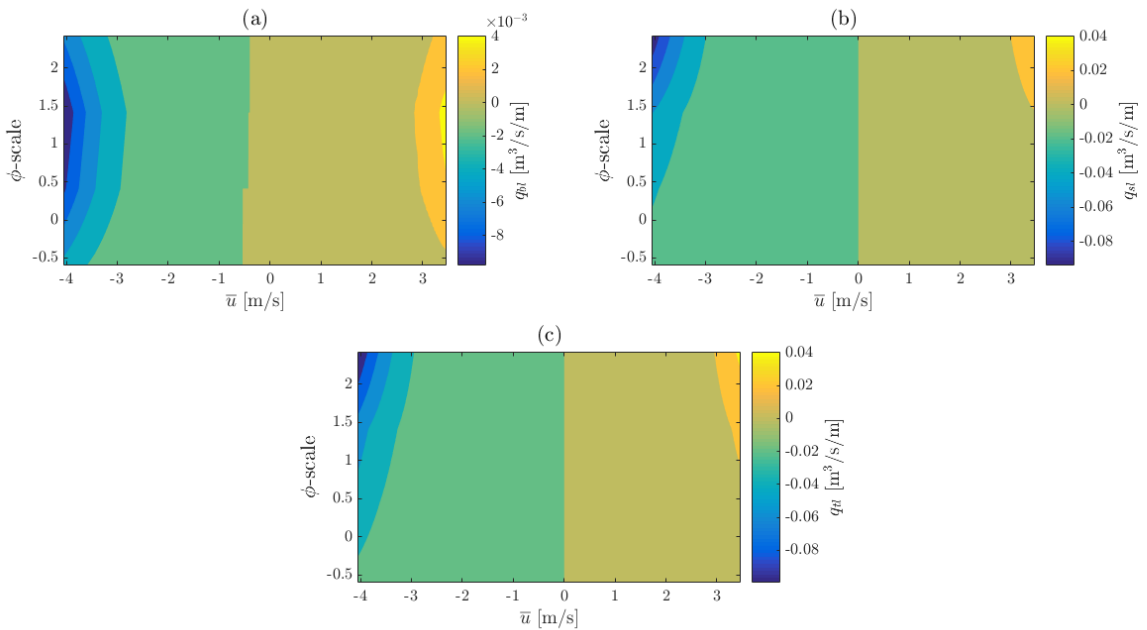
Figure 6.9: Contours of bed-load (a), suspended-load (b) and total-load (c) sediment transport rate for current speed and sediment grain-size.

For the horizontal dispersion of sediment the scaled horizontal eddy viscosity formulation with used, applying a constant value of 1 across the model domain. In the sediment properties window a sediment porosity of 0.4 was chosen (the

mid-point of the recommended values in the model documentation), whilst the relative density was chosen as 2.65 and the sediment grain size was varied across the model runs as described previously (and summarised in Table 6.1).

Finally, in the morphodynamic module, a maximum bed-level change of 1 m/d was set, and a start timestep of 432 was chosen, which is the timestep at which the hydrodynamic model spin-up ends. Further explanation of the above settings is given in DHI [2016c,d].
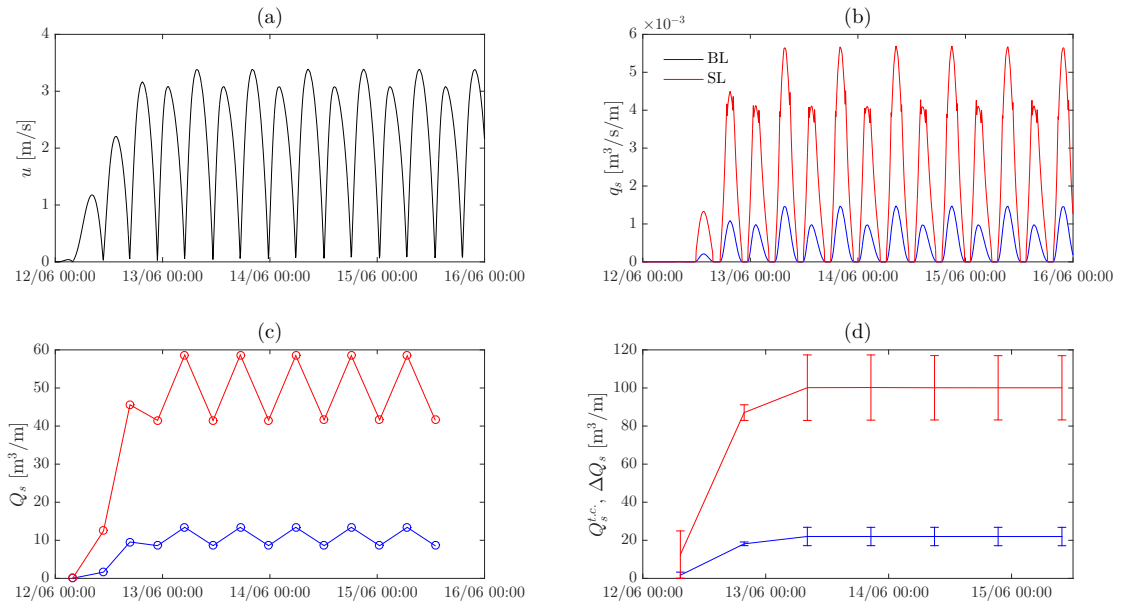
Figure 6.10: Time-series of u-velocity (a), volumetric sediment transport rates, q_s, (b), transported sediment volume per tidal phase, Q_s, (c) and transported sediment volume per tidal cycle, $Q_s^{t.c.}$, (d: line) and net volume of sediment transported per tidal cycle, ΔQ_s, (d: error bar).

In Figure 6.9 contours of the bed-, suspended- and total-load (suspended-load plus bed-load) transport rates for varying current speed and sediment grain size are given, obtained from the model output from Run-24, Run-25, Run-26 and Run-27. In this figure, and in remaining figures in this section the sediment grain size will be given by the ϕ-scale:

$$\phi = -\log_2\left(\frac{d}{d_0}\right) \tag{6.3.2}$$

where d is the sediment grain size, and $d_0 = 1$ mm [Krumbein and Aberdeen, 1937].

Table 6.2: Depth-averaged velocity thresholds of bed-load, $\overline{u}_{c,b}$, and suspended-load transport, $\overline{u}_{c,s}$ and associated parameters for the calculations. From left to right the parameters were calculated using equation 3.1.20, Table 3.2, equation 3.1.25, equation 3.1.24, equation 3.1.23, equations 3.1.28 & 3.1.29, equation 3.1.26 and equation 3.1.23, with $g = 9.81$ m/s^2, $s = 2.65$, $\nu = 1 \times 10^{-6}$ m^2/s, $h = 36$ m and $d = d_{90} = d_{50}$.

d_{50} [mm]	D_*	Θ_c	$u_{f,c,b}$ [mm]	C'	$\overline{u}_{c,b}$ [mm]	w_s [m/s]	$u_{f,c,s}$ [m/s]	$\overline{u}_{c,s}$ [m/s]
1.5	37.94	0.037	0.030	89.68	0.86	0.171	0.069	1.96
0.75	18.97	0.030	0.019	95.10	0.58	0.098	0.039	1.19
0.375	9.49	0.033	0.014	100.52	0.46	0.056	0.023	0.75
0.1875	4.74	0.052	0.013	105.94	0.42	0.023	0.020	0.67

From Figure 6.9 one can see that most sediment transport occurs at peak current values, as one would expect given the dependence of sediment transport rate on bed shear stress, which varies as the square of current speed. One can also see from this figure that transport in the channel will be dominated by suspended load transport, for all grain sizes. Sediment transport is initiated when the bed shear stress exceeds a threshold value. As the current increases, when it exceeds another threshold based on the settling velocity of the sediment the sediment will be transported as suspended load. The methodology for calculating these thresholds is laid out in Chapter 3, §3.1.2, and the thresholds are given as depth-averaged velocities in Table 6.2.

Near the centre of the channel, where the lowest peak velocities are seen (see Figure 4.1) and where the turbine will be deployed, the bed-load transport thresholds for $d_{50} = 1.5$, 0.75, 0.375 and 0.1875 mm were exceeded for 44%, 46%, 47% and 47% of the tidal cycle respectively, and the suspended-load transport thresholds were exceeded for 33%, 41%, 44% and 46% of the tidal cycle respectively. Thus, for 76%, 90%, 94% and 97% of the time that the $d_{50} = 1.5$, 0.75, 0.375 and 0.1875 mm bed-load transport thresholds are exceeded the respective suspended-load thresholds will be exceeded also.

At peak velocities, for bed-load transport, the rate of transport initially increases as the grain size decreases, then decreases with decreasing grain size beyond 0.375 mm ($\phi = 1.42$). This is in contrast to suspended-load transport where the transport

rate always increases with decreasing grain-size. In the non-equilibrium, pure current case (which was the case considered), the sand transport module of MIKE21 uses the following equation to reduce the bedload transport [DHI 2016d (ST user guide)]:

$$q_{s,bl,reduced} = q_{s,bl} \left(\frac{\Delta h}{\Delta h_{crit}} \right)^2 \tag{6.3.3}$$

where Δh is the local (sediment) layer thickness and Δh_{crit} is a critical value below which the transport will be reduced. The values were not altered from pre-set values. It must thus be that the increased transport of sediment for finer grains reduces Δh below Δh_{crit} around peak flow, thus reducing $q_{s,bl}$.
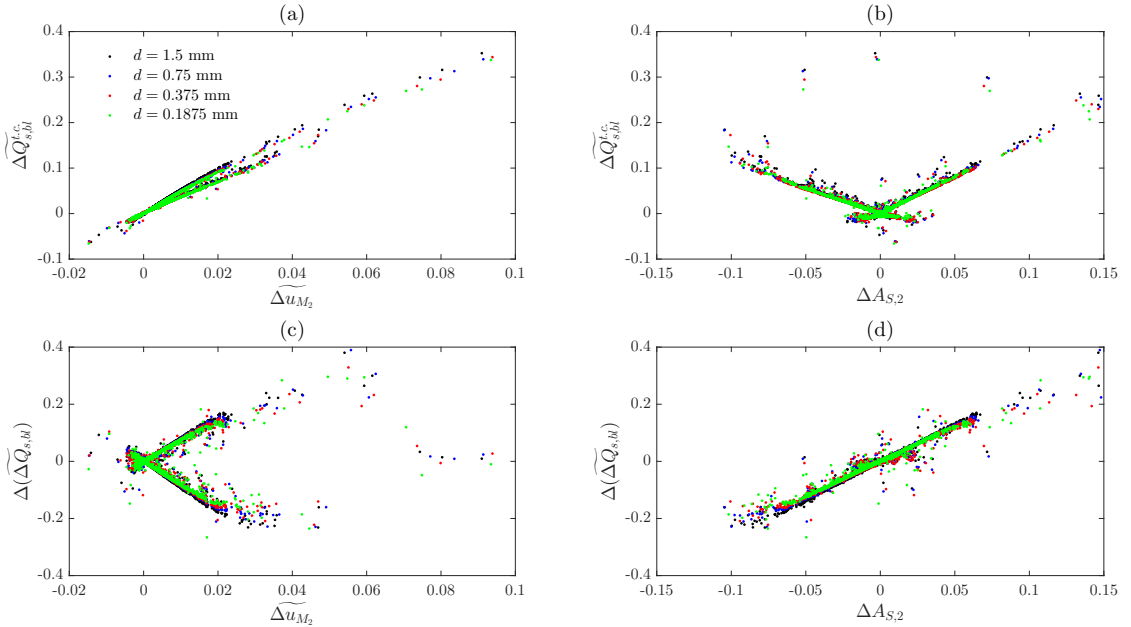
Figure 6.11: Plots of change in volume bed-load transport over a tidal cycle, $\Delta Q_{s,bl}^{t.c.}$, (top row) and change in the net volume bed-load transport, $\Delta(\Delta Q_{s,bl})$, (bottom row) against the change in M$_2$ current amplitude, Δu_{M_2}, (left column) and the change in the asymmetry, $\Delta A_{S,2}$, (right column) between an unoccupied channel and a channel containing a single fixed-C_T turbine at its centre. Plot are repeated for grain-sizes of 1.5 mm (black), 0.75 mm (blue), 0.375 mm (red) and 0.1875 mm (green). Changes normalised by the value of parameter in unoccupied channel run.

A similar methodology will be used to assess the impact of changes to u_{M_2} and $A_{S,2}$ on sediment transport as was used for turbine energy conversion. In Figure

6.10a the u-velocity time-series at the site where the turbine is to be deployed in Run-24 is plotted. Along with this, the bed- and suspended-load sediment volumetric transport rates, $q_{s,bl}$ & $q_{s,sl}$ respectively, are plotted in Figure 6.10b. The volumetric transport rates were converted into volumes of sediment transported over the phases of the tide by integrating the volumetric transport rates over the phases of the tide:

$$Q_s^{f,e} = \int_{f,e} q_s \; dt \qquad (6.3.4)$$

Time-series of volume transport of sediment are given in Figure 6.10c. As for the energy conversion over the phases of the tides, the total volume transport per tidal cycle and the net volume transport per tidal cycle are defined as:

$$Q_s^{t.c.} = Q_s^f + |Q_s^e| \qquad (6.3.5)$$

and

$$\Delta Q_s = 100 \times \frac{2(Q_s^f - |Q_s^e|)}{Q_s^f + |Q_s^e|} \qquad (6.3.6)$$

with positive values of ΔQ_s, indicating net transport in the flood direction and negative values indicating net transport in the ebb direction. Time-series of these two parameters are given in Figure 6.10d with the line giving $Q_s^{t.c.}$ and the amplitude of the error bars giving $Q_s^f - |Q_s^e|$.

As was the case for $E_{t.c.}$ and ΔE, once the spin-up period ends, the values of $Q_s^{t.c.}$ and ΔQ_s remain approximately constant for the rest of the simulation. This allows for an analysis similar to that in Figures 6.2 and 6.3 to be carried out for sediment transport. As was done for $E_{t.c.}$ and ΔE, the changes in $Q_s^{t.c.}$ and ΔQ_s between an unoccupied channel run and a run containing a single fixed-C_T turbine were calculated at each model element and plotted against the changes in u_{M_2} and $A_{S,2}$, producing plots similar to Figure 6.2 and 6.3. These plots are given in Figures 6.11–6.13, and in these plots Δu_{M_2} and $\Delta Q_s^{t.c.}$ have been normalised by their values from the unoccupied channel runs. These figures also include plots for each of the 4 grain-sizes listed in Table 6.2.

The twin tailed structures seen in Figures 6.2 and 6.3 were also seen in the plots of $\widetilde{\Delta Q_s^{t.c.}}$ against $\Delta A_{S,2}$ and $\Delta(\widetilde{\Delta Q_s})$ against $\widetilde{\Delta u_{M_2}}$. The eastern and western halves of the channel have not been plotted separately in these plots but the reason for the twin-tails is as described in §6.2.2 for Figures 6.2 and 6.3. Linear trends between $\widetilde{\Delta Q_s^{t.c.}}$ against $\widetilde{\Delta u_{M_2}}$ and $\Delta(\widetilde{\Delta Q_s})$ against $\Delta A_{S,2}$ were seen, implying that the total transport either as bed-load or suspended-load reduces with reduced M_2 current, as expected, and as the flood-ebb asymmetry of the current increases/decreases, the net sediment transport also increases/decreases.
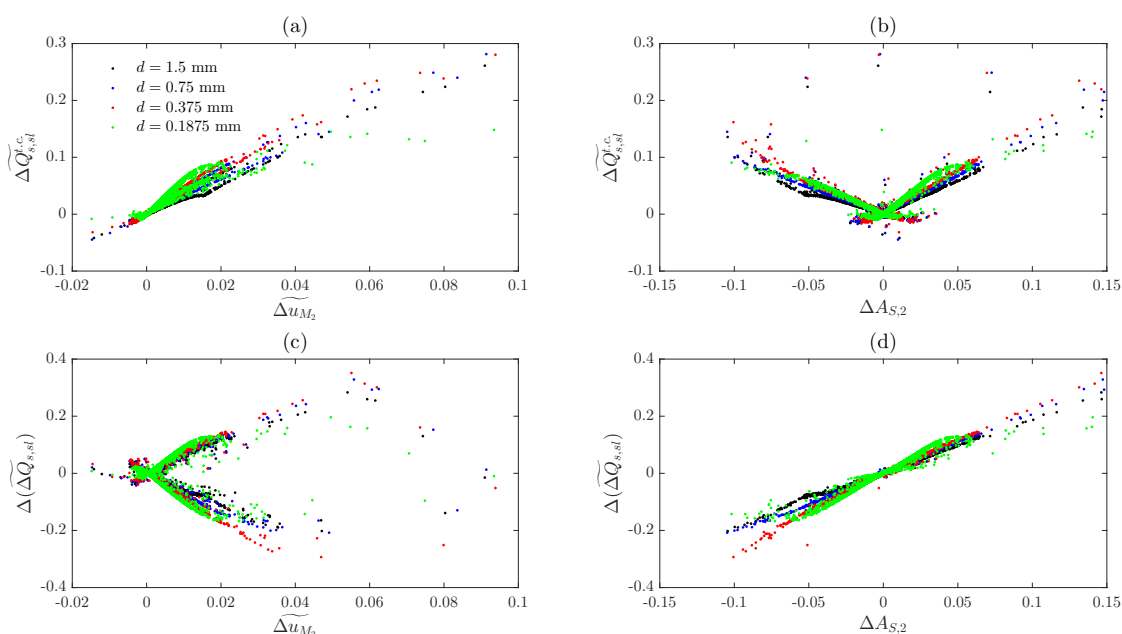
Figure 6.12: As Figure 6.11 but for suspended-load.

The differences between these trends for the different grain-sizes is small and is not clear from Figures 6.11–6.13. Therefore, the trendlines fitted to each scatter-plot in Figures 6.11a–6.13a are plotted in Figures 6.14a–6.16a and likewise the trendlines associated with the scatter-plots in Figures 6.11d–6.13d are plotted in Figures 6.14b–6.16b. In Figures 6.14c-6.16c & 6.14d–6.16d the gradients of each of the trendlines are plotted against grain-size, expressed as ϕ. For each of the trendlines the y-intercept, c, was approximately zero. The numerical values of the gradients and y-intercepts of each linear fit are presented in Table 6.3, along with the associated R^2 and 95% confidence intervals.
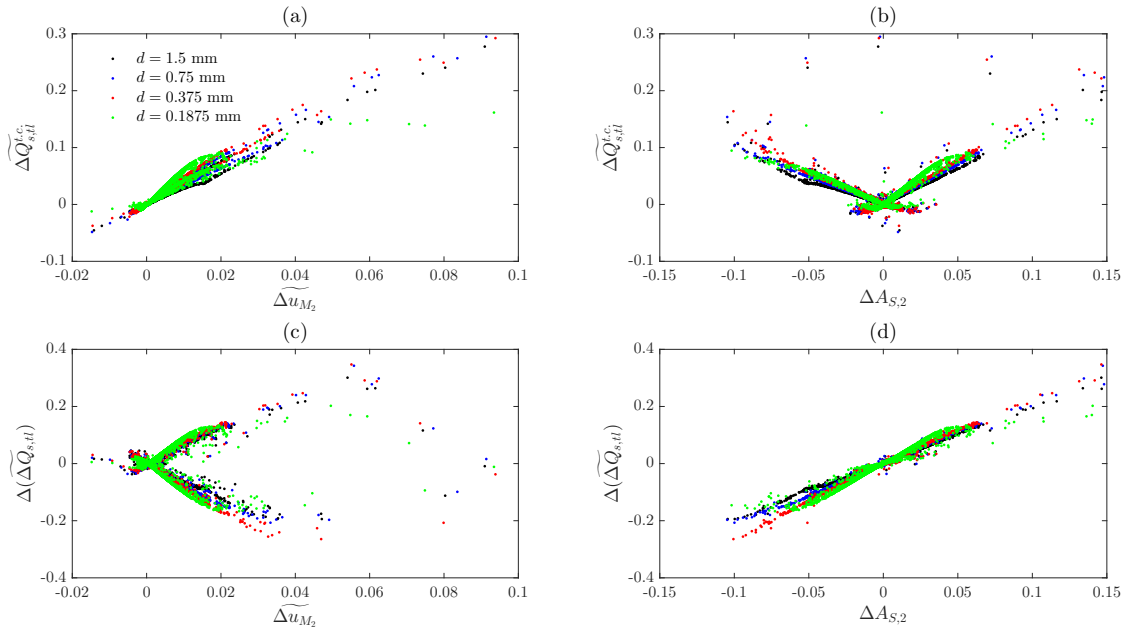
Figure 6.13: As Figure 6.11 but for total-load.
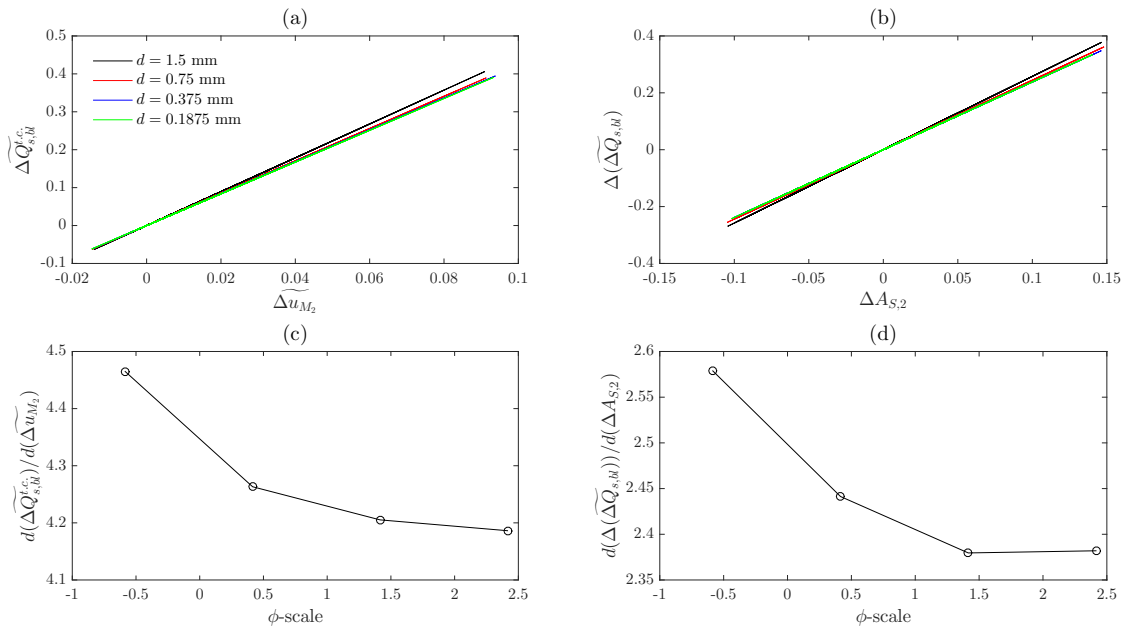
Figure 6.14: Lines of best-fit associated with Figures 6.11a (a) and 6.11d (b), and plots of the gradients of the lines of best fit against sediment grain-size (c & d respectively).
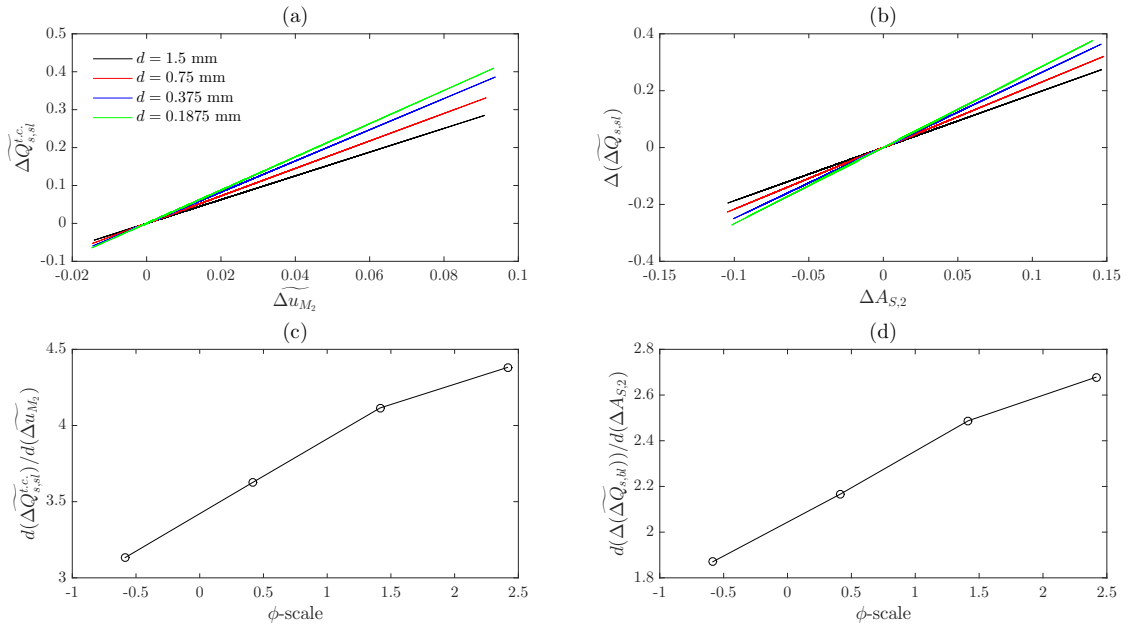
Figure 6.15: Lines of best-fit associated with Figures 6.12a (a) and 6.12d (b), and plots of the gradients of the lines of best fit against sediment grain-size (c & d respectively).
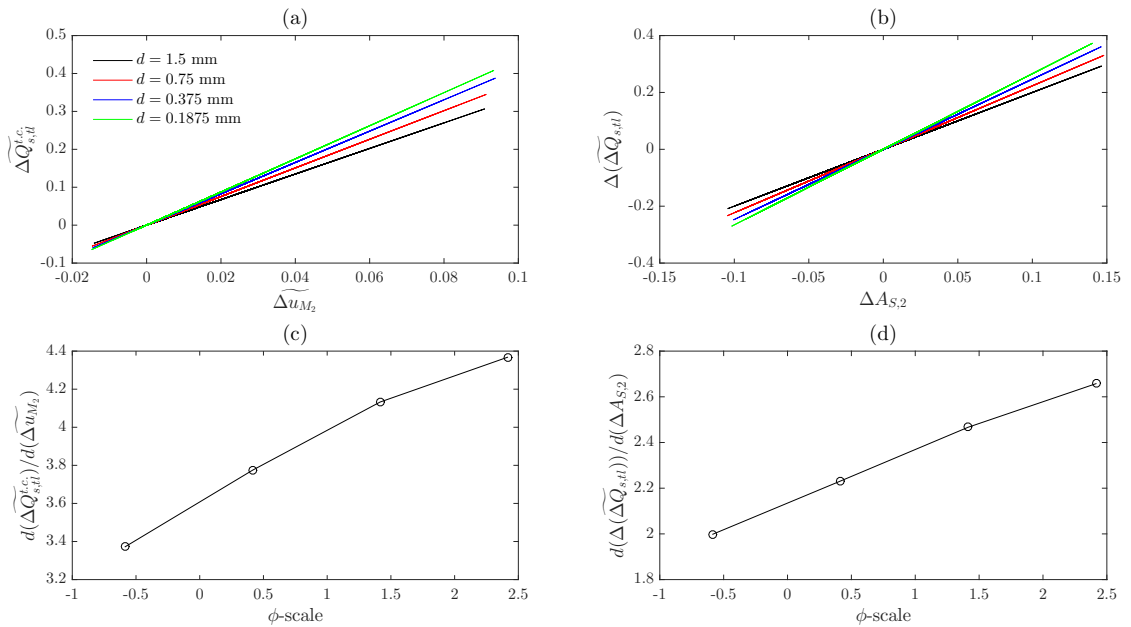
Figure 6.16: Lines of best-fit associated with Figures 6.13a (a) and 6.13d (b), and plots of the gradients of the lines of best fit against sediment grain-size (c & d respectively).

The gradients of the lines of best-fit from Figures 6.14–6.16 can be physically interpreted as the sensitivity of the sediment transport rates to the hydrodynamic changes. For larger/smaller values of m the same changes to $\widetilde{\Delta u_{M_2}}$ or $\Delta A_{S,2}$ will lead to larger/smaller changes to $\widetilde{\Delta Q_s^{t.c.}}$ or $\Delta(\widetilde{\Delta Q_s})$ respectively, as illustrated in equations (6.3.7) and (6.3.8):

$$m = \frac{\Delta y}{\Delta x} \rightarrow m\widetilde{\Delta u_{M_2}} = \widetilde{\Delta Q_s^{t.c.}} \qquad (6.3.7)$$

$$m = \frac{\Delta y}{\Delta x} \rightarrow m\Delta A_{S,2} = \Delta(\widetilde{\Delta Q_s}) \qquad (6.3.8)$$

Therefore, what is seen in Figures 6.14 is that for finer grain-sizes the total bed-load volume transport per tidal cycle is less sensitive to changes to the current magnitude, and likewise, the net bed-load volume transport per tidal cycle is less sensitive to changes to the flood-ebb asymmetry in the current for finer grain-sizes. Figure 6.15 shows that for finer grain-sizes the total suspended-load volume transport per tidal cycle is more sensitive to change to the current magnitude, and likewise, the net suspended-load volume transport per tidal cycle is more sensitive to changes in the flood-ebb asymmetry in the current for finer grain-sizes. Finally, the total-load transport shows the same patterns as seen for suspended-load transport, as suspended-load transport dominates the total-load, as seen in Figure 6.10, where the volumetric transport rates for suspended-load transport were an order of magnitude larger than for bed-load.

From the midpoints and midranges of the sets of gradients in Table 6.3, it can be estimated that a 1% change in u_{M_2} leads to a 4.33±0.14% change to $Q_{s,bl}^{t.c.}$, a 3.76±0.62% change to $Q_{s,sl}^{t.c.}$ and a 3.87±0.50% change to $Q_{s,tl}^{t.c.}$ and a 1% change to $A_{S,2}$ leads to a 5.84±0.07% change to $\Delta Q_{s,bl}$, a 5.69±0.34% change to $\Delta Q_{s,sl}$ and a 5.69±0.21% change to $\Delta Q_{s,tl}$. Including the 95% confidence intervals of the linear regressions it is estimated that a 1% change in u_{M2} leads to a 4.33±0.48% change to $Q_{s,bl}^{t.c.}$, a 3.76±1.39% change to $Q_{s,sl}^{t.c.}$ and a 3.87±1.27% change to $Q_{s,tl}^{t.c.}$ and a 1% change to $A_{S,2}$ leads to a 5.84±0.64% change to $\Delta Q_{s,bl}$, a 5.69±1.08% change to $\Delta Q_{s,sl}$ and a 5.69±1.01% change to $\Delta Q_{s,tl}$.

Table 6.3: Parameter of the lines of best-fit associated with Figures 6.14a–6.16a and 6.14b–6.16b.

	d [mm]	ϕ	m	c	R^2	p	$CI_{95\%}$ [%]
$\Delta\widetilde{Q^{t.c.}_{s,bl}}$	1.5	-0.585	4.465	-4.0×10^{-5}	0.988	0.000	0.34
	0.75	0.415	4.263	-4.4×10^{-5}	0.988	0.000	0.32
	0.375	1.415	4.205	-3.2×10^{-5}	0.988	0.000	0.31
	0.1875	2.415	4.186	-2.8×10^{-5}	0.988	0.000	0.31
$\Delta\widetilde{Q^{t.c.}_{s,sl}}$	1.5	-0.585	3.133	-4.6^{-5}	0.986	0.000	0.25
	0.75	0.415	3.626	-3.7×10^{-5}	0.988	0.000	0.27
	0.375	1.415	4.115	3.2×10^{-5}	0.988	0.000	0.31
	0.1875	2.415	4.381	1.3×10^{-4}	0.937	0.000	0.77
$\Delta\widetilde{Q^{t.c.}_{s,tl}}$	1.5	-0.585	3.373	-4.5×10^{-5}	0.987	0.000	0.26
	0.75	0.415	3.775	-3.8×10^{-5}	0.989	0.000	0.28
	0.375	1.415	4.132	2.0×10^{-5}	0.988	0.000	0.31
	0.1875	2.415	4.368	1.2×10^{-4}	0.942	0.000	0.73
$\Delta(\widetilde{\Delta Q}_{s,bl})$	1.5	-0.585	5.913	1.5×10^{-3}	0.992	0.000	0.47
	0.75	0.415	5.810	1.5×10^{-3}	0.989	0.000	0.54
	0.375	1.415	5.764	1.5×10^{-3}	0.986	0.000	0.57
	0.1875	2.415	5.849	1.5×10^{-3}	0.989	0.000	0.50
$\Delta(\widetilde{\Delta Q}_{s,sl})$	1.5	-0.585	5.537	1.1×10^{-3}	0.995	0.000	0.27
	0.75	0.415	5.728	1.2×10^{-3}	0.999	0.000	0.16
	0.375	1.415	5.928	1.3×10^{-3}	0.996	0.000	0.34
	0.1875	2.415	5.457	1.7×10^{-3}	0.977	0.000	0.84
$\Delta(\widetilde{\Delta Q}_{s,tl})$	1.5	-0.585	5.620	1.2×10^{-3}	0.997	0.000	0.25
	0.75	0.415	5.749	1.2×10^{-3}	0.998	0.000	0.22
	0.375	1.415	5.897	1.4×10^{-3}	0.996	0.000	0.32
	0.1875	2.415	5.480	1.6×10^{-3}	0.979	0.000	0.80

6.4 Summary

In this chapter additional analysis of model output from Chapters 4 & 5 was carried out to look at the impact of the changes to the hydrodynamics identified in those

chapters on the energy conversion of surrounding turbines. Also, an additional experiment looking at the effect of changes to the hydrodynamics on sediment transport was presented and analysed.

From comparisons between a run where the channel was unoccupied and a run with a single fixed-C_T turbine at the channel centre it was seen that changes to the M_2 current were most important for the total energy conversion per tidal cycle and the total volume transport of sediment (by either mode) over a tidal cycle. Whilst changes to the flood-ebb magnitude asymmetry (FVA), largely resulting from changes to the M_4 current, were most important for the flood-ebb asymmetry in energy conversion and the net volume transport of sediment (by either mode) per tidal cycle. From linear models fitted to the normalised changes between the runs it is estimated that, for a fixed-C_T turbine a 1% change to the M_2 current will lead to a 3.0±0.2% change in energy conversion per tidal cycle, and a 4.3±0.5% or 3.8±1.4% change to the total volume of transported sediment per tidal cycle as bed-load or suspended-load respectively. Similarly, a 1% change to the FVA will lead to a 1.8±0.1% change to the flood-ebb asymmetry in energy conversion, and a 5.8±0.6% or 5.7±1.1% change to the net volume of sediment transported as bed-load or suspended-load respectively. The ranges in the percentage changes for the sediment transport parameters arise because of the variation of the effect of the turbine on sediment transport with grain-size. For finer grains, changes to the M_2 current had less effect on bed-load transport but more effect on suspended load transport.

For multiple fixed-C_T turbine deployments, when deployed as a row, each individual turbine on average impacted the M_2 current less and converted more energy per tidal cycle than it would had it been deployed individually. Whilst when deployed as a line, each individual turbine on average impacted the M_2 current more and converted less energy per tidal cycle than they would had they been deployed individually. The difference in the impact on the FVA varied between the turbines for the line deployment test, but with reduced spacing the differences grew larger, leading to larger differences in changes to the flood-ebb asymmetry in energy conversion between the individual and array cases. For the row deployment the inter-turbine spacing was reduced by adding turbines to the row, which increases the

row blockage. With increased row blockage the difference in the energy conversion per tidal cycle between the individual and array cases increases. Changes to the row blockage appeared to have little effect on the average difference in the flood-ebb-variation in the energy conversion between the individual case and array cases.

Chapter 7

Discussion & Limitations

In this chapter the findings from the numerical experiments presented in Chapters 4, 5 and 6 will be related to the research questions set out in Chapter 2. This will be done in §7.1. All the findings from the experiments will be brought together and discussed in §7.2. Finally, in §7.3 the limitations of the work will be considered.

7.1 Research Questions

7.1.1 Research Question 1): "How are the harmonic tides altered locally by TSTs (tidal-stream turbines)?"

7.1.1.1 Research Question 1a): "How is the alteration to the odd and even harmonics similar/different?"

This question was addressed by numerical experiments undertaken in Chapter 4. In these experiments the changes to the overtides (§4.2) and compound tides (§4.4) resulting from the addition of a single fixed-C_T turbine to the channel were explored. There was a significant difference in the changes to the odd and even harmonics. The changes to the M_2, S_2 (two forcing tides), M_6, S_6 and $2SM_6$ were similar, in both pattern and size (in percentage terms). There was only reduction seen, and this occurred approximately symmetrically to either side of the turbine (Figures 4.3, 4.19 & 4.21). In contrast, there was a much larger change (in percentage terms) to the M_4, MS_4 and MS, with augmentation in the negative x-direction and reduction in the positive x-direction (Figures 4.3 & 4.20). The change to the

S_4 was also much larger than the change to the forcing tides and odd harmonics, but the pattern of change differed from all other constituents, in that there was an augmentation peak centred on the turbine. The similarities in the (percentage) size and pattern of change amongst the groups of harmonics is an indication of similar physical origins of the changes. A potential physical interpretation of these differences is an alteration to the current asymmetry. This will be expanded upon in §7.2 and §7.1.2.

In answer to research question *1a)*:

> *The amplitudes of the odd harmonics are predominantly reduced (some augmentation in bypass flow) by the operation of tidal turbines, whilst both augmentation and reduction to the amplitude of the even harmonics may occur.*

7.1.1.2   Research Question 1b): "What effect does the variable efficiency of a TST have on its impact on the harmonic tides, in particular cut-in and cut-out speeds?"

This question was addressed by Experiment 2 of Chapter 4 (§4.3). In this experiment a variable-C_T turbine was deployed in the channel, and the change to the tidal constituents resulting from the operation of this turbine were compared to the changes seen due to the operation of a fixed-C_T turbine as explored in Experiment 1 of Chapter 4 (§4.2). In all cases but that of the phase of the M_6 the pattern of change caused by the turbine was the same (Figure 4.8). In terms of the size of the change, the change to the M_2 and M_4 amplitudes and the M_4 phase was smaller for the variable-C_T turbine (compared to the fixed-C_T turbine) and the change to the M_6 amplitude and the M_2 and M_6 phase was larger for the variable-C_T turbine (Figure 4.8). The reduced effect on the M_2 amplitude is suspected to be related to the cut-in speed of the variable-C_T turbine, which means the turbine is only operational for 44% of the tidal cycle, compared to 100% of the tidal cycle for the fixed-C_T turbine. The smaller reduction to the M_2 amplitude implies a reduced velocity deficit in the turbine wake. This appears to be the cause of the reduced effect on the M_4 tide. The changes to the M_6 tide are suspected to be related to the reduced turbine efficiency of the variable-C_T at higher current speeds.

In answer to research question *1b)*:

Compared to the fixed-C_T turbine the variable-C_T turbine caused a smaller velocity deficit, apparently due to the cut-in speed. Within the area of effect of the turbine, the asymmetric distortion to the current time series is less than in the fixed-C_T case, and the symmetric distortion is increased.

7.1.1.3 Research Question 1c): "How sensitive is the effect of a TST on the harmonic tides to ambient conditions, in particular ambient asymmetry?"

To address this research question, and research question *2c)* (§7.1.2.3) Experiment 1 in Chapter 5 was undertaken (§5.2). In this experiment a single fixed-C_T turbine was deployed at four different locations along the channel based on the contours of ambient asymmetry, i.e. at $A_{S,2} = 0$, 0.1, 0.2 and 0.3, where $A_{S,2}$ is a measure of the flood-ebb current magnitude asymmetry (FVA) (Figure F.1). There was only a minor difference in the effect of the turbine on the M_2 and M_6 tides across the four deployments (Figure 5.1 & 5.2). Conversely, there was a much greater variation in the effect of the turbine on the M_4 tide (Figure 5.1 & 5.2). However, this variation is simply due different ambient conditions meaning a difference change to the M_4 tide is needed to represent the same change to the asymmetry (Figure 5.3).

In answer to research question *1c)*:

The effect of the turbine on the fundamental astronomic tide and the first odd overtide does not appear sensitive to ambient conditions (percentage change to amplitude considered). The effect of the turbine on the first even overtide did however appear sensitive to ambient conditions, but not ambient asymmetry.

7.1.1.4 Research Question 1d): "How does the impact of a single TST on harmonics scale across an array of TSTs?"

To address this research question and research question *2d)* (§7.1.2.4) Experiments 2 and 3 in Chapter 5 were undertaken. These experiments looked at a line of turbines

and a row of turbines respectively. For the line of turbines, there was a greater effect on the M_2 and M_6 amplitude and phase at all turbines in the array, when deployed as an array compared to them being deployed individually (Figures 5.5a, 5.5c, 5.6a, 5.6c, 5.8a, 5.8c, 5.9a, 5.9c, 5.11a, 5.11c, 5.12a, 5.12c). In this arrangement, the effects of the turbines appear to be superimposed upon one-another. Thus, for the west-most turbine (west – negative x-direction) the augmentation peak is larger in the array run than the individual run and the reduction peak is smaller, and for the east-most turbine (east – positive x-direction) the opposite is seen. For the central turbine the difference was minimal (Figures 5.5b, 5.6b, 5.8b, 5.9b, 5.11b, 5.12b). The difference between the array and individual deployments increased as the spacing between the turbine was reduced.

In the row experiments, the blockage of the row (the ratio of the total swept area of all turbines to the cross-sectional area of the channel, ε_0) was altered. In the row runs the per-turbine peak change to the M_2, M_4 and M_6 amplitude and the M_4 phase was smaller than in an individual turbine run, and the per-turbine peak change to the M_2 and M_6 phase was larger. As the row blockage increased, by adding additional turbines to the row, the difference between the per-turbine peak changes grew across all tides (amplitude and phase) (Figure 5.30). Moving from a single turbine ($\varepsilon_0 = 0.008$) to a row of 13 turbines ($\varepsilon_0 = 0.105$) only a small change in the area of effect of the array is seen (defined as the area where change to $M_2 > 2\%$) (Table 5.7). This suggests that there is perhaps a balance between the reduced per-turbine effect with additional turbines, and the fact that there are more turbines in the row each with its own area of effect. Beyond $\varepsilon_0 = 0.105$ with additional turbines in the row the area of effect of the array quickly increased, likely due to a lack of resolution in the mesh to resolve the turbine bypass flow, leading to underprediction of the wake recovery.

In answer to research question *1d)*:

> *The effect of a TST scales differently depending on the array config-uration. When deploying turbines as a row, smaller peak per turbine changes to the amplitude of all tides and the phase of the M_4 is seen, and a larger peak per turbine change to the phase of the M_2 and M_6 is seen, compared to a turbine operating individually. As the number of*

turbines in the row increases, and therefore so too does the row blockage, the difference between the per-turbine effect of the turbines in the row and a turbine operating individually increases. Up to $\varepsilon_0 \sim 0.1$ there is little difference in the area of effect of the array with additional turbines as it appears there is a balance between more turbines being added to the row and the reduced per-turbine effect with increased blockage. When deploying turbines as a line it appears there is a linear superposition of the individual turbine effects. This leads to larger augmentation peaks and smaller reduction peaks for some turbines and larger reduction peaks and smaller augmentation peaks for other turbines, whilst there is little difference between the array and individual case for the central turbine. This is for the more complex pattern of change to the M_4 tide. For M_2 and M_6 tides the peak reduction to the amplitude and phase per-turbine is larger in the array compared to the individual runs, and in the inter-turbine region the current amplitude does not return to ambient levels, but to some reduced intermediate (between peak and ambient) value. The difference that is seen increases as the spacing between the turbines is reduced, the velocity reduction seen in the inter-turbine regions becomes larger.

7.1.2 Research Question 2): "How is the flow asymmetry altered locally by TSTs?"

7.1.2.1 Research Question 2a): "Can the change to the flow asymmetry be predicted from the changes to the tidal constituents (fundamentals and harmonics)?"

This research question was explored as part of Experiments 1 and 3 in Chapter 4 (§4.2 & §4.4 respectively). In §4.2 two metrics are used to measure the change to the FVA. The first, $A_{S,1}$, is based on the interaction of the M_2 and M_4 tides, as illustrated in Figure 2.6 and requires knowledge of the amplitude and phase of the M_2 and M_4 tidal constituents. It is this metric that this research question is concerned with. The second metric used, $A_{S,2}$, was taken from Neill et al. [2014]

and is seen as a direct measure of the FVA as it takes the peak values from the current time-series. There was strong linear correlation ($R^2 = 0.9976$) between the two metrics for the unoccupied channel case (Figure 4.6). This trend does however appear to break-down somewhat in the vicinity of the turbine. Plots of the change to the FVA as measured by the two metrics appeared near identical in terms of pattern (Figure 4.5).

With the addition of the S_2 as a forcing tide and therefore the introduction of the spring-neap cycle a temporal variation in the FVA was introduced (Figure 4.25 & 4.26a) and the metric $A_{S,1}$ appeared to no longer reproduce the average pattern of FVA obtained through the metric $A_{S,2}$ (Figure 4.27). The metric $A_{S,1}$ was extended to also account for the S_2-S_4, M_2-S_2-MS_4 and M_2-M_4-M_6 interactions, (4.4.1), and this extended metric reproduced the patterns of average FVA measured using the metric $A_{S,2}$.

In answer to research question *2a)*:

> *The change to the flow asymmetry can be predicted from the changes to the tidal constituents. In general, the largest constituent interactions satisfying the frequency conditions $2\sigma_A = \sigma_B$ and $\sigma_A + \sigma_B = \sigma_C$ must all be considered for an accurate reproduction of the pattern of change to FVA by the turbine(s). If knowledge of the change to the FVA alone is the goal of the study then a direct measure of asymmetry such as that used in Neill et al. [2014] and Bruder and Haas [2014] are sufficient and harmonic analysis is not required. However, in general there is a temporal variation in the FVA as the tide cycles through its beat periods (e.g. the spring-neap cycle). Thus, a time-series with a length equal to the length of the longest beat period that is of significance to the overall tide must be considered.*

7.1.2.2   Research Question 2b): "What effect does the variable efficiency of a TST have on its impact on the flow asymmetry, in particular cut-in and cut-out speeds?"

Experiment 2 of Chapter 4 (§4.3) was undertaken to address this question along with research question *1b)* (§7.1.1.2). The pattern of change to the FVA was the

same for the fixed- and variable-C_T turbines. The overall size of the changes seen due to the variable-C_T turbine were smaller. This is believed to be due to the cut-in speed, which meant that the turbine was operational for less of the tidal cycle (44%), and therefore had a lesser effect on the FVA.

In answer to research question *2b)*:

> *The variable-C_T turbine has a similar (in terms of pattern) but reduced (in terms of magnitude) effect on the FVA compared to the fixed-C_T turbine. The reason for this reduced effect is likely to be the turbine cut-in speed. This reduces the M_2 current deficit, which in turn reduces the M_4 augmentation / reduction, implying reduced FVA augmentation / reduction.*

7.1.2.3 Research Question 2c): "How sensitive is the effect of a TST on asymmetry to ambient conditions, in particular ambient asymmetry?"

Experiment 1 of Chapter 5 (§5.2) addressed this research question along with research question *1c)* (§7.1.1.3). There was only a small variation to the (percentage) change to the FVA resulting from the turbine operation when the turbine was deployed at the four different locations with different ambient conditions in §5.2. The small variation that was seen did not appear to coincide with any of the ambient physical parameters considered in §5.2 (Figure 5.4). It has not been ruled out that the variation that is seen may be related to the variation in the size and shape of the elements that the turbines are deployed in. Even with the steps taken to mitigate such an effect, as described in Appendix F.

In answer to research question *2c)*:

> *It does not appear that the effect of the TST is sensitive to ambient conditions, including ambient FVA and whether or not the tide is standing or progressive. The effect of the turbine on the M_4 was seen to change however. Therefore, in different ambient conditions the representation of the changes to the FVA by changes to the M_4 differs, but overall, the change to the FVA is the same.*

7.1.2.4   Research Question 2d): "How does the impact of a single TST on asymmetry scale across an array of TSTs?"

Experiments 2 and 3 of Chapter 5 (§5.3 & §5.4 respectively) were undertaken to address this research question along with research question *1d)* (§7.1.1.4). As seen in Figures 5.7, 5.10, 5.13 & 5.15, for the line arrangement of turbines difference in the change to the FVA seen in the array and individual turbines is similar to as described for the M_4 current in §7.1.1.4. For the west-most turbine the augmentation peak was larger in the array run, the reduction peak was smaller in the array run and vice-versa for the east-most turbine, with minimal difference for the central turbine. This difference grew as the spacing between the turbines was reduced.

For the row arrangement with increased blockage the peak per-turbine change to the FVA was reduced and there appeared to be a balance between this reduced per-turbine effect and the introduction of new turbines (each with their own area of effect) which meant that the variation in the area of effect of the array as a whole did not vary a great deal until $\varepsilon_0 > 0.105$, as was the case for the area of effect on the M_2 current. However, beyond $\varepsilon_0 > 0.105$ the model lacked the resolution to adequately resolve the bypass flow between turbines, which is suspected to have led to an overprediction of the area of effect of the array on the asymmetry.

In answer to research question *2d)*:

> *As for the changes seen to the harmonic tides, the way the change to the FVA scales with multiple turbines depends on the turbine configuration. For rows of turbines the peak change to the FVA per-turbine is reduced as the row blockage is increased. There is suggestion of a balance between the reduced per-turbine effect and the addition of turbine to the row which means that there is only a small difference in the total area of effect of the row (on the FVA) as its size is increased up to a blockage of $\varepsilon_0 \sim 0.1$. For lines of turbines there is an additive effect across the line with some turbines having a reduced augmentation peak and an increased reduction peak, others having a smaller reduction peak and a larger augmentation peak, and the central turbine showing little change,*

compared to each turbine operating individually.

7.1.3 Research Question 3): "How is net sediment transport and the technically exploitable resource altered locally by TSTs?"

7.1.3.1 Research Question 3a: "Can the change to the technically exploitable resource be predicted from the changes to the flow asymmetry?"

To address this research question additional analysis of Experiments 1 and 2 of Chapter 4 (§4.2 & §4.3 respectively) and Experiments 2 and 3 of Chapter 5 (§5.3 & §5.4 respectively) was performed. This analysis made use of the turbine power time-series output by MIKE, and power time-series calculated from current speed time-series at elements not containing turbines. Plots of the change to the M_2 current against the change to the energy conversion per tidal cycle showed linear trends and stronger correlations for the fixed- and variable-C_T turbines ($R^2 = 0.99$ and 0.98 respectively, Figures 6.2a & 6.3a) for a turbine operating individually. Similarly, plots of the change to the FVA against the change to the Energy Conversion (flood-ebb) Asymmetry (ECA) also showed a linear trend with strong correlations for the fixed- and variable-C_T ($R^2 = 1.00$ and 0.98 respectively, Figures 6.2d & 6.3d). These results suggest that there is indeed a predictability to the change in the technically exploitable resource one expects to occur due to the changes to the hydrodynamics caused by TSTs. However, this analysis does not consider the interaction of the turbines with each other, and the implications for their power production.

When multiple turbines were deployed in a line along the channel, the energy conversion per tidal cycle by the turbines in the array was less than when those turbines were deployed individually (Figure 6.6a & 6.6b). This is consistent with the conclusion from the single turbine analysis, which showed a linear trend of reduced energy conversion per tidal cycle with reduced M_2 current. As the turbines were deployed closer together the difference between the array and individual cases grew. This is due to larger reductions to the M_2 current being seen closer to the

turbine (Figure 4.8a). The ECA is more complex to explain as there is an east-west difference in the change to the FVA (e.g. Figures 4.5 & 6.2d). On average the ECA for the turbines across the array is larger when the turbines are deployed in an array rather than individually, however in some cases the ECA may be lower in the array.

When the turbines were deployed as a row, the changes seen for the individual turbine are not reflected in the changes seen for the row. Given the rectilinear nature of the flow in the experiments, the changes to the flow occur mainly in the along-channel direction. Therefore, these changes have little influence on the turbines across channel neighbours. Turbines deployed as a row convert more energy per tidal cycle per turbine with lower M_2 velocity reduction. The ECA in the row-configuration runs is slightly larger than in the individual turbine case, ~5% on average. This difference changed little with increasing blockage, however the variability in the ECA seen across the turbine in the row did increase as the row blockage increased. However, it is not clear if this is an artefact of the experimental set-up.

In answer to research question *3a)*:

Changes to the magnitude of the M_2 current are of greater importance to the overall energy conversion by a turbine than changes to the FVA. Therefore, the short answer to this research question is "no". When it comes to the ECA the opposite is true and changes to the M_2 are of little importance in comparison to the changes to the FVA. So, there may still be some value in understanding the changes to the FVA from a resource point of view if one wishes to understand the temporal variability of the energy supply. The changes caused by a single turbine lead to predictable changes to the total (fixed-C_T) and technically exploitable (variable-C_T) resource within the area of effect of that turbine. Additional turbines deployed in that area of effect experience qualitatively predictable changes to the total energy conversion and ECA. When deployed outside of the area of effect of the turbine, such as in a row, the changes seen due to a single turbine do not predict the difference in energy conversion for turbines in this array

configuration compared to an individual deployment.

7.1.3.2 Research Question 3b): "Can the change to net sediment transport be predicted from the changes to the flow asymmetry?"

To address this research question an additional experiment, described in Chapter 6 (§6.3), was undertaken. In this experiment a fixed-C_T turbine was deployed in a channel with a bed with a uniform grain-size, with four different grain-sizes tested. Similar to the effects on energy conversion, linear correlations were found between the change to the M_2 current and gross volume of sediment transported as bed-load and suspended-load. Likewise, there were linear trends between the change to the FVA and the net volume of sediment transported as bed-load and suspended-load. This was the case across all tested grain-sizes, with grain-size influencing the gradient of the linear trend. For bed-load transport the coarsest grain-size had the steepest gradients in both linear trends, with the gradients flattening as the grain-size decreased. For suspended-load the opposite was seen, and the coarsest grain-size had the shallowest gradients, with the gradient steepening as the grain-size increased. This is interpreted as finer sediment transported as suspended loads being more sensitive to changes to the hydrodynamics than their coarser counterparts, and for bed-load transport, coarser grains were more sensitive to the changes in the hydrodynamics.

In response to research question *3b)*:

> *Changes to net sediment transport can be predicted from changes to the FVA. However, further work is needed to explore this problem in greater detail due to the complex nature of sediment transport.*

7.2 Discussion of Findings

In this section, the results of the experiments and analysis of the previous chapters (Chapters 4–6) are discussed together. §7.2.1 considers the physical processes leading to the changes observed; §7.2.2 covers the impact of, and the energy conversion by arrays of turbines compared to individual turbines and §7.2.3 addresses what the changes to the hydrodynamics mean for sediment transport.

7.2.1 Changes to the Flood-Ebb Current Asymmetry Resulting from Tidal-Stream Turbine Operation

The operation of a TST alters the ambient FVA with augmentation to the west (negative x-direction) and reduction to the east (positive x-direction) (Figures 4.5, 4.8 & 4.26b). In comparison to the change in the M_2 current (Figure 4.3, 4.8 & 4.19), which is a proxy for the tidal current, the change to the FVA extended over a much greater area. The change to the M_2 takes the form of a velocity deficit at the turbine location, which decays in both directions. This deficit to the M_2 current is the turbine wake, which forms on both sides of the turbine as the flow is bi-directional and the turbine operates in both directions. The pattern of change to the S_2, M_6, $2SM_6$ and $2MS_6$ follows that of the M_2 as they are all influenced by the quadratic turbine term (QTT: (i) in equation (2.2.8)) as shown by expansions (2.2.13) and (2.2.26). With the addition of the turbine both the QFT and the elevation turbine term (EFT: (j) in equation (2.2.8)) are introduced. However, the EFT is an order of magnitude smaller than the QFT and thus of lesser importance (Figure 4.12). Both these terms only exist in the presence of a turbine, which explains why the largest change occurs at the turbine, and the deficit recovers with distance from the turbine.

With the introduction of the turbine the (momentum) advection term (AT: (e) in (2.2.8)) and the continuity term (CT: (c) in (2.2.5)) both grow in size close to the turbine, to the the same order as the QFT (cf. Figures 4.11 & 4.12). Expansions (2.2.12), (2.2.16), (2.2.24) and (2.2.25) show that the AT and CT alter the M_4, S_4, MS_4 and MS tides (even harmonics, except MS, but this term has the same origin as the aforementioned tides). Both these terms have a dependence on the spatial gradient of velocity. The introduction of the wake introduces a strong velocity gradient, between the wake flow and the bypass flow, increasing the size of the AT and CT (Figure 4.11). It was therefore concluded that the wake of the turbine is the physical mechanism by which the FVA was altered.

The physical explanation for the east-west reduction-augmentation pattern to the FVA is simple. When the current is flowing in the negative x-direction (ebb current) the turbine wake will extend from the turbine in the negative x-direction,

i.e. to the west of the turbine. When the current is flowing in the positive x-direction (flood current) the wake will extend from the turbine in the positive x-direction. Thus, there will be attenuation of the ebb current to the west of the turbine and attenuation of the flood current to the east of the turbine.

At the turbine location, the current is flood-ebb asymmetric, favouring the flood (Figure 4.5a). Attenuation of the ebb current in a region of flood dominant current will augment the FVA whilst attenuation of the flood current in a region of flood dominant current will reduce the FVA. Therefore, there is augmentation of the FVA to the west and reduction to the east. If the ambient current was ebb dominant, then reduction would have been seen to the west and augmentation to the east.

When the turbine is deployed at different locations the pattern of change to the FVA appears approximately the same at each location (Figure 5.3). This seems to be at odds with the previous explanation as to why augmentation occurs to the west and reduction to the east, as for the turbine on the $A_{S,2} = 0$ contour the tide is flood dominant to the east and ebb dominant to the west. This is a sign issue with $A_{S,2}$, as in the definition of $A_{S,2}$ used, $A_{S,2}$ may be positive (flood-dominant) and negative (ebb-dominant). The change to $A_{S,2}$ is more correctly given by:

$$\Delta A_S^\dagger = (A_{S,0} - A_{S,T}) \times \text{sign}(A_{S,0}) \tag{7.2.1}$$

where $A_{S,0}$ is the FVA in the unoccupied channel and $A_{S,T}$ is the FVA in the channel following the deployment of the turbine. Defined this way, whether the tide is flood or ebb dominant, $\Delta A_S^\dagger > 0$ indicates reduction to the FVA and $\Delta A_S^\dagger < 0$ indicates augmentation of the FVA. Using $\Delta A_S^\dagger$ rather than ΔA_S Figure 5.3b is re-plotted in Figure 7.1. In this figure the difference in the effect of the turbine at the $A_{S,2} = 0$ contour compared to the other deployments is more obvious. On the $A_{S,2} = 0$ contour the turbine can clearly be seen to reduce the FVA in both directions, in line with the predictions above.

The ambient asymmetry conditions do therefore influence the effect of the turbine, as there is a difference in the effect of the turbine on the FVA when the turbine is deployed in a magnitude asymmetric current compared to a magnitude symmetric current. However, it did not appear that stronger ambient FVA led to

a greater impact on FVA by the turbine. Figure 7.2 presents a flow chart which considers the form the change to the FVA will take depending on the natural asymmetry conditions. Six possible effects are identified:

1. augmentation to the FVA in the flood-wards direction and reduction in the ebb-wards direction,

2. augmentation to the FVA in the ebb-wards direction and reduction in the flood-wards direction,

3. augmentation to the FVA in both directions,

4. reduction to the FVA in both directions,

5. augmentation to the FVA in the direction of the current used to convert energy by the turbine,

6. reduction to the FVA in the direction of the current used to convert energy by the turbine.

1–4 are possible when the turbine operates on both phases of the tide, and 5 and 6 are possible when the turbine operates on only one phase of the tide.
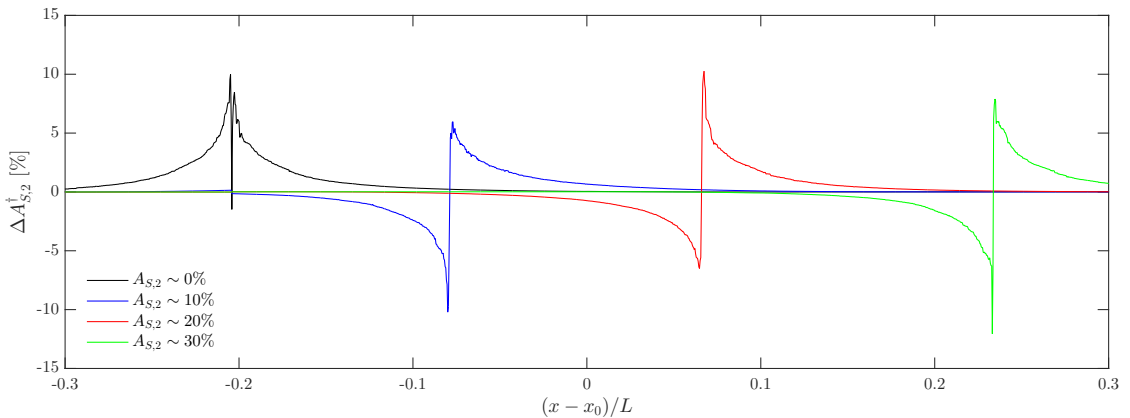
Figure 7.1: Correction to Figure 5.3b, using (7.2.1).

In practice, at sites of interest for tidal energy extraction, such as the Raz de Sein [Gillou and Chapalain, 2017b] and Fromveur Strait [Thiébaut and Sentchev, 2017] (both in Brittany, France), the Raz Blanchard [Thiébot et al., 2015, Gillou et al., 2018] (in Normandy, France) and the Westray Firth, Fall of Warness, Stronsay Firth

system in Orkney, Scotland [Neill et al., 2014], a range of asymmetry conditions are seen across the sites. Thus, a range of effects to the FVA at these sites by TST operation is expected, given the discussion above.
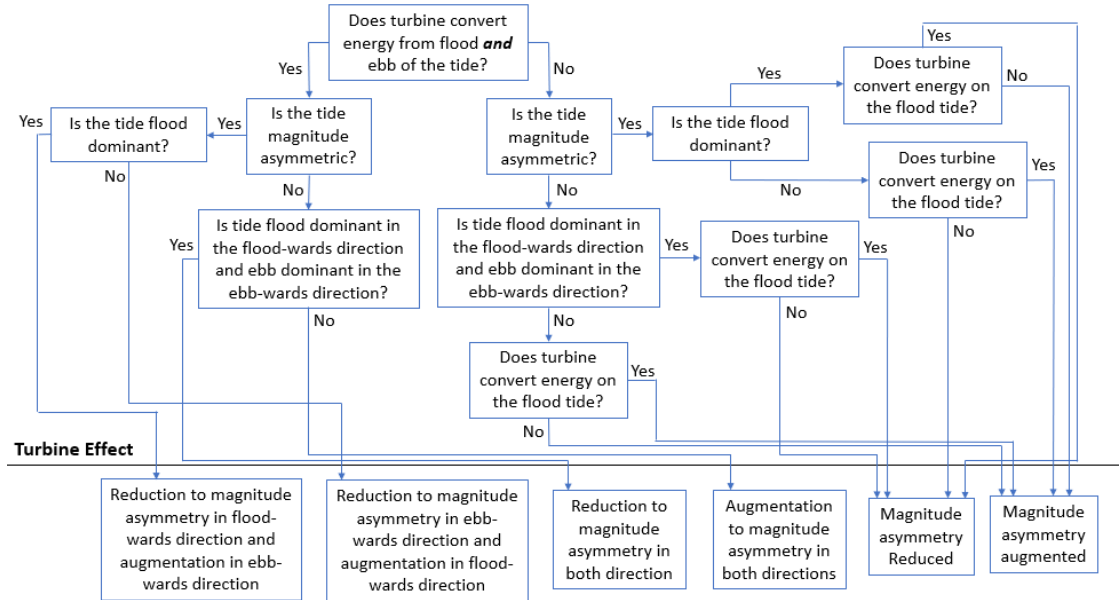
Figure 7.2: Flow chart of the possible pattern of change to the FVA for different turbine types deployed in regions of differing FVA.

In the Fromveur Strait, Gillou and Chapalain [2017a] considered the change to the residual circulation resulting from energy conversion by an array of TSTs. In their results it appeared that the magnitude of the residual currents were reduced slightly in large residual eddies that were seen to either side of the channel due to the addition of tidal turbines to their model. If the turbines were deployed within the region of magnitude symmetry that exists within the Fromveur Strait [Thiébaut and Sentchev, 2017, Gillou et al., 2018] then this is in line with the predictions above. However, it is difficult to draw any conclusions either way from the results presented by Gillou and Chapalain [2017a], a study of the change to FVA by TSTs was not the objective of their work.

Stronger support is given by Thiébot et al. [2015], who explored the impact of TST arrays deployed in the Raz Blanchard (Alderney Race) on residual sediment transport. Their work presents the different areas experiencing current attenuation on the flood and ebb of the tide. They also show the operation of the arrays to alter residual transport, suggesting alteration to the FVA, and report increased

FVA in the areas affected by the arrays. Thiébot et al. [2015] also, independently, offer the same explanation for the change to the FVA, the flood ebb asymmetry in the spatial distribution of current attenuation resulting from turbine operation.

In theory any down-stream reduction to the tidal current by a turbine will lead to a change to the flow velocity asymmetry. When do the changes caused by the turbines become of significance? One approach to addressing this question may be to compare changes by the turbine to the natural variability in asymmetry. A similar approach was taken by Robins et al. [2014].

In Section 4.4 it was seen that there is a temporal variation in asymmetry (e.g. Figure 4.26). One might consider changes caused by the turbine to be "significant" if they alter the asymmetry beyond the range it would be altered naturally. However, the original natural asymmetry will be superimposed upon any change and also may be altered by the turbine(s) operation. Further, the effect of the turbine varies temporally (Figure 4.26). In addition, other physical processes, such as wind induced currents, waves or surge may also induce variability in the current asymmetry. Changes to asymmetry induced by turbines could be compared to these potential natural sources of variation in asymmetry. With the turbine induced changes considered significant when they are on the order of or exceed natural sources.

7.2.2 The Impact of Arrays of Tidal-Stream Turbines and Their Energy Conversion

When multiple turbines were deployed in the channel as a row, the effect of the array did not scale from the effect of a single turbine as one might expect. However, when deployed as a line along the length of the channel the effect of the turbines on the tide seemed to combine in an additive fashion. Reductions were larger in regions where multiple turbines would be expected to simultaneously introduce reductions, based on the changes seen when they operated individually (Figures 5.5a, 5.5c, 5.6a, 5.6c, 5.8a, 5.8c, 5.9a, 5.9c, 5.11a, 5.11c, 5.12a, 5.12c). In regions where reductions and increases were superimposed, the net result was either lesser augmentation or reduction (Figures 5.5b, 5.6b, 5.7, 5.8b, 5.9b, 5.10, 5.11b, 5.12b, 5.13). Thus, the effect of a single turbine scales as one might expect when the

turbines are deployed in the area of effect of their neighbours, i.e. "upstream" or "downstream" from one-another.

When they were deployed in a row, i.e. outside of the area of effect of their neighbours, the effects of each turbine did not scale as one might expect. The array of turbines did not act as a group of individual turbines. The peak reduction to the tidal current caused by each turbine in the row was reduced when the turbines were deployed as a row compared to an individual turbine (Figure 5.30a). Conversely, the phase lag introduced by each turbine was larger when they were deployed in a row (Figure 5.30d). The phase lag suggests increased impediment of the tidal wave for a row of turbines compared to a single turbine, with the degree of impediment increasing with increased blockage of the channel by the row (Figure 5.30d). The impediment of the flow introduced an increased head difference, and therefore a pressure differential across the turbines. This pressure differential will contribute to driving the turbines, thus the turbines draw less energy from the current, and the velocity deficit this introduced is reduced compared to the velocity deficit of an individual turbine [Vennell, 2012, 2013]. These smaller wakes then lead to smaller (peak) changes to the FVA (Figure 5.30g).

In the row configuration, there are multiple turbines in operation, thus, despite the smaller wakes per turbine, given the larger number of turbines one expects a larger overall effect. Again, this is subtler than one might at first expect. When the total area experiencing a change to the M_2 current of $>1\%$ was calculated, there was only a small difference in this area for rows containing 9, 10 and 13 turbines, and in each case the area was similar to that of a single turbine. This suggests a balance between the reduction in the size of each turbine's wake and the increases in the number of turbines, and therefore the total size of all wakes combined. At blockages above $\varepsilon_0 \approx 0.1$ this balance was overcome and the total area of effect of the array increases as the number of turbines in the row is increased.

The suspected explanation for this is that the model lacked the resolution to resolve the inter-turbine bypass flow. Elements containing turbines were located adjacent to one another, with no unoccupied element between them (Figures 5.16d & 5.16e). This will have implications for wake recovery, leading to an over prediction of the area of effect of the array. Higher resolution simulations will therefore be

required in order to investigate if the two highest blockage rows also have a similar area of effect.

The above only considers the local, or near-field effect of the row of turbines. For example, as previously discussed, with increased blockage of the channel by TSTs there is an increased impediment to the propagation of the tidal wave. This will alter the times of high and low tide in the region surrounding the array [Nash et al., 2014] which may interfere with shipping and other maritime activities in the region. Similarly, this influence on the propagation of the tidal wave will alter the inundation of inter-tidal zones that may surround the array [Nash et al., 2014] and in bay / estuary systems the flushing and residence time will be affected [Nash et al., 2014, Wang and Yang, 2017]. Outside of the subtleties of the array effects, in general larger arrays will lead to greater attenuation of tidal currents (e.g. O'Hara-Murray and Gallego [2017]).

As it appears the asymmetric attenuation to the currents at different locations that leads to changes to the magnitude asymmetry the effect seen for a single turbine may scale up simply for arrays with regional scale effects. This is supported by the results of Thiébot et al. [2015], who concluded that the asymmetry in the spatial distribution of current attenuation by the array as a whole led to the changes to FVA that they saw.

The per turbine energy conversion of the turbines deployed as a line was reduced compared to the energy conversion of a single turbine (Figures 6.6a & 6.6b). This difference increased as the turbines were deployed closer together (Figures 6.6a & 6.6b). This is the result of the turbines being deployed in the area of effect of their neighbours. When deployed as a row the per turbine energy conversion was increased compared to the energy conversion of a single turbine (Figures 6.8a & 6.8b). With the difference increasing as the row blockage increases (Figures 6.8a & 6.8b). The cause of this was touched upon previously. With increased blockage the head difference across the row increases and the turbines convert energy from this as well as from the current itself [Vennell, 2012, 2013]. Additionally, with increased blockage the velocity of the bypass flow is reduced, decreasing energy lost to mixing of the bypass flow and the wake flow [Garrett and Cummins, 2007, Vennell, 2010].

The significance of the flow asymmetry effect on overall power production

could again be determined by comparison against natural variability. However, an assessment of the effect on the economics of the array may be a more effective measure. It was seen that changes to the flow velocity asymmetry due to the addition of turbines did not significantly contribute towards the observed changes in energy conversion over a tidal cycle in comparison to changes to the amplitude of the current velocity (Figure 6.2). Therefore, when it comes to the optimisation of turbine positions for maximising power production, changes to the flow velocity asymmetry are not likely to be an important consideration.

Asymmetric power supply to the grid may be of concern. This will perhaps be of more concern to national grid managers looking to flatten variability in energy supply than to tidal-stream developers. Unless there is some imposed economic penalty for variability in supply. It is at this level that the significance of energy conversion asymmetry will be seen, especially for large numbers of turbines connected to the grid in potentially interacting turbine arrays. This lies outside the scope of the present work but is worthy of further consideration in future work.

7.2.3   The Implication of Hydrodynamic Changes for Sediment Transport

It was seen that the changes to the theoretically and practically extractible resource resulting from the operation of a single TST could be predicted from the changes to the hydrodynamics (Figures 6.2 & 6.3 respectively). Similarly, it was seen that changes to gross and net volume of sediment transported could be predicted from changes to the hydrodynamics (Figures 6.11–6.13). Changes to the magnitude of the tidal current led to linear changes to the gross volume of sediment transported per tidal cycle, by both bed- and suspended-load transport. Whilst changes to the FVA led to changes to the net volume of sediment transported by both bed- and suspended-load transport. To the east of the turbine, reductions to the net volume of transported sediment were seen, whilst increases to the net volume of transported sediment were seen to the west.

The above results can be extrapolated to the different turbine locations that were tested in Experiment 1 of Chapter 5, with the conclusion that reduction to the net volume of sediment transported as bed- and suspended-load will be

seen to both sides of the turbine when it is deployed on the $A_{S,2} = 0$ contour. In general, one might further extrapolate these conclusions to all possible patterns of change to the FVA resulting from TST operation identified in Figure 7.2. From this extrapolation one reaches the conclusion that:

1. augmentation to the net volume of sediment transported to the flood-wards side of the turbine and reduction to the ebb-wards side,

2. augmentation to the net volume of sediment transported to the ebb-wards side of the turbine and reduction to the flood-wards side,

3. augmentation to the net volume of sediment transported to both sides,

4. reduction to the net volume of sediment transported to both sides,

5. augmentation to the net volume of sediment transported downstream of the turbine,

6. reduction to the net volume of sediment transported downstream of the turbine,

will occur when situations leading to the corresponding six outcomes from Figure 7.2 are satisfied. In all of these cases, the gross volume of sediment transported will be reduced in both directions for bi-directional turbines, or downstream for a uni-directional turbine (Figure 6.11a, 6.12a & 6.13a).

The reduction to the gross volume of sediment transported and the potential reduction to the net volume of sediment transported implies accumulation of sediment in the vicinity of the turbine. Would such an effect be seen in reality?

Scour around marine structures is well known (e.g. McGovern et al. [2014]) and when one considers the turbine supporting structure, which was not considered in this work, one expects to see scour (erosion of the bed) in the vicinity of the turbine [Chen and Lam, 2014b]. Also, when one considers the flow in three dimensions there will be accelerated bypass flow beneath the turbine [Chen and Lam, 2014a], accompanied by increased bed shear stress, a driver of sediment transport. The turbine wake itself is characterised by increased turbulence [Masters et al., 2013, Stallard et al., 2013]. Near the bed, below the wake, both the speed and vorticity

of the flow will be increased compared to ambient conditions, leading to enhanced erosion of the bed sediment [Vybulkova, 2013].

Martin-Short et al. [2015] found accumulation of sediment in the vicinity of an array of turbines in the inner Sound of Stroma, Pentland Firth, Scotland. However, the authors also raise similar points regarding the three-dimensional nature of the flow around a turbine. In a three-dimensional simulation of energy extraction at the same location Fairley et al. [2015] did not identify accumulation of sediment with the array located within the inner Sound of Stroma. However, the study of Fairley et al. [2015] looked at the cumulative extraction at multiple sites which may contribute to this difference.

It appears Martin-Short et al. [2015] saw only FVA reduction (based on change to residual shear stress as shown in Figure 6 of Martin-Short et al. [2015]) in the vicinity of the array, with the array located in a region of ebb dominant flow (cf. Figures 4 & 6 of Martin-Short et al. [2015] and Figure 11 of Fairley et al. [2015] for indication of array location in flood dominant region). Due to the complex pattern of residual flow in the region, the tide is flood-dominant ebb-wards of the array location (approximately west), and ebb dominant flood-wards of the array location (approximately east) (Figure 6 of Martin-Short et al. [2015]). Hence, one would expect reduced asymmetry, and therefore reduced residual bed shear stress either side of the array, given the discussion of §7.2.1 and §7.2.2. Martin-Short et al. [2015] take this as an indicator of increased sediment deposition.

It is interesting to note here the different apparent changes to the FVA between the works of Martin-Short et al. [2015] and Thiébot et al. [2015] with the turbine arrays deployed in differing ambient FVA conditions. The differences fit with the predictions made in Figure 7.2. Thus, with an understanding of this simple mechanism for the change to the FVA and knowledge of the ambient asymmetry conditions, the effect of an array of turbines on the asymmetry may be broadly predictable prior to simulation or measurement of the effect. A detailed understanding of the spatial distribution of change to the FVA will required simulation to determine, especially at real-world sites with complex bathymetries. Likewise, an understanding of the morphodynamic implications of any changes will also require that simulations are undertaken. However, it will certainly be helpful when

analysing the results of simulations to know roughly what changes to expect.

7.3   Limitations of the Work

It was concluded above that it is the attenuation of one phase of the tide (and not the other) within the wake that leads to the change to the magnitude asymmetry. Given this, it is therefore important that the wake is represented in the model as accurately as possible. A blade element momentum theory or actuator line representation of the turbine rather than an actuator disk representation would result in a more realistic turbine wake (e.g. Masters et al. [2013] and Churchfield et al. [2011] respectively). However, these turbine representations both require much higher mesh resolution and therefore computational power.

Roc et al. [2013] proposed the addition of source and sink terms to the turbulence closure scheme in a coastal model for more accurate representation of a turbine wake. With a code that incorporates the method of Roc et al. [2013] the experiments in this thesis could be repeated with better representation of a TST with relative ease. The code used for this work, DHI's MIKE, is a commercial 'blackbox' code, thus a different code is required, such as ROMS [Shcheptkin and McWilliams, 2005], the code which Roc et al. [2013, 2014] originally used, or FVCOM [Chen et al., 2003], a code in which the Roc et al. [2013] turbine representation been has successfully implemented (e.g. Li et al. [2017]).

Ultimately one might question the benefits of a more complex model without sufficient observational data to validate the model. Future efforts with respect to the effect of a turbine on tidal asymmetry may be better focused on measurements in nature. However, the prohibitive cost and commercial sensitivity of data may mean such work is not practical at the present stage of development of the tidal-stream industry.

In the multiple turbine experiments (Chapter 5) maintaining a uniform element size across the turbine deployments was important, especially when results were presented as profiles (Appendix F). Initially the experiments were intended to be carried out using a uniform square grid, which would have maintained the uniformity of the grid size across the domain. In the model sensitivity tests (Chapter 3) when

using such a grid there was a large change in the turbine run at the boundary (Figure 3.21). It appeared the effect of the turbine was largely contained within a single element width along the channel. A similar effect was seen by Waldman [2018] in MIKE3. Therefore, the structured grid was abandoned in favour of an unstructured grid, which was seen in Chapter 3 to significantly reduce the effect of the turbine at the boundary (Figure 3.22).

Waldman [2018] took a different approach to the problem and nested a structured mesh for the region of turbine deployment within and unstructured mesh for the remaining domain. Such an approach may be more favourable than the use of a purely unstructured mesh and the work that would be required to ensure that all triangular elements that contain turbines are uniform. The differences in the two approaches could be explored in future work.

In the row experiment, the model mesh lacked the resolution to resolve the bypass flow between turbines, which may have led to the overprediction of the area of effect of the higher blockage rows. The mixed structured and unstructured mesh approach discussed above could also be applied to the row experiment, with the unstructured mesh of high enough resolution to resolve the inter-turbine regions, and therefore the turbine bypass flow. Future work should look to repeat the row experiment with such a model set-up.

Additionally, the row blockage was altered by adding additional turbines to the row. In doing this the distance between the turbines was reduced. In the interest of completeness, a further experiment could have been undertaken to establish the effect of the spacing between the turbines. The physical modelling study of Stallard et al. [2013] suggests that for a spacing of $3D$, turbine wakes act individually, whereas at spacings of $2D$ or less the wakes begin to merge. A future numerical study could be compared against these physical modelling results.

Further to the above, uncertainty surrounding the representation of a single turbine by the model casts doubt over the results obtained for multiple turbines. These doubts could be reduced by increasing the confidence in the single turbine results. This could be achieved through comparison of the wake effects of a single turbine against physical modelling results (better still against observations but these are not available at the time of writing). As part of any future work a steady

flow simulation of a turbine wake should be compared against physical experiment results using actuator disks, e.g. Myers and Bahaj [2010].

The sediment transport experiments that were undertaken lack the detail required to give an accurate picture of the morphodynamic change one might expect in the presence of an operational tidal turbine. The model was run for just 4 days and the boundary was forced only by the M_2 tide. As a two-dimensional model the slipstream below the turbine is not represented and the turbulence of the turbine wake may not be adequately represented. The simulations of Vybulkova [2013] show in fine detail the expected changes to the local sediment transport associated with the operation of a tidal turbine, with the rotating blades of the turbine and the associated turbulence resolved.

However, a detailed study of the changes to the sediment transport with view to understanding local erosion and accretion patterns was not the goal of this experiment. The goal was to establish if a predictable link between the change to the asymmetry in the current and any changes in net transport exists. This goal was met. However, in a more complex bathymetry, one more representative of reality the link may be more tenuous and less predictable. Thus, the simple linear trend identified should be treated with caution until a comparison in made in a more complex, realistic bathymetry.

The results from the experiments showed that for the grain-sizes used, suspended-load transport dominated the total load transport. However, in the experiment the initial condition for suspended load sediment concentration was zero, and no suspended sediment was input at the boundaries. Model sensitivity tests, where the effect of these settings, and for example the choice of sediment transport model e.g. Engelund and Fredsøe [1976], should be carried out to check the sensitivity of the model predictions to the user's choice of these settings.

More generally, the specific values of the grain-sizes that were tested were based on the Wentworth [1922] scale and the range of values was based on the range over which the van Rijn [1984a,b] sediment transport model is applicable. A uniform bed of fine, medium or even coarse sand is unlikely to be found at the kind of high energy site of interest for tidal energy development. For example, at the Holyhead Deep site, of interest to the tidal energy developer Minesto, Potter [2014] undertook

sediment grab samples of the site. The 13 sediment grab samples classified the bed (following Wentworth [1922]) as either exposed bedrock (2/13), gravel (9/13) or very coarse sand (1/13), with the lowest $d_{50} = 1.5$ mm. The study of Fairley et al. [2015] ascribed much of the area of the Pentland Firth a grain size classifying it as coarse sand or fine / very fine gravel, with regions of finer sand and exposed bedrock (Figure 5, Fairley et al. [2015]). Gillou and Thiébot [2016] describe the seabed of the Fromveur Strait and wider Moléne archipelago as being comprised of successive sections of gravel deposits in a region of exposed bed rock (see Figure 2, Gillou and Thiébot [2016]). These examples highlight both the heterogeneity of the bed sediments at high energy tidal sites as well as the presence of swept bedrock.

The M_2 current range of ∼2.8–3.8 m/s seen in the model (Figure 4.1) is similar to the M_2 current values at Moléne archipelago [Gillou and Thiébot, 2016], slightly larger than the range of current values seen at Holyhead Deep (e.g. Lewis et al. [2017]) and within the range of current values seen in the Pentland Firth (e.g. Waldman et al. [2017]). Therefore, a more realistic model design would have a bed sediment distribution more reflective of these sites. The issue here is that the van Rijn [1984a,b] sediment transport model is not appropriate for such coarse sediments. An approach similar to Martin-Short et al. [2015] could be used, where the thresholds of sediment motion and the bed shear stress is used as a proxy for expected changes to sediment transport, rather than a full sediment transport model.

In the compound tide experiment (§4.4), the multiple turbine experiments (Chapter 5) and the sediment transport experiment (§6.3) only the fixed-C_T turbines were studied. The variable-C_T turbine is a more realistic representation of a real-world TST. Thus, the accuracy of these experiments would all be improved by also looking at the changes due to this type of turbine in addition to the fixed-C_T turbine.

The methodology of using changes tidal harmonic constituents to represent changes to asymmetry has been successful in the experiments presented in this thesis. However, the presented experiments are physically simple; the bathymetry as simple as possible and the model for the most part forced by only the single most important tidal frequency, the M_2. In the experiment where a second constituent

was added the methodology required modification to account for the increased non-linearity this simple change introduced (Chapter 4, Section 4.4.2). In nature the number of harmonic constituents that would be needed in the analysis for an accurate description of the asymmetry and its temporal variation may be prohibitive. In such a non-linear environment a method involving taking the skewness of a sufficiently long time-series, coupled with harmonic analysis of the time-series, such as those outlined in Section 2.3 may be more favourable.

Chapter 8

Conclusion & Future Work

The main goal of this work was to understand how the operation of tidal-stream turbines alters the flood-ebb asymmetry of tidal currents. Emphasis was put on understanding this problem through changes to the shallow-water tides, and consideration was given to the potential effect of observed changes for sediment transport and the technically exploitable resource of neighbouring turbines. For this investigation harmonic expansions of the non-linear terms in the governing equations were first considered to determine which shallow-water tides might be affected. Numerical experiments were then undertaken to simulate turbine operation in a highly idealised model geometry, to gain a more detailed understanding of the changes to these tides. The effect of a single turbine and multiple turbines with fixed or variable turbine efficiencies was explored in a channel forced by either the M_2 tide only, or by both the M_2 and S_2 tides. Also tested was the effect of a turbine in various ambient conditions, and the effect of a turbine on sediment transport rates. The conclusions drawn from this work are discussed in §8.1, and recommendations on how this work may be expanded and potential future work are discussed in §8.2.

8.1   Conclusions

The most fundamental result of this work is the understanding of the way in which the turbine alters the flood-ebb magnitude asymmetry of the current that is gained from the simple numerical experiments for a single turbine. This change to the

current magnitude asymmetry can be explained by the flood-ebb asymmetry in the areas experiencing current attenuation over a tidal cycle. This result is far simpler than the suggested origin of changes to the current magnitude asymmetry hypothesized at the outset of this work. Namely the non-linear interaction of the turbine with the tide. However, these non-linear interactions may still contribute to the observed changes to the asymmetry, but it is the mechanism described above which appears to be the dominant mechanism by which turbines alter the asymmetry. The simplicity of the mechanism makes it scalable to arrays of turbines with far-field effects. Thus, prior to modelling, one might broadly predict the effect that the turbine will have on asymmetry prior to detailed modelling, provided one has prior knowledge of the ambient asymmetry conditions and flow directions at the intended site.

A simple link between the observed changes to the surrounding technically exploitable resource and the changes to the hydrodynamics by the turbines was observed. The overall reduction to the current was the primary driver of reduced available practical resource surrounding a turbine, rather than changes to the asymmetry. The changes to the current asymmetry do lead to changes to the flood-ebb asymmetry in the available resource. Similarly, the overall reduction to the current led to a reduction to the gross volume of sediment transported, and the changes to the current asymmetry altered the net volume of sediment transported. In all the above cases the knock-on changes were greater than the hydrodynamic changes. A 1% reduction to the current magnitude led to a ∼3% reduction to the theoretically available energy and a ∼4% reduction in the gross volume of sediment transported as bed-load and suspended load per tidal cycle. A 1% change to the current asymmetry led to a ∼2% change to the flood-ebb asymmetry of the theoretically available energy and a ∼6% change to the net bed-load transport. There was a linear trend between the hydrodynamic changes and the knock-on effects.

When multiple turbines were deployed in the channel, their effects were seen to combine where their areas of effect overlapped. Therefore, when deployed as a line each turbine converted less energy per tidal cycle and caused greater hydrodynamic changes than had it been deployed individually. The effect the turbine interactions

had on the asymmetry in the energy conversion depended on where in the array the turbine was located. When multiple turbines were deployed in a row, and therefore not within the area of effect of their neighbours, the peak changes caused by each of the turbines were reduced compared to an individual turbine. The area of effect of rows containing 9, 10 and 13 turbines was similar to the area of effect of a single turbine. For denser rows however, the area of effect increased with additional turbines. The per turbine energy conversion per tidal cycle was greater when the turbines were deployed in rows, compared to an individual turbine, with slightly increased, $\sim$5%, asymmetry in the energy conversion.

8.2 Recommendations for Future Work

In the previous chapter the limitations of the work described in this thesis were considered ($\S$7.3). A number of expansions of, or improvements to this work could be made in order to address these limitations.

The turbine row experiment could be expanded so that small numbers of turbines, e.g. 2, 3, 4, are deployed in the channel with large spacings, as very low blockage rows are not represented in the present experiment. A more complete experiment might add a single turbine at a time to the row, increasing the number of turbines from 1 to 26. Future work examining arrays of turbines should ensure the mesh is designed in such a way that the elements occupied by turbines are uniform in size. The turbine row experiment should also be accompanied by a study of the effect of the across channel inter-turbine spacing on the hydrodynamic changes by the turbines, as the row experiment in this work varies both blockage and inter-turbine spacing simultaneously.

All experiments that were performed in this work might be improved by the mesh refinements suggested above, and the use of an improved turbine representation. The experiments which tested only a fixed-C_T should be expanded to also examine the effect of variable-C_T, in particular arrays of variable-C_T turbines.

The most obvious avenue for the continuation of this work is to investigate the changes to asymmetry for a real-world site, and array. This could be achieved by performing additional analysis of simulations already discussed in the literature, or

through a new modelling study. Analysis of the changes to the current asymmetry across a range of sites with a range of ambient asymmetry conditions should be undertaken to fully test all of the predictions made in this thesis.

A potentially interesting avenue of further study would be to look at the effect of tidal-stream turbines on the tidal asymmetry in an estuarine or tidal inlet system, rather than a channel. In an estuarine system the inundation of the intertidal zones impacts on the flood-ebb asymmetry of the tides. Previous work has found that energy extraction in estuaries can alter the inundation of inter-tidal zones. This alteration to the inundation of the inter-tidal zones may have implications for the asymmetry in both the vertical (change in surface elevation) and horizontal (associated currents) tides.

Finally, beyond improvements to this work specifically field observations of the impacts of tidal-stream turbines are needed. This will help to validate this and other work and is perhaps the most important avenue of future work within the topic of the impacts of tidal-stream energy.

Bibliography

T. Adcock and S. Draper. "Power extraction from tidal channels – Multiple tidal constituents, compound tides and overtides". *Renewable Energy*, **63**:797–806, 2014. doi: 10.1016/j.renene.2013.10.037.

T. Adcock, S. Draper, and T. Nishino. "Tidal power generation – A review of hydrodynamic modelling". *Proceedings of the Institution of Mechanical Engineers, Part A: Journal of Power and Energy*, **229**(7):755–771, 2015. doi: 10.1177/0957650915570349.

R. Ahmadian, R. Falconer, and B. Bockelmann-Evans. "Far-field modelling of the hydro-environmental impact of tidal stream turbines". *Renewable Energy*, **38**(1): 107–116, 2012. doi: 10.1016/j.renene.2011.07.005.

Atlantis Resources Ltd. "MeyGen update – AR1500 turbine deployed in record time", 2017a. Available at: https://www.atlantisresourcesltd.com/2017/02/20/2225/ (Accessed: 2017-11-29).

Atlantis Resources Ltd. "MeyGen", 2017b. Available at: https://www.atlantisresourcesltd.com/projects/meygen/ (Accessed: 2017-11-29).

R. Bagnold. "An Approach to the Sediment Problem From General Physics", 1966. Geological Survey Professional Paper 422-I, U.S. Geological Survey, D.O.I., U.S.A., Available: https://pubs.usgs.gov/pp/0422i/report.pdf.

S. Bastón, S. Waldman, and J. Side. "Modelling Energy Extraction in Tidal Flows". In *TerraWatt Position Papers*, page 102. MASTS, 2014. Available: https://www.masts.ac.uk/media/35656/position_papers_terawatt_e-book.pdf.

BEIS. "Digest of UK Energy Statistics (DUKES) 2016: Main Report", 2016. Department for Buisness, Energy & Industrial Strategy, London. Available: https://www.gov.uk/government/collections/digest-of-uk-energy-statistics-dukes.

BEIS. "Digest of UK Energy Statistics (DUKES) 2017: Main Report", 2017. Department for Buisness, Energy & Industrial Strategy, London. Available: https://www.gov.uk/government/collections/digest-of-uk-energy-statistics-dukes.

T. Blackmore, W. Batten, and A. Bahaj. "Influence of turbulence on the wake of a marine current turbine simulator". *Proceedings of the Royal Society A: Mathematical and Physical Engineering Sciences*, **470**:20140331, 2014. doi: 10.1098/rspa.2014.0331.

J. Blanton, G. Lin, and S. Elston. "Tidal current asymmetry in shallow estuaries and tidal creeks". *Continental Shelf Research*, **22**:1731–1743, 2002. doi: 10.1016/S0278-4343(02)00035-3.

G. Boehlert and A. Gill. "Environmental and ecological effects of ocean renewable energy development: A current synthesis". *Oceanography*, **23**(2):68–81, 2010. doi: 10.5670/oceanog.2010.46.

B. Bruder and K. Haas. "Tidal distortion as pertains to hydrokinetic turbine selection and resource assessment". In *Proceedings of the 2nd Marine Energy Technology Symposium, METS2014, April 15–18, 2014*, Seattle, WA, 2014. Available: https://vtechworks.lib.vt.edu/handle/10919/49241.

D. Burnett, E. Barbour, and G. Harrison. "The UK solar energy resource and the impact of climate change". *Renewable Energy*, **71**:333–343, 2014. doi: 10.1016/j.renene.2014.05.034.

T. Burton, D. Sharpe, N. Jenkins, and E. Bossanyi. *"Wind Energy Handbook"*. John Wiley & Sons, Ltd., Chichester, 2001.

W. Carr and C. Derby. "Chemically stimulated feeding behaviour in ma-

rine animals". *Journal of Chemical Ecology*, **12**:989–1011, 1986. doi: 10.1007/BF01638992.

D. Cartwright, A. Edden, R. Spencer, and J. Vassie. "The tides of the north-east Atlantic Ocean". *Philosophical Transactions of the Royal Society A*, **298**:87–139, 1980. doi: 10.1098/rsta.1980.0241.

C. Chen, H. Liu, and R. Beardsley. "An unstructured grid, finite-volume, three-dimensional, primitive equations ocean model: Application to coastal ocean and estuaries". *Journal of Atmospheric and Oceanic Technology*, **20**(1):159–186, 2003. doi: 10.1175/1520-0426(2003)020<0159:AUGFVT>2.0.CO;2.

L. Chen and W. Lam. "Slipstream between marine current turbine and seabed". *Energy*, **68**:801–810, 2014a. doi: 10.1016/j.energy.2014.02.083.

L. Chen and W. Lam. "Methods for predicting seabed scour around marine current turbine". *Renewable and Sustainable Energy Reviews*, **29**:683–692, 2014b. doi: 10.1016/j.rser.2013.08.105.

W.B. Chen, H. Chen, L.Y. Lin, and Y.C. Yu. "Tidal current power resources and influence of sea-level rise in the coastal waters of Kinmen Island, Taiwan". *Energies*, **10**(5):652, 2017. doi: 10.3390/en10050652.

M. Churchfield, Y. Li, and P. Moriarty. "A large-eddy simulation study of wake propagation and power production in and array of tidal-current turbines". In *Proceedings of EWTEC 2011*, Southampton, 2011.

Climate Change Act. c. 27, 2008. Available at: http://www.legislation.gov.uk/ukpga/2008/27 (Accessed 2017-11-23).

A. Copping, L. Hanna, B. Van Cleve, K. Blake, and R. Anderson. "Environmental risk evaluation system - An approach to ranking risk of ocean energy development on coastal and estuarine environments". *Estuaries and Coasts*, **38**(S.1):287–302, 2015. doi: 10.1007/s12237-014-9816-3.

A. Copping, N. Sather, L. Hanna, J. Whiting, G. Zydlewski, A. Gill, I. Hutchington, A. O'Hagan, T. Simas, J. Bald, C. Sparling, J. Wood, and E. Mas-

den. "Annex IV 2016 Science Report: Environmental Effects of Marine Renewable Energy Development Around the World", 2016. Available: https://tethys.pnnl.gov/sites/default/files/publications/Annex-IV-2016-State-of-the-Science-Report_MR.pdf.

Crown Estate. "UK Wave and Tidal Key Resource Areas Project: Technical Methodology Report", 2013. Available: http://www.marineenergywales.co.uk/wp-content/uploads/2016/01/Summary-Report-FINAL.pdf.

M. Darwish and F. Moukalled. "TVD schemes for unstructured grids". *International Journal of Heat and Mass Transfer*, **46**:559–611, 2003. doi: 10.1016/S0017-9310(02)00330-7.

M. De Dominicis, R. O'Hara-Murray, and J. Wolf. "Multi-scale ocean response to a large tidal-stream turbine array". *Renewable Energy*, **114**(B):1160–1179, 2017. doi: 10.1016/j.renene.2017.07.058.

H. de Swart and J. Zimmerman. "Morphodynamics of tidal inlet systems". *Annual Reviews of Fluid Mechanics*, **41**:203–229, 2009. doi: 10.1146/annurev.fluid.010908.165159.

Z. Defne, K. Hass, and A. Fritz. "Numerical modelling of tidal currents and the effects of power extraction on estuarine hydrodynamics along the Georgia coast, USA". *Renewable Energy*, **36**(12):3461–3471, 2011. doi: 10.1016/j.renene.2011.05.027.

DHI. *"MIKE 21 Flow Model FM, Hydrodynamic User Guide"*, 2016a.

DHI. *"MIKE 21 & MIKE 3 Flow Model FM, Hydrodynamic and Transport Module, Scientific Documentation"*, 2016b.

DHI. *"MIKE 21 & MIKE 3 Flow Model FM, Sand Transport Module, Scientific Documentation"*, 2016c.

DHI. *"MIKE 21 Flow Model FM, Sand Transport Module, incl. Shoreline Morphology, User Guide"*, 2016d.

A. Doodson. "The Harmonic development of the tide-generating potential". *Proceedings of the Royal Society A: Mathematical and Physical Engineering Sciences*, **100**(704):305–329, 1921. doi: 10.1098/rspa.1921.0088.

J. Dronkers. "Tidal asymmetry and estuarine morphology". *Netherlands Journal of Sea Research*, **20**(2/3):119–131, 1986. doi: 10.1016/0077-7579(86)90036-0.

G. Egbert and S. Erofeeva. Efficent inverse modelling of barotropic ocean tides. *Journal of Atmospheric and Ocean Technology*, 19.2:138–204, 2002. doi: 10.1175/1520-0426(2002)019¡:EIMOBO¿2.0.CO;2.

S. Elgar and R. Guza. "Observations of bispectra of shoaling surface gravity waves". *Journal of Fluid Mechanics*, **161**:425–448, 1985. doi: 10.1017/S0022112085003007.

ENERDATA. "Global Energy Statistical Yearbook 2017", 2017. Available at: https://yearbook.enerdata.net/total-energy/world-consumption-statistics.html (Accessed: 2017-11-23).

Energy and Climate Change Committee. DECC Annual Report and Accounts 2014–15, 2015. Oral Evidence: 10 November 2015, HC 544, Q2.

F. Engelund and J. Fredsøe. "A sediment transport model for straight alluvial channels". *Nordic Hydrology*, **7**:296–306, 1976. doi: 10.2166/nh.1976.0019.

European Union. Directive 2009/28/EC of the European Parliament and the Council of 23 April 2009 on the promotion of the use of energy from renewable sources and amending subsequently repealing Directives 2001/77/EC and 2003/30/EC. *Official Journal of the European Union*, 2009. L 140/16, 5.6.2009.

I. Fairley, I. Masters, and H. Karunarathna. "The cumulative impact of tidal stream turbine arrays on sediment transport in the Pentland Firth". *Renewable Energy*, **80**:755–769, 2015. doi: 10.1016/j.renene.2015.03.004.

D. Fallon, M. Hartnett, A. Olbert, and S. Nash. "The effects of array configuration on the hydro-environmental impacts of tidal turbines". *Renewable Energy*, **64**: 10–25, 2014. doi: 10.1016/j.renene.2013.10.035.

P. Fraenkel. "Development and testing of Marine Current Turbine's SeaGen 1.2 MW tidal stream turbine". In *Proceedings of the 3rd International Conference on Ocean Energy*, Bilbao, 2010.

C. Friedrichs and D. Aubrey. "Non-linear tidal distortions in shallow well-mixed estuaries: A synthesis". *Estuarine, Coastal and Shelf Science*, **27**:521–545, 1988. doi: 10.1016/0272-7714(88)90082-0.

C. Garrett and P. Cummins. "Generating power from tidal currents". *Journal of Waterway, Port and Ocean Engineering*, **130**(3):114–119, 2004. doi: 10.1061/(ASCE)0733-950X(2004)130:3(114).

C. Garrett and P. Cummins. "The power potential of tidal currents in channels". *Proceedings of the Royal Society A: Mathematical, Physical and Engineering Sciences*, **461**:2563–2572, 2005. doi: 10.1098/rspa.2005.1494.

C. Garrett and P. Cummins. "The efficiency of a turbine in a tidal channel". *Journal of Fluid Mechanics*, **588**:243–251, 2007. doi: 10.1017/S0022112007007781.

C. Garrett and P. Cummins. "Limits to tidal current power". *Renewable Energy*, **33**(11):2485–2490, 2008. doi: 10.1016/j.renene.2008.02.009.

A. Gill. "Offshore renewable energy: Ecological implications of generating electricity in the coastal zone". *Journal of Applied Ecology*, **42**(4):605–615, 2005. doi: 10.1111/j.1365-2664.2005.01060.x.

N. Gillou and G. Chapalain. "Assessing the impact of tidal stream energy extraction on the Lagrangian circulation". *Applied Energy*, **203**:321–332, 2017a. doi: 10.1016/j.apenergy.2017.06.022.

N. Gillou and G. Chapalain. "Tidal turbines' Layout in a Stream with Asymmetry and Misalignment". *Energies*, **10**(11):1892, 2017b. doi: 10.3390/en10111892.

N. Gillou and J. Thiébot. "The impact of seabed rock roughness on tidal stream power extraction". *Energy*, **112**:762–773, 2016. doi: 10.1016/j.energy.2016.06.053.

N. Gillou, S. Neill, and P. Robins. "Characterising the tidal stream power resource around France using a high-resolution harmonic database". *Renewable Energy*, **123**:706–718, 2018. doi: 10.1016/j.renene.2017.12.033.

G. Godin and G. Gutiérrez. "Non-linear effects in the tide of the Bay of Fundy". *Continental Shelf Research*, **5**(3):379–402, 1986. doi: 10.1016/0278-4343(86)90004-X.

W. Gong, H. Schuttelaars, and H. Zhang. "Tidal asymmetry in a funnel-shaped estuary with mixed semidiurnal tides". *Ocean Dynamics*, **66**:637–658, 2016. doi: 10.1007/s10236-016-0943-1.

S. Gooch, J. Thomson, B. Polagye, and D. Meggitt. "Site characterisation for tidal power". In *OCEANS 2009 – Marine Technology for Our Future: Global and Local Challenges, October 26–29, 2009*, Biloxi, MS, 2009.

P. Groen. "On the residual transport of suspended matter by an alternating tidal current". *Netherlands Journal of Sea Research*, **3**(4):564–574, 1967. doi: 10.1016/0077-7579(67)90004-X.

D. Hasegawa, J. Sheng, D. Greenberg, and K. Thompson. "Far-field effects of tidal energy extraction in the Minas Passage on tidal circulation in the Bay of Fundy and Gulf of Maine using a nested-grid coastal circulation model". *Ocean Dynamics*, **61**(11):1845–1868, 2011. doi: 10.1007/s10236-011-0481-9.

M. Hashemi, S. Neil, P. Robins, A. Davies, and M. Lewis. "Effect of waves on the tidal energy resource at a planned tidal stream array". *Renewable Energy*, **75**: 626–639, 2015. doi: 10.1016/j.renene.2014.10.029.

C. Hirsch. *"Numerical Computation of Internal and External Flows, Volume 2: Computational Methods for Inviscid and Viscous Flows"*. Wiley, New York, 1990.

H.M. Government. "2050 Pathway Analysis", 2010. DECC, London. Available: https://beisgovuk.citizenspace.com/decc-policy/2050_pathways/supporting_documents/8626DECCPt1Introduction.pdf.

M. Howarth. "Tidal Currents on the Continental Shelf". In A. Stride, editor, *Offshore Tidal Sands — Processes and Deposits*. Chapman and Hall, London, 1982.

A. Iyer, S. Couch, G. Harrison, and A. Wallace. "Variability and phasing of tidal current energy around the United Kingdom". *Renewable Energy*, **51**:343–357, 2013. doi: 10.1016/j.renene.2012.09.017.

P. Jawahar and H. Kamath. "A high-resolution procedure for Euler and Navier-Stokes computations on unstructured grids". *Journal of Computational Physics*, **164**:165–203, 2000. doi: 10.1006/jcph.2000.6596.

A. Kabbaj and C. Le Provost. "Nonlinear tidal waves in channels: A perturbation method adapted to the importance of quadratic bottom friction". *Tellus*, **32**: 143–163, 1980. doi: 10.1111/j.2153-3490.1980.tb00942.x.

R. Karsten, J. McMillan, M. Lickly, and R. Haynes. "Assessment of tidal current energy in the Minas Passage, Bay of Fundy". *Proceedings of the Institution of Mechanical Engineers, Part A: Journal of Power and Energy*, **222**(5):493–507, 2008. doi: 10.1243/09576509JPE555.

G. Keenan, C. Sparling, H. Williams, and F. Fortune. SeaGen Environmental Monitoring Programme: Final Report, 2011. Report by Royal Haskoning. Available: http://srmprojects.ca/wp-content/uploads/2012/12/SeaGen-Final-EnvMonitProg-Report-MCT-2011.pdf.

S. Kramer, M. Piggott, J. Hill, L. Kregting, D. Pritchard, and B. Elsaesser. The modelling of tidal turbine farms using multi-scale, unstructured mesh models. In *Proceedings of the 2nd International Conference on Environmental Interactions of Marine Renewable Energy Technologies (EMIR 2014), Stornoway, Scotland*, 2014.

W. Krumbein and E. Aberdeen. "The sediments of Barataria Bay". *Journal of Sedimentary Petrology*, **7**(1):3–17, 1937. doi: 10.1306/D4268F8B-2B26-11D7-8648000102C1865D.

M. Lewis, S. Neill, P. Robins, and M. Hashemi. "Resource assessment for future generations of tidal-stream energy arrays". *Energy*, **83**:403–415, 2015. doi: 10.1016/j.energy.2015.02.038.

M. Lewis, A. Angeloudis, P. Robins, P. Evans, and S. Neil. "Influence of storm surge on tidal range energy". *Energy*, **122**:25–36, 2017. doi: 10.1016/j.energy.2017.01.068.

X. Li, M. Li, S. McLelland, L.B. Jordan, S. Simmons, L. Amoudry, R. Ramirez-Mendoza, and P. Thorne. "Modelling tidal stream turbines in a three-dimensional wave-current fully coupled oceanographic model". *Renewable Energy*, **114**: 297–307, 2017. doi: 10.1016/j.renene.2017.02.033.

D. MacKay. Enhancing Electrical Supply by Pumped Storage in Tidal Lagoons, 2007. Available at: https://democracy.kent.gov.uk/documents/s11499/Lagoons.pdf (Accessed: 2017-11-25).

D. MacKay. *"Sustainable Energy - Without the Hot Air"*. UIT Cambridge Ltd., Cambridge, 2009.

R. Malki, I. Masters, A. Williams, and T. Croft. "The variation in wake structure of a tidal stream turbine with flow velocity". In *MARINE 2011, IV International Conference on Computational Methods in Marine Engineering*, page 137–148. Springer, 2011.

G. Marsh. "Tidal turbines harness the power of the sea". *Reinforced Plastics*, **48**(6):44–47, 2004. doi: 10.1016/S0034-3617(04)00344-3.

R. Martin-Short, J. Hill, S. Kramer, A. Avdis, P. Allison, and M. Piggott. "Tidal resource extraction in the Pentland Firth, UK: Potential impacts on flow regime and sediment transport in the Inner Sound of Stroma". *Renewable Energy*, **76**: 596–607, 2015. doi: 10.1016/j.renene.2014.11.079.

I. Masters, R. Malki, A. Williams, and T. Croft. "The influence of flow acceleration on tidal stream turbine wake dynamics: A numerical study using a coupled BEM–CFD model". *Applied Mathematical Modelling*, **37**:7905–7918, 2013. doi: 10.1016/j.apm.2013.06.004.

D. McGovern, S. Ilić, A. Folkard, S. McLelland, and B. Murphy. "Time development of scour around a cylinder in simulated tidal currents". *Journal of Hydraulic Engineering*, **140**(6):04014014, 2014. doi: 10.1061/(ASCE)HY.1943-7900.0000857.

I. Milne, R. Sharma, and R. Flay. The structure of turbulence in a rapid tidal flow. *Proceedings of the Royal Society A: Mathematical, Physical and Engineering Science*, 473:2017295, 2017. doi: 10.1098/rspa.2017.0295.

W. Minchinton. "Early Tide Mills: Some Problems". *Technology and Culture*, **20**(4):777–786, 1979. doi: 10.2307/3103639.

P. Munday, D. Dixon, J. Donelson, G. Jones, M. Pratchett, G. Devitsina, and K. Døving. "Ocean acidification impairs olfactory discrimination and homing ability of marine fish". *PNAS*, **106**(6):1848–1852, 2009. doi: 10.1073/pnas.0809996106.

L. Myers and A. Bahaj. "Experimental analysis of the flow field around horizontal axis tidal turbines by use of scale mesh disk rotor simulators". *Ocean Engineering*, **37**:218–227, 2010. doi: 10.1016/j.oceaneng.2009.11.004.

S. Nash, N. O'Brien, A. Olbert, and M. Hartnett. "Modelling the far field hydro-environmental impacts of tidal farms — A focus on tidal regime, intertidal zones and flushing". *Computers & Geoscience*, **71**:20–27, 2014. doi: 10.1016/j.cageo.2014.02.001.

National Grid. "Future Energy Scenarios 2016", 2016. Available at: http://fes.nationalgrid.com/media/1253/final-fes-2017-updated-interactive-pdf-44-amended.pdf.

National Grid. "Future Energy Scenarios 2017", 2017. Available at: http://fes.nationalgrid.com/media/1292/2016-fes.pdf.

S. Neill, E. Litt, S. Couch, and A. Davies. "The impact of tidal stream turbines on large scale sediment dynamics". *Renewable Energy*, **34**:2803–2812, 2009. doi: 10.1016/j.renene.2009.06.015.

S. Neill, J. Jordan, and S. Couch. "Impact of tidal energy converter (TEC) arrays on the dynamics of headland sand banks". *Renewable Energy*, **37**(1):387–397, 2012. doi: 10.1016/j.renene.2011.07.003.

S. Neill, M. Hashemi, and M. Lewis. "The role of asymmetry in characterizing the tidal resource of Orkney". *Renewable Energy*, **68**:337–350, 2014. doi: 10.1016/j.renene.2014.01.052.

A. Nicolle and M. Karpytchev. "Evidence for spatially variable bottom friction from tidal amplification and asymmetry in Pertuis Breton (France)". *Continental Shelf Research*, **27**:2346–2356, 2007. doi: 10.1016/j.csr.2007.06.005.

N. Nidzieko. "Tidal asymmetry in estuaries with mixed semidiurnal/diurnal tides". *Journal of Geophysical Research*, **115**:C08006, 2010. doi: 10.1029/2009JC005864.

R. O'Hara-Murray and A. Gallego. "A modelling study of the tidal stream resource of the Pentland Firth, Scotland". *Renewable Energy*, **102**:326–340, 2017. doi: 10.1016/j.renene.2016.10.053.

Orbital Marine Power. The concept, 2019. Available at: https://orbitalmarine.com/technology-development/the-concept (Accessed: 2019-03-10).

B. Parker. *"Frictional Effects on the Tidal Dynamics of a Shallow Estuary"*. PhD thesis, The John Hopkins University, 1984.

B. Parker. "The relative importance of the various nonlinear mechanisms in a wide range of tidal interactions (review)". In B. Parker, editor, *Tidal Hydrodynamics*. John Wiley & Sons, New York, 1991.

B. Parker. *"Tidal Analysis and Prediction"*. NOAA Special Publication NOS CO-OPS 3, 2007. Available: tidesandcurrents.noaa.gov/publications/Tidal_Analysis_and_Predictions.pdf.

R. Pawlowicz, B. Beardsley, and S. Lentz. "Classical tidal harmonic analysis including error estimates in MATLAB using *t_tide*". *Computers & Geoscience*, **28**:929–937, 2002. doi: 10.1016/S0098-3004(02)00013-4.

R. Pingree and D. Griffiths. "Sand transport pathways around the British Isles resulting from M_2 and M_4 tidal interactions". *Journal of the Marine Biological Association of the U.K.*, **59**:497–513, 1979. doi: 10.1017/S0025315400042806.

B. Polagye, B. Van Cleve, A. Copping, and K. Kirkendall. "Environmental Effects of Tidal Energy Development: Proceedings of a Scientific Workshop, March 22–25, 2010", 2010. NOAA Technical Memorandum NMFS F/SPO-116.

H. Postma. "Hydrography of the Dutch Wadden Sea". *Archives Néerlandaise de Zoologie*, **10**:405–511, 1954. Available: uuid:c39e4430-b9da-41c2-9465-402d7a7686a6.

H. Postma. "Transport and accumulation of suspended matter in the Dutch Wadden Sea". *Netherlands Journal of Sea Research*, **1**:148–190, 1961. doi: 10.1016/0077-7579(61)90004-7.

D. Potter. "A Multi-Disciplinary Investigation of the Fate of Disposed Dredge Spoil at Holyhead Deep, Anglesey". Master's thesis, Bangor University, 2014.

D. Pugh. *Tides, Surges and Mean Sea-Level.* John Wiley & Sons Ltd., Chichester, 1987.

V. Ramos, R. Carballo, M. Álvarez, M. Sánchez, and G. Iglesias. "Assessment of the impacts of tidal stream energy through high-resolution numerical modelling". *Energy*, **61**:541–554, 2013. doi: 10.1016/j.energy.2013.08.051.

reNEWS. Atlantis snaps up MCT, 2015. Available at: http://renews.biz/87791/atlantis-snaps-up-mct/ (Accessed: 29.11.17).

P. Robins, S. Neill, and M. Lewis. "Impact of tidal-stream arrays in relation to the natural variability of sedimentary processes". *Renewable Energy*, **72**:311–321, 2014. doi: 10.1016/j.renene.2014.07.037.

P. Robins, S. Neill, M. Lewis, and S. Ward. "Characterising the spatial and temporal variability of the tidal-stream energy resource over northwest European shelf seas". *Applied Energy*, **147**:510–522, 2015. doi: 10.1016/j.apenergy.2015.03.045.

I. Robinson. "The tidal dynamics of the Irish and Celtic Seas". *Geophysical Journal of the Royal Astronomical Society*, **56**:159–197, 1979. doi: 10.1111/j.1365-246X.1979.tb04774.x.

T. Roc, D. Conley, and D. Greaves. "Methodology for tidal turbine representation in ocean circulation model". *Renewable Energy*, **51**:448–464, 2013. doi: 10.1016/j.renene.2012.09.039.

T. Roc, D. Greaves, K. Thyng, and D. Conley. "Tidal turbine representation in an ocean circulation model: Towards realistic applications". *Ocean Engineering*, **78**: 95–111, 2014. doi: 10.1016/j.oceaneng.2013.11.010.

P. Roe. "Approximate Riemann solvers, parameter vectors, and difference-schemes". *Journal of Computational Physics*, **43**:357–372, 1981. doi: 10.1016/0021-9991(81)90128-5.

A. Shcheptkin and J. McWilliams. "The Regional Oceanic system (ROMS): A split-explicit, free-surface, topography-following-coordinate oceanic model". *Ocean Modelling*, **9**:347–404, 2005. doi: 10.1016/j.ocemod.2004.08.002.

M. Shields, D. Woolf, E. Grist, S. Kerr, A. Jackson, R. Harris, M. Bell, R. Beharie, A. Want, E. Osalusi, S. Gibb, and J. Side. "Marine Renewable Energy: The ecological implications of altering the hydrodynamics of the marine environment". *Ocean & Coastal Management*, **54**:2–9, 2011. doi: 10.1016/j.ocecoaman.2010.10.036.

J. Smagorinsky. "General circulation experiments with the primitive equations. I. The basic experiment". *Monthly Weather Review*, **91**(3):99–164, 1963. doi: 10.1175/1520-0493(1963)091<0099:GCEWTP>2.3.CO;2.

D. Song, X. Wang, A. Kiss, and X. Bao. "The contribution to tidal asymmetry by different combinations of tidal constituents". *Journal of Geophysical Research*, **116**:C12007, 2011. doi: 10.1029/2011JC007270.

A. Souza and A. Hill. "Tidal dynamics in channels: Single Channels". *Journal of Geophysical Research*, **111**:C09037, 2006. doi: 10.1029/2006JC003469.

R. Spain. "A possible Roman tidal mill", 2002. Paper 005, Kent Archaeological Society. Available at: http://www.kentarchaeology.ac/authors/005.pdf (Accessed: 2017-11-29).

P. Speer and D. Aubrey. "A study of non-linear tidal propagation in shallow inlet/estuarine systems part II: Theory". *Estuarine, Coastal and Shelf Science*, **21**:207–224, 1985. doi: 10.1016/0272-7714(85)90097-6.

P. Speer, D. Aubrey, and C. Friedrichs. "Nonlinear hydrodynamics of shallow tidal inlet/bay systems". In B. Parker, editor, *Tidal Hydrodynamics*. John Wiley & Sons, New York, 1991.

T. Stallard, R. Collings, T. Feng, and J. Whelan. "Interactions between tidal turbine wakes: Experimental study of a group of three-bladed rotors". *Philosophical Transactions of the Royal Society A: Mathematical, Physical and Engineering Sciences*, **371**:20120159, 2013. doi: 10.1098/rsta.2012.0159.

T. Stallard, T. Feng, and P. Stansby. "Experimental study of the mean wake of a tidal stream rotor in a shallow turbulent flow". *Journal of Fluids and Structures*, **54**:235–246, 2015. doi: 10.1016/j.jfluidstructs.2014.10.017.

R. Stewart. *"Introduction to Physical Oceanography"*. Texas A&M University, College Station, Texas, 2008. Available: http://oaktrust.library.tamu.edu/handle/1969.1/160216.

M. Thiébaut and A. Sentchev. "Asymmetry of tidal currents off the W. Brittany coast and assessment of tidal energy resource around Ushant Island". *Renewable Energy*, **105**:735–747, 2017. doi: 10.1016/j.renene.2016.12.082.

J. Thiébot, P. Bally du Bois, and S. Gillou. "Numerical modelling of the effect of tidal stream turbines on the hydrodynamics and the sediment transport – Application to the Alderney Race (Raz Blanchard), France". *Renewable Energy*, **75**:356–365, 2015. doi: 10.1016/j.renene.2014.10.021.

D. Tritton. *Physical Fluid Dynamics*. Clarendon Press, London, 2nd edition, 1988.

A. Urbaninsky. *"Electricity in the Service of Man"*. Cassell and Company, London, 1896.

J. van de Kreeke and K. Robaczemska. "Tide-induced residual transport of coarse sediment: Application to the Ems Estuary". *Netherlands Journal of Sea Research*, **31**(3):209–220, 1993. doi: 10.1016/0077-7579(93)90022-K.

L. van Rijn. "Sediment transport, part 1: Bed load transport". *Journal of Hydraulic Engineering*, 110:1431–1456, 1984a.

L. van Rijn. Sediment transport, part II: Suspended load transport. *Journal of Hydraulic Engineering*, **110**(11):1613–1641, 1984b. doi: 10.1061/(ASCE)0733-9429(1984)110:11(1613).

R. Vennell. "Oscillating barotropic currents along short channels". *Journal of Physical Oceanography*, **28**:1561–1569, 1998. doi: https://doi.org/10.1175/1520-0485(1998)028<1561:OBCASC>2.0.CO;2.

R. Vennell. "Tuning tidal turbines in a channel". *Journal of Fluid Mechanics*, **663**: 253–267, 2010. doi: 10.1017/S0022112010003502.

R. Vennell. "Realizing the potential of tidal currents and the efficiency of turbine farms in a channel". *Renewable Energy*, **47**:95–102, 2012. doi: 10.1016/j.renene.2012.03.036.

R. Vennell. "Exceeding the betz limit with tidal turbines". *Renewable Energy*, **58**: 277–285, 2013. doi: 10.1016/j.renene.2012.12.016.

L. Vybulkova. *"A study of the Wake of an Isolated Tidal Turbine with Application to its Effects on Local Sediment Transport"*. PhD thesis, University of Glasgow, 2013. Available: http://theses.gla.ac.uk/4997/1/2013vybulkovaphd.pdf.

S. Waldman. Personal Communication, 15th April, 2018.

S. Waldman, G. Genet, S. Bastón, and J. Side. "Correcting for mesh size dependency in a regional model's representation of tidal turbines". In *Proceedings of the 11th European Wave and Tidal Energy Conference (EWTEC 2015), Nantes, France*, 2015. doi: 10.13140/RG.2.1.3571.6726.

S. Waldman, S. Baston, R. Nemalidinne, A. Chatzirodou, V. Venugopal, and J. Side. "Implementation of tidal turbines in MIKE3 and Delft3D models of Pentland Firth & Orkney Waters". *Ocean & Coastal Management*, **147**:21–36, 2017. doi: 10.1016/j.ocecoaman.2017.04.015.

T. Wang and Z. Yang. "A modelling study of tidal energy extraction and the associated impact on tidal circulation in a multi-inlet bay system of Puget Sound". *Renewable Energy*, **114**:204–214, 2017. doi: 10.1016/j.renene.2017.03.049.

Z. Wang, C. Jeuken, and H. de Vriend. "Tidal Asymmetry and Residual Sediment Transport in Estuaries", 1999. Technical Report Z2749 WL Delft, Delft Hydraulics, Delft, Netherlands. Available: uuid:31beab81-e6d9-490b-b564-e88dd72be8af.

C. Wentworth. "A scale of grade and class terms for clastic sediments". *The Journal of Geology*, **30**(5):377–392, 1922. doi: 10.1086/622910.

G. Whittaker and G. Watson. *"A Course of Modern Analysis"*. University Press, 4$^{\text{th}}$ edition, 1963.

B. Wilson, R. Batty, F. Daunt, and C. Carter. "Collision Risk Between Marine Renewable Energy Devices and Mammals, Fish and Diving Birds", 2007. Report by Centre for Ecology & Hydrology and Scottish Association for Marine Science (SAMS). Available: tethys.pnnl.gov/sites/default/files/publications/Wilson%20et%20al%202007.pdf.

J. Xing, E. Jones, A. Davies, and P. Hall. "Modelling tide-surge interaction effects using finite volume and finite element models of the Irish Sea". *Ocean Dynamics*, **61**:1137–1174, 2011. doi: 10.1007/s10236-011-0418-3.

E. Zangibadi, M. Edmunds, I. Fairley, M. Togneri, A. Williams, I. Masters, and N. Croft. "Computational fluid dynamics and visualisation of coastal flows in tidal channels supporting ocean energy development. *Energies*, 8:5997–6012, 2015. doi: 10.3390/en8065997.

Appendix A

Derivation of the Governing Equations[1]

Consider a fluid. Each point within the fluid may be described by the position vector:

$$\underline{\boldsymbol{r}} = x\underline{\hat{x}} + y\underline{\hat{y}} + z\underline{\hat{z}} \tag{A.1}$$

At each point, $\underline{\boldsymbol{r}}$, at a time t, the fluid has the mass density $\rho(\underline{\boldsymbol{r}}, t)$, where $\rho(\underline{\boldsymbol{r}}, t) \geq 0$ for all $\underline{\boldsymbol{r}}$ and t. Now consider an infinitesimal element of the fluid with mass dM and volume dV at the point $\underline{\boldsymbol{r}}$ and the time t, these will be such that:

$$dM = \rho(\underline{\boldsymbol{r}}, t)dV \tag{A.2}$$

The element is acted on by both body forces, which act on the entire element, and contact forces, which act across only the surfaces of the element. The body force acting on the element is:

$$\underline{d\boldsymbol{F}}_{body} = \underline{\boldsymbol{f}}_{body}(\underline{\boldsymbol{r}}, t)dV \tag{A.3}$$

where $\underline{\boldsymbol{f}}_{body}$ is the body force density, and the contact force acting across a surface of the element dS, with normal $\underline{\boldsymbol{n}}$ is:

---

[1]The derivation of the Navier-Stoke equations in this section follows closely notes taken from the from the 'Physics of Fluids' lecture course (PHYS323) given by Dr Jonathan Gratus at Lancaster Universtity.

$$d\boldsymbol{F}^{\boldsymbol{n}}_{contact} = \boldsymbol{f}^{\boldsymbol{n}}_{contact} \tag{A.4}$$

where $\boldsymbol{f}^{\boldsymbol{n}}_{contact}$ is the contact force per unit area acting across dS. The total force, $d\boldsymbol{F}_{total}$ on the element is:

$$d\boldsymbol{F}_{total} = d\boldsymbol{F}_{body} + \sum_{i}^{N_S} d\boldsymbol{F}^{\boldsymbol{n_i}}_{contact} \tag{A.5}$$

where N_s is the total number of surfaces of the element.

According to Newton's second law, the rate of change of linear momentum of the element equals the force on the element:

$$\frac{d}{dt}(\boldsymbol{v}dM) = d\boldsymbol{F}_{body} + \sum_{i}^{N_S} d\boldsymbol{F}^{\boldsymbol{n_i}}_{contact} \tag{A.6}$$

where $\boldsymbol{v} = \underline{v}(\boldsymbol{r}, t)$ is the velocity of the element. According to Newton's third law, the contact forces across adjoining faces of neighbouring elements cancel. This leaves only the sum of the outer surfaces of the fluid, ∂V, for a fluid of total volume V. The global equation of momentum balance is therefore:

$$\frac{d}{dt}\int_V \rho_v \ dV = \int_V \boldsymbol{f}_{body} \ dV + \int_{\partial V} \boldsymbol{f}^{\boldsymbol{n}}_{contact} \ dS \tag{A.7}$$

A fundamental principle of nature is that of mass conservation. Applying this principle to the fluid under consideration yields:

$$\frac{d}{dt}\int_V \rho(\boldsymbol{r}.t) \ dV = \int_V \frac{\partial \rho}{\partial t} \ dV + \int_{\partial V} \rho\boldsymbol{v} \cdot \boldsymbol{n} \ dS = 0 \tag{A.8}$$

By application of the divergence theorem:

$$\int_V \nabla \cdot \boldsymbol{v} \ dV = \oint_{\partial V} \boldsymbol{v} \cdot \boldsymbol{n} \ dS \tag{A.9}$$

equation (A.8) becomes:

$$\int_V \left(\frac{\partial \rho}{\partial t} + \nabla \cdot (\rho\boldsymbol{v}) \right) dV = 0 \tag{A.10}$$

which is true for all V, therefore:

$$\frac{\partial \rho}{\partial t} + \nabla \cdot (\rho \underline{v}) = 0 \tag{A.11}$$

which is the continuity equation.

The only body force that will be considered to be acting on the fluid in question will be gravity. The body force density due to gravity is:

$$\underline{f}_{body} = \rho \underline{g} \tag{A.12}$$

where $\underline{g} = \underline{g}(\underline{r}, t)$ is the vector field describing gravitational acceleration. Contact forces are comprised of two components, a shear force, $\underline{f}^{\underline{n}}_{shear}$, tangential to the surface, and a pressure force, $\underline{f}^{\underline{n}}_{pressure}$, normal to the surface:

$$\underline{f}^{\underline{n}}_{contact} = \underline{f}^{\underline{n}}_{shear} + \underline{f}^{\underline{n}}_{pressure} \tag{A.13}$$

The pressure force density is given by:

$$\underline{f}^{\underline{n}}_{pressure} = -p(\underline{r}, t)\underline{n} \tag{A.14}$$

where $p(\underline{r}, t)$ is pressure, a *scalar* field. The total pressure force is then:

$$d\underline{F}^{\underline{n}}_{pressure} = \int_{\partial V} (-p(\underline{r}, t)\underline{n}) \; dS \tag{A.15}$$

which, by equation (A.9) (the divergence theorem), becomes:

$$d\underline{F}^{\underline{n}}_{pressure} = -\int_{V} \nabla p \; dV \tag{A.16}$$

Applying equation (A.13) to equation (A.7), one arrives at:

$$\frac{d}{dt} \int_{V} \rho_v \; dV = \int_{V} \underline{f}_{body} \; dV + \int_{\partial V} \underline{f}^{\underline{n}}_{shear} \; dS + \int_{\partial V} \underline{f}^{\underline{n}}_{pressure} \; dS \tag{A.17}$$

Similar to the steps shown in equations (A.8)–(A.10), (A.17) becomes:

$$\int_{V} \rho \left(\frac{\partial \underline{v}}{\partial t} + (\underline{v} \cdot \nabla)\underline{v} \right) \; dV = \int_{V} \underline{f}_{body} \; dV + \int_{\partial V} \underline{f}^{\underline{n}}_{shear} \; dS + \int_{\partial V} \underline{f}^{\underline{n}}_{pressure} \; dS \tag{A.18}$$

Substituting (A.12) and (A.16) into (A.18), and applying the divergence theorem, (A.9), to the shear term in (A.18) gives:

$$\int_V \rho \left(\frac{\partial \underline{v}}{\partial t} + (\underline{v} \cdot \nabla)\underline{v} \right) \, dV = \int_V \rho \underline{g} \, dV + \int_{\partial V} \underline{f}^{\underline{n}}_{shear} \, dS - \int_V \nabla p \, dV \qquad \text{(A.19)}$$

If the concept of viscosity is now introduced, i.e., a measure of the fluid's resistance to a shear force, and the fluid is assumed to be a Newtonian fluid (viscosity remains constant regardless of the applied shear force or temperature), then Newton's law of viscosity can be applied:

$$\underline{f}_{shear} = \mu \frac{du}{dy} \hat{\underline{x}} \qquad \text{(A.20)}$$

for a fluid element moving with velocity $\underline{v} = u\hat{\underline{x}}$, where μ is the coefficient of viscosity. The shear force acts on the x-y plane who's normal, $\underline{n}$, is in the $\hat{\underline{z}}$ direction. On this surface, (A.20) can be written:

$$\underline{f}_{shear} = \mu \underline{n} \cdot (\nabla u)\hat{\underline{x}} \qquad \text{(A.21)}$$

Substituting (A.21) into (A.19):

$$\int_V \rho \left(\frac{\partial \underline{v}}{\partial t} + (\underline{v} \cdot \nabla)\underline{v} \right) \, dV = \int_V \rho \underline{g} \, dV + \mu \hat{\underline{x}} \int_{\partial V} (\nabla u) \cdot \underline{n} \, dS - \int_V \nabla p \, dV \quad \text{(A.22)}$$

Applying the divergence theorem, (A.9), to (A.22) gives:

$$\int_V \rho \left(\frac{\partial \underline{v}}{\partial t} + (\underline{v} \cdot \nabla)\underline{v} \right) \, dV = \int_V \rho \underline{g} \, dV + \mu \int_V \nabla^2 \underline{v} \, dV - \int_V \nabla p \, dV \qquad \text{(A.23)}$$

This holds for all V, therefore:

$$\frac{\partial \underline{v}}{\partial t} + (\underline{v} \cdot \nabla)\underline{v} = \underline{g} + \nu \nabla^2 \underline{v} - \frac{1}{\rho} \nabla p \qquad \text{(A.24)}$$

where $\nu = \mu/\rho$ is the kinematic viscosity.

If the fluid in question is a body of water within a basin on the Earth, the observer may want to consider (A.24) from a frame of reference stationary with

respect to the Earth, i.e. rotating with the same angular velocity as the Earth, Ω. If one rewrites (A.24) as:

$$\frac{D\underline{v}}{dt} = \underline{g} + \nu\nabla^2\underline{v} - \frac{1}{\rho}\nabla p \tag{A.25}$$

where

$$\frac{D}{dt} = \left(\frac{\partial}{\partial t} + \underline{v} \cdot \nabla\right) \tag{A.26}$$

is the convective derivative. In a rotating frame of reference:

$$\left(\frac{D\underline{v}_I}{dt}\right)_I = \left(\frac{D\underline{v}_R}{dt}\right)_R + 2\underline{\Omega} \times \underline{v}_R + \underline{\Omega} \times \underline{\Omega} \times \underline{r} \tag{A.27}$$

where a subscript I and R denote the inertial and rotating frames of reference respectively, and $\underline{\Omega}$ is the angular velocity field of the Earth. The second term on the r.h.s. is the Coriolis force, and the third term the Centrifugal force. Substituting (A.27) into (A.25) and combining the centrifugal and gravity terms (both 'forces' act along the axis perpendicular to the axis of rotation), gives:

$$\frac{D\underline{v}}{dt} + 2\underline{\Omega} \times \underline{v} = -\frac{1}{\rho}\nabla p + \widetilde{\underline{g}} + \nu\nabla^2\underline{v} \tag{A.28}$$

Appendix B

Derivation of Turbine Term[1]

Consider a fluid at rest, so that $\underline{\boldsymbol{f}}^{\boldsymbol{n}}_{shear} = 0$, and equation (A.13) reduces to:

$$\underline{\boldsymbol{f}}^{\boldsymbol{n}}_{contact} = \underline{\boldsymbol{f}}^{\boldsymbol{n}}_{pressure} = -p\underline{\boldsymbol{n}}\ dS \qquad \text{(B.1)}$$

The total force on the fluid must be zero for the fluid to be at rest, thus:

$$\int_V \underline{\boldsymbol{f}}_{body}\ dV - \int_{\partial V} p\underline{\boldsymbol{n}}\ dS = 0 \qquad \text{(B.2)}$$

Which is the global equation of hydrostatic equilibrium. By application of the divergence theorem, (A.9), this becomes:

$$\int_V \underline{\boldsymbol{f}}_{body}\ dV - \int_V \underline{\boldsymbol{\nabla}}p\ dV = 0 \qquad \text{(B.3)}$$

Which leads to the local equation of hydrostatic equilibrium:

$$\underline{\boldsymbol{f}}_{body} - \underline{\boldsymbol{\nabla}}p = 0 \qquad \text{(B.4)}$$

Applying (A.12) to (B.4) gives:

$$\rho\underline{\boldsymbol{g}} - \underline{\boldsymbol{\nabla}}p = 0 \qquad \text{(B.5)}$$

If $\underline{\boldsymbol{g}}$ is independent of x and y, which will be assumed to be the case, then so too is the pressure. This reduces (B.5) to:

---

[1]In this section, the discussion surrounding streamlines again closely follows notes taken from the 'Physics of Fluids' (PHYS323) lecture course given by Dr Jonathan Gratus at Lancaster University.

$$\frac{\partial p}{\partial z} + \rho g = 0 \tag{B.6}$$

$[\underline{\boldsymbol{g}} = -g\hat{z}]$ where g is the acceleration due to gravity. Equation (B.6) is solved by integrating over z, which, taking the pressure at the water surface to be the atmospheric pressure, p_a, gives:

$$p_0 = -\rho g z + p_a \tag{B.7}$$

Which is the hydrostatic pressure. Assume the existence of a fluid, for which:

$$\underline{\boldsymbol{f^n}}_{contact} = -p_0\underline{\boldsymbol{n}} \tag{B.8}$$

holds when the fluid is in motion. Such a fluid is an ideal fluid (i.e. no shear force when in motion). For such a fluid, from the global equation of momentum balance, (A.18), we arrive at the Euler equation:

$$\rho\frac{D\underline{\boldsymbol{v}}}{dt} = -\underline{\boldsymbol{\nabla}}p_0 + \rho\underline{\boldsymbol{g}} \tag{B.9}$$

The additional condition, that the volume of the fluid does not change with time (i.e. the fluid is incompressible), will be imposed:

$$\frac{d}{dt}\int_V dV = 0 \tag{B.10}$$

Using the convective derivative in (B.10) gives:

$$\frac{d}{dt}\int_V dV = \int_V \underline{\boldsymbol{\nabla}}\cdot\underline{\boldsymbol{v}}\, dV \tag{B.11}$$

Since (B.11) must hold for all V:

$$\underline{\boldsymbol{\nabla}}\cdot\underline{\boldsymbol{v}} = 0 \tag{B.12}$$

which is the local equation of incompressibility. Comparing (B.12) with the continuity equation, (A.11), implies that the density is constant, $\rho = \rho_0$.

For a steady flow, fluid particles follow *streamlines*. If a fluid particle were to, by some means, leave a trail behind it, then the path it traces is the streamline. Mathematically, the streamline, $\underline{\boldsymbol{r}}(t)$, is the solution to the equation:

$$\frac{d\underline{r}(t)}{dt} = \underline{v}(\underline{r}(t)) \tag{B.13}$$

Now, for an ideal, incompressible fluid, in a steady flow, the governing equations are:

$$\underline{\boldsymbol{\nabla}} \cdot \underline{v} = 0 \tag{B.14}$$

$$\rho_0(\underline{v} \cdot \underline{\boldsymbol{\nabla}})\underline{v} = -\underline{\boldsymbol{\nabla}}p_0 + \rho_0\underline{g} \tag{B.15}$$

Introducing the potential gravity, Φ, where:

$$\underline{g} = -\underline{\boldsymbol{\nabla}}\Phi \tag{B.16}$$

and the identity:

$$(\underline{\boldsymbol{\nabla}} \cdot \underline{v})\underline{v} = (\underline{\boldsymbol{\nabla}} \times \underline{v}) \times \underline{v} + \underline{\boldsymbol{\nabla}}\left(\frac{1}{2}|\underline{v}|^2\right) \tag{B.17}$$

equation (B.15) may be written:

$$(\underline{\boldsymbol{\nabla}} \times \underline{v}) \times \underline{v} = -\underline{\boldsymbol{\nabla}}\left(\frac{p_0}{\rho_0} + \Phi + \frac{1}{2}|\underline{v}|^2\right) \tag{B.18}$$

The Bernoulli field, H, will now be introduced:

$$H = \frac{1}{2}|\underline{v}|^2 + \frac{p_0}{\rho_0} + \Phi \tag{B.19}$$

Therefore:

$$(\underline{\boldsymbol{\nabla}} \times \underline{v}) \times \underline{v} = -\underline{\boldsymbol{\nabla}}H \tag{B.20}$$

$$\rightarrow \underline{v} \cdot [(\underline{\boldsymbol{\nabla}} \times \underline{v}) \times \underline{v}] = -\underline{v} \cdot \underline{\boldsymbol{\nabla}}H \tag{B.21}$$

Using the identity:

$$\underline{A} \cdot (\underline{B} \times \underline{C}) = \underline{B} \cdot (\underline{A} \times \underline{C}) = \underline{C} \cdot (\underline{A} \times \underline{C}) \tag{B.22}$$

(B.21) becomes:

$$(\boldsymbol{\nabla} \times \underline{\boldsymbol{v}}) \cdot (\underline{\boldsymbol{v}} \times \underline{\boldsymbol{v}}) = -\underline{\boldsymbol{v}} \cdot \boldsymbol{\nabla} H \tag{B.23}$$

however, $\underline{\boldsymbol{v}} \times \underline{\boldsymbol{v}} = 0$, so (B.23) becomes:

$$\underline{\boldsymbol{v}} \cdot \boldsymbol{\nabla} H = 0 \tag{B.24}$$

The value of $H(\underline{\boldsymbol{r}})$ on the streamline $\underline{\boldsymbol{r}}(t)$ is $H(\underline{\boldsymbol{r}}(t))$, therefore, using the convective derivative:

$$\frac{d}{dt} H(\underline{\boldsymbol{r}}(t)) = \frac{d\underline{\boldsymbol{r}}(t)}{dt} \cdot \boldsymbol{\nabla} H \tag{B.25}$$

Applying (B.13) to (B.25) gives:

$$\frac{d}{dt} H(\underline{\boldsymbol{r}}(t)) = \underline{\boldsymbol{v}} \cdot \boldsymbol{\nabla} H \tag{B.26}$$

However, given (B.24), (B.26) becomes:

$$\frac{d}{dt} H(\underline{\boldsymbol{r}}(t)) = 0 \tag{B.27}$$

which is Bernoulli's theorem. This implies that the H function for a steady flow of an incompressible, ideal fluid is constant along streamlines.

The idea of a streamline will now be extended to a *streamtube.* For a streamline, there is no flow across the line, a stream tube will be a long cylinder with a boundary comprised of streamlines so there is no flow across the boundary of the streamtube.

Consider now a turbine in the flow, and assume that the fluid upstream and downstream of the turbine, affected by the turbine remains separate from the fluid that is not affected, then a streamtube can be formed surrounding the former. As the fluid is incompressible, as the speed of the fluid reduces, the cross-sectional area of the stream tube must expand. As the flow approaches the turbine it slows, if the potential gravity remains constant, then to compensate for the reduced velocity there is an increase in pressure (B.19), as no work has yet been done by the turbine. Due to the decrease in the velocity there will also be an expansion of the streamtube.

When the fluid passes through the turbine there is a designed drop in pressure, below the ambient pressure. The fluid downstream has a reduced velocity and pressure (same Φ), implying a reduction in energy, due to the turbine. This downstream flow is the wake. Far downstream the pressure returns to ambient levels.

In order to quantify the momentum reduction due to the turbine a conceptual tool known as an actuator disk will be employed. An actuator disk is a theoretical, infinitely thin, permeable disk with an area equal to the swept area of the turbine, A_d. As with the turbine above, the streamtube up-stream of the disk will have a cross-sectional area $A_\infty < A_d$, and $A_w > A_d$ in the wake. The mass flow rate must be conserved within the stream tube, therefore:

$$\rho_0 A_\infty u_\infty = \rho_0 A_d u_d = \rho_0 A_w u_w \qquad (B.28)$$

where the subscripts ∞, w and d refer to far-up-stream, at the disk and the wake respectively. The velocity at the disk is given by [Burton et al., 2001]:

$$u_d = u_\infty(1 - a) \qquad (B.29)$$

where a is the axial induction factor, i.e. the fractional reduction in flow velocity. The fluid passing through the disk experiences a reduction in velocity. The change in momentum is given by:

$$\rho_0 \frac{du}{dt} = (u_\infty - u_d)\rho_0 A_d u_d \qquad (B.30)$$

The force causing the momentum change results from the pressure drop across the disk:

$$F_d = (p_d^+ - p_d^-)A_d = (u_\infty - u_w)\rho_0 A_d u_\infty(1 - a) \qquad (B.31)$$

where the superscript $+$ and $-$ denote the pressure just up-stream and down-steam of the disk. From (B.19):

$$\frac{1}{2}\rho_0 u^2 + p + \rho_0 g z = \text{const.} \qquad (B.32)$$

Upstream of the disk, for horizontal flow:

$$\frac{1}{2}\rho_0 u_\infty^2 + p_\infty = \frac{1}{2}\rho_0 u_d^2 + p_d^+ \tag{B.33}$$

similarly, downstream of the disk:

$$\frac{1}{2}\rho_0 u_w^2 + p_\infty = \frac{1}{2}\rho_0 u_d^2 + p_d^- \tag{B.34}$$

Subtracting (B.34) from (B.33):

$$(p_d^+ - p_d^-) = \frac{1}{2}\rho_0(u_\infty^2 - u_w^2) \tag{B.35}$$

applying this to (B.31) gives:

$$\frac{1}{2}\rho_0(u_\infty^2 - u_w^2)A_d = (u_\infty - u_w)\rho_0 A_d u_\infty(1-a) \tag{B.36}$$

and therefore:

$$u_w = (1 - 2a)u_\infty \tag{B.37}$$

The force exerted on the disk by the flow, and therefore on the flow by the disk (by Newton's 3$^{\text{rd}}$ law of motion) is given by substituting (B.37) and (B.35) into (B.31):

$$F_d = (p_d^+ - p_d^-)A_d = 2\rho_0 A_d u_\infty^2 a(1-a) \tag{B.38}$$

A thrust coefficient will be defined by non-dimensionalising (B.38) by a force on the same area in a flow with no actuator disk:

$$C_T = \frac{F_d}{\frac{1}{2}\rho_0 A_d u_\infty^2} \tag{B.39}$$

$$\rightarrow C_T = 4a(1-a) \tag{B.40}$$

The force exerted on the flow by the actuator disk, representing a turbine, is:

$$F_T = -\frac{1}{2}\rho_0 C_T \delta_T \boldsymbol{v}|\boldsymbol{v}| \tag{B.41}$$

where,

$$\sum_{i=1}^{N_T} \int_V \delta_T^i \, dV = NA \tag{B.42}$$

where the subscript d has been dropped, so A is the turbine swept-area, and N is the number of turbines. In (B.41) the minus sign represents the turbine acting on the flow, the horizontal velocity component has been replaced with the velocity vector, and finally the modulus has been included to preserve the directionality of the force. The delta-function employed in (B.41) implies that the turbine force only exists in the presence of a turbine.

Appendix C

One-Dimensional Form of the Governing Equations

In Appendix A the Navier-Stokes equations were derived, consisting of a momentum equation, (A.28), and a continuity equation, (A.11). Both these equations will be reduced to a one-dimensional (1D) form. However, first the momentum equation will be modified to include the effect of tidal turbines (B.41), as derived in Appendix B:

$$\frac{D\underline{\boldsymbol{v}}}{dt} + 2\underline{\boldsymbol{\Omega}} \times \underline{\boldsymbol{v}} = -\frac{1}{\rho_0}\nabla p + \widetilde{\underline{\boldsymbol{g}}} + \nu\nabla^2\underline{\boldsymbol{v}} - \frac{1}{2}\delta_T C_T \underline{\boldsymbol{v}}|\underline{\boldsymbol{v}}| \tag{C.1}$$

The following steps towards the 1D equations closely follows those of Parker [1984], Appendix A, with the addition of the turbine momentum sink.

To deal with turbulent motion the velocity will be decomposed into mean and fluctuating parts, along with the pressure:

$$\underline{\boldsymbol{v}} = \overline{\underline{\boldsymbol{v}}} + \underline{\boldsymbol{v}}' \tag{C.2}$$

$$p = \overline{p} + p' \tag{C.3}$$

where an overbar denotes the mean and a prime the fluctuation. Substituting (C.2) and (C.3) into (C.1) gives:

$$\frac{\partial}{\partial t}(\overline{\underline{v}} + \underline{v}') + (\overline{\underline{v}} + \underline{v}') \cdot \nabla(\overline{\underline{v}} + \underline{v}') + 2\underline{\Omega} \times (\overline{\underline{v}} + \underline{v}') = -\frac{1}{\rho}\nabla(\overline{p} + p') + \tilde{\underline{g}}$$
$$+ \nu\nabla^2(\overline{\underline{v}} + \underline{v}') - \frac{1}{2}\delta_T C_T(\overline{\underline{v}} + \underline{v}')|(\overline{\underline{v}} + \underline{v}')| \quad \text{(C.4)}$$

The temporal average of the fluctuating part of the fluid motion is zero. So, taking the temporal average and writing the momentum equation for each Cartesian coordinate one gets:

$$\frac{\partial \overline{u}}{\partial t} + \overline{u}\frac{\partial \overline{u}}{\partial x} + \overline{v}\frac{\partial \overline{u}}{\partial y} + \overline{w}\frac{\partial \overline{u}}{\partial z} - f\overline{v} = -\frac{1}{\rho}\frac{\partial \overline{p}}{\partial x} - \left(\frac{\partial}{\partial x}(\overline{u'u'}) + \frac{\partial}{\partial y}\overline{u'v'} + \frac{\partial}{\partial z}\overline{u'w'}\right)$$
$$+ \nu\left(\frac{\partial^2 \overline{u}}{\partial x^2} + \frac{\partial^2 \overline{u}}{\partial y^2} + \frac{\partial^2 \overline{u}}{\partial z^2}\right) - \frac{1}{2}\delta_T C_T\overline{u}|\overline{u}| \quad \text{(C.5)}$$

$$\frac{\partial \overline{v}}{\partial t} + \overline{u}\frac{\partial \overline{v}}{\partial x} + \overline{v}\frac{\partial \overline{v}}{\partial y} + \overline{w}\frac{\partial \overline{v}}{\partial z} + f\overline{u} = -\frac{1}{\rho}\frac{\partial \overline{p}}{\partial y} - \left(\frac{\partial}{\partial x}\overline{v'u'} + \frac{\partial}{\partial y}\overline{v'v'} + \frac{\partial}{\partial z}\overline{v'w'}\right)$$
$$+ \nu\left(\frac{\partial^2 \overline{v}}{\partial x^2} + \frac{\partial^2 \overline{v}}{\partial y^2} + \frac{\partial^2 \overline{v}}{\partial z^2}\right) - \frac{1}{2}\delta_T C_T\overline{v}|\overline{v}| \quad \text{(C.6)}$$

$$\frac{\partial \overline{w}}{\partial t} + \overline{u}\frac{\partial \overline{w}}{\partial x} + \overline{v}\frac{\partial \overline{w}}{\partial y} + \overline{w}\frac{\partial \overline{w}}{\partial z} = -\frac{1}{\rho}\frac{\partial \overline{p}}{\partial x} + g - \left(\frac{\partial}{\partial x}\overline{w'u'} + \frac{\partial}{\partial y}\overline{w'v'} + \frac{\partial}{\partial z}\overline{w'w'}\right)$$
$$+ \nu\left(\frac{\partial^2 \overline{w}}{\partial x^2} + \frac{\partial^2 \overline{w}}{\partial y^2} + \frac{\partial^2 \overline{w}}{\partial z^2}\right) - \frac{1}{2}\delta_T C_T\overline{w}|\overline{w}| \quad \text{(C.7)}$$

where $f = 2\Omega\sin\varphi$ is the Coriolis frequency, φ is latitude, u, v and w are the x, y and z components of the velocity field. The averaged pairs of fluctuating velocities are interpreted as turbulent stresses. For flows of high Reynolds number, the viscous stresses (second last terms r.h.s.) can be neglected relative to these turbulent stresses.

The pressure can be decomposed into the hydrostatic pressure and the pressure resulting from fluid motion:

$$\overline{p}(\underline{r}, t) = \overline{p}_{hydrostatic} + \overline{p}_{motion} = -\rho g z + \tilde{p}(\underline{r}, t) \quad \text{(C.8)}$$

Applying (C.8) to equations (C.5)–(C.7) and assuming a high Reynolds number flow gives:

$$\frac{\partial \overline{u}}{\partial t} + \overline{u}\frac{\partial \overline{u}}{\partial x} + \overline{v}\frac{\partial \overline{u}}{\partial y} + \overline{w}\frac{\partial \overline{u}}{\partial z} - f\overline{v} = -\frac{1}{\rho}\frac{\partial \widetilde{p}}{\partial x} - \left(\frac{\partial}{\partial x}\overline{u'u'} + \frac{\partial}{\partial y}\overline{u'v'} + \frac{\partial}{\partial z}\overline{u'w'}\right)$$
$$-\frac{1}{2}\delta_T C_T \overline{u}|\overline{u}| \quad \text{(C.9)}$$

$$\frac{\partial \overline{v}}{\partial t} + \overline{u}\frac{\partial \overline{v}}{\partial x} + \overline{v}\frac{\partial \overline{v}}{\partial y} + \overline{w}\frac{\partial \overline{v}}{\partial z} + f\overline{u} = -\frac{1}{\rho}\frac{\partial \widetilde{p}}{\partial y} - \left(\frac{\partial}{\partial x}\overline{v'u'} + \frac{\partial}{\partial y}\overline{v'v'} + \frac{\partial}{\partial z}\overline{v'w'}\right)$$
$$-\frac{1}{2}\delta_T C_T \overline{v}|\overline{v}| \quad \text{(C.10)}$$

$$\frac{\partial \overline{w}}{\partial t} + \overline{u}\frac{\partial \overline{w}}{\partial x} + \overline{v}\frac{\partial \overline{w}}{\partial y} + \overline{w}\frac{\partial \overline{w}}{\partial z} = -\frac{1}{\rho}\frac{\partial \widetilde{p}}{\partial x} - \left(\frac{\partial}{\partial x}\overline{w'u'} + \frac{\partial}{\partial y}\overline{w'v'} + \frac{\partial}{\partial z}\overline{w'w'}\right)$$
$$-\frac{1}{2}\delta_T C_T \overline{w}|\overline{w}| \quad \text{(C.11)}$$

It will be assumed that the body of fluid under consideration is well-mixed sea-water in a channel, acted upon only by tidal forces. This will allow the assumption of uniform density (due to the fluid being well mixed) to be made, which reduces equation (A.11) to:

$$\frac{\partial u}{\partial x} + \frac{\partial v}{\partial y} + \frac{\partial w}{\partial z} = 0 \quad \text{(C.12)}$$

It will also be assumed that characteristic length, velocity and time scales exist:

- a vertical length-scale, D_0, characterised by a mean/representative basin depth,

- a lateral length-scale, B_0, characterised by a mean/representative basin width,

- a longitudinal length-scale, L_0, characterised by basin length,

- velocity scales, U_0, V_0 and W_0, in the longitudinal, lateral and vertical,

- a pressure scale for the tidal motion, P_0,

- and a time scale, T_0, characterised by the tidal period.

Scales for the turbulent motion, L_0', B_0', D_0', U_0', V_0' and W_0', are also assumed to exist.

Equation (C.12),

$$\frac{\partial u}{\partial x} + \frac{\partial v}{\partial y} + \frac{\partial w}{\partial z} = 0 \tag{C.12}$$

therefore scales as follows:

$$\frac{U_0}{L_0} \; (+) \; \frac{V_0}{B_0} \; (+) \; \frac{W_0}{D_0} \; (= 0) \tag{C.13}$$

From which one arrives at:

$$V_0 \sim \frac{U_0 B_0}{L_0} \tag{C.14}$$

$$W_0 \sim \frac{U_0 D_0}{L_0} \tag{C.15}$$

Likewise, the turbulent equivalents to (C.14) and (C.15) are:

$$V_0' \sim \frac{U_0' B_0'}{L_0'} \tag{C.16}$$

$$W_0' \sim \frac{U_0' D_0'}{L_0'} \tag{C.17}$$

Equation (C.9),

$$\frac{\partial \overline{u}}{\partial t} + \overline{u}\frac{\partial \overline{u}}{\partial x} + \overline{v}\frac{\partial \overline{u}}{\partial y} + \overline{w}\frac{\partial \overline{u}}{\partial z} - f\overline{v} = -\frac{1}{\rho}\frac{\partial \widetilde{p}}{\partial x}$$
$$- \left(\frac{\partial}{\partial x}\overline{u'u'} + \frac{\partial}{\partial y}\overline{u'v'} + \frac{\partial}{\partial z}\overline{u'w'} \right) - \frac{1}{2}\delta_T C_T \overline{u}|\overline{u}| \tag{C.9}$$

scales like:

$$\frac{U_0}{T_0} \; (+) \; \frac{U_0^2}{L_0} \; (+) \; \frac{U_0 V_0}{B_0} \; (+) \; \frac{U_0 W_0}{D_0} \; (-) \; fV_0 \; (= -) \; \frac{P_0}{\rho L_0}$$
$$(+) \; \frac{U_0'^2}{L_0} \; (+) \; \frac{U_0' V_0'}{B_0} \; (+) \; \frac{U_0' W_0'}{D_0} \; (-) \; NR^2 C_T U_0^2 \tag{C.18}$$

where R is the radius of the turbines. Dividing (C.18) through by U_0^2/L_0 and substituting in the Strouhal number, $S_0 = L_0/(U_0 T_0) = C_0 D_0$ (where $C_0 = \sqrt{(gD_0)}$

is the characteristic wave propagation velocity), the Rossby number, $R_0 = U_0/(fL_0)$, and equations (C.14), (C.15), (C.16) and (C.17) gives:

$$S_0 \ (+) \ 1 \ (+) \ 1 \ (+) \ 1 \ (-) \ \frac{B_0}{R_0 L_0} \ (= -) \ \frac{P_0}{\rho U_0^2}$$

$$(-) \ \left(\frac{U_0'}{U_0}\right)^2 \ (-) \ \frac{U_0'^2 L_0 B_0'}{U_0^2 B_0 L_0'} \ (-) \ \frac{U_0'^2 L_0 D_0'}{U_0^2 D_0 L_0'} \ (-) \ NR^2 C_T L_0 \quad \text{(C.19)}$$

Likewise, (C.10),

$$\frac{\partial \overline{v}}{\partial t} + \overline{u}\frac{\partial \overline{v}}{\partial x} + \overline{v}\frac{\partial \overline{v}}{\partial y} + \overline{w}\frac{\partial \overline{v}}{\partial z} + f\overline{u} = -\frac{1}{\rho}\frac{\partial \widetilde{p}}{\partial y}$$

$$- \left(\frac{\partial}{\partial x}\overline{v'u'} + \frac{\partial}{\partial y}\overline{v'v'} + \frac{\partial}{\partial z}\overline{v'w'}\right) - \frac{1}{2}\delta_T C_T \overline{v}|\overline{v}| \quad \text{(C.10)}$$

scales like:

$$\frac{V_0}{T_0} \ (+) \ \frac{U_0 V_0}{L_0} \ (+) \ \frac{V_0^2}{B_0} \ (+) \ \frac{V_0 W_0}{D_0} \ (+) \ fU_0 \ (= -) \ \frac{P_0}{\rho B_0}$$

$$(-) \ \frac{V_0' U_0'}{L_0} \ (-) \ \frac{V_0'^2}{B_0} \ (-) \ \frac{V_0' W_0'}{D_0} \ (-) \ NR^2 C_T V_0^2 \quad \text{(C.20)}$$

which becomes:

$$S_0 \frac{B_0}{L_0} \ (+) \ \frac{B_0}{L_0} \ (+) \ \frac{B_0}{L_0} \ (+) \ \frac{B_0}{L_0} \ (+) \ \frac{1}{R_0} \ (= -) \ \frac{P_0 L_0}{\rho B_0 U_0^2}$$

$$(-) \ \frac{U_0'^2 B_0'}{U_0^2 L_0'} \ (-) \ \frac{U_0'^2 B_0'^2 L_0}{U_0^2 B_0 L_0'^2} \ (-) \ \frac{U_0'^2 B_0' D_0' L_0}{U_0^2 D_0 L_0'^2} \ (-) \ \frac{NR^2 C_T B_0^2}{L_0} \quad \text{(C.21)}$$

And (C.11):

$$\frac{\partial \overline{w}}{\partial t} + \overline{u}\frac{\partial \overline{w}}{\partial x} + \overline{v}\frac{\partial \overline{w}}{\partial y} + \overline{w}\frac{\partial \overline{w}}{\partial z} = -\frac{1}{\rho}\frac{\partial \widetilde{p}}{\partial x}$$

$$- \left(\frac{\partial}{\partial x}\overline{w'u'} + \frac{\partial}{\partial y}\overline{w'v'} + \frac{\partial}{\partial z}\overline{w'w'}\right) - \frac{1}{2}\delta_T C_T \overline{w}|\overline{w}| \quad \text{(C.11)}$$

scales like:

$$\frac{U_0 D_0}{T_0 L_0} \ (+) \ \frac{U_0^2 D_0}{L_0^2} \ (+) \ \frac{U_0^2 D_0}{L_0^2} \ (+) \ \frac{U_0^2 D_0}{L_0^2} \ (= -) \ \frac{P_0}{\rho L_0}$$

$$(-) \ \frac{U_0'^2 D_0'}{L_0 L_0'} \ (-) \ \frac{U_0'^2 B_0' D_0'}{B_0 L_0'^2} \ (-) \ \frac{U_0'^2 D_0'^2}{D_0 L_0'^2} \ (-) \ \frac{NR^2 C_T U_0^2 D_0^2}{L_0^2} \quad \text{(C.22)}$$

which becomes:

$$S_0 \frac{D_0}{L_0} \; (+) \; \frac{D_0}{L_0} \; (+) \; \frac{D_0}{L_0} \; (+) \; \frac{D_0}{L_0} \; (= -) \; \frac{P_0}{\rho L_0}$$
$$(-) \; \frac{U_0'^2 D_0'}{U_0^2 L_0'} \; (-) \; \frac{U_0'^2 B_0' D_0' L_0}{U_0^2 B_0 L_0'^2} \; (-) \; \frac{U_0'^2 L_0 D_0'^2}{U_0^2 D_0 L_0'^2} \; (-) \; \frac{NR^2 C_T D_0^2}{L_0} \quad \text{(C.23)}$$

A number of assumptions will be made, in order to simplify equations (C.9), (C.10), and (C.11), firstly, it will be assumed that the depth length-scale is much shorter than both the length and width length-scales, i.e.:

$$D_0 \ll L_0 \qquad\qquad\qquad\qquad \text{(C.24)}$$

$$D_0 \ll B_0 \qquad\qquad\qquad\qquad \text{(C.25)}$$

which is the shallow-water approximation. From (C.24) one can see that $D_0/L_0 \ll 1$. With this in mind, consider the last but one terms in (C.19) and (C.21), these terms will dominate the turbulent stress terms. Equations (C.9) and (C.10) therefore become:

$$\frac{\partial \overline{u}}{\partial t} + \overline{u}\frac{\partial \overline{u}}{\partial x} + \overline{v}\frac{\partial \overline{u}}{\partial y} + \overline{w}\frac{\partial \overline{u}}{\partial z} - f\overline{v} = -\frac{1}{\rho}\frac{\partial \widetilde{p}}{\partial x} - \frac{\partial}{\partial z}\overline{u'w'} - \frac{1}{2}\delta_T C_T \overline{u}|\overline{u}| \qquad \text{(C.26)}$$

$$S_0 \; (+) \; 1 \; (+) \; 1 \; (+) \; 1 \; (-) \; \frac{B_0}{R_0 L_0} \; (= -) \; \frac{P_0}{\rho U_0^2} \; (-) \; \frac{U_0'^2 L_0 D_0'}{U_0^2 D_0 L_0'}$$
$$(-) \; NR^2 C_T L_0 \quad \text{(C.27)}$$

$$\frac{\partial \overline{v}}{\partial t} + \overline{u}\frac{\partial \overline{v}}{\partial x} + \overline{v}\frac{\partial \overline{v}}{\partial y} + \overline{w}\frac{\partial \overline{v}}{\partial z} + f\overline{u} = -\frac{1}{\rho}\frac{\partial \widetilde{p}}{\partial y} - \frac{\partial}{\partial z}\overline{v'w'} - \frac{1}{2}\delta_T C_T \overline{v}|\overline{v}| \qquad \text{(C.28)}$$

$$S_0 \frac{B_0}{L_0} \; (+) \; \frac{B_0}{L_0} \; (+) \; \frac{B_0}{L_0} \; (+) \; \frac{B_0}{L_0} \; (+) \; \frac{1}{R_0} \; (= -) \; \frac{P_0 L_0}{\rho B_0 U_0^2} \; (-) \; \frac{U_0'^2 B_0' D_0' L_0}{U_0^2 D_0 L_0'^2}$$
$$(-) \; \frac{NR^2 C_T B_0^2}{L_0} \quad \text{(C.29)}$$

With $D_0/L_0 \ll 1$ again in mind consider (C.23), all terms on the l.h.s. will be considered small and neglected. The vertical turbulent stress term will again dominate the horizontal terms. However, relative to the remaining turbulent stress terms in (C.26) and (C.28), this term will be considered small, and therefore neglected, likewise with the turbine term. This reduces (C.11) to:

$$0 = -\frac{1}{\rho}\frac{\partial \widetilde{p}}{\partial z} \tag{C.30}$$

Applying (C.8) to (C.30) and integrating w.r.t z, results in the hydrostatic equation:

$$\overline{p} = -\rho g(\eta - z) + p_a \tag{C.31}$$

where η is the elevation of the water surface. If the atmospheric pressure is assumed constant then differentiating (C.31) w.r.t. x and y yields:

$$\frac{1}{\rho}\frac{\partial \widetilde{p}}{\partial x} = \frac{1}{\rho}\frac{\partial \overline{p}}{\partial x} = g\frac{\partial \eta}{\partial x} \tag{C.32}$$

$$\frac{1}{\rho}\frac{\partial \widetilde{p}}{\partial y} = \frac{1}{\rho}\frac{\partial \overline{p}}{\partial y} = g\frac{\partial \eta}{\partial y} \tag{C.33}$$

Substituting (C.32) and (C.33) into (C.26) and (C.28) respectively, gives:

$$\frac{\partial \overline{u}}{\partial t} + \overline{u}\frac{\partial \overline{u}}{\partial x} + \overline{v}\frac{\partial \overline{u}}{\partial y} + \overline{w}\frac{\partial \overline{u}}{\partial z} - f\overline{v} = -g\frac{\partial \eta}{\partial x} - \frac{\partial}{\partial z}\overline{u'w'} - \frac{1}{2}\delta_T C_T \overline{u}|\overline{u}| \tag{C.34}$$

$$S_0 \; (+) \; 1 \; (+) \; 1 \; (+) \; 1 \; (-) \; \frac{B_0}{R_0 L_0} \; (=-) \; \frac{gN_0}{U_0^2} \; (-) \; \frac{U_0'^2 L_0 D_0'}{U_0^2 D_0 L_0'} \; (-) \; NR^2 C_T L_0 \tag{C.35}$$

$$\frac{\partial \overline{v}}{\partial t} + \overline{u}\frac{\partial \overline{v}}{\partial x} + \overline{v}\frac{\partial \overline{v}}{\partial y} + \overline{w}\frac{\partial \overline{v}}{\partial z} + f\overline{u} = -g\frac{\partial \eta}{\partial y} - \frac{\partial}{\partial z}\overline{v'w'} - \frac{1}{2}\delta_T C_T \overline{v}|\overline{v}| \tag{C.36}$$

$$S_0\frac{B_0}{L_0} \; (+) \; \frac{B_0}{L_0} \; (+) \; \frac{B_0}{L_0} \; (+) \; \frac{B_0}{L_0} \; (+) \; \frac{1}{R_0} \; (=-) \; \frac{gN_0 L_0}{B_0 U_0^2} \; (-) \; \frac{U_0'^2 B_0' D_0' L_0}{U_0^2 D_0 L_0'^2}$$
$$(-) \; \frac{NR^2 C_T B_0^2}{L_0} \tag{C.37}$$

where N_0 is the length-scale for the tidal amplitude.

Now the additional assumption that the lateral length-scale is much smaller than the longitudinal length-scale will be made, i.e.:

$$B_0 \ll L_0 \tag{C.38}$$

This reduces (C.34) and (C.36) to:

$$\frac{\partial \overline{u}}{\partial t} + \overline{u}\frac{\partial \overline{u}}{\partial x} + \overline{v}\frac{\partial \overline{u}}{\partial y} + \overline{w}\frac{\partial \overline{u}}{\partial z} - f\overline{v} = -g\frac{\partial \eta}{\partial x} - \frac{\partial}{\partial z}\overline{u'w'} - \frac{1}{2}\delta_T C_T \overline{u}|\overline{u}| \tag{C.39}$$

$$S_0 \;(+)\; 1 \;(+)\; 1 \;(+)\; 1 \;(-)\; \frac{B_0}{R_0 L_0} \;(=-)\; \frac{gN_0}{(U_0^2} \;(-)\; \frac{U_0'^2 L_0 D_0'}{U_0^2 D_0 L_0'} \;(-)\; NR^2 C_T L_0 \tag{C.40}$$

$$f\overline{u} = -g\frac{\partial \eta}{\partial y} \tag{C.41}$$

$$\frac{1}{R_0} \;(=)\; \frac{gN_0 L_0}{U_0^2 B_0} \tag{C.42}$$

The scaling (C.40) will be re-written:

$$1 \;(+)\; \frac{1}{S_0} \;(+)\; \frac{1}{S_0} \;(+)\; \frac{1}{S_0} \;(-)\; \frac{B_0}{L_D} \;(=-)\; \frac{S_0 N_0}{D_0} \;(-)\; \frac{U_0'^2 L_0 D_0'}{S_0 U_0^2 D_0 L_0'}$$
$$(-)\; \frac{NR^2 C_T L_0}{S_0} \tag{C.43}$$

where $L_D = \frac{\sigma L_0}{f}$ is the constant density Rossby radius of deformation, and σ is the tidal frequency. If:

$$\frac{B_0}{L_D} \ll \frac{1}{S_0} \tag{C.44}$$

then then Coriolis term may be neglected. The condition (C.44) may be re-written:

$$\frac{2T_0 \sin\varphi}{T_{sr}} \ll \frac{L_0}{C_0 D_0 B_0} \tag{C.45}$$

where φ is latitude, and T_{sr} is the sidereal day (period of 1 Earth rotation). On the l.h.s. of (C.45), $2T_0/T_{sr} \sim 1$, therefore if:

$$L_0 \gg C_0 D_0 B_0 \sin\varphi \tag{C.46}$$

is satisfied, then the Coriolis terms may be neglected, it will be assumed that this condition is met, reducing (C.39) and (C.41) to:

$$\frac{\partial \overline{u}}{\partial t} + \overline{u}\frac{\partial \overline{u}}{\partial x} + \overline{v}\frac{\partial \overline{u}}{\partial y} + \overline{w}\frac{\partial \overline{u}}{\partial z} = -g\frac{\partial \eta}{\partial x} + \frac{1}{\rho}\frac{\partial \tau_{xz}}{\partial z} - \frac{1}{2}\delta_T C_T \overline{u}|\overline{u}| \tag{C.47}$$

$$0 = -g\frac{\partial \eta}{\partial y} \tag{C.48}$$

where $\tau_{xy} = -\rho\overline{u'w'}$ is the longitudinal-vertical Reynolds stress component.

In order to convert (C.12) and (C.47) to their proper one-dimensional form they must be integrated over the cross-sectional area of the basin containing the fluid. The integral for (C.12) is:

$$\int_0^b \int_{-h}^\eta \left(\frac{\partial u}{\partial x} + \frac{\partial v}{\partial y} + \frac{\partial w}{\partial z}\right)\ dz\ dy = 0 \tag{C.49}$$

for a uniform rectangular basin of width b and depth h. Following Parker [1984], this integration will be performed using Leibnitz's Rule:

$$\int_{A(X)}^{B(X)} \frac{\partial}{\partial X}F(X,T)\ dT = \frac{d}{dX}\int_{A(X)}^{B(X)} F(X,T)\ dT - F(B,T)\frac{dB}{dX} + F(A,T)\frac{dA}{dX} \tag{C.50}$$

Applying (C.50) to (C.49):

$$\int_0^b \left[\frac{\partial}{\partial x}\left(\int_{-h}^\eta u\ dz\right) - u(\eta)\frac{\partial \eta}{\partial x} - u(-h)\frac{\partial h}{\partial x} + \frac{\partial}{\partial y}\left(\int_{-h}^\eta v\ dz\right)\right.$$
$$\left. - v(\eta)\frac{\partial \eta}{\partial x} - v(-h)\frac{\partial h}{\partial x} + w(\eta) - w(-h)\right]\ dy = 0 \tag{C.51}$$

h is constant, so (C.51) becomes:

$$\int_0^b \frac{\partial}{\partial x}\left(\int_{-h}^\eta u\ dz\right)\ dy + \int_0^b \frac{\partial}{\partial y}\left(\int_{-h}^\eta v\ dz\right)\ dy$$
$$- \int_0^b \left(u(\eta)\frac{\partial \eta}{\partial x} + v(\eta)\frac{\partial \eta}{\partial x} - (w(\eta) - w(-h))\right)\ dy = 0 \tag{C.52}$$

Applying (C.50) to (C.52):

$$\frac{\partial}{\partial x}\left(\int_0^b \int_{-h}^{\eta} u \; dz \; dy\right) + \int_{-h}^{\eta} v(b) \; dz$$

$$-\int_0^b \left(u(\eta)\frac{\partial \eta}{\partial x} + v(\eta)\frac{\partial \eta}{\partial x} - w(\eta) + w(-h)\right) \; dy = 0 \quad \text{(C.53)}$$

as b is also constant. At the walls and bed the no slip boundary condition will be applied, meaning the second term in (C.53) equals zero, as does $w(-h)$. If a fluid particle on the boundary of a surface specified by $F = 0$, stays on the boundary, then:

$$\frac{DF}{dt} = 0 = \frac{\partial F}{\partial t} + u\frac{\partial F}{\partial x} + v\frac{\partial F}{\partial y} + w\frac{\partial F}{\partial z} \quad \text{(C.54)}$$

If F is the free surface:

$$F = \eta - z = 0 \quad \text{(C.55)}$$

Applying (C.55) to (C.54) gives:

$$\frac{\partial \eta}{\partial t} + u(\eta)\frac{\partial \eta}{\partial x} + v(\eta)\frac{\partial \eta}{\partial y} - w(\eta) = 0 \quad \text{(C.56)}$$

which is the boundary condition for the free-surface. Rearranging (C.56) and substituting into (C.53) gives:

$$\frac{\partial}{\partial x}\left(\int_0^b \int_{-h}^{\eta} u \; dz \; dy\right) + \int_0^b \frac{\partial \eta}{\partial t} \; dy = 0 \quad \text{(C.57)}$$

Applying (C.50) to (C.57):

$$\frac{\partial}{\partial x}\left(\int_0^b \int_{-h}^{\eta} u \; dz \; dy\right) + \frac{\partial}{\partial t}\int_0^b \eta \; dy - \eta(b)\frac{\partial b}{\partial t} = 0 \quad \text{(C.58)}$$

The channel is uniform, and it will be further assumed that it is uniform above the mean water level to a height greater than the maximum elevation, so that b does not change with time. Also, recall (C.48), which implies that η is uniform in y. Finally, the cross-sectionally averaged flow velocity is defined as:

$$\hat{u} = \frac{1}{E} \int\limits_{0}^{b} \int\limits_{-h}^{\eta} u \, dz \, dy \qquad (C.59)$$

where $E = b(h + \eta)$ is the cross-sectional area of the basin. With all this, (C.58) becomes:

$$\frac{\partial(E\hat{u})}{\partial x} + \frac{\partial(b\eta)}{\partial t} = 0 \qquad (C.60)$$

Which can also be written:

$$\frac{\partial \eta}{\partial t} + h\frac{\partial \hat{u}}{\partial x} + \frac{\partial(\eta\hat{u})}{\partial x} = 0 \qquad (C.61)$$

Returning to (C.47) and adding to it (C.12) multiplied by u gives:

$$\frac{\partial \overline{u}}{\partial t} + 2\overline{u}\frac{\partial \overline{u}}{\partial x} + \left(\overline{v}\frac{\partial \overline{u}}{\partial y} + \overline{u}\frac{\partial \overline{v}}{\partial y}\right) + \left(\overline{w}\frac{\partial \overline{u}}{\partial z} + \overline{u}\frac{\partial \overline{w}}{\partial x}\right) = -g\frac{\partial \eta}{\partial x} - \frac{1}{\rho}\frac{\partial \tau_{xz}}{\partial z}$$
$$- \frac{1}{2}\delta_T C_T \overline{u}|\overline{u}| \quad (C.62)$$

Applying the product rule:

$$\frac{dY}{dX} = U\frac{dV}{dX} + V\frac{dU}{dX}, \qquad \text{if } Y = UV \qquad (C.63)$$

to (C.62) we get:

$$\frac{\partial \overline{u}}{\partial t} + \frac{\partial(\overline{u}^2)}{\partial x} + \frac{\partial(\overline{uv})}{\partial y} + \frac{\partial(\overline{uw})}{\partial z} = -g\frac{\partial \eta}{\partial x} - \frac{1}{\rho}\frac{\partial \tau_{xz}}{\partial z} - \frac{1}{2}\delta_T C_T \overline{u}|\overline{u}| \qquad (C.64)$$

Integrating (C.64) over the cross-sectional area gives:

$$\int\limits_{0}^{b} \int\limits_{-h}^{\eta} \left(\frac{\partial \overline{u}}{\partial t} + \frac{\partial \overline{u}^2}{\partial x} + \frac{\partial(\overline{uv})}{\partial y} + \frac{\partial(\overline{uw})}{\partial z} + g\frac{\partial \eta}{\partial x} - \frac{1}{\rho}\frac{\partial \tau_{xz}}{\partial z}\right.$$
$$\left. + \frac{1}{2}\delta_T C_T \overline{u}|\overline{u}|\right) \, dz \, dy = 0 \quad (C.65)$$

Applying (C.50) to (C.65) gives:

$$\int_0^b \left(\frac{\partial}{\partial t} \int_{-h}^{\eta} \overline{u} \; dz - \overline{u}(\eta) \frac{\partial \eta}{\partial t} - \overline{u}(-h) \frac{\partial h}{\partial t} \right) \; dy$$

$$+ \int_0^b \left(\frac{\partial}{\partial x} \int_{-h}^{\eta} (\overline{u}^2) \; dz - \overline{u}^2(\eta) \frac{\partial \eta}{\partial x} - \overline{u}^2(-h) \frac{\partial h}{\partial x} \right) \; dy$$

$$+ \int_0^b \frac{\partial}{\partial y} \left(\int_{-h}^{\eta} (\overline{uv}) \; dz - \overline{u}(\eta)\overline{v}(\eta) \frac{\partial \eta}{\partial y} - \overline{u}(-h)\overline{v}(-h) \frac{\partial h}{\partial y} \right) \; dy$$

$$+ \int_0^b (\overline{u}(\eta)\overline{w}(\eta) - \overline{u}(-h)\overline{w}(-h)) \; dy$$

$$+ g \int_0^b \int_{-h}^{\eta} \frac{\partial \eta}{\partial x} \; dz \; dy - \frac{1}{\rho} \int_0^b \int_{-h}^{\eta} \frac{\partial \tau_{xz}}{\partial z} \; dz \; dy + \frac{1}{2} C_T \int_0^b \int_{-h}^{\eta} \delta_T \overline{u} |\overline{u}| \; dz \; dy = 0 \quad \text{(C.64)}$$

h is again constant in space and time, τ_{xz} is not a function of y, and the no-slip boundary condition is taken at the bed, so (C.64) simplifies to:

$$\int_0^b \left(\frac{\partial}{\partial t} \int_{-h}^{\eta} \overline{u} \; dz - \overline{u}(\eta) \frac{\partial \eta}{\partial t} \right) \; dy + \int_0^b \left(\frac{\partial}{\partial x} \int_{-h}^{\eta} (\overline{u}^2) \; dz - \overline{u}^2(\eta) \frac{\partial \eta}{\partial x} \right) \; dy$$

$$+ \int_0^b \left(\frac{\partial}{\partial y} \int_{-h}^{\eta} (\overline{uv}) \; dz - \overline{u}(\eta)\overline{v}(\eta) \frac{\partial \eta}{\partial y} \right) \; dy + \int_0^b (\overline{u}(\eta)\overline{w}(\eta)) \; dy + gE \frac{\partial \eta}{\partial x}$$

$$- \frac{b}{\rho} (\tau_{xz}(\eta) - \tau_{xz}(-h)) + \frac{1}{2} C_T \int_0^b \int_{-h}^{\eta} \delta_T \overline{u} |\overline{u}| \; dz \; dy = 0 \quad \text{(C.67)}$$

Applying (C.50) to (C.67) gives:

$$
\frac{\partial}{\partial t} \int_0^b \int_{-h}^{\eta} \overline{u} \; dz \; dy - \frac{\partial b}{\partial t} \int_{-h}^{\eta} \overline{u}(b) \; dz
$$

$$
- \int_0^b \left[\overline{u}(\eta) \left(\frac{\partial \eta}{\partial t} + \overline{u}(\eta) \frac{\partial \eta}{\partial x} + \overline{v}(\eta) \frac{\partial \eta}{\partial y} - \overline{w}(\eta) \right) \right] \; dy
$$

$$
+ \frac{\partial}{\partial x} \int_0^b \int_{-h}^{\eta} \overline{u}^2 \; dz \; dy - \frac{\partial b}{\partial x} \int_{-h}^{\eta} \overline{u}^2(b) \; dz + \left[\int_{-h}^{\eta} (\overline{uv}) \; dz \right]_0^b + gE \frac{\partial \eta}{\partial x}
$$

$$
- \frac{b}{\rho} (\tau_{xz}(\eta) - \tau_{xz}(-h)) + \frac{1}{2} C_T \int_0^b \int_{-h}^{\eta} \delta_T \overline{u}|\overline{u}| \; dz \; dy = 0 \quad \text{(C.68)}
$$

Using (C.56), applying the no-slip boundary condition at the basin walls and as b is constant in space and time, (C.68) simplifies to:

$$
\frac{\partial}{\partial t} \int_0^b \int_{-h}^{\eta} \overline{u} \; dz \; dy + \frac{\partial}{\partial x} \int_0^b \int_{-h}^{\eta} \overline{u}^2 \; dz \; dy + gE \frac{\partial \eta}{\partial x} - \frac{b}{\rho} (\tau_{xz}(\eta) - \tau_{xz}(-h))
$$

$$
+ \frac{1}{2} C_T \int_0^b \int_{-h}^{\eta} \delta_T \overline{u}|\overline{u}| \; dz \; dy = 0 \quad \text{(C.69)}
$$

The shear stress at the free-surface will be due to wind shear. In this example wind will be ignored reducing the shear at the free-surface to zero. The term $\overline{u}|\overline{u}|$ will be replaced with $\overline{u}^2 \cdot \text{sign}(\overline{u})$, which is equivalent. Then substituting in (C.59) gives:

$$
E \frac{\partial(\hat{u})}{\partial t} + E \frac{\partial(\hat{u}^2)}{\partial x} = -gE \frac{\partial \eta}{\partial x} - \frac{b}{\rho} \tau_{xz}(-h) - \frac{1}{2} NAC_T \hat{u}^2 \cdot \text{sign}(\hat{u}) \quad \text{(C.70)}
$$

where, as the integral is over the cross-section rather than the volume, N can be split into N_T and N_R, the number of turbines in a row (assumed uniform) and the number of rows of turbines respectively. For simplicity, it will be assumed that $N_R = 1$, so that $N_T = N$. In order to integrate the $\overline{u}^2$ terms additional assumptions have been made. If the flow at the point $\underline{r}$ at time t is given by:

$$
\overline{u}(\underline{r}, t) = \hat{u}(x, t) + u''(\underline{r}, t) \quad \text{(C.71)}
$$

where u'' is the deviation of the flow from $\hat{u}$ at $\underline{r}$, then:

$$\int\limits_{0}^{b}\int\limits_{-h}^{\eta} u''(\underline{r},t)\ dz\ dy = 0, \quad \text{and,} \quad \int\limits_{0}^{b}\int\limits_{-h}^{\eta} \hat{u}(x,t)\ dz\ dy = E\hat{u} \qquad (C.72)$$

and,

$$\int\limits_{0}^{b}\int\limits_{-h}^{\eta} \overline{u}^2\ dz\ dz = \int\limits_{0}^{b}\int\limits_{-h}^{\eta} (\hat{u}^2 + 2\hat{u}u'' + u''^2)\ dz\ dy = E\hat{u}^2 + \int\limits_{0}^{b}\int\limits_{-h}^{\eta} u''^2\ dz\ dy \quad (C.73)$$

If the deviation is small then the final term in (C.73) may be neglected. For the second term in (C.69), (C.73) will be differentiated w.r.t. x. Therefore, if the final term in (C.73) varies little with x, which will be assumed for our uniform (along x) basin, then it may be neglected, leading to the second term in (C.70).

The turbine term requires a different approach, as it only exists in the presence of turbines, therefore the integration over the cross-section does not lead to $E\hat{u}^2$, as turbines will not be present over the whole cross-section, the result is seen in (C.70). The value of the flow averaged over the turbine swept area will be assumed to be $\hat{u}$. So, for the turbine term, u'' will assumed to be small, which may be approximately true if the turbine is deployed away from the bed. Ignoring concerns regarding navigation of the basin by ships, given the larger currents will be nearer the surface than the bed, it is regarded to be a reasonable assumption that turbines will be deployed away from the bed, and that the assumption of small u'' at the turbine holds.

If the bed stress is now represented using a quadratic friction law, then (C.70) can be rewritten:

$$\frac{\partial \hat{u}}{\partial t} + 2\hat{u}\frac{\partial \hat{u}}{\partial x} = -g\frac{\partial \eta}{\partial x} - \frac{1}{1 + \eta/h}\left(\frac{C_F}{h} + \frac{1}{2}\varepsilon_0 C_T\right)\hat{u}|\hat{u}| \qquad (C.74)$$

where $\varepsilon_0 = NA/E$ is the turbine blockage ratio, which is the ratio of the total swept area of all turbines in a row to the basin cross-section. The second term in (C.74) results from application of the product rule to the second term in (C.70), the factor of 2 may be removed using (C.60) for time-scales where η is constant in time, in a similar manner as was done in going from (C.62) to (C.64). However, equation (C.74) will be left as is to avoid this assumption. In reaching this equation it is also assumed that the blockage ratio for each row is uniform.

Appendix D

Expanding the Non-Linear Terms for a Single-Constituent Tide

If the free-surface is forced by a single-constituent tide then η and $\hat{u}$ will be given by:

$$\eta = \eta_0 \cos(\theta(x,t) + \gamma(x)) \tag{D.1}$$

and

$$\hat{u} = \hat{u}_0 \cos(\theta(x,t)) \tag{D.2}$$

respectively, where η_0 and $\hat{u}_0$ are the amplitudes of η and $\hat{u}$, $\theta = \sigma t - \psi(x)$, σ is the tidal frequency, ψ is the phase of $\hat{u}$, $\gamma = \psi(x) - \phi(x)$, and ϕ is the phase of η. The 1D governing equations were derived in Appendices A, B & C as:

$$\underbrace{\frac{\partial \eta}{\partial t}}_{(a)} + \underbrace{h\frac{\partial \hat{u}}{\partial x}}_{(b)} + \underbrace{\frac{\partial(\eta\hat{u})}{\partial x}}_{(c)} = 0 \tag{D.3}$$

and

$$\underbrace{\frac{\partial \hat{u}}{\partial t}}_{(d)} + \underbrace{\hat{u}\frac{\partial \hat{u}}{\partial x}}_{(e)} = \underbrace{-g\frac{\partial \eta}{\partial x}}_{(f)} - \underbrace{\frac{C_F}{h}\hat{u}|\hat{u}|}_{(g)} + \underbrace{\frac{C_F}{h^2}\eta\hat{u}|\hat{u}|}_{(h)} - \underbrace{\frac{\varepsilon_0 C_T}{2}\hat{u}|\hat{u}|}_{(i)} + \underbrace{\frac{\varepsilon_0 C_T}{2h}\eta\hat{u}|\hat{u}|}_{(j)} \tag{D.4}$$

Substituting (D.1) and (D.2) into the continuity term (CT: (c) in (D.3)) and (momentum) advection term (AT: (e) in (D.4)) gives:

$$\frac{\partial(\eta\hat{u})}{\partial x} = \eta_0\hat{u}_0\frac{\partial}{\partial x}(\cos(\theta+\gamma)\cos(\theta)) \tag{D.5}$$

$$\hat{u}\frac{\partial\hat{u}}{\partial x} = \hat{u}_0^2\frac{\partial\phi}{\partial x}\cos(\theta)\sin(\theta) \tag{D.6}$$

Using the product-to-sum identity:

$$2\cos(X)\cos(Y) = \cos(X-Y) + \cos(X+Y) \tag{D.7}$$

and the double-angle formula:

$$\sin(2X) = 2\sin(X)\cos(X) \tag{D.8}$$

in (D.5) and (D.6) respectively gives:

$$\frac{\partial(\eta\hat{u})}{\partial x} = \frac{\eta_0\hat{u}_0}{2}\left[\frac{\partial}{\partial x}(\cos(\gamma)) + \frac{\partial}{\partial x}(\cos(2\theta+\gamma))\right]$$
$$= \frac{\eta_0\hat{u}_0}{2}\left[\frac{\partial(\phi+\psi)}{\partial x}\sin(2\theta+\gamma) + \frac{\partial\gamma}{\partial x}\sin(\gamma)\right] \tag{D.9}$$

and

$$\hat{u}\frac{\partial\hat{u}}{\partial x} = \frac{\hat{u}_0^2}{2}\frac{\partial\psi}{\partial x}\sin(2\theta) \tag{D.10}$$

In (D.9) the last term on the l.h.s. implies a residual resulting from this term.

Substituting (D.2) into the quadratic friction term (QFT: (g) in (D.4)) and expanding as a Fourier series:

$$\frac{C_F}{h}\hat{u}|\hat{u}| = \frac{C_F}{h}\left[\frac{a_0^Q}{2} + \sum_{n=1}^{\infty}a_n^Q\cos(n\theta) + \sum_{n=1}^{\infty}b_n^Q\sin(n\theta)\right] \tag{D.11}$$

where

$$a_0^Q = \frac{\hat{u}_0^2}{\pi}\int_0^{2\pi}\cos(\theta)|\cos(\theta)|\ d\theta \tag{D.12}$$

$$a_n^Q = \frac{\hat{u}_0^2}{\pi}\int_0^{2\pi}\cos(\theta)|\cos(\theta)|\cos(n\theta)\ d\theta \tag{D.13}$$
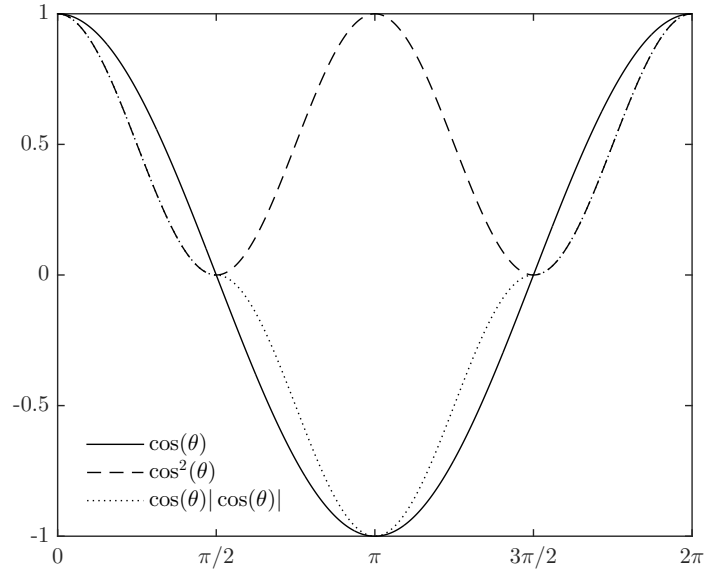
Figure D.1: Plots of a $\cos(\theta)$ (solid), $\cos^2(\theta)$ (dashed) and $\cos(\theta)|\cos(\theta)|$ (dotted).

$$b_n^Q = \frac{\hat{u}_0^2}{\pi} \int\limits_0^{2\pi} \cos(\theta)|\cos(\theta)|\sin(n\theta)\ d\theta \tag{D.14}$$

The limits of the integrals above are 0 to 2π representing a complete tidal cycle. Figure D.1 shows the behaviour of $\cos(\theta)|\cos(\theta)|$ and $\cos^2(\theta)$ over a tidal cycle. The two functions differ between $\theta = \pi/2$ and $\theta = 3\pi/2$ where they are equal, but opposite in sign. Taking this into account the integrals (D.12)–(D.14) become:

$$a_0^Q = \frac{\hat{u}_0^2}{\pi} \left[\int\limits_0^{\frac{\pi}{2}} - \int\limits_{\frac{\pi}{2}}^{\frac{3\pi}{2}} + \int\limits_{\frac{3\pi}{2}}^{2\pi} \right] \cos^2(\theta)\ d\theta \tag{D.15}$$

$$a_n^Q = \frac{\hat{u}_0^2}{\pi} \left[\int\limits_0^{\frac{\pi}{2}} - \int\limits_{\frac{\pi}{2}}^{\frac{3\pi}{2}} + \int\limits_{\frac{3\pi}{2}}^{2\pi} \right] \cos^2(\theta)\cos(n\theta)\ d\theta \tag{D.16}$$

$$b_n^Q = \frac{\hat{u}_0^2}{\pi} \left[\int\limits_0^{\frac{\pi}{2}} - \int\limits_{\frac{\pi}{2}}^{\frac{3\pi}{2}} + \int\limits_{\frac{3\pi}{2}}^{2\pi} \right] \cos^2(\theta)\sin(n\theta)\ d\theta \tag{D.17}$$

The integrals (D.15)–(D.17) can be solved by applying the angle-reduction formulae:

$$\cos^2(X) = \frac{1}{2} + \frac{1}{2}\cos(2X) \tag{D.18}$$

and

$$\cos^3(X) = \frac{3}{4}\cos(X) + \frac{1}{4}\cos(3X) \tag{D.19}$$

and the product-to-sum identities, (D.7), and:

$$2\cos(X)\sin(Y) = \sin(X+Y) - \sin(X-Y) \tag{D.20}$$

The solution to (D.15) is:

$$a_0^Q = \frac{\hat{u}_0^2}{2\pi}\left[\int_0^{\frac{\pi}{2}} - \int_{\frac{\pi}{2}}^{\frac{3\pi}{2}} + \int_{\frac{3\pi}{2}}^{2\pi}\right](1+\cos(2\theta))\;d\theta = \left[\theta + \frac{1}{2}\sin(2\theta)\right]_{0-\frac{\pi}{2}+\frac{3\pi}{2}}^{\frac{\pi}{2}-\frac{3\pi}{2}+2\pi}$$

$$= \frac{\pi}{2} - \pi + \frac{\pi}{2} = 0 \quad \text{(D.21)}$$

For $n = 1$, the solutions to (D.16) & (D.17) are:

$$a_1^Q = \frac{\hat{u}_0^2}{\pi}\left[\int_0^{\frac{\pi}{2}} - \int_{\frac{\pi}{2}}^{\frac{3\pi}{2}} + \int_{\frac{3\pi}{2}}^{2\pi}\right]\cos^3(\theta)\;d\theta$$

$$= \frac{\hat{u}_0^2}{4\pi}\left[\int_0^{\frac{\pi}{2}} - \int_{\frac{\pi}{2}}^{\frac{3\pi}{2}} + \int_{\frac{3\pi}{2}}^{2\pi}\right](3\cos(\theta)+\cos(3\theta))\;d\theta$$

$$= \frac{\hat{u}_0^2}{4\pi}\left[3\sin(\theta) + \frac{1}{3}\sin(3\theta)\right]_{0-\frac{\pi}{2}+\frac{3\pi}{2}}^{\frac{\pi}{2}-\frac{3\pi}{2}+2\pi} = \frac{\hat{u}_0^2}{\pi}\left(\frac{2}{3}+\frac{4}{3}+\frac{2}{3}\right) = \frac{8\hat{u}_0^2}{3\pi} \quad \text{(D.22)}$$

$$b_1^Q = \frac{\hat{u}_0^2}{\pi}\left[\int_0^{\frac{\pi}{2}} - \int_{\frac{\pi}{2}}^{\frac{3\pi}{2}} + \int_{\frac{3\pi}{2}}^{2\pi}\right]\cos^2(\theta)\sin(\theta)\;d\theta$$

$$= \frac{\hat{u}_0^2}{2\pi}\left[\int_0^{\frac{\pi}{2}} - \int_{\frac{\pi}{2}}^{\frac{3\pi}{2}} + \int_{\frac{3\pi}{2}}^{2\pi}\right](\sin(\theta)+\cos(2\theta))\sin(\theta)\;d\theta$$

$$= -\frac{\hat{u}_0^2}{4\pi}\left[\int_0^{\frac{\pi}{2}} - \int_{\frac{\pi}{2}}^{\frac{3\pi}{2}} + \int_{\frac{3\pi}{2}}^{2\pi}\right](\sin(\theta)-\sin(3\theta))\;d\theta$$

$$= -\frac{\hat{u}_0^2}{12\pi}\left[3\cos(\theta) + \frac{1}{3}\cos(3\theta)\right]_{0-\frac{\pi}{2}+\frac{3\pi}{2}}^{\frac{\pi}{2}-\frac{3\pi}{2}+2\pi} = -\frac{\hat{u}_0^2}{12\pi}\left[\frac{2}{3}-0-\frac{2}{3}\right] = 0 \quad \text{(D.23)}$$

For $n = 2$,

$$a_2^Q = \frac{\hat{u}_0^2}{\pi} \left[\int_0^{\frac{\pi}{2}} - \int_{\frac{\pi}{2}}^{\frac{3\pi}{2}} + \int_{\frac{3\pi}{2}}^{2\pi} \right] \cos^2(\theta) \cos(2\theta) \, d\theta$$

$$= \frac{\hat{u}_0^2}{4\pi} \left[\int_0^{\frac{\pi}{2}} - \int_{\frac{\pi}{2}}^{\frac{3\pi}{2}} + \int_{\frac{3\pi}{2}}^{2\pi} \right] (1 + 2\cos(2\theta) + \cos(4\theta)) \, d\theta$$

$$= \frac{\hat{u}_0^2}{4\pi} \left[\theta + \sin(2\theta) + \frac{1}{4}\sin(4\theta) \right]_{0 - \frac{\pi}{2} + \frac{3\pi}{2}}^{\frac{\pi}{2} - \frac{3\pi}{2} + 2\pi} = \frac{\hat{u}_0^2}{4\pi} \left[\frac{\pi}{2} - \pi + \frac{\pi}{2} \right] = 0 \quad \text{(D.24)}$$

$$b_2^Q = \frac{\hat{u}_0^2}{\pi} \left[\int_0^{\frac{\pi}{2}} - \int_{\frac{\pi}{2}}^{\frac{3\pi}{2}} + \int_{\frac{3\pi}{2}}^{2\pi} \right] \cos^2(\theta) \sin(2\theta) \, d\theta$$

$$= \frac{\hat{u}_0^2}{4\pi} \left[\int_0^{\frac{\pi}{2}} - \int_{\frac{\pi}{2}}^{\frac{3\pi}{2}} + \int_{\frac{3\pi}{2}}^{2\pi} \right] (2\sin(2\theta) + \sin(4\theta)) \, d\theta$$

$$= -\frac{\hat{u}_0^2}{4\pi} \left[\cos(2\theta) + \frac{1}{4}\cos(4\theta) \right]_{0 - \frac{\pi}{2} + \frac{3\pi}{2}}^{\frac{\pi}{2} - \frac{3\pi}{2} + 2\pi} = \frac{\hat{u}_0^2}{4\pi} [2 - 0 - 2] = 0 \quad \text{(D.25)}$$

For $n = 3$,

$$a_3^Q = \frac{\hat{u}_0^2}{\pi} \left[\int_0^{\frac{\pi}{2}} - \int_{\frac{\pi}{2}}^{\frac{3\pi}{2}} + \int_{\frac{3\pi}{2}}^{2\pi} \right] \cos^2(\theta) \cos(3\theta) \, d\theta$$

$$= \frac{\hat{u}_0^2}{4\pi} \left[\sin(\theta) + \frac{2}{3}\sin(3\theta) + \frac{1}{5}\sin(5\theta) \right]_{0 - \frac{\pi}{2} + \frac{3\pi}{2}}^{\frac{\pi}{2} - \frac{3\pi}{2} + 2\pi}$$

$$= \frac{\hat{u}_0^2}{\pi} \left[\frac{2}{15} + \frac{4}{15} + \frac{2}{15} \right] = \frac{8\hat{u}_0^2}{15\pi} \quad \text{(D.26)}$$

$$b_3^Q = \frac{\hat{u}_0^2}{\pi} \left[\int_0^{\frac{\pi}{2}} - \int_{\frac{\pi}{2}}^{\frac{3\pi}{2}} + \int_{\frac{3\pi}{2}}^{2\pi} \right] \cos^2(\theta) \sin(3\theta) \, d\theta$$

$$= -\frac{\hat{u}_0^2}{4\pi} \left[\cos(\theta) + \frac{2}{3}\cos(3\theta) + \frac{1}{5}\cos(5\theta) \right]_{0 - \frac{\pi}{2} + \frac{3\pi}{2}}^{\frac{\pi}{2} - \frac{3\pi}{2} + 2\pi}$$

$$= -\frac{\hat{u}_0^2}{4\pi} \left[\frac{28}{15} - 0 - \frac{28}{15} \right] = 0 \quad \text{(D.27)}$$

For $n = 4$,

$$a_4^Q = \frac{\hat{u}_0^2}{\pi} \left[\int_0^{\frac{\pi}{2}} - \int_{\frac{\pi}{2}}^{\frac{3\pi}{2}} + \int_{\frac{3\pi}{2}}^{2\pi} \right] \cos^2(\theta) \cos(4\theta) \, d\theta$$

$$= \frac{\hat{u}_0^2}{4\pi} \left[\frac{1}{2} \sin(2\theta) + \frac{1}{2} \sin(4\theta) + \frac{1}{6} \cos(6\theta) \right]_{0 - \frac{\pi}{2} + \frac{3\pi}{2}}^{\frac{\pi}{2} - \frac{3\pi}{2} + 2\pi} = 0 \quad \text{(D.28)}$$

$$b_4^Q = \frac{\hat{u}_0^2}{\pi} \left[\int_0^{\frac{\pi}{2}} - \int_{\frac{\pi}{2}}^{\frac{3\pi}{2}} + \int_{\frac{3\pi}{2}}^{2\pi} \right] \cos^2(\theta) \sin(4\theta) \, d\theta$$

$$= -\frac{\hat{u}_0^2}{4\pi} \left[\frac{1}{2} \cos(2\theta) + \frac{1}{2} \cos(4\theta) + \frac{1}{6} \cos(4\theta) \right]_{0 - \frac{\pi}{2} + \frac{3\pi}{2}}^{\frac{\pi}{2} - \frac{3\pi}{2} + 2\pi} = 0 \quad \text{(D.29)}$$

For $n = 5$,

$$a_5^Q = \frac{\hat{u}_0^2}{\pi} \left[\int_0^{\frac{\pi}{2}} - \int_{\frac{\pi}{2}}^{\frac{3\pi}{2}} + \int_{\frac{3\pi}{2}}^{2\pi} \right] \cos^2(\theta) \cos(5\theta) \, d\theta = -\frac{8\hat{u}_0^2}{105\pi} \quad \text{(D.30)}$$

$$b_5^Q = \frac{\hat{u}_0^2}{\pi} \left[\int_0^{\frac{\pi}{2}} - \int_{\frac{\pi}{2}}^{\frac{3\pi}{2}} + \int_{\frac{3\pi}{2}}^{2\pi} \right] \cos^2(\theta) \sin(5\theta) \, d\theta = 0 \quad \text{(D.31)}$$

For $n = 6$,

$$a_6^Q = 0 \quad \text{(D.32)}$$

$$b_6^Q = 0 \quad \text{(D.33)}$$

Applying (D.21)–(D.33) to (D.11) results in:

$$\frac{C_F}{h} \hat{u}|\hat{u}| = \frac{8\hat{u}_0^2 C_F}{3\pi h} \left[\cos(\theta) + \frac{1}{5} \cos(3\theta) - \frac{1}{35} \cos(5\theta) \right] + \dots \quad \text{(D.34)}$$

The process above [(D.11)–(D.34)] will be repeated for the elevation friction term (EFT: (h) in (D.4)), this time both (D.1) and (D.2) will be substituted in and expanded as a Fourier Series:

$$\frac{C_F}{h^2}\eta\hat{u}|\hat{u}| = \frac{C_F}{h^2}\left[\frac{a_0^E}{2} + \sum_{n=1}^{\infty} a_n^E \cos(n\theta) + \sum_{n=1}^{\infty} b_n^E \sin(n\theta)\right] \tag{D.35}$$

where:

$$a_0^E = \frac{\eta_0 \hat{u}_0^2}{\pi} \int_0^{2\pi} \cos(\theta + \gamma)\cos(\theta)|\cos(\theta)| \ d\theta \tag{D.36}$$

$$a_n^E = \frac{\eta_0 \hat{u}_0^2}{\pi} \int_0^{2\pi} \cos(\theta + \gamma)\cos(\theta)|\cos(\theta)|\cos(n\theta) \ d\theta \tag{D.37}$$

$$b_n^E = \frac{\eta_0 \hat{u}_0^2}{\pi} \int_0^{2\pi} \cos(\theta + \gamma)\cos(\theta)|\cos(\theta)|\sin(n\theta) \ d\theta \tag{D.38}$$

Figure D.2 shows the behaviour of $\cos(\theta + \gamma)\cos^2(\theta)$ and $\cos(\theta + \gamma)\cos(\theta)|\cos(\theta)|$ over a tidal cycle for a range of γ values. As before the functions are equal, but opposite in sign between $\theta = \pi/2$ and $\theta = 3\pi/2$ for all values of γ. Therefore, (D.36)–(D.38) may be written:

$$a_0^E = \frac{\eta_0 \hat{u}_0^2}{\pi}\left[\int_0^{\frac{\pi}{2}} - \int_{\frac{\pi}{2}}^{\frac{3\pi}{2}} + \int_{\frac{3\pi}{2}}^{2\pi}\right]\cos(\theta + \gamma)\cos^2(\theta) \ d\theta \tag{D.39}$$

$$a_n^E = \frac{\eta_0 \hat{u}_0^2}{\pi}\left[\int_0^{\frac{\pi}{2}} - \int_{\frac{\pi}{2}}^{\frac{3\pi}{2}} + \int_{\frac{3\pi}{2}}^{2\pi}\right]\cos(\theta + \gamma)\cos^2(\theta)\cos(n\theta) \ d\theta \tag{D.40}$$

$$b_n^E = \frac{\eta_0 \hat{u}_0^2}{\pi}\left[\int_0^{\frac{\pi}{2}} - \int_{\frac{\pi}{2}}^{\frac{3\pi}{2}} + \int_{\frac{3\pi}{2}}^{2\pi}\right]\cos(\theta + \gamma)\cos^2(\theta)\sin(n\theta) \ d\theta \tag{D.41}$$

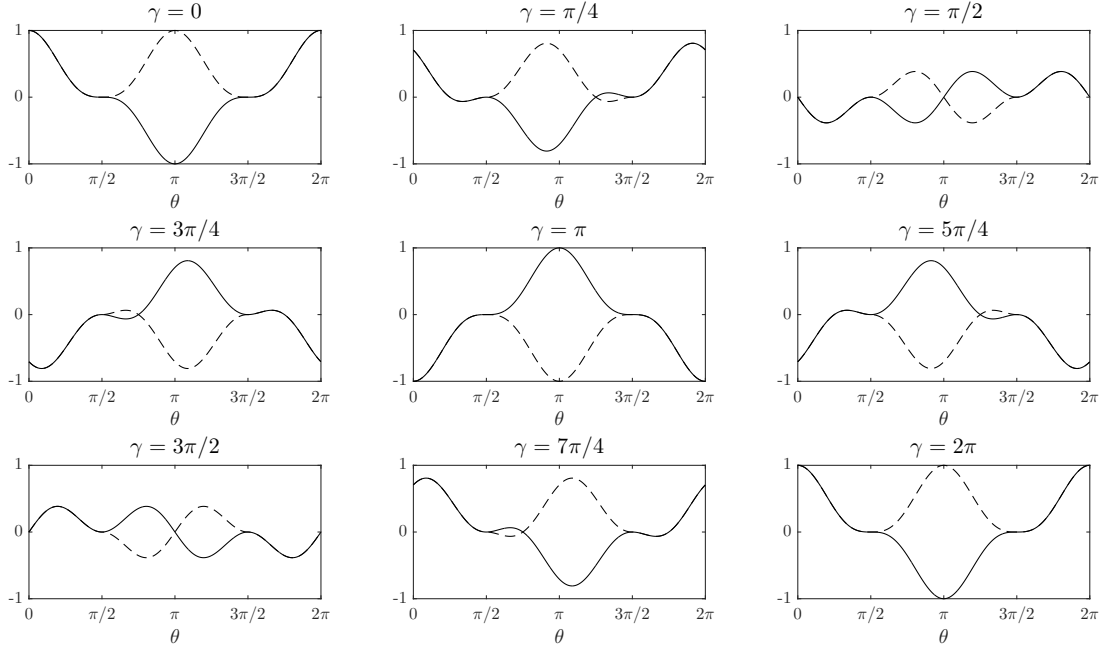Using (D.7) & (D.18)–(D.20), the integrals (D.39)–(D.41) can be solved:

Figure D.2: Plots of $\cos(\theta + \gamma)\cos^2(\theta)$ (solid) and $\cos(\theta + \gamma)\cos(\theta)|\cos(\theta)|$ (dashed) for various values of γ.

$$
\begin{aligned}
a_0^E &= \frac{\eta_0 \hat{u}_0^2}{\pi} \left[\int_0^{\frac{\pi}{2}} - \int_{\frac{\pi}{2}}^{\frac{3\pi}{2}} + \int_{\frac{3\pi}{2}}^{2\pi} \right] \cos(\theta + \gamma)\cos^2(\theta) \; d\theta \\
&= \frac{\eta_0 \hat{u}_0^2}{2\pi} \left[\int_0^{\frac{\pi}{2}} - \int_{\frac{\pi}{2}}^{\frac{3\pi}{2}} + \int_{\frac{3\pi}{2}}^{4\pi} \right] \left(\cos(\theta - \gamma) + 2\cos(\theta + \gamma) + \cos(3\theta + \gamma) \; d\theta \right. \\
&= \frac{\eta_0 \hat{u}_0^2}{4\pi} \left[\sin(\theta - \gamma) + 2\sin(\theta + \gamma) + \frac{1}{2}\sin(3\theta + \gamma) \right]_{0 - \frac{\pi}{2} + \frac{3\pi}{2}}^{\frac{\pi}{2} - \frac{3\pi}{2} + 2\pi} \\
&= \frac{\eta_0 \hat{u}_0^2}{\pi} \left[\frac{1}{3}(2\cos(\gamma) - \sin(\gamma)) + \frac{4}{3}\cos(\gamma) + \frac{1}{3}(\sin(\gamma) + 2\cos(\gamma)) \right] \\
&= \frac{8}{3}\cos(\gamma) \quad \text{(D.42)}
\end{aligned}
$$

For $n = 1$,

$$a_1^E = \frac{\eta_0 \hat{u}_0^2}{\pi} \left[\int_0^{\frac{\pi}{2}} - \int_{\frac{\pi}{2}}^{\frac{3\pi}{2}} + \int_{\frac{3\pi}{2}}^{2\pi} \right] \cos(\theta + \gamma) \cos^3(\theta) \; d\theta$$

$$= \frac{\eta_0 \hat{u}_0^2}{8\pi} \left[\int_0^{\frac{\pi}{2}} - \int_{\frac{\pi}{2}}^{\frac{3\pi}{2}} + \int_{\frac{3\pi}{2}}^{2\pi} \right] (3\cos(\gamma) + \cos(2\theta - \gamma) + 3\cos(2\theta + \gamma)$$

$$+ \cos(4\theta + \gamma)) \; d\theta$$

$$= \frac{\eta_0 \hat{u}_0^2}{8\pi} \left[\frac{1}{2}\sin(2\theta - \gamma) + \frac{3}{2}\sin(2\theta + \gamma) + \frac{1}{4}\sin(4\theta + \gamma) \right.$$

$$\left. + 3\theta\cos(\gamma) \right]_{0 - \frac{\pi}{2} + \frac{3\pi}{2}}^{\frac{\pi}{2} - \frac{3\pi}{2} + 2\pi}$$

$$= \frac{\eta_0 \hat{u}_0^2}{\pi} \left[\frac{1}{2}(3\pi\cos(\gamma) - 4\sin(\gamma)) - 3\pi\cos(\gamma) \right.$$

$$\left. + \frac{1}{2}(4\sin(\gamma) + 3\pi\cos(\gamma)) \right] = 0 \quad \text{(D.43)}$$

$$b_1^E = \frac{\eta_0 \hat{u}_0^2}{\pi} \left[\int_0^{\frac{\pi}{2}} - \int_{\frac{\pi}{2}}^{\frac{3\pi}{2}} + \int_{\frac{3\pi}{2}}^{2\pi} \right] \cos(\theta + \gamma) \cos^2(\theta) \sin(\theta) \; d\theta$$

$$= \frac{\eta_0 \hat{u}_0^2}{8\pi} \left[\int_0^{\frac{\pi}{2}} - \int_{\frac{\pi}{2}}^{\frac{3\pi}{2}} + \int_{\frac{3\pi}{2}}^{2\pi} \right] (-\sin(\gamma) + \sin(2\theta - \gamma) + \sin(2\theta + \gamma)$$

$$+ \sin(4\theta + \gamma)) \; d\theta$$

$$= -\frac{\eta_0 \hat{u}_0^2}{8\pi} \left[4\theta\sin(\gamma) + \frac{1}{2}\cos(2\theta - \gamma) + \frac{1}{2}\cos(2\theta + \gamma) \right.$$

$$\left. + \frac{1}{4}\cos(4\theta + \gamma) \right]_{0 - \frac{\pi}{2} + \frac{3\pi}{2}}^{\frac{\pi}{2} - \frac{3\pi}{2} + 2\pi}$$

$$= -\frac{\eta_0 \hat{u}_0^2}{8\pi} \left[\frac{1}{2}(4\cos(\gamma) - \pi\sin(\gamma)) + \pi\sin(\gamma) \right.$$

$$\left. - \frac{1}{2}(\pi\sin(\gamma) + 4\cos(\gamma)) \right] = 0 \quad \text{(D.44)}$$

For $n = 2$,

$$a_2^E = \frac{\eta_0 \hat{u}_0^2}{\pi} \left[\int_0^{\frac{\pi}{2}} - \int_{\frac{\pi}{2}}^{\frac{3\pi}{2}} + \int_{\frac{3\pi}{2}}^{2\pi} \right] \cos(\theta + \gamma) \cos^2(\theta) \cos(2\theta) \, d\theta$$

$$= \frac{\eta_0 \hat{u}_0^2}{8\pi} \left[2\sin(\theta - \gamma) + 2\sin(\theta + \gamma) + \frac{1}{3}\sin(3\theta - \gamma) \right.$$

$$\left. + \frac{2}{3}\sin(3\theta + \gamma) + \frac{1}{5}\sin(5\theta + \gamma) \right]_{0 - \frac{\pi}{2} + \frac{3\pi}{2}}^{\frac{\pi}{2} - \frac{3\pi}{2} + 2\pi}$$

$$= \frac{\eta_0 \hat{u}_0^2}{\pi} \left[\frac{1}{15}(6\cos(\gamma) - \sin(\gamma)) + \frac{4}{5}\cos(\gamma) \right.$$

$$\left. + \frac{1}{15}(\sin(\gamma) + 6\cos(\gamma)) \right] = \frac{8\eta_0 \hat{u}_0^2}{5\pi}\cos(\gamma) \quad \text{(D.45)}$$

$$b_2^E = \frac{\eta_0 \hat{u}_0^2}{\pi} \left[\int_0^{\frac{\pi}{2}} - \int_{\frac{\pi}{2}}^{\frac{3\pi}{2}} + \int_{\frac{3\pi}{2}}^{2\pi} \right] \cos(\theta + \gamma) \cos^2(\theta) \sin(2\theta) \, d\theta$$

$$= -\frac{\eta_0 \hat{u}_0^2}{8\pi} \left[2\cos(\theta - \gamma) + \frac{1}{3}\cos(3\theta - \gamma) + \frac{2}{3}\cos(3\theta + \gamma) \right.$$

$$\left. + \frac{1}{5}\cos(5\theta + \gamma) \right]_{0 - \frac{\pi}{2} + \frac{3\pi}{2}}^{\frac{\pi}{2} - \frac{3\pi}{2} + 2\pi}$$

$$= \frac{\eta_0 \hat{u}_0^2}{\pi} \left[\frac{1}{15}(6\cos(\gamma) - 4\sin(\gamma)) - \frac{8}{15}\sin(\gamma) \right.$$

$$\left. - \frac{1}{15}(4\sin(\gamma) + 6\cos(\gamma)) \right] = -\frac{16\eta_0 \hat{u}_0^2}{15\pi}\sin(\gamma) \quad \text{(D.46)}$$

For $n = 3$,

$$a_3^E = \frac{\eta_0 \hat{u}_0^2}{\pi} \left[\int_0^{\frac{\pi}{2}} - \int_{\frac{\pi}{2}}^{\frac{3\pi}{2}} + \int_{\frac{3\pi}{2}}^{2\pi} \right] \cos(\theta + \gamma) \cos^2(\theta) \cos(3\theta) \, d\theta$$

$$= \frac{\eta_0 \hat{u}_0^2}{8\pi} \left[\theta\cos(\gamma) + \sin(2\theta - \gamma) + \frac{1}{2}\sin(2\theta + \gamma) + \frac{1}{4}\sin(4\theta - \gamma) \right.$$

$$\left. + \frac{1}{2}\sin(4\theta + \gamma) + \frac{1}{6}\sin(4\theta + \gamma) \right]_{0 - \frac{\pi}{2} + \frac{3\pi}{2}}^{\frac{\pi}{2} - \frac{3\pi}{2} + 2\pi} = 0 \quad \text{(D.47)}$$

$$b_3^E = \frac{\eta_0 \hat{u}_0^2}{\pi} \left[\int_0^{\frac{\pi}{2}} - \int_{\frac{\pi}{2}}^{\frac{3\pi}{2}} + \int_{\frac{3\pi}{2}}^{2\pi} \right] \cos(\theta + \gamma) \cos^2(\theta) \sin(3\theta) \ d\theta$$

$$= -\frac{\eta_0 \hat{u}_0^2}{8\pi} \left[\theta \sin(\gamma) + \cos(2\theta - \gamma) + \frac{1}{2} \cos(2\theta + \gamma) + \frac{1}{4} \cos(4\theta - \gamma) \right. $$
$$\left. + \frac{1}{2} \cos(4\theta + \gamma) + \frac{1}{6} \cos(6\theta + \gamma) \right]_{0 - \frac{\pi}{2} + \frac{3\pi}{2}}^{\frac{\pi}{2} - \frac{3\pi}{2} + 2\pi} = 0 \quad \text{(D.48)}$$

For $n = 4$,

$$a_4^E = \frac{\eta_0 \hat{u}_0^2}{\pi} \left[\int_0^{\frac{\pi}{2}} - \int_{\frac{\pi}{2}}^{\frac{3\pi}{2}} + \int_{\frac{3\pi}{2}}^{2\pi} \right] \cos(\theta + \gamma) \cos^2(\theta) \cos(4\theta) \ d\theta = \frac{8\eta_0 \hat{u}_0^2}{35\pi} \cos(\gamma) \quad \text{(D.49)}$$

$$b_4^E = \frac{\eta_0 \hat{u}_0^2}{\pi} \left[\int_0^{\frac{\pi}{2}} - \int_{\frac{\pi}{2}}^{\frac{3\pi}{2}} + \int_{\frac{3\pi}{2}}^{2\pi} \right] \cos(\theta + \gamma) \cos^2(\theta) \sin(4\theta) \ d\theta = -\frac{32\eta_0 \hat{u}_0^2}{105\pi} \sin(\gamma) \quad \text{(D.50)}$$

For $n = 5$,

$$a_5^E = 0 \quad \text{(D.51)}$$

$$b_5^E = 0 \quad \text{(D.52)}$$

For $n = 6$,

$$a_6^E = \frac{8\eta_0 \hat{u}_0^2}{315\pi} \cos(\gamma) \quad \text{(D.53)}$$

$$b_6^E = \frac{16\eta_0 \hat{u}_0^2}{315\pi} \sin(\gamma) \quad \text{(D.54)}$$

Applying (D.42)–(D.54) to (D.35) results in:

$$\frac{C_F}{h^2} \eta \hat{u} |\hat{u}| = \frac{4\eta_0 \hat{u}_0^2 C_F}{\pi h^2} \left[\left(\frac{2}{3} + \frac{2}{5} \cos(2\theta) + \frac{2}{35} \cos(4\theta) + \frac{2}{315} \cos(6\theta) \right) \cos(\gamma) \right. $$
$$\left. - \left(\frac{4}{15} \sin(2\theta) - \frac{8}{105} \sin(4\theta) + \frac{4}{315} \sin(6\theta) \right) \sin(\gamma) \right] + \ldots \quad \text{(D.55)}$$

Appendix E

Expansion of Non-Linear Terms for a Two-Constituent Tide

If the free-surface is forced by a two-constituent tide then η and $\hat{u}$ will be given by:

$$\eta = \eta_0 \cos(\theta + \gamma) + \eta_0' \cos(\theta' + \gamma') \tag{E.1}$$

$$\hat{u} = \hat{u}_0 \cos(\theta) + \hat{u}_0' \cos(\theta') \tag{E.2}$$

where η_0 and $\hat{u}_0$ are the amplitudes of η and $\hat{u}$ for the first constituent, $\theta = \sigma t - \psi(x)$, σ is the tidal frequency for the first constituent, ψ is the phase of $\hat{u}$ for the first constituent, η_0', $\hat{u}_0'$, $\theta' = \sigma' t - \psi'(x)$ are like said for the second constituent and, $\gamma' = \psi'(x) - \phi'(x)$ is the phase difference between high water and maximum flood for the second constituent, and ϕ' is the phase of η for the second constituent. The 1D governing equations were derived in Appendices A, B & C as:

$$\underbrace{\frac{\partial \eta}{\partial t}}_{(a)} + \underbrace{h\frac{\partial \hat{u}}{\partial x}}_{(b)} + \underbrace{\frac{\partial(\eta\hat{u})}{\partial x}}_{(c)} = 0 \tag{E.3}$$

and

$$\underbrace{\frac{\partial \hat{u}}{\partial t}}_{(d)} + \underbrace{\hat{u}\frac{\partial \hat{u}}{\partial x}}_{(e)} = \underbrace{-g\frac{\partial \eta}{\partial x}}_{(f)} - \underbrace{\frac{C_F}{h}\hat{u}|\hat{u}|}_{(g)} + \underbrace{\frac{C_F}{h^2}\eta\hat{u}|\hat{u}|}_{(h)} - \underbrace{\frac{\varepsilon_0 C_T}{2}\hat{u}|\hat{u}|}_{(i)} + \underbrace{\frac{\varepsilon_0 C_T}{2h}\eta\hat{u}|\hat{u}|}_{(j)} \tag{E.4}$$

Substituting (E.1) and (E.2) into the continuity term (CT: (c) in (E.3)) and (momentum) advection term (AT: (E.4)) gives:

$$\hat{u}\frac{\partial \hat{u}}{\partial x} = -\hat{u}_0^2 \frac{\partial \psi}{\partial x}\cos(\theta)\sin(\theta) - \hat{u}_0\hat{u}_0'\frac{\partial \psi}{\partial x}\cos(\theta')\sin(\theta)$$
$$-\hat{u}_0\hat{u}_0'\frac{\partial \psi'}{\partial x}\cos(\theta)\sin(\theta') - \hat{u}_0'^2\frac{\partial \psi'}{\partial x}\cos(\theta')\sin(\theta')) \quad \text{(E.5)}$$

$$\frac{\partial(\eta\hat{u})}{\partial x} = \frac{\partial}{\partial x}(\eta_0\hat{u}\cos(\theta+\gamma)\cos(\theta) + \eta_0\hat{u}_0'\cos(\theta+\gamma)\cos(\theta')$$
$$+ \eta_0'\hat{u}_0\cos(\theta'+\gamma')\cos(\theta) + \eta_0'\hat{u}_0'\cos(\theta'+\gamma')\cos(\gamma')) \quad \text{(E.6)}$$

Applying (D.20) to (E.5) gives:

$$\hat{u}\frac{\partial \hat{u}}{\partial x} = \frac{\hat{u}_0^2}{2}\frac{\partial \psi}{\partial x}\sin(2\theta) + \frac{\hat{u}_0'^2}{2}\frac{\partial \psi'}{\partial x}\sin(2\theta')$$
$$+ \frac{\hat{u}_0\hat{u}_0'}{2}\left(\frac{\partial(\psi-\psi')}{\partial x}\sin(\theta-\theta') + \frac{\partial(\psi+\psi')}{\partial x}\sin(\theta+\theta')\right) \quad \text{(E.7)}$$

Applying the product-to-sum formulae:

$$2\cos(X)\cos(Y) = \cos(X-Y) + \cos(X+Y) \quad \text{(E.8)}$$

to (E.6) gives:

$$\frac{\partial(\eta\hat{u})}{\partial x} = \frac{\partial}{\partial x}\left(\frac{\eta_0\hat{u}_0}{2}(\cos(\gamma) + \cos(2\theta+\gamma)) + \frac{\eta_0'\hat{u}_0'}{2}(\cos(\gamma') + \cos(2\theta'+\gamma')\right.$$
$$+ \frac{\eta_0\hat{u}_0'}{2}(\cos(\theta-\theta'+\gamma) + \cos(\theta+\theta'+\gamma))$$
$$\left.+ \frac{\eta_0'\hat{u}_0}{2}(\cos(\theta-\theta'-\gamma') + \cos(\theta+\theta'+\gamma'))\right) \quad \text{(E.9)}$$

which becomes:

$$\frac{\partial(\eta\hat{u})}{\partial x} = -\frac{1}{2}\left(\eta_0\hat{u}_0\frac{\partial(2\psi+\gamma)}{\partial x}\sin(2\theta+\gamma) + \eta_0'\hat{u}_0'\frac{\partial(2\psi'+\gamma)}{\partial x}\sin(2\theta'+\gamma')\right.$$
$$+ \eta_0\hat{u}_0'\frac{\partial(\psi-\psi'+\gamma)}{\partial x}\sin(\theta-\theta'+\gamma) + \eta_0'\hat{u}_0\frac{\partial(\psi-\psi'-\gamma')}{\partial x}\sin(\theta-\theta'-\gamma')$$
$$+ \eta_0\hat{u}_0'\frac{\partial(\psi+\psi'+\gamma)}{\partial x}\sin(\theta+\theta'+\gamma) + \eta_0'\hat{u}_0\frac{\partial(\psi+\psi'+\gamma)}{\partial x}\sin(\theta+\theta'+\gamma')$$
$$\left.+ \eta_0\hat{u}_0\frac{\partial\gamma}{\partial x}\sin(\gamma) + \eta_0'\hat{u}_0'\frac{\partial\gamma'}{\partial x}\sin(\gamma')\right) \quad \text{(E.10)}$$

For the two-constituent case, one runs into a problem when attempting to substitute (E.1) and (E.2) into the quadratic friction term (QFT: (g) in (E.4)) and elevation friction term (EFT: (h) in (E.4)) and expand as a Fourier series. The terms are a function of both θ and θ', so one a can no longer expand as a series of θ. To circumnavigate this problem a mathematical trick shall be employed following Godin and Gutiérrez [1986]. First, $|\hat{u}|$ will be replaced with $\sqrt{\hat{u}^2}$, the square root will then be estimated using the Babylonian method (or Hero's method), which is an iterative algorithm used to approximate a square root. The algorithm works in the following way, first, one takes a test value, ideally as close to the actual value of the square root as possible: $m_0 \sim \sqrt{S}$. This estimate is then improved by taking the average of m_0 and S/m_0, giving m_1. This process is repeated many times with the estimate converging towards the true value. In general:

$$m_{n+1} = \frac{1}{2}\left(m_n + \frac{S}{m_n}\right) \tag{E.11}$$

where $\sqrt{S} = \lim_{n\to\infty} m_n$. Applying this to the QFT and EFT one gets:

$$\frac{C_F}{h}\hat{u}|\hat{u}| = \frac{C_F}{h}\hat{u}\sqrt{\hat{u}^2} \sim \frac{C_F}{2h}\left(m\hat{u} + \frac{\hat{u}^3}{m}\right) \tag{E.12}$$

$$\frac{C_F}{h^2}\eta\hat{u}|\hat{u}| \sim \frac{C_F}{2h^2}\left(m\eta\hat{u} + \frac{\eta\hat{u}^3}{m}\right) \tag{E.13}$$

Substituting (E.2) into (E.12):

$$\frac{C_F}{h}\hat{u}|\hat{u}| \sim \frac{C_F}{2h}\Bigg(m[\hat{u}_0\cos(\theta) + \hat{u}_0'\cos(\theta')] + \frac{1}{m}[\hat{u}_0^3\cos^3(\theta)$$
$$+ 3\hat{u}_0'\hat{u}_0^2\cos(\theta')\cos^2(\theta) + 3\hat{u}_0'^2\hat{u}_0\cos^2(\theta')\cos(\theta) + \hat{u}_0'^3\cos^2(\theta')]\Bigg) \tag{E.14}$$

Applying (D.18), (D.19) and (E.8) to (E.14) gives:

$$\frac{C_F}{h}\hat{u}|\hat{u}| \sim \frac{C_F}{2h}\left(\left(m + \frac{3\hat{u}_0^2}{2}\left(\frac{\hat{u}_0^2}{2} + \hat{u}_0'\right)\right)\cos(\theta')\right.$$

$$+ \left(m + \frac{3\hat{u}_0'}{2}\left(\hat{u}_0^2 + \frac{\hat{u}_0'^2}{2}\right)\right)\cos(\theta') + \frac{\hat{u}_0^3}{4}\cos(3\theta) + \frac{\hat{u}_0'^3}{4}\cos(3\theta')$$

$$+ 3\hat{u}_0\hat{u}_0'(\hat{u}_0\cos(2\theta - \theta') + \hat{u}_0'\cos(2\theta' - \theta))$$

$$\left. + 3\hat{u}_0\hat{u}_0'(\hat{u}_0\cos(2\theta + \theta') + \hat{u}_0'\cos(2\theta' + \theta))\right) \quad \text{(E.15)}$$

Likewise, substituting (E.1) and (E.2) into (E.13) gives:

$$\frac{C_F}{h^2}\eta\hat{u}|\hat{u}| \sim \frac{C_F}{2h^2}\left(m[\eta_0\hat{u}_0\cos(\theta + \gamma)\cos(\theta) + \eta_0\hat{u}_0'\cos(\theta + \gamma)\cos(\theta')\right.$$

$$+ \eta_0'\hat{u}_0\cos(\theta' + \gamma')\cos(\theta)] + \frac{1}{m}[\eta_0\hat{u}_0^3\cos(\theta + \gamma)\cos^3(\theta)$$

$$+ 3\eta\hat{u}_0^2\hat{u}_0'\cos(\theta + \gamma)\cos^2(\theta)\cos(\theta')$$

$$+ 3\eta\hat{u}_0\hat{u}_0^2\cos(\theta + \gamma)\cos^2(\theta')\cos(\theta) + \eta_0\hat{u}_0'^3\cos(\theta + \gamma)\cos^3(\theta')$$

$$+ \eta_0\hat{u}_0^3\cos(\theta' + \gamma')\cos^3(\theta) + 3\eta_0'\hat{u}_0^2\hat{u}_0'\cos(\theta' + \gamma')\cos^2(\theta)\cos(\theta')$$

$$\left. + 3\eta_0\hat{u}_0\hat{u}_0'^2\cos(\theta' + \gamma')\cos^2(\theta')\cos(\theta) + \eta_0'\hat{u}_0'^3\cos(\theta' + \gamma')\cos^3(\theta')]\right) \quad \text{(E.16)}$$

Applying (D.18) and (D.19) to (E.16) and rearranging gives:

$$\frac{C_F}{h^2}\eta\hat{u}|\hat{u}| \sim \frac{C_F}{2h^2}\left(m[\eta_0\hat{u}_0\cos(\theta + \gamma)\cos(\theta) + \eta_0\hat{u}_0'\cos(\theta + \gamma)\cos(\theta')\right.$$

$$+ \eta_0'\hat{u}_0\cos(\theta' + \gamma')\cos(\theta)] + \frac{1}{m}\left[\frac{3\eta_0\hat{u}_0}{2}\left(\frac{\hat{u}_0^2}{2} + \hat{u}_0'^2\right)\cos(\theta + \gamma)\cos(\theta)\right.$$

$$+ \frac{3\eta_0\hat{u}_0'}{2}\left(\hat{u}_0^2 + \frac{\hat{u}_0'^2}{2}\right)\cos(\theta + \gamma)\cos(\theta') + \frac{\eta_0\hat{u}_0^3}{4}\cos(\theta + \gamma)\cos(3\theta)$$

$$+ \frac{\eta_0\hat{u}_0'^3}{4}\cos(\theta + \gamma)\cos(3\theta') + \frac{3\eta_0\hat{u}_0^2\hat{u}_0'}{2}\cos(\theta + \gamma)\cos(2\theta)\cos(\theta')$$

$$+ \frac{3\eta_0\hat{u}_0\hat{u}_0'^2}{2}\cos(\theta + \gamma)\cos(2\theta')\cos(\theta) + \frac{3\eta_0'\hat{u}_0}{2}\left(\frac{\hat{u}_0^2}{2} + \hat{u}_0'^2\right)\cos(\theta' + \gamma')\cos(\theta)$$

$$+ \frac{3\eta_0'\hat{u}_0'}{2}\left(\hat{u}_0^2 + \frac{\hat{u}_0'^2}{2}\right)\cos(\theta' + \gamma')\cos(\theta') + \frac{\eta_0'\hat{u}_0^3}{4}\cos(\theta' + \gamma')\cos(3\theta)$$

$$+ \frac{\eta_0'\hat{u}_0'^3}{4}\cos(\theta' + \gamma')\cos(3\theta') + \frac{3\eta_0'\hat{u}_0^2\hat{u}_0'}{2}\cos(\theta' + \gamma')\cos(2\theta)\cos(\theta')$$

$$\left.\left. + \frac{3\eta_0'\hat{u}_0\hat{u}_0'^2}{2}\cos(\theta' + \gamma')\cos(2\theta')\cos(\theta)\right]\right) \quad \text{(E.17)}$$

Applying (E.8) to (E.17) and rearranging gives:

$$
\begin{aligned}
\frac{C_F}{h^2}\eta\hat{u}|\hat{u}| \sim \frac{C_F}{h^2}\Bigg(&\frac{\eta_0\hat{u}_0}{2}\left(m + \frac{3}{2m}(\frac{\hat{u}_0^2}{2} + \hat{u}_0'^2)\right)\cos(2\theta + \gamma) + \frac{\eta_0\hat{u}_0^3}{8m}\cos(2\theta - \gamma) \\
&+ \frac{3\eta_0\hat{u}_0^2\hat{u}_0'}{8m}\cos(2\theta + \gamma') + \frac{3\eta_0'\hat{u}_0^2\hat{u}_0'}{8m}\cos(2\theta - \gamma') + \frac{3\eta_0\hat{u}_0\hat{u}_0'^2}{8m}\cos(2\theta' + \gamma) \\
&+ \frac{3\eta_0\hat{u}_0\hat{u}_0'^2}{8m}\cos(2\theta' - \gamma) + \frac{\eta_0'\hat{u}_0'}{2}\left(m + \frac{3}{2m}\left(\hat{u}_0^2 + \frac{\hat{u}_0'^2}{2}\right)\right)\cos(2\theta' + \gamma') \\
&+ \frac{\eta_0'\hat{u}_0'^3}{8m}\cos(2\theta' - \gamma') + \frac{\eta_0\hat{u}_0^3}{8m}\cos(4\theta + \gamma) + \frac{\eta_0'\hat{u}_0'^3}{8m}\cos(4\theta' + \gamma') \\
&+ \frac{\eta_0\hat{u}_0'}{2}\left(m + \frac{3}{2m}\left(\hat{u}_0^2 + \frac{\hat{u}_0'^2}{2}\right)\right)\cos(\theta - \theta' + \gamma) + \frac{3\eta_0\hat{u}_0^2\hat{u}_0'}{8m}\cos(\theta - \theta' - \gamma) \\
&+ \frac{3\eta_0'\hat{u}_0\hat{u}_0'^2}{8m}\cos(\theta - \theta' + \gamma') + \frac{\eta_0'\hat{u}_0}{2}\left(m + \frac{3}{2m}\left(\frac{\hat{u}_0^2}{2} + \hat{u}_0'^2\right)\right)\cos(\theta - \theta' - \gamma') \\
&+ \frac{\eta_0\hat{u}_0'}{2}\left(m + \frac{3}{2m}\left(\hat{u}_0^2 + \frac{\hat{u}_0'^2}{2}\right)\right)\cos(\theta + \theta' + \gamma) + \frac{3\eta_0\hat{u}_0^2\hat{u}_0'}{8m}\cos(\theta + \theta' - \gamma) \\
&+ \frac{\eta_0'\hat{u}_0}{2}\left(m + \frac{3}{2m}\left(\frac{\hat{u}_0^2}{2} + \hat{u}_0'^2\right)\right)\cos(\theta + \theta' + \gamma') + \frac{3\eta_0'\hat{u}_0\hat{u}_0'^2}{8m}\cos(\theta + \theta' - \gamma') \\
&+ \frac{3\eta_0\hat{u}_0^2\hat{u}_0'}{8m}\cos(3\theta - \theta' + \gamma) + \frac{\eta_0'\hat{u}_0^3}{8m}\cos(3\theta - \theta' - \gamma') + \frac{\eta_0\hat{u}_0'^3}{4m}\cos(3\theta' - \theta - \gamma) \\
&+ \frac{3\eta_0'\hat{u}_0\hat{u}_0'^2}{8m}\cos(3\theta' - \theta + \gamma') + \frac{3\eta_0\hat{u}_0^2\hat{u}_0'}{8m}\cos(3\theta + \theta' + \gamma) \\
&+ \frac{\eta_0'\hat{u}_0^3}{8m}\cos(3\theta + \theta' + \gamma') + \frac{\eta_0\hat{u}_0'^3}{4m}\cos(3\theta' + \theta + \gamma) + \frac{3\eta_0'\hat{u}_0\hat{u}_0'^2}{8m}\cos(3\theta' + \theta + \gamma') \\
&+ \frac{3\eta_0\hat{u}_0\hat{u}_0'^2}{8m}\cos(2(\theta - \theta') + \gamma) + \frac{3\eta_0'\hat{u}_0^2\hat{u}_0'}{8m}\cos(2(\theta - \theta') - \gamma') \\
&+ \frac{3\eta_0\hat{u}_0\hat{u}_0'^2}{8m}\cos(2(\theta + \theta') + \gamma) + \frac{3\eta_0'\hat{u}_0^2\hat{u}_0'}{8m}\cos(2(\theta + \theta') + \gamma') \\
+\frac{\eta_0\hat{u}_0}{2}&\left(m + \frac{3}{2m}\left(\frac{\hat{u}_0^2}{2} + \hat{u}_0'^2\right)\right)\cos(\gamma) + \frac{\eta_0'\hat{u}_0'}{2}\left(m + \frac{3}{2m}\left(\hat{u}_0^2 + \frac{\hat{u}_0'^2}{2}\right)\right)\cos(\gamma')\Bigg)
\end{aligned}
$$

$$(E.19)$$

Appendix F

Chapter 5 Mesh Correction

The simplest approach to introducing the reasoning for the mesh correction is to present the issue with the analysis of the uncorrected mesh. In experiment 1 in Chapter 5 (§5.2) turbines are to be deployed on the contours of flood-ebb current magnitude asymmetry (FVA), as illustrated in Figure F.1 for the uncorrected mesh (Mesh-1). Across the four locations shown in Figure F.1 the element size varies considerably. The profiles of change to the amplitude and phase of the M_2, M_4 and M_6 tides, and the resulting change to the FVA, due to the turbine deployments are presented in Figures F.2–F.4.

The variation in effect across the four turbine deployments does not appear to correlate with the variation in natural FVA across the four deployment locations. The correlation in-fact appears to be with the distance the turbine is deployed from the channel centre. This is supported by the Pearson correlation coefficient, $\rho_{(X,Y)}$, and p-value between the peak values of the various change profiles and the distance from channel centre, $|\Delta \widetilde{x}|$, and the natural FVA at the location $A_{S,n}$, given in Table F.1. In the calculation of these parameters the change profile from the fixed-C_T experiment from Chapter 4 was also included to increase the number of datapoints involved in the analysis. In Table F.1 low values of $\rho_{(X,Y)}$ and high p-values suggest no relationship between $A_{S,n}$ and any of the peak change values. Higher $\rho_{(X,Y)}$ and lower p-vales hint at a possible relationship between $|\Delta \widetilde{x}|$ and the peak change values. However, only the p-values for the $|\Delta \widetilde{x}|$-$\Delta \psi_{M_2}$ and $|\Delta \widetilde{x}|$-$\Delta \psi_{M_6}$ relationships met the $p < 0.05$ criteria commonly considered strong evidence against the null hypothesis. The sample size was however only 5 points.
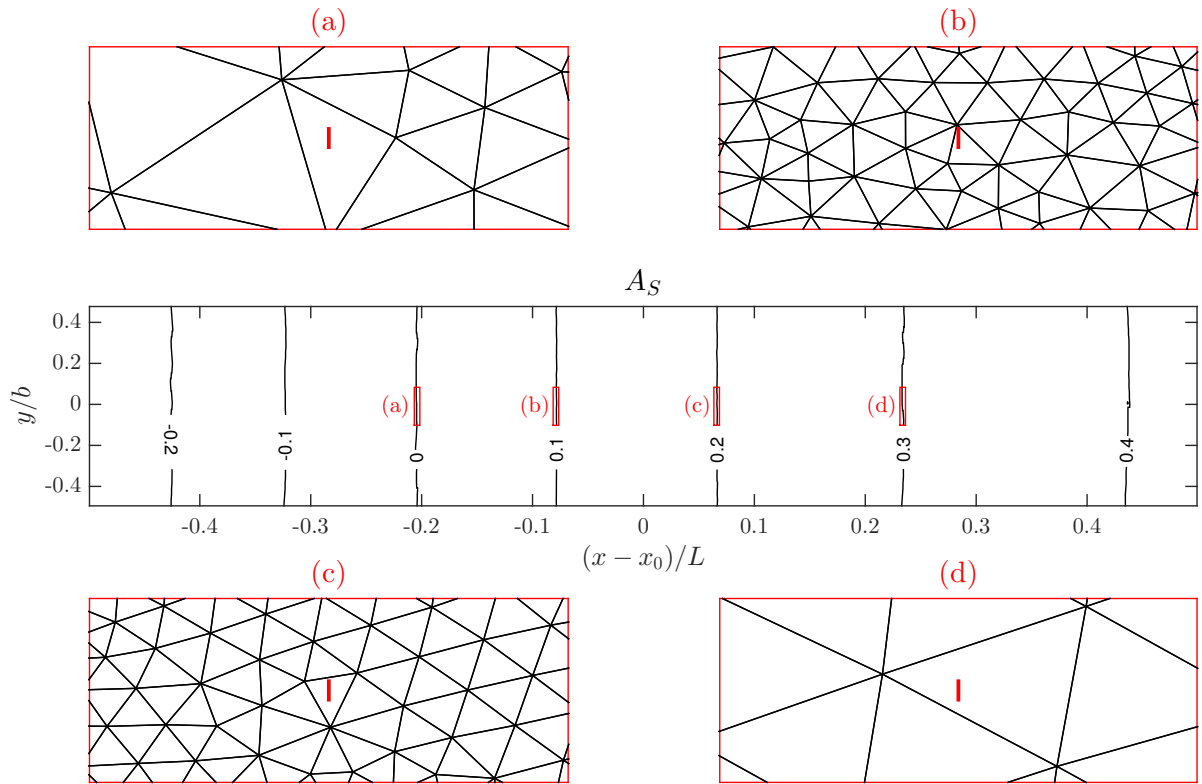
Figure F.1: Locations of turbines on asymmetry contours in Mesh-1.

Despite the stronger suggestion of a pattern between the effect of the turbines and the distance from channel centre a physical mechanism for this relationship could not be identified. However, the scaling of the element size was based on the distance from the channel centre, and comparison of Figure F.1 with Figure F.2–F.4 does hint that there may indeed be a relationship between the element size and the impact of the turbine. This subjective interpretation is supported by Pearson correlation coefficients and p-values calculated as in Table F.1 but for the element area, A_E, and the flow facing width of the element, $\Delta y_E = \max(y_E) - \min(y_E)$, presented in Table F.2.

From Table F.2 one can see that there is suggestion, by the reasonably large $\rho_{(X,Y)}$ values and reasonably low p-values between the peak change values and the flow facing width of the element, with the exception of the changes to the M_4 phase. Although the statistical significance of the relationship between turbine impact and the flow facing width of the element is on the whole weaker there is a potential
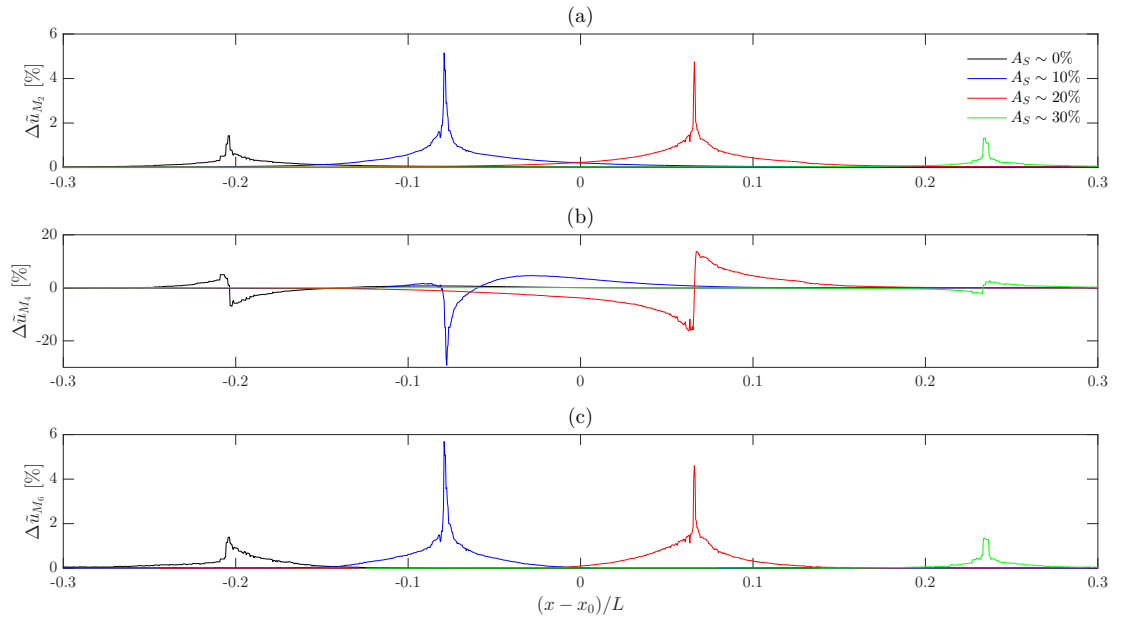
explanation for this pattern.

Figure F.2: Change to M_2 (a), M_4 (b) and M_6 (c) current amplitudes due to a single fixed-C_T turbine deployed on various asymmetry contours.
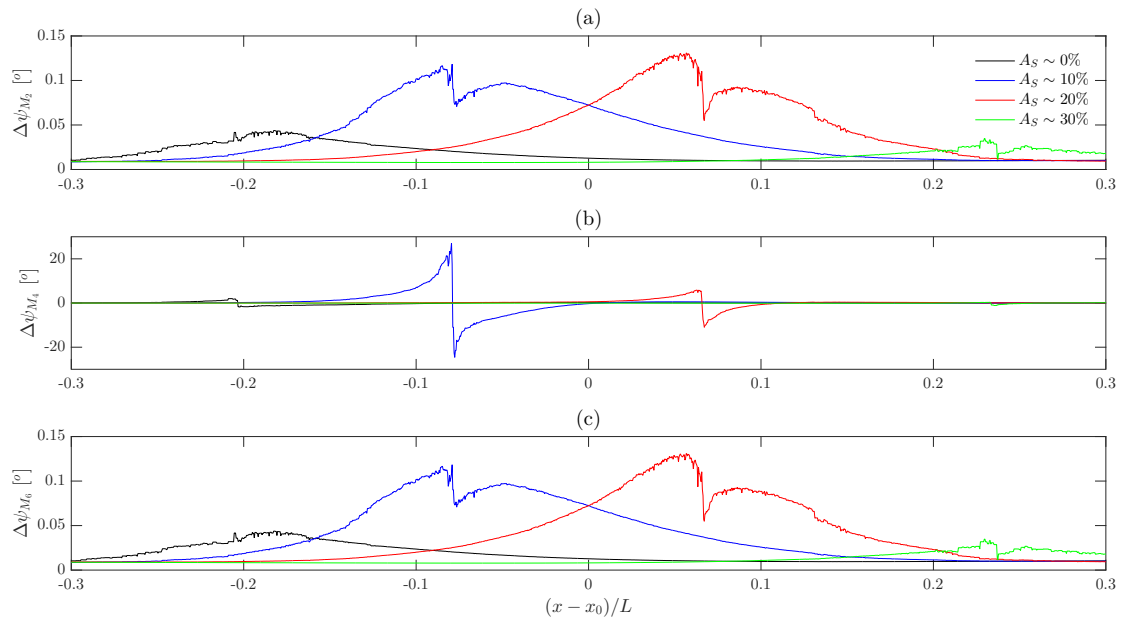

Figure F.3: Change to M_2 (a), M_4 (b) and M_6 (c) phase amplitudes due to a single fixed-C_T turbine deployed on various asymmetry contours.
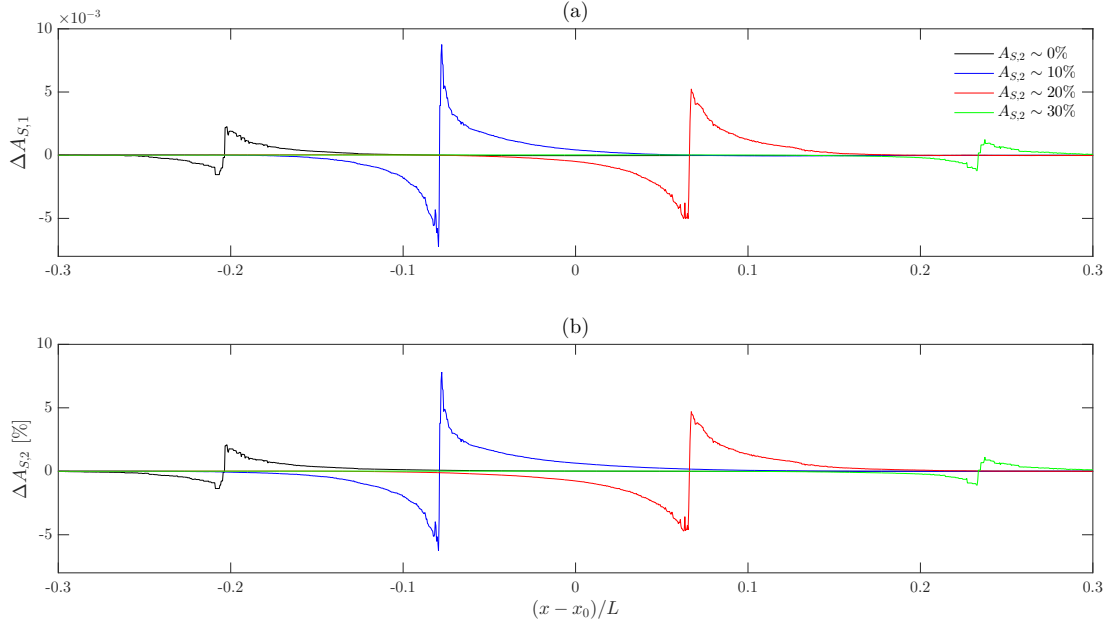
Figure F.4: Change to current FVA due to a single fixed-C_T turbine deployed on various asymmetry contours, measured by (4.2.1) (a) and (4.2.2) (b).

Table F.1: Pearson correlation coefficients, $\rho_{(X,Y)}$, between changes to harmonic analysis and asymmetry caused by turbines and the natural asymmetry, and longitudinal distance from centre at the locations of the turbines, $\Delta\widetilde{x} = (x - x_0)/L$. Colour-scale shading based on p-value, $p \leq 0.01$ – green, $0.01 < p \leq 0.05$ – yellow, $0.05 < p \leq 0.1$ – orange and $p > 0.1$ – red.

		$\Delta\widetilde{u}_{\mathrm{M_2}}$	$\Delta\widetilde{u}_{\mathrm{M_4}}$		$\Delta\widetilde{u}_{\mathrm{M_6}}$	$\Delta\psi_{\mathrm{M_2}}$	$\Delta\psi_{\mathrm{M_4}}$		$\Delta\psi_{\mathrm{M_6}}$	$\Delta A_{S,2}$	
		Max	Min	Max	Max	Max	Min	Max	Max	Min	Max
$A_{S,n}$	$\rho_{X,Y}$	-0.009	0.188	0.087	-0.029	-0.017	0.066	-0.236	-0.087	0.052	-0.11
	p	0.9886	0.7616	0.8898	0.9631	0.9778	0.9156	0.7028	0.8892	0.9339	0.8604
$|\Delta\widetilde{x}|$	$\rho_{X,Y}$	-0.946	0.936	-0.755	-0.954	-0.998	0.867	-0.75	-0.98	0.943	-0.898
	p	0.015	0.0191	0.1397	0.0117	0.0001	0.0572	0.1444	0.0035	0.0161	0.0387

The turbine representation requires modification based on the flow facing width of the element, due to the fact that in smaller elements, the local velocity diverges from the free-stream velocity for which the turbine term is defined [Kramer et al., 2014, Waldman et al., 2015]. This correction is built into the MIKE21 modelling system. The correction was however tested after the effect illustrated in Figures F.2–F.4 was discovered, by reproducing the test case from Waldman et al. [2015]

in 2D. This test case looked at the turbine thrust for a fixed steady current across a range of turbine element sizes. Testing confirmed the correction to the turbine thrust. This testing also illustrates the origin of the pattern of change seen Figures F.2–F.4.

Table F.2: Pearson correlation coefficients, $\rho_{(X,Y)}$, between changes to harmonic analysis and asymmetry caused by turbines and element size parameters. Colour-scale shading based on p-value, $p \leq 0.01$ – green, $0.01 < p \leq 0.05$ – yellow, $0.05 < p \leq 0.1$ – orange and $p > 0.1$ – red.

		$\Delta\widetilde{u}_{M_2}$	$\Delta\widetilde{u}_{M_4}$		$\Delta\widetilde{u}_{M_6}$	$\Delta\psi_{M_2}$	$\Delta\psi_{M_4}$		$\Delta\psi_{M_6}$	$\Delta A_{S,2}$	
		Max	Min	Max	Max	Max	Min	Max	Max	Min	Max
A_E	$\rho_{X,Y}$	-0.787	0.791	-0.691	-0.812	-0.895	0.449	0.101	-0.855	0.790	-0.743
	p	0.1140	0.1114	0.1967	0.0954	0.0402	0.4482	0.8717	0.0648	0.1122	0.1503
$\lvert\Delta\widetilde{x}\rvert$	$\rho_{X,Y}$	-0.887	0.0581	-0.653	0.917	-0.963	0.168	-0.251	-0.909	0.890	-0.829
	p	0.0446	0.0581	0.2327	0.0282	0.0084	0.7877	0.6837	0.0324	0.0434	0.0827

Figure F.5 shows the velocity deficit downstream of the turbine from Waldman et al. [2015] for the different element sizes tested. It shows a larger velocity deficit near the turbine for smaller elements. This is simply a resolution issue as the same momentum reduction, resulting from the same thrust exerted by the turbine, applied to a larger volume of water, and therefore larger mass, will result in a smaller reduction to the velocity of that volume of water. This then becomes an issue when the velocity deficit values are presented as a profile which says nothing of the size of the elements the data points are taken from. This is the suspected origin of variation in the turbine effect seen in Figures F.2–F.4, an artefact of the analysis rather than a physical difference in the change caused by the turbine.

To correct for this the mesh was redesigned so that the element flow facing area was approximately constant across the turbine deployment elements. The flow facing widths of the elements where the turbines are to be deployed in this new mesh are: $\Delta y_E = 30.6, 30.3, 30.4, 30.9$ and 30.8 m for the $A_{S,n} = 0, 0.1, 0.2$ and 0.3 deployments, and the deployment from Chapter 4 respectively. This is compared to values of $\Delta y_E = 176.5, 42.5, 59.0, 173.9$ and 32.3 m respectively for the original mesh.
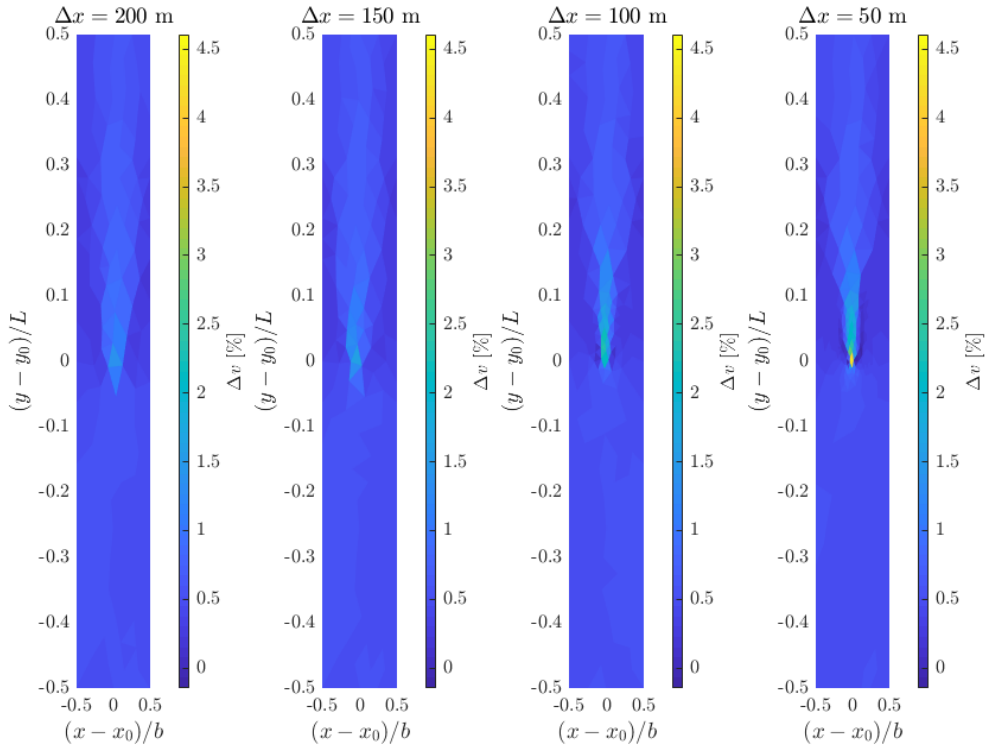
Figure F.5: Wake of $D = 20$ m, $C_T = 0.9$ turbine in a steady flow of $v_0 = 2.07$ m/s for various mesh resolutions. Meshes reproduced from Waldman et al. [2015], Figure 1.

Experiment 1 in Chapter 5 is where this effect is of greatest importance. In Chapter 4 the original mesh was used, but the turbine was always located in the same element. Likewise, in Chapter 6. Thus, comparison were always like-for-like. In the remaining experiments in Chapter 5 this effect will be at play, but to a much smaller degree as the additional turbines will always be located in the central 10 km high-resolution region of the original mesh. There will be some small variability of the flow facing width across the elements in this region, which will account for some of the variability that will be seen when looking at turbine change profiles. This variation will be quantified in the discussion around those experiments.

The equivalents of Figures F.2–F.4 obtained using the corrected mesh are given in Figures F.6–F.8. One can see from comparison of this set of figures with the those obtained using the original mesh element size pattern has been removed from the change profiles. A more detailed analysis of these figures is carried out in Chapter 5 §5.2.
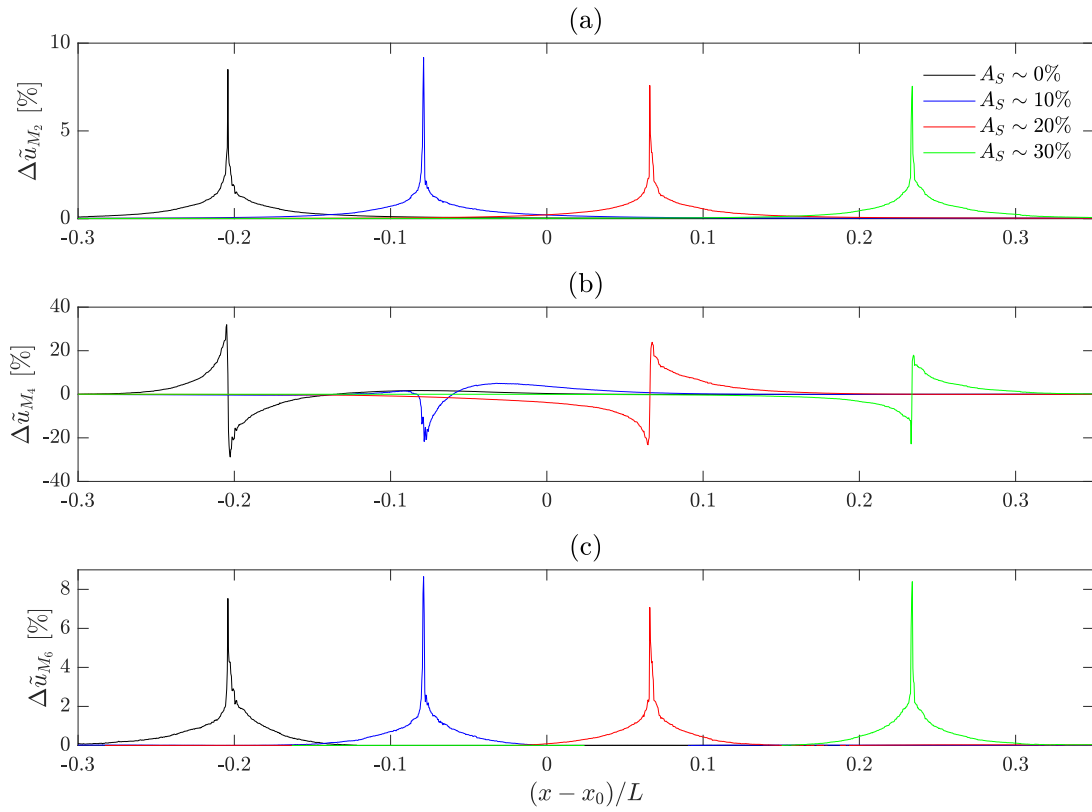
Figure F.6: Change to M_2 (a), M_4 (b) and M_6 (c) current amplitudes due to a single fixed-C_T turbine deployed on various asymmetry contours (locations shown in Figure F.1) obtained from the updated mesh.
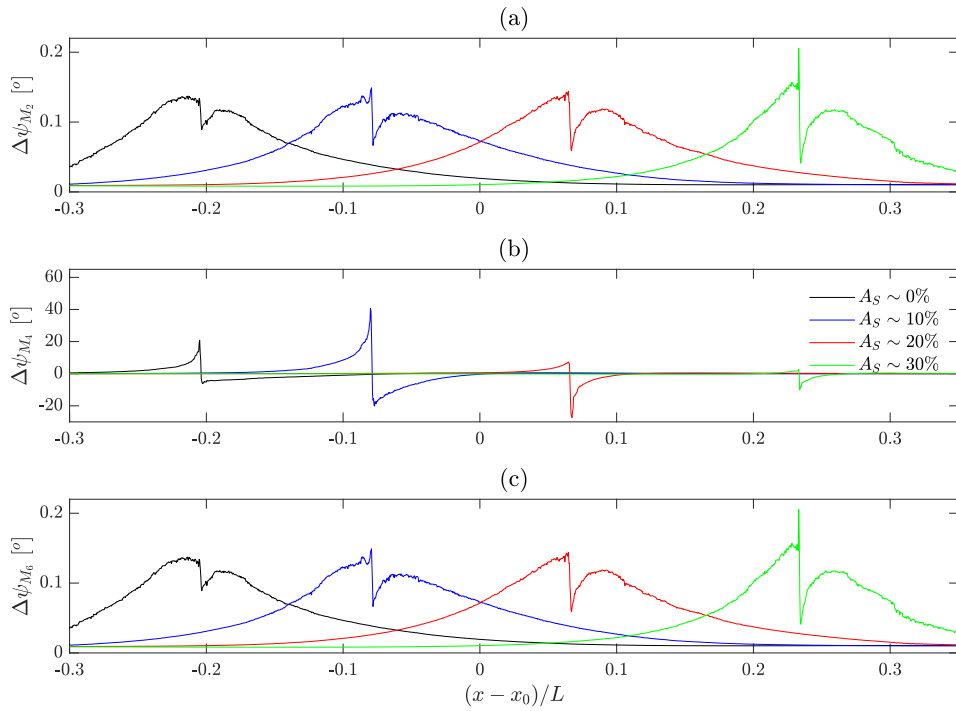
Figure F.7: Change to M_2 (a), M_4 (b) and M_6 (c) current phases due to a single fixed-C_T turbine deployed on various asymmetry contours (locations shown in Figure F.1) obtained from the updated mesh.
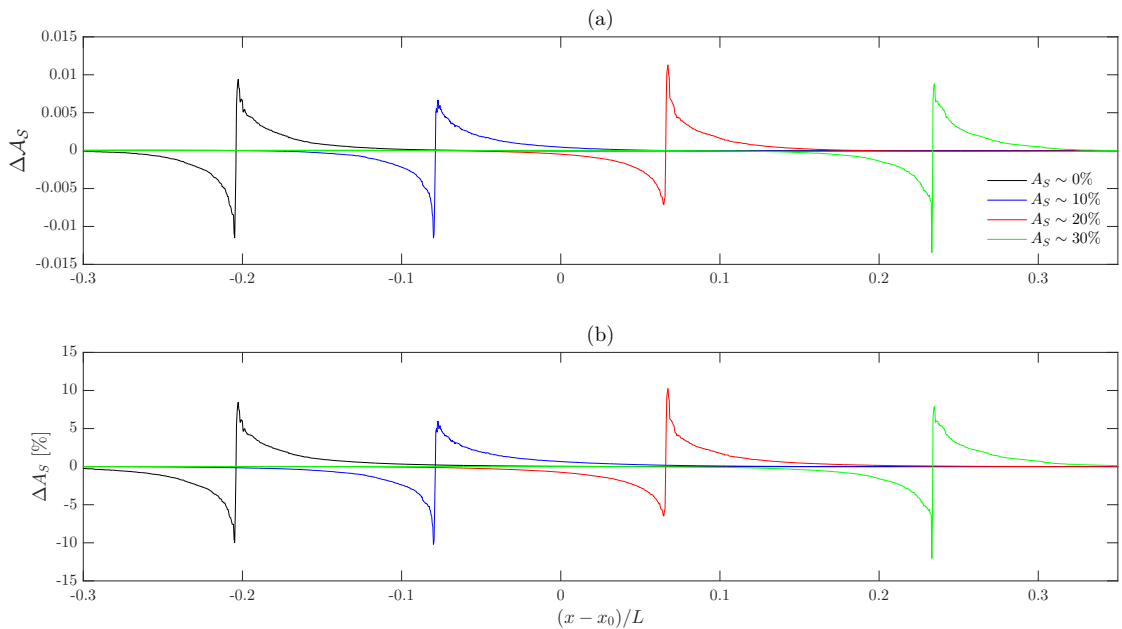

Figure F.8: Change to current FVA due to a single fixed-C_T turbine deployed on various asymmetry contours (locations shown in Figure F.1), measured by (4.2.1) (a) and (4.2.2) (b), obtained from the updated mesh.